Characterisation of CrN-NbN Superlattice Coatings, including their simulated wear debris, for total joint prosthesis bearing surface applications

Conor J. Smith

Thesis submitted to the University of Nottingham for the degree of Doctor of Philosophy

March 2022

Acknowledgements

I would like to acknowledge Zimmer Biomet and the University of Nottingham for funding my PhD. I would also like to express my appreciation to Prof. David Grant, and Dr. Colin Scotchford for their supervision, support, and endless patience during the course of this project.

I would also like to thank Julie Thompson for the advice, guidance and help within the cell laboratory and the rest of the Wolfson technical team for their assistance with laboratory and characterisation techniques over the years.

XPS characterisation of materials involving the KRATOS were performed by Dr. Emily Smith in the Nottingham Nanotechnology and Nanoscience Centre (NNNC), who I would also like to thank for their assistance.

Finally, I would like to offer my thanks to my family and friends for their support throughout this project.

Contents

List of Abbreviations

CoC	Ceramic-on-ceramic
DCMS	Direct current magnetron sputtering
DLC	Diamond-like carbon
DMEM	Dulbecco's Modified Eagle Medium
DMSO	Dimethyl Sulphoxide
EDX	Energy-dispersive X-ray spectroscopy
ELISA	Enzyme linked immunosorbent sandwich assays
FBGC	Foreign body giant cell
FBS	Fetal bovine serum
FWHM	Full width at half maximum
GM-CSF	Granulocyte macrophage colony-stimulating factor
HBSS	Hanks Balanced Salt Solution
HEPES Buffer	4-(2-hydroxyethyl)-1-piperazineethanesulfonic acid
HIPIMS	High power impulse magnetron sputtering
IFN-γ	Interferon gamma
IL-1	Interleukin-1
IL-3	Interleukin-3
IL-6	Interleukin-6
IPVD	Ionised physical vapour deposition
LAL	Limulus Amebocyte Lysate
LDPA	Laser Diffraction Particle Analysis
LPS	Lipopolysaccharide
MCP-1	Monocyte Chemoattractant Protein-1
M-CSF	Macrophage colony-stimulating factor
MFAT	Micro-fragmented Adipose Tissue Injection
MIP-1α	Macrophage Inflammatory Protein-1 Alpha
MMPs	matrix metalloproteases
MoM	Metal-on-metal
NNNC	Nottingham Nanotechnology and Nanoscience Centre
NEAA	Non-essential amino acids
OPG	Osteoprotegerin
PBS	Phosphate Buffered Saline
PCU	Polycarbonate-Urethane
PDGF	Platelet-Derived Growth Factor
PGE2	Prostaglandin E2
PIRAC	Powder immersion reaction assisted coating

PMMA	Polymethylmethacrylate
PRP	Platelet-rich plasma
PTFE	Polytetrafluoroethylene
PVD	Physical vapour deposition
RANKL	Receptor activator of nuclear factor kappa-B ligand
SCF	Stem cell factor
SEM	Scanning electron microscopy
TCP	Tissue culture plastic
THR	Total hip replacement
TMB	3,3',5,5'-tetramethylbenzidine
TNF-α	Tumour Necrosis Factor alpha
UHMWPE	Ultra-high molecular weight polyethylene
Vitamin E	α-tocopherol
XLPE	Highly crosslinked polyethylene
XPS	X-ray Photoelectron Spectroscopy
XRD	X-ray Diffraction
Y-TZP	Yttria stabilised tetragonal zirconia polycrystal
ZTA	Zirconia toughened alumina

Abstract

Total joint replacements have historically favoured a hard material for the femoral head with Ultra high molecular weight polyethylene (UHMWPE) as the material for the acetabular cup. There has recently been more interest in metal on metal (MoM) and ceramic on ceramic (CoC) pairings for total joint replacements influenced by a desire to reduce the volumes of wear debris produced by these systems as MoM and CoC pairings have generally been shown to have lower wear rates than those with a UHMWPE acetabular cup, with <0.1mm^3 per million cycles for ceramic on ceramic, 1.23±0.5mm^3 per million cycles for metal on metal and 13mm^3 per million cycles for metal on UHMWPE [1] [2] [3].

In work previously conducted by Zimmer Biomet the chromium nitride – niobium nitride (CrN-NbN) superlattice coating produced by high power impulse magnetron sputtering (HIPIMS) was identified as having significant potential yet little was known about the influence of these wear particles to influence late aseptic loosening. This coating method had already been shown to produce coatings with improved density, adhesion, surface roughness and through a HIPIMS deposition route a claimed greater control over composition, microstructure and mechanical properties of the coating produced. Such coatings are usually highly resistant to wear when compared with other materials used for articulating surfaces of joint replacements, making them of

significant interest for articulating surfaces. While this potentially leads to a joint replacement surface that produces less wear debris and has improved device lifespans it is important to investigate first in vitro then in vivo what influence such wear particles may have in terms of cytocompatibility and tissue response.

The work presented here aims to characterize the CrN-NbN coating and generated particles from that coating. The biological characterisation of the particles is of particular interest in determining the potential for osteolysis.

Characterisation of the CrN-NbN superlattice coating demonstrated droplets, pits, and seams as surface features of the coating and in the case of the droplets may be a source of wear particles. The CrN-NbN superlattice coating was shown to have a surface layer of NbN that was oxidised and an underlying layer of CrN that was partially oxidised and appears to create a passivating layer. The layer thickness of the CrN-NbN superlattice was found to be approximately 6nm for both the CrN and NbN layers.

Simulated wear debris was produced through a thermal shock method using CrN-NbN superlattice coated knee implants produced by Zimmer Biomet.

Characterisation of the CrN-NbN wear particles showed a mixture of granular and columnar particles below 10 µm in size, generally smaller particles appeared to be more granular while larger particles appeared to be columnar.

Then the potential for late aseptic loosening was investigated through analysis of the release of inflammatory cytokines by macrophages and osteoblasts in response to the coating and particles produced from the coating and compared with other commonly used implant materials.

The CrN-NbN superlattice coating surface by itself was not shown to produce higher levels of inflammatory cytokines when compared to other common implant materials such as titanium nitride or cobalt chrome in macrophages or osteoblasts. However, the particles produced from the CrN-NbN superlattice coating did however show significantly higher levels of IL-6 release in macrophages when compared to titanium nitride and alumina, with an average increased release of 914.6 pg/ml and 999 pg/ml over 7 days respectively. The particles produced from the CrN-NbN superlattice coating also showed significantly higher levels of TNF-α release when compared to titanium nitride and alumina, with an average increased release of 543.4 pg/ml and 542.2 pg/ml over 7 days respectively.

Particles produced from the CrN-NbN superlattice coating did not show a significant increase in IL-6 release from osteoblasts initially, it then however showed a significant increase when compared to titanium nitride at day 3 and when compared to alumina at day 14. The release of IL-6 was not significantly increased when compared to tissue culture plastic, however. The average increase in release of IL-6 for osteoblasts exposed to titanium nitride and alumina was 1314.8 pg/ml and 544.0 pg/ml respectively.

While these results would indicate that the potential for osteolysis and late aseptic loosening is higher in the CrN-NbN superlattice coating when compared with other available materials. This increase may be as a result of differing particle sizes, as the comparison materials are 3 µm in size while the CrN-NbN superlattice particles are in the range of <10 µm. It is however important to note that these are the results when comparing identical particle concentrations. As the material is expected to have a significantly lower wear rate when compared to other commonly used materials this may mitigate the higher release of inflammatory cytokines. An approximation of cytokine release in response to the CrN-NbN superlattice particles at expected concentrations from wear simulations, based on the results found in this research, indicate a higher TNF-α release and lower IL-6 release when compared to other commonly used materials. This should however be investigated as part of a larger study.

1 INTRODUCTION

1.1 OVERVIEW OF JOINT PROSTHESES

Total joint replacements operations involve the replacement of the joints of the musculoskeletal system. The reason for replacement of the joint typically is either as a result of severe disfunction of the joint or pain. Typically, other less invasive methods are used prior to total joint replacement as the operation often carries a risk of mortality and higher cost than some other treatments such as steroids in the case of osteoarthritis as a primary cause [4].

A total joint replacement typically involves the removal of the surfaces of the affected joint and the replacement with a prosthetic surface. These surfaces typically have a stem that is placed within the bone where the surface is being replaced to ensure that the prosthetic is secure. A wide variety of methods are used to affix these stems in place, including polymethylmethacrylate (PMMA) bone cement, roughening of the stem surface to promote bone integration and the use of porous stem surfaces to allow for bone ingrowth into the implant. The use of PMMA bone cement allows for the patient to bear weight on the affected joint immediately as opposed to after 12 weeks for uncemented total joint replacements [5]. The use of hybrid fixation has seen a significant increase in popularity since 2012 in hip replacement procedures [6]. Hybrid fixation involves cemented fixation of one bearing surface and uncemented fixation of the other, for hip implants the acetabular cup is typically uncemented.

Total joint replacements are comprised of two components minimum, designed to fit each other. Usually, the replacement is comprised of more components for ease of manufacture and to allow for different materials for different parts of the overall joint replacement. One instance is a hip replacement, as can be seen in figure 1, in which the femoral components typically have metal neck and stem pieces with a removeable head piece. This allows for the use of dissimilar materials between the femoral head and neck such as UHMWPE femoral heads, coated metal femoral heads, or ceramic femoral heads with an uncoated metal femoral neck. This also allows for differing sizes of femoral heads to be attached to the femoral neck, with larger femoral head components resulting in better stability but with lower lifetimes of the total joint replacement [7]. The other bearing surface of a hip implant, the acetabular cup, can either comprise of a shell and a liner or be of a single material.

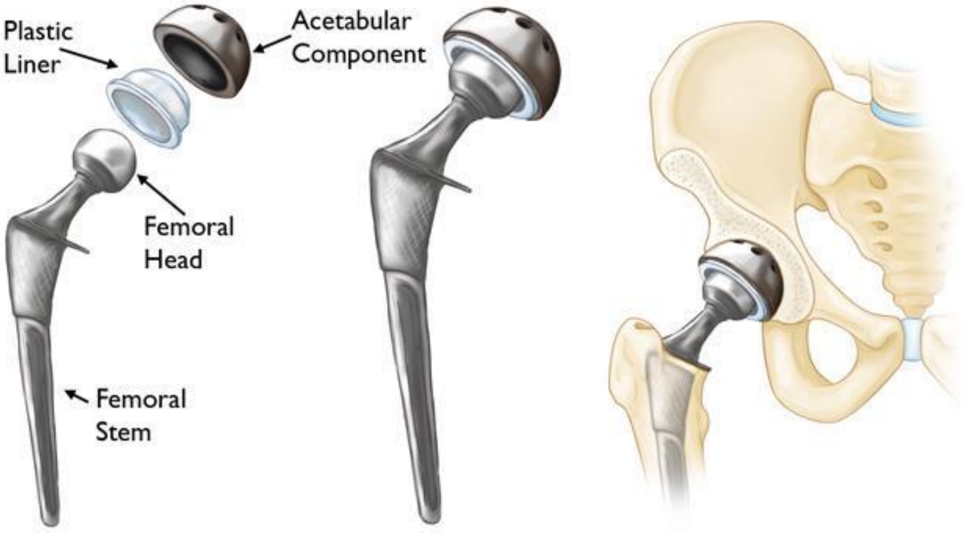

Figure 1. The components that make up a total hip replacement and the configuration in which they are implanted [8].

Knee replacements differ from the hip replacements described in the previous paragraph. They are typically composed of a single femoral component while the tibial component is typically two parts, a tibial component cemented into the bone and a bearing surface or liner, typically this is made of a polymer, as can be seen in figure 2. There is also the potential for a patellar component, usually made UHMWPE although this is not always used, there is no evidence that using a patellar component has any benefits over not using one [9].

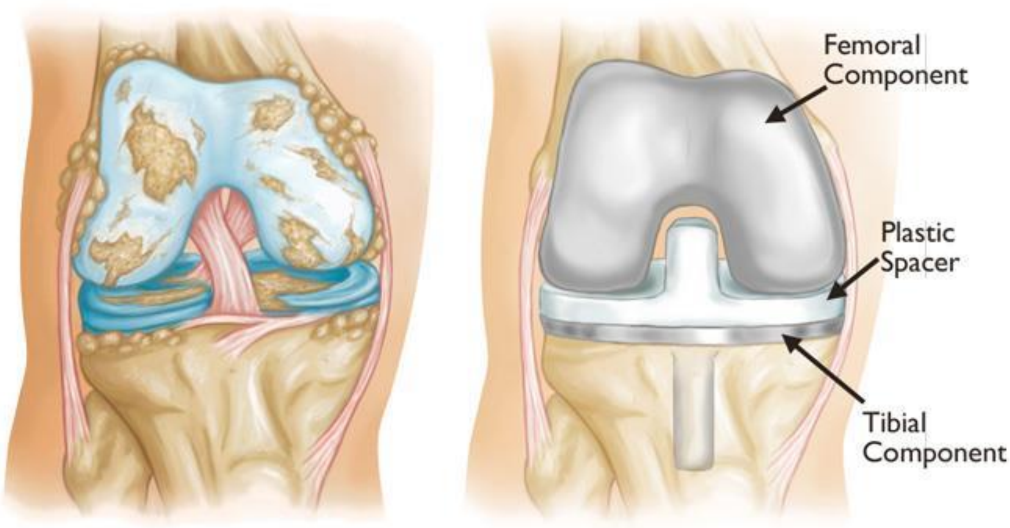

Figure 2. (left) A diagram of a knee joint damaged by osteoarthritis. (right) The components and configuration of a total knee replacement [10].

The CrN-NbN superlattice coating being characterised here is intended for use on the bearing surfaces of hip and knee replacements. Knee and hip replacements are targeted for this as they undergo more wear than other joint replacements likely as a result of the increased stress the joints are under. These types of total joint replacements are more likely to require revisions as a result of late aseptic loosening when compared to shoulder, elbow, or ankle total joint replacements. As the CrN-NbN superlattice coating is aimed at reducing wear and therefore wear debris and wear debris is linked to late aseptic loosening, it makes hip and knee total joint replacements the primary joint replacements for this type of coating [11].

1.2 DRIVERS OF THE RESEARCH

The most common cause of failure in total joint replacements is late aseptic loosening, being the reason for 48.1% of all hip revisions, 34.6% of knee revisions and 43.5% of shoulder revisions [1]. Late aseptic loosening is where a prosthesis fails through loosening without infection or mechanical cause. This is becoming a more prominent issue with an increase in the number of younger, more active patients requiring total joint replacements. In 1993 patients under 65 made up 25-32% of total joint replacements, this has increased to 40-46% in 2009 [2]. This leads to more replacements needed over the patient's lifetime, causing more risk to patients, and incurring further cost. It is therefore important to develop joint replacements that last longer before late aseptic loosening occurs or to prevent it occurring at all. Late aseptic loosening is often attributed to osteolysis induced by the presence of wear debris produced through the articulation of the joint replacement.

The number of primary hip replacements has increased from 42,796 recorded in the UK in 2004 to 92,874 recorded in the UK in 2018 [6]. This increase in primary hip replacements has however not led to an increase in the number of revision operations required.

As these total joint replacement surgeries pose inherent risk to the patients, for example up to a 1.71% risk of mortality in the 30 days following a total hip replacement in males over the age of 85 [6], as well as having a significant cost it is vital to reduce the number of these operations. While preventing these operations being required entirely is currently not feasible as the conditions leading to requiring a total joint replacement are highly varied, it is possible to reduce the number of revision operations required to reduce the risk to patients and cost associated with the operations.

The most common cause of these revision operations is late aseptic loosening, accounting for 24.3% of revisions. The next most common reason for revision surgery is adverse soft tissue reaction to particulate debris, accounting for 16.3% of revisions (it should be noted that the authors of the cited report believe this to be an underestimate due to changes in data collection) [6]. Both of these issues have a root cause in wear debris produced by the total joint replacement. This leads to a potential to reduce the number of revision surgeries required by up to 40% by achieving a significant reduction of the wear debris produced by the implants.

There has been, contrary to what would be expected, a steady decrease in the number of revision operations required, this however was linked to a decrease in the use of metal-on-metal (MoM) pairings following a peak in revision operations in 2012 [6]. MoM pairings were associated with a higher number of revisions as a result of metal sensitivity and runaway wear in some pairings [1] [11]. It would however be expected for the revision operations to begin to increase again, as a result of an increasing number of primary joint replacement operations, following the decrease as a result of fewer MoM pairings.

Superlattice coatings, multi-layered structures with alternating layers a few nm thick, applied to articulating surfaces have the potential to reduce wear significantly. This is due to the increased hardness and therefore wear resistance of these coatings when compared to ceramic coatings [12]. In particular, the CrN-NbN superlattice coating shows a low wear rate of 1.3 mg per million cycles [13], this is significantly lower than the current gold standard pairing materials, as is discussed in the literature review [14] [15] [16].

This lower wear rate is of interest for reducing the number of revision operations required through reduction in the amount of wear particles the implant will produce. A lower wear rate alone however does not necessarily mean that the material will reduce the total number of revision operations required. It is important that the material and its reduced wear debris also will not cause a significant inflammatory response, which can lead to late aseptic loosening or an adverse soft tissue reaction.

1.3 AIMS AND OBJECTIVES

The aim of this research to investigate the inflammatory response to both the CrN-NbN superlattice coating both intact and clinically relevant particles of the CrN-NbN superlattice coating. Simulating wear particles to provide an insight into how the material will perform as the bearing surface of an implant. Therefore, the following objectives were undertaken:

- Characterisation of the CrN-NbN superlattice coating surface chemistry and structure
- Investigate macrophage and osteoblast cytocompatibility and IL-6 and TNF-α release in response to CrN-NbN superlattice coating.
- Production of clinically relevant CrN-NbN superlattice particles in sufficient volumes for use in cell culture.
- Characterise simulated CrN-NbN superlattice wear particle morphology, size distribution and structure.
- Investigate macrophage and osteoblast cytocompatibility and IL-6 and TNF-α release in response to simulated CrN-NbN superlattice wear debris.

2 LITERATURE REVIEW

2.1 REASONS FOR JOINT PROSTHESES

Osteoarthritis is listed as the primary reason for total joint replacements in a large number of joint types. It is listed as the sole reason for 96.2% of primary knee replacements, and as a reason in 97.4% of procedures [6]. It is listed as the sole reason for 88.5% of primary hip replacements, 34.2% of primary elbow replacements and 61.1% of primary shoulder replacements [6].

The other reasons for total joint replacements are usually more specific to the joint. Cuff tears are another common reason for primary shoulder arthroplasty, with and without arthroplasty accounting for 28.2% and 4.3% of primary operations respectively [6]. Elbow joints replacements commonly have inflammatory arthritis other than osteoarthritis as a cause in 50.6% of cases. Hip replacements are primarily osteoarthritis but a further 3.2% of primary replacement operations are due to fracture of the neck of the femur [6].

Total ankle replacements are also a common joint to replace although less common than the others previously mentioned. The primary cause of total ankle replacement operations is not listed in the same data set as those previously mentioned, likely as the author cautions that the data is likely incomplete as a result of incomplete data collection. Other sources list trauma as the leading reason for total ankle replacements however the sample sizes are significantly smaller than the source for other joint replacement reasons

[17]. The percentage of total ankle replacements caused by trauma varies significantly between these sources from 12-88%, likely as a result of small sample sizes. Autoimmune and idiopathic are also listed as other reasons for total ankle replacements.

2.2 MODES OF FAILURE OF TOTAL JOINT PROSTHESES

There are several modes of failure for total joint prostheses, including wear (associated with 5.3% of revisions in total hip replacements), dislocation (associated with 17.1% of revisions in total hip replacements), metal sensitivity (associated with 16.4% of revisions in total hip replacements) and periprosthetic fracture (associated with 14% of revisions in total hip replacements) [18]. It is important to note that total hip replacements may have more than a single indication for revision [6]. The most common method of failure for total joint prostheses is osteolysis (associated with 24.3% of revisions in total hip replacements) [19] [6]. This osteolysis can be as a result of infection or of late aseptic loosening, which is often attributed to wear debris [20] [11].

The general wearing of the bearing surfaces aside from this catastrophic wearing also pose some significant effects on the longevity of the implants, including inducing late aseptic loosening and metal sensitivity [11]. Wearing failure of a total joint prostheses can occur as a catastrophic run away wearing of the prosthesis [1]. This run away wearing of the total joint replacements appears to occur primarily in metal-on-metal bearing surface pairings [1].

Dislocation of the total joint prosthesis occurs most frequently in the period immediately following the total joint replacement procedure [18]. The reasons that dislocation can occur in total joint replacements is primarily mechanical, as the result of patient activity or as a result of poor placement of the implant [18]. There is evidence that decreasing the implant head-to-neck ratio increases the risk of dislocation in hip replacements, alongside if the neck impinges against the liner, scar tissue or bone cement [18].

Infection of the tissues surrounding the total joint prosthesis is a risk as part of the total joint replacement procedure. The rate of infections has overall dropped as a result of decreased operation times, surgical technique and antibiotic use, however some more recent increases may be as a result of biofilm forming pathogens [18]. Low level infections also play a role in reducing the lifespan of the total joint replacement [18].

Metal sensitivity can result from metal ion release from the prosthesis [11]. It is thought that this sensitivity is mediated by the metal ions binding to proteins on the surface of dendritic cells [11]. The metal ion concentration is likely to be highest in metal-on-metal prostheses which produce primarily metal wear debris, which significantly increases the surface area of metals for ions to leech from [11]. This leads to synovitis and necrosis around the total joint prosthesis and increased blood ion concentrations [18].

Periprosthetic fractures are associated with a high mortality rate for patients [18]. The incidence of these fractures also increases as patient longevity does which may contribute to the high mortality rate for this particular method of failure [18]. These periprosthetic fractures are at higher risk of occurring if the procedure is a revision procedure, this is likely to be as a result of damage to the bone tissue from previous procedures and the manner in which the previous prosthesis failed [18]. Other risk factors for this method of failure include many conditions that weaken the bone such as osteoporosis and osteoarthritis [18].

2.2.1 Late Aseptic loosening

Late aseptic loosening is the loosening of the prosthesis without the presence of infection or any other failure mechanism. This failure is often attributed to wear debris leading to a cascade of inflammation, osteoclastogenesis and reduced osteoblast functionality [18] [21] [22]. Late aseptic loosening typically occurs 10-20 years following the joint replacement operation [22].

Late aseptic loosening typically starts with the generation of wear debris from the articulating surfaces of the joint replacement, along with other interfaces such as the prosthesis-bone interface [22] [23]. These particles have a wide array of morphologies, sizes and compositions depending on the materials used in the prosthesis, although typically most wear debris is under 5 µm [22]. The cell response to the wear debris is dependent on the size and morphology of the particles [22] [24] [25]. It has been shown that particles with a sufficiently high surface area to volume ratio can lead to cell damage and death in macrophages [24]. The primary size range for particles phagocytosed by macrophages, osteoblasts or fibroblasts is 0.1-10 µm [22] [26]. The interaction between these cells and the particles leads to the release of proinflammatory cytokines as well as cytokines that promote osteoclastogenesis, such as RANKL, and decrease osteoblast function, although this may also be as a result of particle interactions directly with osteoblasts [22] [25] [26] [27]. The changes in osteoclast and osteoblast activity as a result of this leads to bone resorption around the site of the implant, leading to loosening of the implant. It is important to note that this response is ongoing during the lifetime of the joint prosthesis, as a result of the wear debris typically being resistant to enzymatic digestion [22].

2.3 WEAR DEBRIS AS THE ISSUE

It is well documented that late aseptic loosening is the most common cause of failure in total hip replacement (THR) [19]. This is often attributed to the presence of UHMWPE wear debris produced through the articulation of the THR [20]. Substantial research has been done into the biological effects of wear debris of various types and this has identified several possible areas that may cause this effect as well as showing the mechanisms through which osteolysis occurs.

The particles of wear debris produced have been characterised in a number of different papers. There does not seem to be a consensus on the size range of the wear debris produced as this differs from material to material [11] [23]. The size range of most importance has, however, been discovered to be below 10 µm, as any wear debris above this range has a much-reduced effect on macrophages and other cells in the periprosthetic tissue [24] [11] [25] [28]. While most studies report that there is little wear debris produced below 1 µm size it is possible that this is a limitation of the light microscopy methods used to measure the wear debris [11]. It has, however, been shown that UHMWPE wear debris does produce nanoparticle sized wear debris in vivo, even showing that most of the wear debris produced was nanoparticle sized [2] [28]. It is possible that in the studies showing mainly micron sized wear particles that either the techniques used to measure the size was unable to resolve particles below micron size, or the methods used in tissue digestion/sample preparation caused the agglomeration of particles [28] [11]. Nanometre sized wear debris has been recovered in patients with metal-on-metal hip implants, indicating that nanometre wear debris is produced in vivo [11]. The nanometre size range wear debris has also been shown to move through lymphatic tissue and cause damage to lymph nodes where it may build up and cause issues such as lymphadenopathy, sinus histiocytosis, necrosis and fibrosis in the lymph node [11]. Generally size ranges for wear debris averages seem to vary between 1-10 µm depending on the materials [25] [11] [23]. Typically, the larger sized wear particles account for the majority of the volume of wear but only a small number of the particles generated [11]. Examples of sizes and morphologies of wear particles produced by total joint prosthesis can be found in table 1.

Particle Material	**Material Pairing**	**Size**	**Morphology**	**Source**
Various metal	Metal-on-metal	51-116 nm	Rounded, slight elongation	[11]
UHMWPE	UHMWPE - CoCr	0.1-2.0 µm	Spheroid	[29]
UHMWPE	UHMWPE - CoCr	0.2-0.3µm wide and up to 10µm in length	Clusters joined by fibrils	[29]
UHMWPE	UHMWPE - CoCr	1-3µm in diameter and 20-200µm long	Rolled plates	[29]
Ti	Stem material	200-400µm in length and 10-20µm thick	Plates	[29]
Ti	Stem material	300-400µm	Wire-like	[29]
TiN	TiN-TiN	3.3 – 840.3 nm	Not disclosed	[30]
CrN	CrN-CrN	2.5 – 15.2 nm	Not disclosed	[30]
CrCN	CrCN-CrCN	3.5 – 17.9 nm	Not disclosed	[30]
CoCr	CoCr-CoCr	19 - 106 nm	Rounded oval – Spike shaped	[31]
Alumina	Alumina-Alumina	5 – 90 nm	Shard-like	[32]
Alumina	Alumina-Alumina	0.05 – 3.20 µm	Polygonal	[32]

Table 1. Showing the material, size and morphology of retrieved particles produced through the wear of bearing surfaces.

2.4 HOW THE PROBLEM CAN BE ADDRESSED

One of the clearest solutions to addressing the problem of late aseptic loosening is to minimise the production of wear debris that leads to this ongoing process of osteoclastogenesis and inflammation. This can primarily be achieved by producing joint prostheses that have low wear rates, this is also apparent as a solution based on the amount of research into producing surfaces with low wear rates [3] [33] [34] [35] [36]. Typically, these rely on using materials harder than traditional metal on UHMWPE joint prostheses, such as pairing metal-on-metal or ceramic-on-ceramic or using XLPE. There is also a possible avenue of ceramic-on-metal pairings although this does not appear to have been heavily explored [37].

2.5 BEARING SURFACE PAIRS AND MATERIALS IN TOTAL JOINT REPLACEMENT

XLPE is a more wear resistance material when compared to UHMWPE, showing roughly 87% less wear when compared to UHMWPE [1]. This improvement in wear resistance does, however, come with a trade-off in fatigue fracture resistance and oxidation resistance [38]. XLPE has recently replaced UHMWPE as the gold standard for total joint replacements that use a polymer as one of the bearing surfaces [39].

Total joint replacements that use ceramic-on-ceramic bearing surfaces have also emerged as one option to reduce the amount of wear produced and reduce the potential for late aseptic loosening. These types of bearing pairs typically do produce significantly reduced wear rates, typically <0.1mm^3 per million cycles [1] [2]. They do however have the capacity to produce significantly increased wear rates under certain circumstances such as where the femoral neck of a hip replacement impinges on the acetabular cup [11].

Metal-on-metal total joint replacements were a focal point of research for a time although this appears to have slowed down significantly recently [6]. This is likely as a result of the high revision rate for these pairings and generally worse performance than other pairings [6]. This is despite metal-on-metal prostheses generally having low wear rates, roughly 1.23±0.5mm^3 per million cycles [2]. This is, however, not consistent with metal-on-metal pairings showing significant variation in the wear rates, sometimes resulting in run-away wearing of the joint prostheses [1]. These metal-on-metal pairings result in a significantly higher number of particles when compared to metal-on-UHMWPE pairings, despite the lower wear rate [11]. This means that the particles produced by the metal-on-metal pairings must be significantly smaller than those produced by metal-on-UHMWPE, which is also found in the literature [21] [37] [11]. This results in a very large surface area through which metal ions can leach into the surrounding fluid, leading to a high metal ion concentration around the implant [19]. This can lead to metal sensitivity which can significantly reduce the lifespan of these joint prostheses [11]. The metal leaching ions is also of concern as some metal ions can cause more damage than others. Cobalt ions are of significant concern as they can result in cell necrosis at high concentrations or apoptosis at lower concentrations [11]. This is not the only mechanism through which the nano-size metal wear debris may cause tissue damage though as commercially pure titanium particles were shown to cause significant levels of DNA damage and apoptosis in mesenchymal stem cells [40]. This also leads to the potential that the metal wear debris may have carcinogenic effects [40]. While not statistically significant it should be noted that one study saw an increase in the incidence of leukaemia by 3.8% in patients with metal-on-metal prostheses when compared to metal-on-UHMWPE [11].

While metal components provide good strength and are not prone to sudden failure in the same manner that ceramics are the metal-on-metal pairings have significant drawbacks that the ceramic-on-ceramic pairings do not have. One potential solution to this is to coat the metal components in a metal-on-metal pairing with a ceramic in order to reduce the metal ion leaching and metal wear debris produced by the pairing. This does introduce another risk, delamination, so good adhesion of the coating to the substrate is vital.

2.6 MATERIALS USED IN JOINT PROSTHESES

Joint prostheses are often described based on the material used in the bearing surface of the joint. It is the convention to list the material of the femoral head before the acetabular cup [6]. Typically, these are kept to the type of material such as metal or ceramic and often abbreviated such a MoM referring to metal on metal prostheses.

Several coating materials are used in total joint replacements, historically PTFE was used to reduce the coefficient of friction of the bearing surfaces however this is no longer used as a result of the poor wearability of PTFE [5]. While coefficient of friction of these materials is taken into account, generally coatings used in the bearing surfaces of total joint replacements have high hardness to reduce the production of wear debris. This section will review types of materials currently in use or under investigation for use.

2.6.1 Polymers

Polymers are commonly used as a material for the liner of the acetabular cup. Across all combinations of bearing surfaces the acetabular cup is made from polymers in 73.7% of all pairings. This is due to UHMWPE's inertness, impact and abrasion resistance and lubricity [41]. Typically, the polymers used, particularly for bearing surfaces are ultra-high molecular weight polyethylene (UHMWPE) or highly crosslinked polyethylene (XLPE). Historically a polytetrafluoroethylene (PTFE) coating has also been used as the bearing surface in some implants. However, this is no longer common practice as those components suffered from poor wear resistance (as high as 0.5mm per month) and warping [5, 42].

UHMWPE is comprised of polyethylene molecules with a molecular weight of 2-6 million atomic mass units (u), varying depending on the usage, formation and processing the part must undergo. These long-chained polyethylene molecules typically have a crystallinity of 58-75% [43], it is noted that an increase in crystallinity increases the resistance of the UHMWPE to fatigue crack propagation [43]. UHMWPE became widely used for the bearing surface of total joint replacements in the 1970s, typically against a metal or ceramic bearing surface [39].

XLPE is another polymer used for the bearing surfaces of total joint replacements. Cross-linking of the polymer chains in XLPE leads to better wear resistance (up to 87% less wear than UHMWPE) of the material but at the cost of decreased fatigue fracture resistance, with a decrease in crack driving force (ΔK_{incep}) of 35% at 50kGy, a reduction of 51% ΔK_{incep} at 100kGy, and a reduction of 61% ΔK_{incep} at 200kGy [38, 1, 44]. There is also potential for decreased oxidation resistance if the cross-linking of the polymer is produced through radiation methods as this is at risk of creating free radicals in the polymer [38, 33]. These free radicals are usually stabilised by doping the XLPE with vitamin E (α-tocopherol) as a result of its free radical scavenging [33]. As the cross linking reduces polymer chain mobility this results in a decrease in the toughness of the XLPE when compared to UHMWPE [45]. XLPE also shows improved fatigue crack propagation when compared to UHMWPE, likely as a result of reduced polymer chain mobility [33]. Examples of the polymer chain structures of various polyethylene polymers can be seen in figure 3. UHMWPE has more recently been replaced by cross linked ultra-high molecular weight polyethylene (XLPE) as the gold-standard in joint replacements as it shows higher wear resistance than UHMWPE [39].

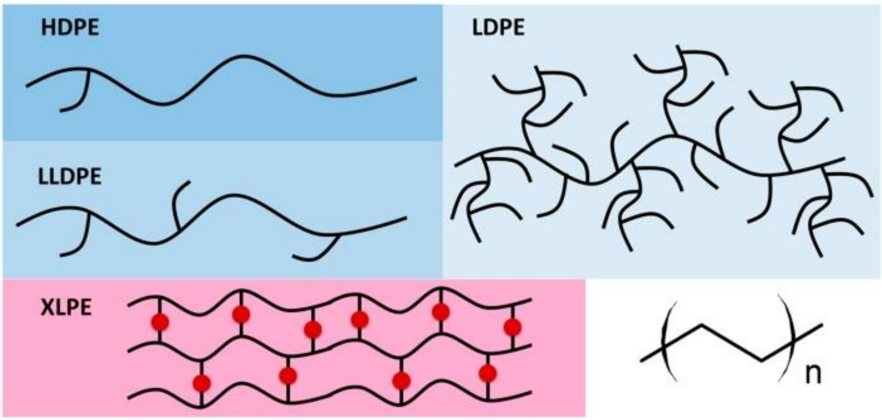

Figure 3. The polymer chain structure for various polyethylene polymers, UHMWPE is not shown here but is similar to HDPE [46].

Polycarbonate-Urethane (PCU) has been largely researched in efforts to mimic native articular cartilage. It has a very low coefficient of friction when compared to UHMWPE and showed lower wear rates, approximately 77.2% lower, than UHMWPE when paired with a CoCr femoral head in hip simulators [42] [47]. It is however also prone to producing a squeaking sound, lowering patient quality of life, similarly to alumina [42].

PMMA is also a common polymer used in total joint replacements although it is typically not used for the joint replacement itself but as a cement between the component and the surrounding bone. As the PMMA must cement the component to the bone this means that the PMMA must be cured in vivo. This poses a few issues as the monomer that is used to create PMMA has high cytotoxicity, and the curing reaction is highly exothermic, potentially damaging the surrounding tissue [48]. PMMA however is widely used as bone cement despite this as it produces a good bond with the component, conforms to the space between the component and the bone and evenly distributes the load between the bone and the joint replacement [48]. Powdered polymer is mixed with the monomer to reduce the increase in temperature as less material must cure [43]. X-ray contrast mediums such as zirconium dioxide or barium sulphate are also included to ensure the bone cement shows up on x-rays [43].

2.6.2 Metals

Historically, metallic components have been made with stainless steel, namely 316L stainless steel, as a result of the materials good biocompatibility, corrosion resistance, and high strength. However, stainless steel components do suffer as a result of having a significantly higher elastic modulus (200 GPa) than bone (18 GPa) [43, 5]. This leads to stress shielding of the surrounding bone where the load is taken off of the bone surrounding the implant. As increased stress promotes bone formation the removal of this results in reduced bone formation around the joint replacement and contributes to loosening of the components [5]. Stainless steel components are also less corrosion resistant than other used materials, despite forming a surface layer of highly adherent Cr_2O_3 that provides a passivating layer [5]. Typically, if a stainless-steel component does begin to corrode it does so through pitting, crevice, and galvanic corrosion [5]. As a result of this less-than-optimal corrosion resistance they are more often used for temporary medical devices such as screws and plates to fix fractures [49]. There is also concern about the toxicity of nickel ions released from stainless steel components as these can be cytotoxic and potentially lead to a hypersensitivity to nickel [49] [50] [51].

Cobalt-chromium alloys are also used for total joint replacements, one significant one being CoCrMo. These alloys are stronger and more corrosion resistant than stainless steel, however, as they have a slightly higher elastic modulus (240-250 GPa) than stainless steel, they are slightly more likely to cause stress shielding [43, 5]. There are four types of CoCr alloys recommended for use in biomedical applications, cast CoCrMo alloy (F75), wrought CoCrWNi alloy (F90), wrought CoNiCrMo alloy (F562), and wrought CoNiCrMoFe alloy (F563) although F75 and F562 are currently the most commonly used of the four [49]. There is, however, concern relating to the release of nickel ions from the F562 alloy as a large number of nickel ions are initially released from the alloy, which can lead to a hypersensitivity to nickel. [49] [50] [51].

Titanium alloys have been extensively used, Ti 6-Al 4-V in particular has seen significant use as a material for total joint replacements [43]. As these alloys have an elastic modulus (110 GPa) roughly half that of stainless steel or cobalt-chromium alloys they are less likely to cause stress shielding [43, 5]. Titanium alloys have also shown excellent biocompatibility and osseointegration, producing an excellent bond between the component and the surrounding tissue [43]. These properties along with the alloys high strength and corrosion resistance make it an excellent material for total joint replacements [43]. They are however limited by poor wear resistance, having significant material loss as a result of articulation, leading to them largely being used for other parts of total joint replacements such as the stem of hip replacements rather than articulating surfaces [52] [42].

2.6.3 Ceramics

Ceramic materials are often used in the bearing surfaces of the total joint replacements, having high hardness, and producing fewer wear particles leading to reduced tendency for osteolysis [5, 53]. Alumina is a common material for this as it has high hardness and fracture toughness while showing good biocompatibility [43]. Alumina also shows high resistance to third body wear as a result of its high hardness [54]. Alumina also shows excellent stability in a biological environment with minimal corrosion or degradation [43]. As evidenced by the lack of ion release from either bulk material or the wear debris [54]. As a result of this stability and low reactivity alumina often invokes very little biological reaction, leading to alumina often being used as a reference in biological testing [54]. Alumina also demonstrates better wettability than polymers and metals, leading to better frictional properties [54]. This increase in wettability is also associated with the alumina surface being quickly coated in serum proteins upon implantation [54]. These alumina components can also be toughened by additions of zirconia up to 25% by weight, these are commonly known as zirconia toughened alumina (ZTA) [54]. Alumina does however suffer from concerns about noise production and its poor strength under tension [42].

Zirconia is another ceramic material that can be used, usually as a bearing surface of the joint. The form of this Zirconia is typically Yttria stabilised tetragonal zirconia polycrystal (Y-TZP) [54]. The high toughness of Y-TZP is linked with the phase transition of tetragonal grains to monoclinic, which expand by 3-4% in volume, dissipating the fracture energy [54]. There are however concerns about this phase transition occurring through thermal degradation, increasing the risk of fracture, and reducing the wear resistance of the component [42]. Zirconia also has superior wettability compared to metallic components, leading to a fluid film being possible at the bearing surfaces, improving performance of these components [54].

While hydroxyapatite is not used as the bulk material for total joint replacement components, it has been used as a coating to improve osseointegration of components [43]. Typically, this is applied to a roughened or porous surface to further improve the bond between the component and the bone [43]. The thickness of these hydroxyapatite coatings is between 50-

110 µm, thicker coatings are not used as they become brittle and thinner coatings tend to resorb too fast for proper osseointegration [55]. These coatings are also required to be of at least 62% crystallinity and a crystallinity of around 70% has proven most effective [55]. While these coatings promote osseointegration of the component they do have a risk of worsening late aseptic loosening as particles of hydroxyapatite may be released from the coating [56].

Titanium nitride coatings, typically with titanium alloy as a substrate, show excellent properties for the bearing surface of a total joint replacement. Titanium nitride coatings show decreased UHMWPE and metal wear debris production, in both metal-on-polymer and metal-on-metal pairings, when compared with other materials, reducing the potential for late aseptic loosening [57, 58]. The TiN coatings also show increased surface hardness and increased fretting resistance [57]. They are, however, not very resistant to third-body wear, particularly for metal-on-metal pairings, especially in areas where the softer substrate may become exposed through delamination of the coating [59]. This may increase the amount of wear of the other bearing surface as it was found the TiN coatings caused higher wear rates for the paired surfaces than other materials [19]. Delamination is a significant risk with metal-on-metal TiN coatings, particularly through coatings produced through conventional physical vapour deposition (PVD) methods. As a result, research is largely focused on improved TiN coating production methods. One such example is powder immersion reaction assisted coating (PIRAC). PIRAC nitriding, briefly, involves immersing samples in unstable nitrides (such as Cr_2N) and heating the samples to thermally decompose the nitride, producing a moderate pressure of reactive nitrogen [36]. TiN coatings do show impressive biocompatibility however overall, indicating that there is potential for TiN to become more common if adhesion issues are solved [60].

Diamond-like carbon (DLC) is a coating that was considered for the bearing surface of joint replacements as it has high corrosions resistance and high hardness. This leads to a reduced wear rate of the coated component [19], however, it was found to be prone to failure through late aseptic loosening in early clinical studies as a result of increased polyethylene wear as a result of abrasive DLC particles [42].

Silicon nitride coatings have also been of interest in more recent research, demonstrating high hardness, high flexural strength, and biocompatibility similar to alumina [42, 35]. It has been shown to have very low wear rates, particularly when articulating against another Silicon Nitride bearing surface [35] [34]. Silicon nitrides are also predicted to slowly dissolve in polar solvents and, as such, the wear debris would slowly be resorbed, reducing the potential for late aseptic loosening as this is linked with wear debris production [34].

CrN-NbN superlattice coatings have not been previously used as the bearing surface of total joint replacements. Though they show a high hardness of 24±3 GPa and low wear rate of 1.3 mg/$1x10^6$ cycles, making it an ideal material for a bearing surface [13] [61]. There is significant research into the corrosion behaviour of the material, showing excellent potential corrosion resistance in theory while in practice surface defects can lead these materials to corrode more quickly than expected, a schematic of these defects and the corrosion mechanisms can be seen in figure 4 [62]. There is currently little research into the biocompatibility of these coatings.

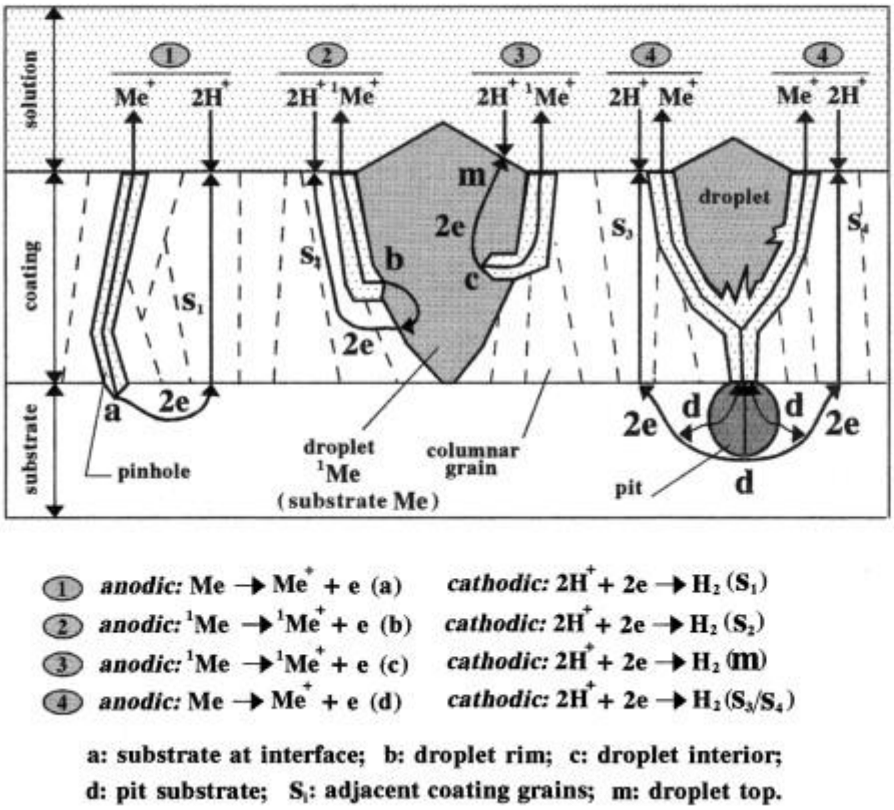

Figure 4. Schematic diagram outlining the corrosion mechanisms of macroparticle and growth defects (reaction 2 and 3) and the galvanic corrosion of the substrate associated with these (reaction 4) and other defects such as droplet shrinkage pinholes (reaction 1) [62].

2.7 WEAR DEBRIS FROM JOINT PROSTHESES

The bearing surfaces of total joint replacements produce wear debris, which is small particles of material that have been removed from the bearing surface along with the interface between the total joint replacement and the bone. The mechanisms through which wear debris generation occurs is varied across different materials and material pairs. UHMWPE are typically thought to produce wear particles through large plastic strain at the surface, however, if paired with a TiN bearing surface that exhibits delamination it is likely to produce wear through third body abrasive wear [39].

Historically, up until at least 2000, late aseptic loosening was linked with particles of bone cement and thought that bone cement was the cause of it [43]. It is now known, however, that wear particles can come from many of the interfaces involved in a total joint replacement.

Usually, the softer material in the pairing of bearing surfaces tends to have a more significant effect on the wear rate of a total joint replacement [24] [1]. This leads to the majority of the wear debris originating from the softer material [29]. Wear debris from the other components is, however, still found but does not make up a significant proportion of the wear debris. For instance, in low carbon wrought cobalt chrome alloy femoral heads articulating on high carbon wrought cobalt chrome alloy acetabular cups the particles were found to be 75% low carbon wrought cobalt chrome [63].

The wearing of ceramic-on-ceramic pairings has shown an initial ‘run-in’ stage of wear lasting for approximately a million cycles before a slightly reduced wear rate during the ‘steady state’ of wear is accomplished [3]. Metal-on-polymer and ceramic-on-polymer also showed this ‘run in’ stage of wear although this is significantly shorter, typically in the order of tens of thousands of cycles [64].

The wear of materials themselves has been extensively researched and it has been concluded that there are different stages of wear for metal-on-metal pairings. The initial ‘running in’ stage of wear lasts for approximately 0.5×10^6 cycles and is a stage of accelerated wearing of the component [3] [20]. After this stage there is a linear lower wear rate provided that there is no third body wear occurring [3] [20]. The wear rate is often shown to decrease threefold by volume during this steady state wear [3]. This clear change in the wear rate does not seem to occur as distinctively in other pairings [3]. It was found that the wear debris produced during this initial ‘running in’ stage of wear is much larger than wear debris produced after the first 0.5×10^6 cycles [24]. This larger debris is not thought to contribute to inflammation and osteolysis as it often is above the critical size range to activate macrophages, the critical size range is thought to be between 0.1-10 µm [24].

While metals have a period of accelerated wear this does not mean that they produce more wear than other pairings, it has been noted that by volume metal on metal pairings produce up to 100 times less wear debris than metal/ceramic on UHMWPE [20]. Ceramic coatings on these materials produce even further reduced volumes of wear debris [1]. Ceramic on ceramic pairings have showed further lowering of wear volumes, roughly 50 times lower than the metal-on-metal pairings [1]. There has been concern as to the reliability of some of these pairings with both metal on metal and ceramic on ceramic pairings sometimes showing much higher wear rates than average [1]. The wear rates of the material have a good correlation to the biological reaction to the implant, with implants wearing more than 0.2mm/year producing a much higher incidence of osteolysis in the implants than those with a wear rate of less than 0.05mm/year [21].

2.7.1 Modes of wear, wear debris size, volumes, and morphology

2.7.1.1 Modes

It is important to understand what affects the rate of wear for the bearing surfaces of joint replacements and how these different factors affect the wear debris that is produced. It is also important in understanding possible methods for wear debris creation.

It is shown in the literature by Clarke et al and Scholes et al that are usually two stages of wear in metal-on-metal pairings, one accelerated period of wearing for roughly 0.5×10^6 cycles, followed by a slower period of wear after that, an example of this can be seen in figure 5 [3] [20]. This accelerated period of wear produces larger wear particles that usually lie outside of the range for macrophage activation [24]. This means this initial period of wear is unlikely to result in an inflammatory response and is unlikely to contribute to late aseptic loosening [24]. The decrease in wear rate following this 'run in' wear stage is typically threefold [3].

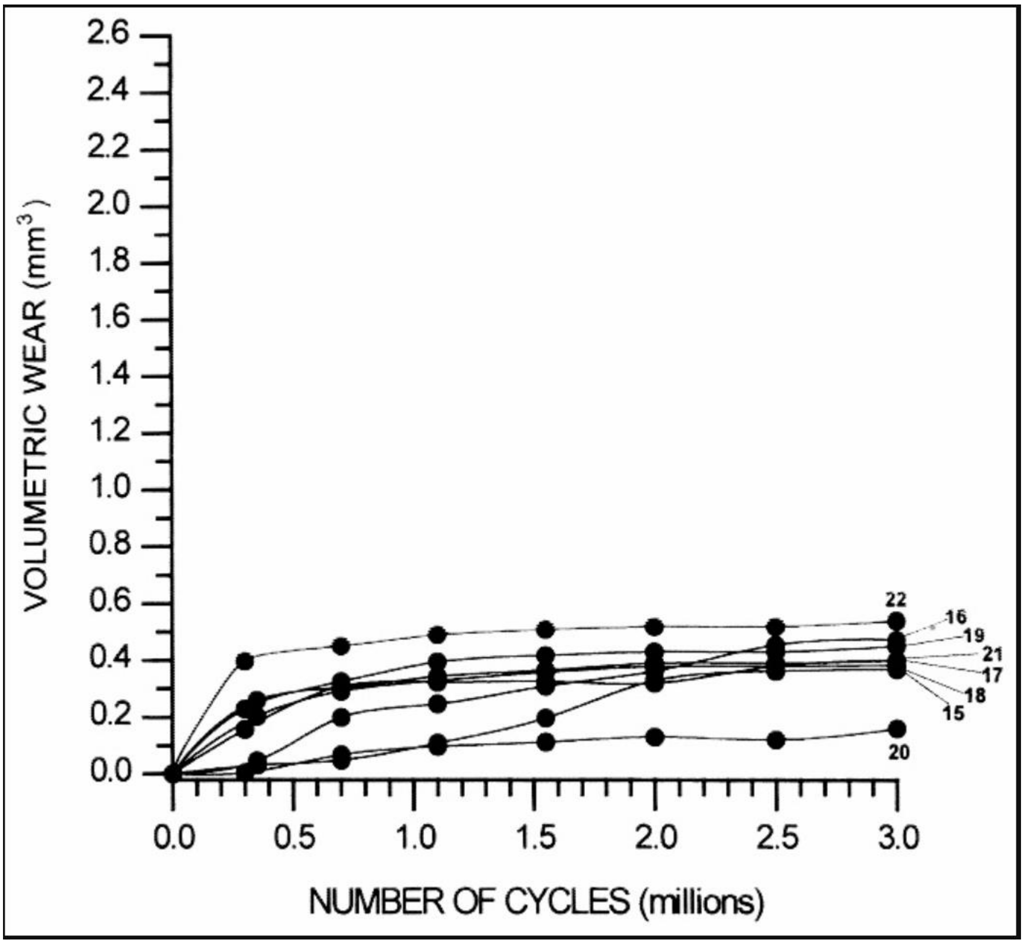

Figure 5. Total volumetric wear of high C cast F75-92 implants plotted against the number of cycles [65].

During the 'run in' period of wear it is likely that larger asperities are removed from the bearing surfaces. This would result in a period of faster wear and explain why this period of increased wear stops as all large asperities are worn. Wear following this 'run in' stage is thought to result from grain release through fatigue [24].

2.7.1.2 Volumes

The volume of wear debris produced by implants appears to have a direct correlation on the risk of the implant failing through late aseptic loosening [21]. This leads to a potential solution to late aseptic loosening through low wearing implants, ceramic on ceramic pairings is of particular interest here as they have shown very low wear rates (<0.1mm^3/10^6 cycles) [11] [1] [2]. By comparison ceramic-on-polymer pairings have shown wear rates of 31mm^3/10^6 cycles which is significantly higher than the ceramic-on-ceramic [66]. Metal on metal pairings may also be of interest as they can have a wear rate similar to ceramic-on-ceramic pairings however show significant variance in the wear rate, some showing up to 30-40mm^3/10^6 cycles [1]. By comparison metal-on-polymer pairings have shown wear rates of up to 74mm^3/10^6 cycles which is significantly higher than the highest metal-on-metal wear rates [3].

2.7.1.3 Size ranges of wear particles in joint simulations and in vivo

The size of the wear debris produced is highly variable between materials, manufacturing methods and designs. Typical size ranges of interest are those that would cause macrophage activation at 0.1-10 µm [24] [11] [23].

The modal size of UHMWPE wear particles produced in the literature appears to be 0.3-0.5 µm [11]. Other studies show similar results with recovered tissues surrounding hip implants showing average wear particle sizes of 0.53±0.3 µm on average [23]. Both of these figures are for metal on UHMWPE joint replacements, it should also be noted that this particle size is similar to the particle size used in the creation of acetabular cups [23]. UHMWPE components are generally created through either hot pressing or ram extrusion, both of these methods involve the heating and compression of UHMWPE particles, usually these are 0.3-0.5 µm [23] [67]. Metallic wear debris in these joint replacements seem to vary quite significantly with reported ranged of 10 nm to 400 µm [11] [25] [23].

There is also evidence for a significant number of wear particles being produced in the nanometre size range, which are less likely to cause macrophage activation but may result in necrosis of the surrounding tissues [40]. These particles have been found in patients lymph nodes, liver, spleen, and bone marrow [11]. This could pose a more significant problem than late aseptic loosening should it result in necrosis of the tissues within those areas and organs.

2.7.1.4 Morphology of wear particles from joint simulations and in vivo

The morphology of wear debris particles affects the cell response along with the size of the particles [24]. Particles of sufficiently high surface area to volume ratio can cause cell damage and death in macrophages [24].

The morphology of the particles varies significantly depending on the material, size, and wear mode, leading to significant variation in the morphology of the particles [11] [23]. This leads to significant difficulty in predicting the morphology of the wear debris produced without directly observing some. There are, however, some general trends in that larger pieces of wear debris tend to form plates or wires while smaller particles tend to be more granular or spheroid in shape [11].

UHMWPE particles produced through UHMWPE-on-metal and UHMWPE-on-ceramic pairings produced small spheroid particles 0.1-2.0 µm in size, fibril-like particles 0.2-0.3 µm in diameter and up to 10 µm in length, and rolled plate-like particles, 1-3 µm in diameter and 20-200 µm in length [23] [68] [69]. It is important to note that UHMWPE articulating on metals or ceramics also produce some wear particles from the harder material too. Alumina articulating on UHMWPE has been shown to produce polygonal alumina particles 5-90 nm and 0.05-2 µm in size [68]. CoCrMo alloys articulating of UHMWPE has been shown to produce round, oval, and needle shaped CoCrMo particles 25-90 nm in size [68] [66]. The needle shaped particles are more likely to cause problems for patients as they are associated with greater cell necrosis [24]. As they will also have a higher surface area to volume ratio they will typically leach more metal ions than spherical particles [27].

The particles recovered from patients with metal-on-metal total joint replacements show significant variety in the particles found in the tissues. Needle shapes particles, 40-120 nm in size, were found alongside globular particles 90 nm in size and below from CoCr metal-on-metal bearing surfaces [68]. Round to oval shaped wear particles 6-834 nm in size were also observed from CoCr metal-on-metal pairings [70]. There is evidence that these nano-sized particles tend to be found in agglomerates within the tissues of patients

[70]. There is also evidence for the generation of larger particles from metal-on-metal in cases where edge loading occurs, generating wear debris 100-6000 nm in size that tended towards an elongated morphology [71]. These smaller wear particles pose differing risks to patients, often leaving the joint space and being found in areas such as the lymph nodes in other areas of the body [11]. Examples of typical particle morphologies can be seen in figure 6.

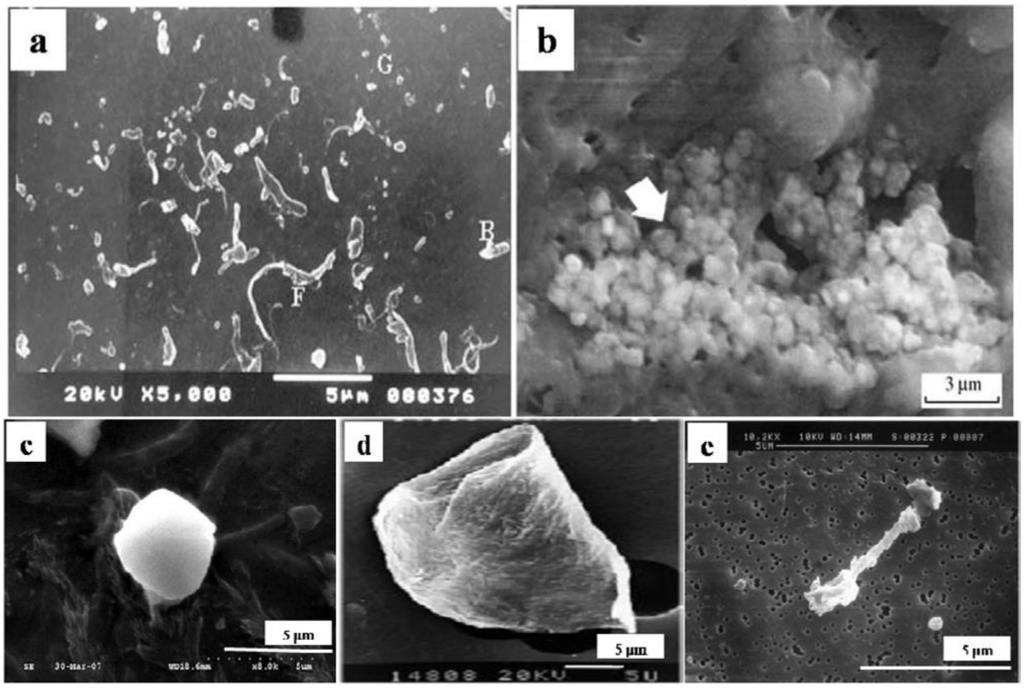

Figure 6. Typical morphologies of wear debris from periprosthetic tissue; (a) UHMWPE [90]; and (b) Alumina [103]; (c) Spherical (UHMWPE) [34]; (d) Sheet/Flake type (UlHMWPE) [112] and (e) Fibril (UHMWPE) [68].

Particles recovered from ceramic-on-ceramic pairings once again shows a variety of particles sizes. Alumina ceramic-on-ceramic hip simulators showed evidence of a bi-modal polygonal particles size for wear particles, with particles 5-20 nm and 0.2-10 μm in size [72] [73] [74].

Particles produced through hip simulators using coated metal-on-metal pairings, both CrN-CrN and TiN-TiN, were observed to be up to 200 nm in most cases with some evidence of particles up to 500 nm [75]. There is also evidence for the size of the wear debris in coated metal-on-metal pairings being similar to those found in uncoated metal-on-metal pairings [76]. The literature on the wear particles produced by these coated metal-on-metal pairings is however quite sparse and cannot be used to draw a conclusion on the full range of particles sizes and morphologies to be expected from coated metal-on-metal pairings. This nanometre sized wear debris can leave the joint space and has been found in the lymph nodes, liver, spleen, and bone marrow [11]. Where this wear debris is found in lymph nodes it has been noted to cause lymphadenopathy, necrosis and fibrosis inside the lymph node [11].

The particles recovered from the tissues of patients with titanium components showed some particles may originate from non-bearing surfaces of the implants [23]. Titanium flakes 200-400 µm in size and 10-20 µm in thickness were observed, these were thought to originate from the stem of the implant [23]. Wire-like fragments 300-400 µm in diameter and of varying lengths were observed and believed to originate from the mesh pad on the implants [23]. These larger particles are associated with an increased foreign body giant cell response, these foreign body giant cells will then release inflammatory cytokines in response to the particles [21] [11].

2.8 ALTERNATIVES TO JOINT PROSTHESES

There are several alternatives to total joint prostheses, although not all of these alternatives are permanent solutions and simply delay the need for a total joint prosthesis. The following is not a comprehensive list and other alternatives are available such as Autologous chondrocyte implantation and Myo-regeneration exist, although these are typically used in instances of cartilage damage and are less relevant to osteoarthritis which accounts for the majority of primary hip and knee total joint replacements [6] [77] [78].

One such alternative is Micro-fragmented Adipose Tissue Injection (MFAT). MFAT treatment involves harvesting adipose tissue from the patient (approximately 50ml), fragmenting, and filtering that adipose tissue and then injecting it near to the joint site. This results in an improved quality of life for patients suffering from osteoarthritis, delaying the requirement for a total joint replacement. The effect of MFAT is likely as a result of the multi-lineage progenitor cells that act in a similar manner to Mesenchymal stem cells, potentially repairing the damaged tissues and reducing the inflammation in the area [79]. This is however not typically a permanent solution [79] [80].

Another alternative is platelet-rich plasma (PRP) therapy, PRP contains platelet growth factors and proteins that can trigger healing pathways in damaged tissues [81]. PRP therapy shows significant improvement in the joint mobility and pain of the patients receiving it [82]. It should be noted however that PRP therapy has seen the best results in early osteoarthritis and is not as effective a treatment when used for advanced osteoarthritis [82]. It can be used to slow the progression of osteoarthritis although it is unlikely to prevent the need for total joint replacements in the patient entirely [82].

Partial joint replacements are also an option as an alternative to a total joint replacement. This involves resurfacing only a single bearing surface of the joint while leaving the other intact. This is typically useful for situations where the damage is limited to one side of the joint and is typically used for younger patients. In these cases, partial joint replacement is preferable as it carries less risk to the patient and results in faster recovery when compared to total joint replacements [83].

2.9 HIGH IMPULSE MAGNETRON SPUTTERING

High impulse magnetron sputtering (HIPIMS) is a method of thin film physical vapour deposition (PVD) used to produce coatings on components. It is a form of magnetron sputtering using a specialised power supply to produce high voltage low frequency pulses of power [84]. Magnetron sputtering involves the bombardment of a target, made of the material intended to become the coating or a precursor of it, using energetic ions of inert gases such as argon, known as the process gas [85]. HIPIMS differs from magnetron sputtering through the use of an applied voltage of 500-1000 V and a pulse length of 100-500 µs [84]. The pulse frequency is typically tens of hertz which prevents melting of the target, preventing the generation of large droplets of target material [84]. The typical schematic for this coating process can be seen in figure 7.

The end result of this type of pulse is a peak energy density at the target of several kilowatts per square centimetre, resulting in a high-density plasma [84]. This high-density plasma leads to a higher number of ionised atoms than neutral atoms, this leads to self-sputtering where ionised metal atoms are attracted back to the target and sputter further material [84]. This leads to coatings with improved density and adhesion to the substrate [84]. This improved density must be managed however as the compressive stress (roughly 3 GPa) in the coating may lead to delamination [84] [86].

The overall energy flux is shown to be roughly the same magnitude or lower in HIPIMS when compared to direct current magnetron sputtering (DCMS) [84]. This is due to the much higher energy of the ions hitting the target, typically 90% higher at 20-30 eV [84]. There is however a reduction in deposition rate of coatings through this method, between 30-80% that of DCMS, as a result of metal ions being attracted back to the target [84].

In order to deposit ceramic materials reactive HIPIMS is used where a reactive gas such as N_2 is used for sputtering alongside the process gas, this leads to a reaction between the metal ions and the reactive gas at the surface of the target, known as target poisoning [84]. The deposition rate for this method is lower than when depositing without the reactive gas [84].

Typically, sample preparation for HIPIMS involves etching of the sample to remove oxides and surface organic compounds such as oils, this involves apply a large negative bias voltage to the substrate (in the study given this is -1200V) [87] [86]. This etching step also results in embedding of metal ions up to 5 nm into the surface of the substrate, producing a thin intermediary film between the substrate and the coating [87].

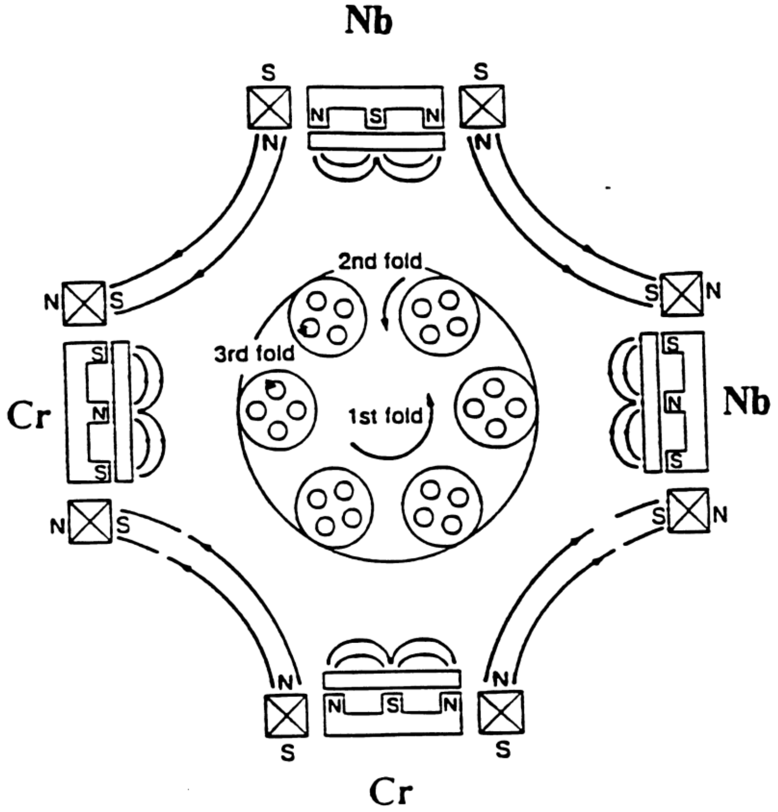

Figure 7. Schematic diagram of four target HTC 1000-4 ABS PVD coating system as would be used to produce a CrN-NbN superlattice coating [88].

2.10 WHAT CRN-NBN SUPERLATTICE COATING OFFER TO BEARING SURFACES

The CrN-NbN superlattice coating is a coating developed by Zimmer Biomet using the HIPIMS method for the bearing surface of joint replacements. A superlattice is a multi-layered structure with alternating layers, typically a few nm thick. This requires alternating coatings using the HIPIMS method, typically using multiple targets in a rotating system. A TEM of what a typical superlattice coating looks like can be seen in figure 8.

The CrN-NbN superlattice coating is a multilayer coating of CrN and NbN with a layer thickness <10 nm [89]. This multilayer structure results in residual compressive stress within the material, measured to be 1.8-7.5 GPa [89]. These compressive stresses in the coating act to close cracks and increase the density of the coating, as well as improving resistance to pitting corrosion [90]. The CrN-NbN superlattice also offers the ability to be produced economically using commercially available PVD equipment, although for the HIPIMS method of manufacture a different power source is required [89] [91] [84].

Coating adhesion to the substrate is an essential requirement of a coating used in total joint replacements as delamination of the coating leads to significantly increase wear as a result of third body wear [92] [57]. The CrN-NbN superlattice coating shows excellent coating adhesion, with a scratch test demonstrating critical loads (L_c, N) of $2.1\text{x } 10^{-15}$, 50 N vs $4.5 \text{ x } 10^{-16}$, 39 N for TiAlYN-VN, as a result of the ion treatment of substrate, resulting in an intermediate layer that reduces the compressive stress in the coating [89].

As previously discussed, there is a strong link between the wear debris produced by the articulating surfaces of total joint replacements and failure by late aseptic loosening of those joint replacements [11] [20]. It has been shown that low wearing total joint replacements are associated with a lower risk of failure through late aseptic loosening [21]. The CrN-NbN superlattice coating pairings has been shown to have a wear rate of 1.3mg per million cycles [13]. This wear rate is significantly lower than those shown for titanium nitride pairings, 4.27mg per million cycles, or those shown for alumina pairings, 3.8-19mg per million cycles [16] [93].

The CrN-NbN superlattice coating has also shown good corrosion resistance when compared to 304 steels [94]. This corrosion resistance is likely as a result of the passivation behaviour of the coating [88]. It does however show worse corrosion resistance when compared to similar ceramic materials used as coatings such as TiN [62] [94]. This worse corrosion resistance is linked with macro-particles inclusions in the CrN-NbN superlattice coating that then result in galvanic or crevice corrosion [62]. This does however demonstrate a route to improve the corrosion resistance in these coatings by reducing or eliminating this macro-particle inclusion in the coating, potentially through arc filtering or similar means [62].

Overall, the CrN-NbN superlattice coating has the potential to be a corrosion resistant, low wearing, economical option for the bearing surfaces of total joint replacements. There is still however little in the literature on the biological properties, such as cytotoxicity, of the material or the wear debris generated from the material.

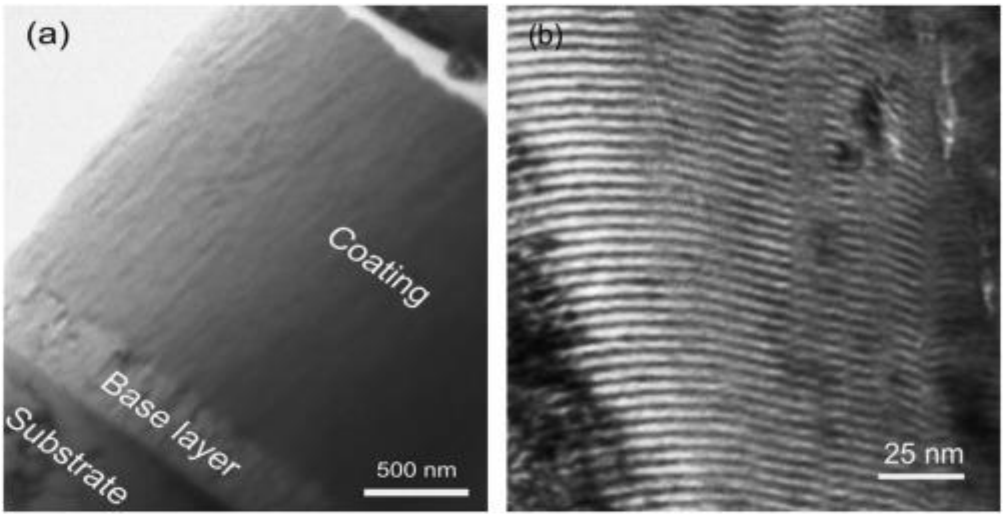

Figure 8. Bright field TEM (a) low magnification cross-section of the coating (b) high magnification showing the multilayers in a CrN-NbN superlattice coating [12].

	Compressive Stress (GPa)	Typical Wear Rate mg / 10^6 cycles	Hardness (GPa)	Coeff. Fr.
CrN-NbN superlattice	1.8-7.5 [89]	1.3 [13]	20-35 [95]	0.69 [89]
TiN	3.0-11.0 [96]	4.27 [16]	33.4 ± 10 [97]	14.4-16.3 [96]
CoCr	-	19.7 [98]	0.5-0.8 [99]	0.25-0.35 [100]

Table 2. Comparing CrN-NbN to other commonly used coating materials.

2.11 NATURE OF TISSUES AROUND JOINT PROSTHESES

2.11.1 Overview of general biological response to wear debris

In order to fully understand the issues that arise from wear debris produced by total joint replacements we need to understand the biological response to this wear debris. There are several results of the biological response to wear debris, inflammation resulting from macrophage activation [11] [27], decreased osteoblast function and increased osteoclast function and recruitment [27] [11] [25] [26] [21]. These cell types are not the only ones involved in the response to wear debris, it has also been indicated the lymphocytes and dendritic cells also react to wear debris by releasing cytokines and phagocytosis of the particles [21] [101]. It is also possible for the wear debris to be cytotoxic, leading to cell death around the wear particles and therefore the implant. This inflammation may contribute to osteolysis or late aseptic loosening [11].

2.11.1.1 Inflammation

The inflammatory response mediated by macrophages is reliant on the presence of particles between the critical size for macrophage activation, with this range lying between 0.01-10 μm [24]. Above this size it is believed that the particles stimulate the foreign body giant cell response up to 10 μm [11]. Macrophage infiltration into the capsule surrounding implants has been high in recovered tissues of implants that failed due to aseptic loosening [27] [11]. Macrophages near the implant have been shown to release many inflammatory cytokines as well as cytokines that affect osteoclast development and activation, Interleukin-1 (IL-1), Interleukin-3 (IL-3), Interleukin-6 (IL-6), TNF-α, Granulocyte macrophage colony-stimulating factor (GM-CSF), Macrophage colony-stimulating factor (M-CSF), Stem cell factor (SCF), Platelet-Derived Growth Factor (PDGF), Prostaglandin E2 (PGE_2), Interferon gamma (IFN-γ) and matrix metalloproteases (MMPs) [27] [11] [25] [21] [26]. Both IL-6 and TNF-α have been shown to activate osteoclasts which shows a link between the inflammatory response by macrophages and the bone resorption along with the increase in MMPs which may add to tissue loss in osteolysis [27]. IFN-γ has also been shown to stimulate differentiation of macrophages into osteoclasts [21]. Macrophages that have phagocytosed particles have also shown activation of protein tyrosine kinases that result in the activation of NF-κB [26]. This activation of NF-κB in macrophages results in the release of Receptor activator of nuclear factor kappa-B ligand (RANKL), which was previously thought to not be produced by macrophage lineages [21]. This release of RANKL contributes to osteolysis through increasing osteoclast activity [21].

2.11.1.2 Cells involved in osteolysis and the regulation of bone

2.11.1.2.1 Osteoblasts

Osteoblasts synthesize bone, and as such, are of significant interest in terms of their interactions with wear debris in late aseptic loosening. Osteoblasts are known to phagocytose particles which has been known to affect the morphology of the cells [26] [25] [27]. Particle laden osteoblasts have been shown to have ruffled membranes, less developed endoplasmic reticulum, swollen mitochondria and vacuolic inclusions [25].

Osteoblasts have been known to produce various cytokines in response to particles, namely IL-6, IL-8, Monocyte Chemoattractant Protein-1 (MCP-1), transforming growth factor beta 1 (TGF-β1) and PGE_2 [27]. IL-6 has no effect on bone resorption alone but may act to recruit and activate osteoclasts through upregulating other cytokines [11] [27] [102]. PGE_2 results in decreased osteoblast function and procollagen α1 expression [26] [27]. IL-8 acts as a chemokine, attracting neutrophils, T-lymphocytes, and basophils [103]. MCP-1 is a powerful chemoattractant for monocytes [104]. TGF-β1 triggers collagen accumulation and is often associated with wound healing and fibrosis [105].

Particles are also known to produce a change in gene expression in osteoblasts, reducing the expression of procollagen α1 [26] [27]. This change occurs even when phagocytosis of the particles is inhibited through a mechanism such as using cytochalasin D, indicating that this change is not in response to phagocytosis of the particles [27]. It may be the case that this change is as a result of surface receptor interaction with the particles. This leads to a reduction in osteogenesis as the product of procollagen α1, type I collagen, makes up 90% of the bone matrix [26] [27] [106].

There is also some debate in the literature as to the effect of particles on the expression of other genes such as alkaline phosphatase, osteonectin, and osteocalcin. A number of studies claim no suppression of these genes in response to wear particles [26]. Other studies, however, claim to have seen reduction in the expression of these genes in response to particles [25]. There was also some evidence that certain metal ions such as Al^{3+} can cause a suppression of these genes at non-toxic doses of the ions [27]. The reduction in expression of these genes as a result of metal ions, however, is unlikely to be the difference between these two studies as both compared UHMWPE particles.

2.11.1.2.2 Osteoclasts

Osteoclasts degrade bone and therefore may play a significant role in late aseptic loosening. They have been shown to phagocytose particles which then leads to osteoclast activation [27].

Many of the cytokines released by other cell types in reaction to particles have an effect on osteoclasts. TNF-α has been shown to lead to osteoclastogenesis, osteoclast activation and an increase in osteoclast lifespan while IL-1β has been shown to cause macrophages to differentiate into osteoclasts along with recruiting them to the implant site [25] [21] [11] [107] [108] [109]. RANKL also acts to induce osteoclastogenesis as well as prolonging the lifespan of osteoclasts [21] [27] [110]. The majority of the cytokines mentioned act through activating NF-κB in monocytes and macrophages, resulting in differentiation into osteoclasts [111] [27].

As many of the cytokines released in response to particles lead to osteoclast and osteoclast precursor cell recruitment to the implant site and osteoclastogenesis the increase in osteoclasts is likely to lead to osteolysis and late aseptic loosening [21].

2.11.1.2.3 Macrophages

Macrophages are phagocytic cells that are typically involved in inflammatory responses and make up part of the innate immune system. In late aseptic loosening it is likely that they are involved in the phagocytosis of particles and release of cytokines to that lead to osteoclastogenesis and osteoclast activation along with reducing osteoblast activity [26] [27] [25] [11].

Macrophages typically phagocytose particles within their activation range of 0.1-10 µm although particles above 3 µm are typically associated with the formation of foreign body giant cells [11] [24]. Macrophages that have phagocytosed particles have been shown to release Eicosanoids (such as PGE_2), IL-1, IL-6, TNF-α, MMPs, MCP-1, Macrophage Inflammatory Protein-1 Alpha (MIP-1α) and IFN-γ [26] [27] [25]. PGE_2 results in decreased osteoblast function and procollagen α1 expression [26] [27]. MCP-1 is a powerful chemoattractant for monocytes [104]. IL-1 can be either IL-1α or IL-1β, these are associated with the recruitment of macrophages and osteoblasts [11]. IL-6 has no effect on bone resorption alone but may act to recruit and activate osteoclasts through upregulating other cytokines [11] [27] [102]. TNF-α induces the differentiation of osteoclasts from precursors and reduces procollagen α1 expression in osteoblasts [26] [27] [21]. MIP-1α is a chemoattractant for monocytes and T-lymphocytes [112]. IFN-γ acts to activate macrophages [113].

2.11.1.2.4 Fibroblasts

Fibroblasts are cells that typically produce extracellular matrix. Fibroblasts have been found to contain particles in the periprosthetic space indicating that they do phagocytose particles [26]. While fibroblasts are not directly involved in the maintenance of bone they may act to release pro-inflammatory cytokines that attract monocytes, macrophages and osteoclasts to the periprosthetic space and increase osteolysis [27] [21] [102].

Fibroblasts are also shown to release TNF-α, IL-1, IL-6, RANKL, IL-1β PGE_2 and MMPs in response to particles [102] [27]. They have also been shown to release increased collagenase and gelatinase in response to particles which may contribute to the degradation of the bone tissue [102].

2.11.1.2.5 Foreign Body Giant Cells

Foreign body giant cells (FBGCs) are multi-nucleated cells formed from macrophages [114]. Typically, these FBGCs are formed from macrophages adhering to a surface, followed by the fusion of those macrophages, mediated by the presence of IL-4 [114] [115]. FBGCs are capable of releasing oxygen free radicals, enzymes, and acids into the space between the cell and the material to which they are attached [115], this may lead to the degradation of those materials, particularly those that are not corrosion resistant.

FBGCs are found at the interface between the tissue and the joint prosthesis and are also associated with wear debris that is above 3 µm in size [114] [11]

[27]. They are capable of producing RANKL in response to wear debris, which leads to the activation of osteoclasts [21]. It has been shown that implant sites with a higher number of FBGCs have greater fibrosis and encapsulation of the implants [114].

2.11.1.3 CYTOKINE RELEASE

2.11.1.3.1 Tumour Necrosis Factor alpha (TNF- α)

TNF-α is a relevant cytokine to the analysis of late aseptic loosening, being a cytokine linked with inflammation. There are numerous studies that show links between TNF-α and areas that are likely to affect late aseptic loosening [26] [27] [21].

The release of TNF-α has been shown in macrophages at the site of implants [11]. The presence of wear particles has also been shown to induce the release of TNF-α in J774a.1 macrophages, human mononuclear phagocytes and human synoviocytes [11].

There are several different pathways through which TNF-α may potentially influence the resorption of bone in late aseptic loosening. One method is through acting itself to cause the release and upregulation of other cytokines. TNF-α has been shown to cause the upregulation of TGF-β1 and RANKL [21] [26]. TGF-β1 triggers collagen accumulation and is often associated with wound healing and fibrosis [105]. RANKL causes the differentiation into osteoclasts from precursor cells and the activation of osteoclasts along with increasing the lifespan of osteoclasts [21] [108] [109]. TNF-α has also been shown to cause the release of IL-6, IL-6 has no effect on bone resorption alone but may act to recruit and activate osteoclasts through upregulating other cytokines [11] [27] [102]. TNF-α has also been shown to reduce osteoblast differentiation which would affect the rate at which new bone growth occurs [27].

Another method in which TNF-α may influence late aseptic loosening is through affecting gene regulation. It has been shown to cause the downregulation of procollagen α1 expression, which would lead to reduced bone matrix production and potentially lead to late aseptic loosening as a result of reduced bone production [26].

TNF-α has also been indicated to act in a similar way to RANKL by interacting with NF-κB which leads to osteoclastogenesis and the activation of osteoclasts [27]. This would lead to an imbalance in the resorption and creation of new bone material leading to a reduction in bone around the implant site.

Overall, the presence of TNF-α has many routes to cause potential late aseptic loosening although the pathways that it uses are not solely responsible for late aseptic loosening. In mice that were TNF-α deficient a reduced level of bone resorption in response to various particles was noted when compared to mice that were not TNF-α deficient [11]. This implies that while TNF-α plays a role in the resorption of bone in late aseptic loosening, it is not the only factor that causes it.

2.11.1.3.2 Interleukins-6 (IL-6)

IL-6 is a cytokine of clinical relevance to bone resorption, having been shown to be released by macrophages around the implant site [11]. This is reflected in other studies that show the release of IL-6 in response to wear particles in osteoblasts, synoviocytes and monocytic cells [27] [11] [25].

IL-6 alone has been shown to not directly cause bone resorption it does however have a number of potential pathways to influence the amount of bone resorption that occurs in late aseptic loosening [11]. IL-6 may induce osteoclast differentiation and proliferation, increasing the rate at which bone is resorbed [26].

The release of IL-6 is thought to aid in the recruitment of macrophages into the implant site [102]. This alone is unlikely to cause bone resorption, however as macrophages are involved in an inflammatory response, they are likely to lead to an increased local inflammatory response should inflammation occur. Macrophages also differentiate into osteoclasts in response to certain cytokines, which could produce more bone resorption if the cytokines to influence osteoclastogenesis are also present [21].

2.11.1.3.3 Interleukins -1β (IL-1β)

The role of IL-1β in bone resorption is similar to that of IL-6, while alone it is not thought to directly cause bone resorption it is thought to influence the recruitment of macrophages and osteoclasts into the joint space [11] [107] [27].

There are several indications that IL-1β plays a role in late aseptic loosening, elevated levels of IL-1β were found in the periprosthetic membrane surrounding failed implants [116]. There is also indication that IL-1β is released in response to the presence of wear debris in human monocytes [117] [118].

IL-1β is also known to cause the differentiation of macrophages into osteoclasts, which along with recruiting them to the implant site is likely to lead to bone resorption [27] [11]. It is also shown to lead to potential damage to the cells surrounding the implant by inducing the release of MMPs from synovial cells [119].

The interactions do get quite complicated as IL-1β is also shown to reverse the reduction in procollagen α1 caused by TNF-α, PGE_2 or the presence of particles [26]. This would help to increase bone matrix production, although this may still not outweigh the potential increase in bone resorption cause by recruiting macrophages into the joint space, inducing osteoclastogenesis and damaging the surrounding tissue.

2.11.1.3.4 Receptor activator of nuclear factor kappa-B ligand (RANKL)

The key role of RANKL in the context of osteolysis is in osteoclast activation along with prolonging the lifespan of osteoclasts [27] [110] [108] [109]. RANKL promotes osteoclast activation which can directly lead to osteolysis around the joint space [27]. RANKL is regulated by Osteoprotegerin (OPG), which binds to RANKL and prevents it binding to RANK [21]. The balance between the two cytokines is key in the regulation of bone resorption and an increase in RANKL expression in the joint space and a decrease in OPG expression [21].

Several cell types have been shown to express RANKL, osteoblasts, fibroblasts, and T-lymphocytes [21]. Fibroblasts have been shown to release RANKL in response to particles or PGE_2, indicating that the release of RANKL may have multiple pathways leading to an increase in RANKL and osteoclast activation [21]. Both IL-1 and TNF-α are shown to increase expression of RANKL across many cell types [21].

2.11.1.3.5 Osteoprotegerin (OPG)

OPG acts as a regulator to RANKL by acting as a decoy and binding to it [21]. This in turn results in OPG acting as a regulator of osteoclastogenesis with an increase in OPG expression being related to a decrease in osteoclastogenesis and in turn osteolysis [120]. OPG is produced by Osteoblasts and B-cells, with B-cells potentially being responsible for the majority of OPG found within the bone marrow [120].

One interesting interaction regarding OPG is a study showing an increase in OPG expression in human monocytic cells in response to particles [11]. Other studies show an increase in RANKL and decrease in OPG expression around the joint space which would lead to the conclusion that another cytokine acts to reduce the expression of OPG [21].

2.11.1.3.6 Prostaglandin E2 (PGE_2)

The role of PGE_2 in late aseptic loosening is complex and PGE_2 alone does not lead to an increase in bone resorption [11]. It does however have many interactions that may worsen late aseptic loosening, which is of relevance as particles have been shown to induce the release of PGE_2 from Fibroblasts, macrophages, monocytes and osteoblasts [11] [26] [27].

PGE_2 has been shown to upregulate the release of RANKL and TGF-β1 while at the same time decreasing the expression of procollagen α1 [27] [21] [26]. This would result in recruitment of macrophages and osteoclasts into the joint space and lead to increase macrophage and osteoclast activation while decreasing creation of the bone matrix which would lead to increased bone resorption [11] [107] [119] [21].

2.11.1.3.7 Procollagen α1

Collagen type I is a critical component of bone matrix making up roughly 90% of the proteins in the bone matrix [27]. Procollagen α1 is the major component of type I collagen [27]. As such any decrease in procollagen α1 expression is going to result in decreased osteogenesis and lead to an imbalance of osteogenesis and osteolysis.

There are a large number of cytokines that change the expression of procollagen α1 in late aseptic loosening. TNF-α and PGE2 both cause a reduction in procollagen α1 expression while IL-1β causes an increase in procollagen α1 expression [26].

2.11.1.3.8 Matrix metalloproteinases (MMPs)

Matrix metalloproteinases (MMPs) that are responsible for the degradation of the extracellular matrix and may contribute to late aseptic loosening by degrading the bone matrix. An increase in release of multiple different MMPs from macrophages and synoviocytes can be observed in response to wear debris [27]. These MMPs are also affected by inflammatory cytokines with TNF-α and IL-1β inducing MMP activity [119]. This leads to another route where the cytokines can act to cause further osteolysis and late aseptic loosening of the joint replacement.

2.11.2 Bone Tissue

Bone is a complex tissue of mineralised fibres that form the individual bones of the musculoskeletal system. Typically, the proportion of organic material to mineral in bone tissue is 30% organic material and 70% mineral, water is also a component found in bone [121].

The organic fibres of bone are primarily comprised of type I collagen, around 90% [121]. Collagen’s basic unit consists of three tightly folded alpha chains, each roughly 1000 amino acids in length [122]. These basic units are then arranged into larger collagen fibrils, staggering the basic units a quarter the length of the adjoining units [122]. This structure and crosslinking between the units gives collagen excellent tensile strength [122]. This collagen provides the nucleation site for the generation of bone mineral [121].

The mineral component of bone is hydroxyapatite ($Ca_{10}(PO_4)_6(OH)_2$), although this is not pure hydroxyapatite and contains a number of impurities such as carbonate, magnesium, fluoride, and citrate [121] [122]. The hydroxyapatite forms crystals roughly 2.5-7.5 nm in diameter and 20 nm in length [122]. The hydroxyapatite crystals are responsible for the strength of the bone in compression [122].

Bone is found in two types, cortical bone, and cancellous bone [123] [122]. Cortical bone is denser and occurs along the shaft of the long bones [122]. Cancellous bone is a network of interconnecting trabeculae that occurs in the axial bones and the end of the long bones [122]. Bones are also usually covered in a periosteum which is comprised of two layers, an outer fibrous layer with blood vessels and nerves and an inner layer containing osteoprogenitor cells [122].

Bone is organised into osteons, which are concentric layers of mineralised bone around a central vascular canal known as a Haversian canal, typically 200 µm in diameter [121, 122]. These canals contain blood vessels, nerve fibres and lymphatic channels [122]. The boundaries of each layer of mineralised bone have small gaps called lacunae which contain osteocytes [122]. These are connected together and to the Haversian canal through canaliculi, these contain cell processes in order to allow nutrients from Haversian canal to be distributed to the osteocytes [122]. Each osteon is surrounded by a thin area cement line, comprised of non-collagenous proteins such as glycoaminoglycans, osteocalcin, bone sialoprotein, and osteopontin [122] [124]. The canaliculi and collagen fibres do not cross this cement line, which may explain why the cement line is the most common point of failure in bone [122]. Bone also acts as a reserve of calcium and phosphates [122].

Bone is constantly undergoing remodelling as a result of the activity of osteoblasts and osteoclasts [122]. Osteoblasts are cells responsible for the generation of the bone material, including the hydroxyapatite, collagen and glycoaminoglycans [122]. Osteoclasts are multinucleated cells responsible for bone resorption, removing first the mineral component of the bone followed by the collagen matrix up to a depth of 1-2 µm [122]. This allows the bone tissue to replenish if it gets damaged and to adapt to changes in mechanical needs of the bone by regulating the activity of the osteoblasts and osteoclasts.

2.11.3 Cartilage

The articular cartilage covers the ends of the long bones and provides a smooth surface for articulation [125]. This articular cartilage is avascular and lacks nerve fibres or lymphatic channels [125]. Articular cartilage also has limited capacity for repair, which is very important in the context of total joint replacements [125].

Articular cartilage is usually 2-4mm in thickness and is comprised of dense extracellular matrix with chondrocytes sparsely distributed within the cartilage

[125]. The extracellular matrix of the cartilage is primarily composed of water, type II collagen, and proteoglycans [125].

The cartilage is generally formed of several zones, the superficial, middle, deep and calcified zones [125]. The superficial zone is a thin layer at the top, roughly 10-20% the thickness of the cartilage. This is comprised of densely packed collagen fibres parallel to the articular surface and has a high number of chondrocytes. This dense layer of collagen fibres allows the cartilage to resist shear [125].

The middle zone is comprised of proteoglycans and thick collagen fibrils and makes up roughly 50% of the thickness of the cartilage [125]. The collagen fibres of the middle zone are obliquely arranged and contains a low density of chondrocytes [125]. This zone of the cartilage helps protect against the compressive forces on the cartilage [125].

The deep zone is comprised of collagen fibres arranged perpendicular to the surface of the collagen and is responsible for most of the resistance to compressive forces on the cartilage [125]. The collagen fibres here are larger in diameter than in other zones. The deep zone also contains a large percentage of proteoglycans compared to other zones [125]. This zone is roughly 30% of the thickness of the cartilage [125].

The calcified zone plays an important role in securing the cartilage to the bone, this connects to the collagen fibres of the deep zone [125] [126].

2.11.4 Synovial membrane

The synovial membrane is a fibrocollagenous capsule around joints [127]. The inner layer of this fibrous capsule is the synovium which secretes synovial fluid into the joint space. This aids in the articulation of the joint [127]. The synovial fluid contains mostly hyaluronic acid and glycoproteins along with a low number of leukocytes [127]. This membrane provides the metabolic support for the cells of the articular cartilage as well as providing a lubricant for the articulating surface of the cartilage [127].

2.11.5 Periprosthetic membrane

The periprosthetic membrane is a membrane between the bone tissue and the prosthesis or bone cement if bone cement is used [128]. These periprosthetic membranes are typically split into four types. Type I periprosthetic membranes, otherwise known as the wear-particle-induced type, are typically characterised by macrophage and foreign body giant cell infiltration alongside significant wear debris presence [128] [129]. Type II periprosthetic membranes, also called infectious type membranes, are characterised by activated fibroblasts, angiogenesis, and inflammation. Type III periprosthetic membranes, also known as combined type membranes, show a mixture of both type I and type II features, likely as a result of infection and wear debris. Type IV periprosthetic membranes, known as indeterminate type membranes, are typically connective tissue rich in collagen fibres, similar to scar tissue [128] [129].

Knowledge of the difference between these types of periprosthetic membrane is quite important when considering revision procedures in loosened prostheses, as it allows the treatment of potential low-level infections, reducing the incidence of repeated loosening.

2.12 CELL CULTURE TESTS

2.12.1 alamarBlue®

An alamarBlue® assay is used to indicate cell viability and cytotoxicity and is one of the most commonly referenced assays in cell culture [130]. It has uses with a wide variety of cell types, including cultured mammalian cells, fungi, and bacteria [130]. It has advantages over other measures of cell viability and cytotoxicity as it does not damage or destroy the cells, allowing for kinetic studies.

The assay itself relies on the reducing environment inside the cell. The reagent 7-Hydroxy-3H-phenoxazin-3-one 10-oxide (Resazurin) is reduced to 7-Hydroxy-3H-phenoxazin-3-one (Resorufin) as a result of aerobic respiration of metabolically active cells. This changes the reagent from weakly fluorescent to strongly fluorescent with an excitation range of 530-560 nm and emission of 590 nm [130]. This allows for a measure of cell viability in the sample as the metabolically active cells reduce Resazurin to Resorufin, which can be measured at the 590 nm emission peak.

2.12.2 ELISA

Enzyme-linked immunosorbent assays (ELISA) are immunoassays that are considered to be the gold standard for detecting low quantities of substances. They are incredibly sensitive, typically having assay ranges from tens of pg to hundreds of pg. They are typically used to quantify various forms of proteins, such as antigens, cytokines, and antibodies [131].

ELISA assays have multiple forms; Direct, Indirect, Sandwich, and Competitive. Briefly, direct and indirect ELISA assays involve binding the protein of interest to the ELISA plates. This requires incubation for 1 hour at 37 °C or overnight at 4 °C. The plate is then washed to remove unbound proteins and then any unbound sites are blocked using other proteins such as ovalbumin to prevent the antibodies from binding to these site and resulting in a false positive. Here the direct and indirect assays differ. Direct assays use an enzyme-conjugated primary detection antibody which can affect a substrate such as Horseradish peroxidase to create a detectable colour change. Indirect assays use two antibodies to achieve this result, one primary detection antibody and one enzyme-linked antibody that is complementary to the primary detection antibody [132].

The sandwich ELISA assays begin differently with the ELISA plates being coated with a capture antibody, this typically requires incubation for 1 hour at 37 °C or overnight at 4 °C. The plates are washed using phosphate buffered saline (PBS) and any unbound areas blocked with protein and then washed with PBS again.

The antigen is then added to the plate and is typically incubated at 37 °C for 90 minutes. The plate is then rewashed with PBS and a primary detection antibody added to the plate and incubated at room temperature for 1-2 hours. The plate is then washed using PBS and an enzyme-linked secondary antibody is added that is complementary to the primary detection antibody. This enzyme-linked antibody is then used to affect a colour change as mentioned above [132].

A competitive ELISA uses a method of signal interference to detect the antigens. This utilises a plate with antibodies specific to the antigen to be detected and also requires a labelled version of the antigen. This labelled antigen is added to each well and any decrease in the visibility of this labelled antigen from a well containing only this sample, indicates the presence of the antigen [132].

These tests have various advantages and disadvantages. The direct ELISA is fast and reduces the risk of cross-reactivity with a second antibody, however it is limited by fewer choices of primary antibodies available. The indirect ELISA is much more versatile when compared to the direct ELISA and maintains primary antibody reactivity as it is not enzyme-linked, it also has some signal amplification as the primary antibody has several binding sites for the secondary antibody. The indirect ELISA does have some disadvantages in increased risk of cross-reactivity with the secondary antibody and the extra steps required. Sandwich ELISA have the advantage of being highly sensitive and highly specific but involve more steps and require more development into the antibody pairs than the previous methods. Competitive ELISA allow for uses with less sample purification however is unsuitable for any dilute samples [131].

Overall as a result of the specificity and high sensitivity the sandwich ELISA are most suitable to detect specific cytokines in cell culture media samples while minimising the cross-reactivity with other substances in the samples.

3 CHARACTERISATION OF CRN-NBN COATING

3.1 MATERIALS AND METHODS

This section details the methods and materials used in the characterisation of the CrN-NbN Superlattice coating. Details of the materials used in these methods is included alongside how they were stored prior to use in these methods. Production of the CrN-NbN Superlattice coated discs is included from the polishing method of the initial CoCr substate through to the coating method. Sterilisation and preparation of the materials for cell culture, such as endotoxin removal and testing, is then detailed as these steps were vital in ensuring accurate data from the cell culture assays.

Following these sections, we look at the methods used to characterise the properties of the coating. Key areas that are characterised are surface properties such as the surface topography through profilometry and chemical composition of the coating through X-ray Photoelectron Spectroscopy (XPS).

Characterisation of the particles produced through the methods detailed in the sample preparation section follow this. The key areas to characterise for these particles was particle size and endotoxin load as these have a significant effect on cell response to the particles.

The methods used in cell culture as well as the cytotoxicity assays and cytokine assays are then detailed. Alongside this are the calibration curves used to calculate the concentrations for cytokines released through cell culture.

3.1.1 Sample Preparation and Handling

3.1.1.1 Materials

ASTM F75 CoCr discs were used as the substrate for the coating materials and as a comparison material. The discs were 25 mm diameter and 10 mm in height.

This coating was compared with Titanium nitride in both coating and powder forms in the cell culture work. Titanium nitride was coated by Ionbond using cathodic arc deposition at a temperature of 500°C onto the polished ASTM F75 CoCr discs. Titanium nitride powder was supplied by Sigma-Aldrich, with a size of 3 µm.

Alumina powder was also used as a comparison material for the cell culture with particles. Alumina powder was supplied by Sigma-Aldrich with a size of 3 µm.

Tissue culture plastic was also used as a control in both cases, using 75cm^2 flasks from Corning. Lipopolysaccharide (LPS) used as a positive control in cell culture was LPS from Escherichia Coli O111:B4 supplied by Sigma-Aldrich and was gamma irradiated to sterilise. Enzyme-linked immunosorbent assay (ELISA) testing kits were supplied by Sigma-Aldrich.

A 35mm (I.D.) x 10mm (H) agate pestle and mortar, supplied by Agar Scientific, was used for all manual grinding in sample preparation. This was chosen to minimise the contamination from the pestle and mortar while grinding the hard particles.

3.1.1.2 Storage of coated discs and uncoated discs

ASTM F75 CoCr discs were stored in polystyrene AGG3319 membrane boxes supplied by Agar Scientific. Once coated with either TiN or CrN-NbN they were stored in the vacuum sealed bags provided by Zimmer Biomet until they were required to be used, they were then opened and transferred to either a AGG3319 membrane boxes supplied by Agar Scientific or clean aluminium foil if they were to be used for X-ray Photoelectron Spectroscopy (XPS) to prevent the plastic in the membrane boxes from affecting the results.

3.1.1.3 Polishing of uncoated CoCr discs

These discs were polished using a Struers Labopol-5 and Laboforce-3. The samples were fixed to a brass plate by heating the plate to 130°C and melting wax onto it, the discs were then placed in the wax, and it was allowed to cool to room temperature before proceeding with the polish. Samples were polished with increasing grade silicon carbide grit paper, 120, 320, 600, 1200 and then 4000. The brass plate was then removed and used to polish the discs with a Struers Labopol-5 manually on a final polishing plate with Struers 0.04 µm colloidal silica suspension. Discs were then removed from the brass plate by heating it to 130°C and removing them with tweezers. Discs were then cleaned using washes of acetone followed by industrial methylated spirits followed by distilled water in order to remove all of the silica and wax, they were then air dried and stored in AGG3319 membrane boxes supplied by Agar Scientific in order to prevent scratching. These discs were then used for coating with TiN or CrN-NbN or as a comparison material.

The discs were polished in batches for coating and were marked on the underside to ensure that they could be tracked. Overall, there were 5 batches totalling 588 samples. Batches were of uneven number as can be seen in table E. Sample selection for experiments was spread across batches in order to ensure uniformity of results.

Batch Number	Number of Samples	Sample number range
001	185	1-185
002	55	186-240
003	91	241-331
004	77	332-408
005	180	409-588

Table 3. Detailing the sample numbers per batch and the sample numbers those encompassed.

3.1.1.4 Coating Manufacture

The superlattice material being investigated was a CrN-NbN superlattice coating produced through high power impulse magnetron sputtering (HIPIMS) by Zimmer Biomet by Sheffield Hallam University. This method is a form of ionised physical vapour deposition (IPVD) that uses very short pulses of power to produce the vapour, typically between 50-500 µs, with a pulse frequency of tens of hertz to kilohertz. This leads to a peak power two magnitudes higher than the time averaged power. The applied voltage of this method is typically between 500-1000 V and produces a high-density plasma, with an electron density of 10^{18}-10^{19} m^{-3} in area of the target surface compared to 10^{17} for direct current magnetron sputtering (DCMS) [84].

The CrN-NbN superlattice coating was manufactured using the method described by Purandare et al [132]. The coating was produced through HIPIMS and was shown to produce a coating with higher density and adhesion as well as better control over composition, microstructure, and mechanical and optical properties than coatings produced through direct current magnetron sputtering (DCMS).

Co-Cr discs were coated with the CrN-NbN superlattice coating for characterisation. This method used two Chromium targets and two Niobium targets with a substrate of ASTM F75 CoCr with an HTC 1000-4 PVD coater. The substrate was treated prior to coating with the CrN and NbN with a bombardment of Cr+ ions produced in an Ar atmosphere. A chamber temperature of 200°C was used and coating was performed for 120 minutes. A bias voltage of -65V was applied to the substrate for coating. The chamber was kept at 0.35Pa with a mixed atmosphere of Ar and N.

3.1.2 Surface Analysis

3.1.2.1 Profilometry

Profilometry was performed using a Fogale Photomap 3D on both ASTM F75 CoCr samples and CrN-NbN coated CoCr discs. Samples were placed using tweezers onto the sample stand. Samples were scanned using red light at 160x magnification. The Fogale Photomap 3D was on a vibration isolation table to reduce the vibrational noise. Vibrational noise produced waves on the surface parallel to the scanning beam. Profiles were taken along these waves to minimise the effect this had on the results. The direction of these waves did not change over 500+ samples regardless of orientation indicating that it was noise rather than surface topography. Results were levelled and a threshold of 95% put onto the sample's data. This removes 5% of the data with the greatest difference compared to the average and is necessary to reduce the impact of noise on the data and produce accurate results. Samples were marked on the underside prior to coating to enable the comparison before and after coating.

Measurements of the surface measured the roughness using the R_a, R_{sk}, and R_{rms}. The R_a is calculated as the average deviation from the total sample average. It uses the following formula for calculation:

$$R_a = \frac{1}{l_r}\int_0^{l_r} |z(x)|dx$$

The R_{rms} is calculated as the root mean square of the average deviation from the total sample average. It uses the following formula for calculation:

$$R_{rms} = \sqrt{\frac{1}{l_r}\int_0^{l_r} |z(x)^2|dx}$$

The R_{sk} is calculated as the measure of asymmetry of the profile from the total sample average. It uses the following formula for calculation:

$$R_{sk} = \frac{1}{Rq^3}\left[\frac{1}{l_r}\int_0^{l_r} Z^3(x)dx\right]$$

3.1.2.2 Contact Angle Analysis

Contact angle measurement was performed using sessile drop technique on samples before and after coating. Firstly, the camera was aligned to the surface of the samples to ensure accurate results. A droplet was then carefully dropped from a syringe mounted above the sample, followed by taking an image with the camera after 5 seconds. This used an FTÅ 200 instrument using deionised water. The images taken were then analysed using the FTÅ32 software to calculate the contact angle of the droplet with the material. This was repeated four times for each sample.

3.1.2.3 Coating Scanning electron microscopy (SEM)

The superlattice coated samples were analysed using Scanning electron Microscopy (SEM) after being carbon coated using an Agar Turbo Carbon Coater and Sputter Coater. Analysis was performed on the Philips FEI XL30 SEM and images taken using secondary electron imaging and back scattered electron imaging at 10.0 kV and a spot size of 4.0.

3.1.2.4 X-ray Diffraction (XRD)

Low angle X-ray Diffraction (XRD) was performed on the CrN-NbN coated discs in order to measure the superlattice spacing, this is the distance between each layer, as can be seen in figure 8. Samples were handled using gloves to ensure the samples were clean. Samples were then mounted on a stand, and this was performed using the Bruker D8 Advanced X-ray Diffractometer. The Bruker D8 Advanced X-ray Diffractometer used a Cu Kα source producing x rays at a wavelength of 0.15418 nm with a power of 40 kV and 35 mA. The starting angle was 1.0° and increased in steps of 0.020° up until 5.0° with a step time of 8 seconds. This is converted to a d spacing value using Braggs law as follows:

$$n\lambda = 2dsin\theta$$

3.1.2.5 X-ray Photoelectron Spectroscopy (XPS)

XPS was used to determine the chemical environment of the surface layer using angle resolved XPS. This used the VG ESCALab Mark II X-ray Photoelectron Spectrometer and used take off angles of 90° and 15°. The VG ESCALab Mark II

X-ray Photoelectron Spectrometer used an Al kα non-monochromatic X-ray source. Scans were collected using 20 mA and 12kV emissions.

XPS was also used to determine the effects of cell culture media on the coating (This analysis was performed using a Kratos AXIS XPS Instrument operated by Dr. Emily Smith in the Nottingham Nanotechnology and Nanoscience Centre (NNNC).) The Kratos AXIS XPS Instrument uses a Monochromated X-ray source Al Kα emission at 1486.6 eV and scans were collected using 10 mA and 15kV emissions. Three samples were placed in cell culture media for 72 hours then removed and compared to three samples that were not placed in cell culture media.

XPS was also performed on a sample of CrN-NbN particles produced through ball milling. The sample was dried onto some adhesive tape on a stand before analysis (This analysis was performed using a Kratos AXIS XPS Instrument operated by Dr. Emily Smith in the Nottingham Nanotechnology and Nanoscience Centre (NNNC).) The Kratos AXIS XPS Instrument uses a Monochromated X-ray source Al Kα emission at 1486.6 eV and scans were collected using 10 mA and 15kV emissions.

All XPS data was peak fitted and analysed using CasaXPS software. The NIST database was used to assign peaks and the closest fitting peak assigned to that peak. Each spectra was charge fitted to the C 1s peak as is standard procedure [133].

3.1.2.6 Coating Cross section analysis

The cross section of the CrN-NbN coating was analysed through SEM and EDX. A CrN-NbN disc was mounted in conductive resin using a MetaServ mounting press. The sample was then polished down to show a cross section using a Labopol-5 using increasing grit values (120, 320, 600, 1200, 4000) of silicon carbide grit paper, provided by Stuers. This sample was then carbon coated using an Agar Turbo Carbon Coater and Sputter Coater. The sample was then mounted on a stand using a carbon tab and analysed through SEM and EDX using a Philips FEI XL30 SEM at 20.0 kV and a spot size of 4.0.

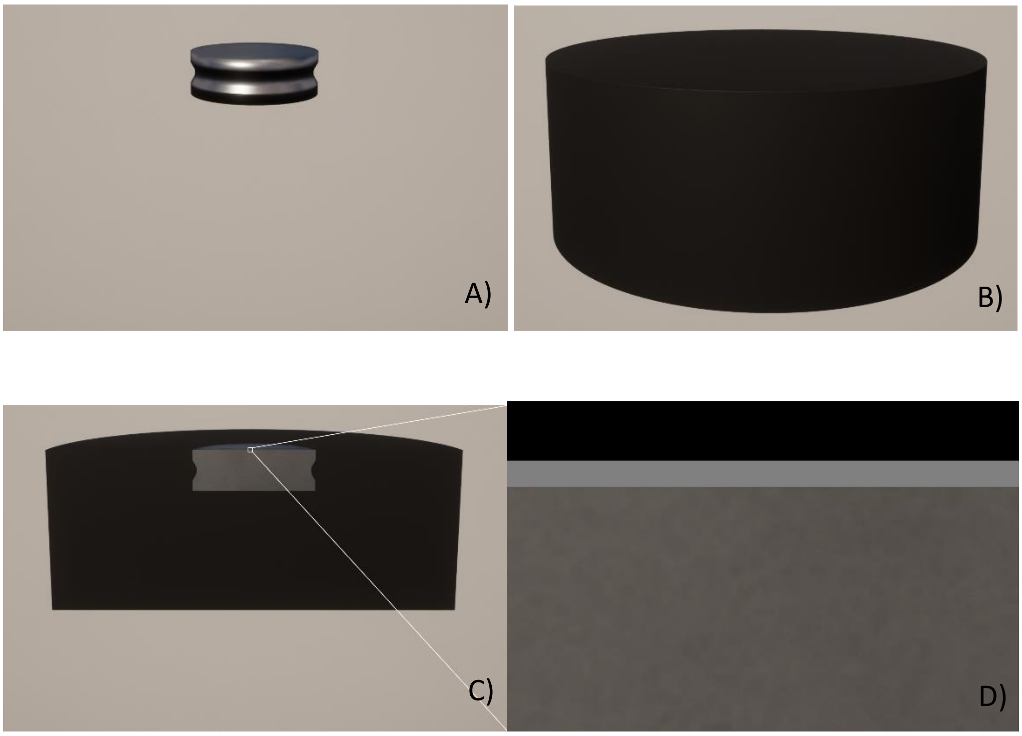

Figure 9. Indicating the process through which the sample is prepared for cross section analysis. A) The sample to undergo cross section analysis is selected. B) The sample is then encased in conductive resin. C) The side of the resin and the sample is then polished to reveal the sample. D) The edge of the sample is then analysed using SEM.

3.1.3 Statistics

All tests were repeated at least once to ensure their validity. Microsoft Excel and GraphPad Prism were used for the statistical analysis of all data produced.

All experiments were performed at least twice, with XPS experiments being performed three times. Typical n values for XPS, SEM and EDX were 3 samples of each type. Typical n values for cytotoxicity assays were 6 of each sample type. The typical sample number for all cytokine assays was 4. All n values are also listed below their respective results figure.

Significance between samples was determined using two-way ANOVA tests with Tukey's multiple comparison tests where $p<0.05$ was used as the threshold to determine significance. For concentration calculations regression lines were calculated to best fit the standard curve produced and were chosen to be linear based on the instructions with the specific kits as can be seen in figures 37-40, and 63-66.

3.2 RESULTS

3.2.1 Surface properties of the material

The surface properties such as surface roughness values and contact angle analysis are presented in the following section. The surface morphology is also presented here through SEM images of the surface.

3.2.2 Surface Morphology

3.2.2.1 Profilometry

The mean results of the 15 uncoated CoCr discs are shown in Table 4. Compared to the result for the same 15 samples after coating also shown in Table 4. R_a, R_{sk} and R_{rms} can be seen in these tables. R_a and R_{rms} are measures of the average surface roughness of the sample thought R_{rms} is more affected by large peaks or valleys due to the calculation method. R_{sk} is a measure of the skew of the surface, a positive value larger peaks and smaller valleys while a negative value indicates small peaks and deep valleys. As a result of the coating process, the surface roughness, as measured by R_a, can be seen to increase by 3.5x that of the uncoated CoCr surface. This increase is more pronounced when comparing the surface roughness as measured by R_{rms} as this increases 3.75x as a result of the coating process.

Images from profilometry revealed changes in the topography of the samples before and after coating shown in figure 10a and 10b respectively. Figure 10a has been levelled while figure 10b has not been levelled in order to improve visibility of the surface topography. Neither image had a threshold put onto it as this increased the prominence of the waves from vibrational noise.

On the CoCr sample there are ridges across the sample 0.2-1.0 µm in height and some peaks 0.2-1.0 µm in height. There are no other clearly visible features on the CoCr samples.

The CrN-NbN superlattice coated samples demonstrate many pits, 3–22 µm in diameter, formed on the surface, the depth of which is beyond the ability of the equipment to measure (> 10 µm). Scratch marks are clearly visible on the surface and do not show any directionality. The surface also has a visible textured appearance.

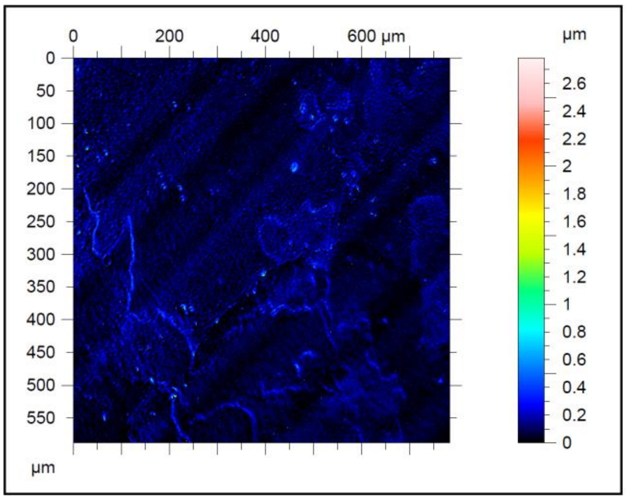

Figure 10a. An example profilometry image of a polished CoCr sample disc showing raised ridges over the surface in light blue, vibrational noise is visible as diagonal waves across the surface. This image was produced using a Fogale Photomap 3D.

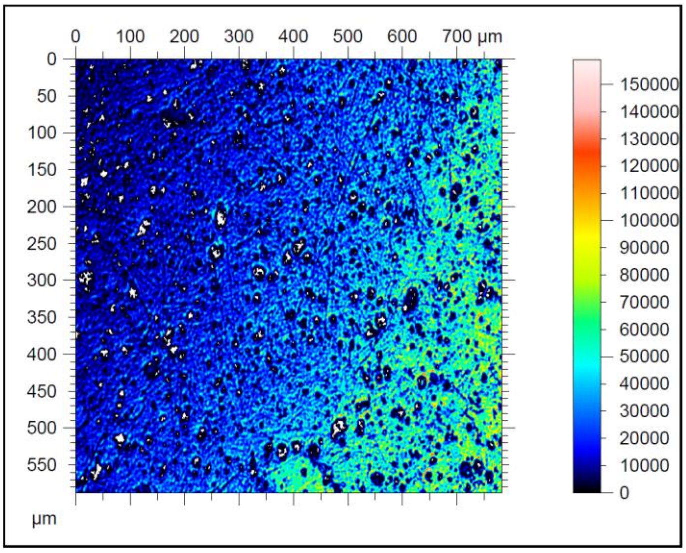

Figure 10b. An example profilometry image of a CrN-NbN superlattice coated CoCr disc showing scratches along the surface in dark blue and pits in darker blue/black. White areas are areas that were not scanned due to the pits being too deep. As the image was not levelled vibrational noise is not as prominent. This image was produced using a Fogale Photomap 3D.

		R_a (nm)	R_{sk}	R_{rms} (nm)
Uncoated CoCr	Mean	52	0.054	67
	Standard Deviation	13	0.465	17
CrN-NbN coated CoCr	Mean	181	0.008	253
	Standard Deviation	57	0.940	76

Table 4. Mean and standard deviation of R_a, R_{sk} and R_{rms} values from red light interferometry on 15 polished CoCr samples before coating with a CrN-NbN superlattice and after coating using a Fogale Photomap 3D.

3.2.2.2 Contact Angle Analysis

A summary of the contact angle analysis for the uncoated CoCr discs is shown in Table 5, compared to the contact angle data for the superlattice coated discs. Example images of the drop of water on the surface of the uncoated CoCr disc and superlattice coated disc can be seen in figures 10a and 10b respectively. An increase in contact angle can be seen as a result of the coating process, likely as a result of the change in surface chemistry and surface topography. This also causes a decrease in the standard deviation of the contact angle despite the increase in standard deviation of the surface roughness.

		Contact Angle (°)
Uncoated CoCr	Mean	71.1
	Standard Deviation	7.7
CrN-NbN coated CoCr	Mean	90.8
	Standard Deviation	4.2

Table 5. Mean and standard deviation of contact angles of fifteen polished CoCr sample discs before coating and following coating with the CrN-NbN superlattice as determined by sessile drop technique using deionised water five seconds after droplet impact with the sample on an FTA200.

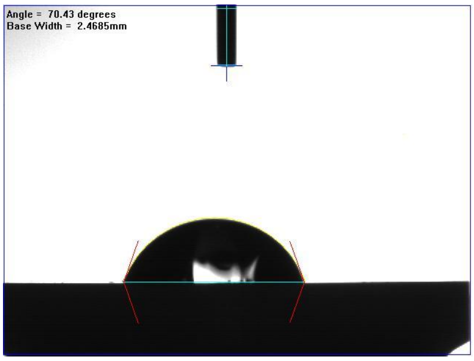

Figure 11a. An example image showing the contact angle and base width of a sample polished CoCr disc as determined by sessile drop technique using deionised water, taken five seconds after impact with the sample on an FTA200. A relatively low contact angle can be seen here with a wider base than seen post-coating.

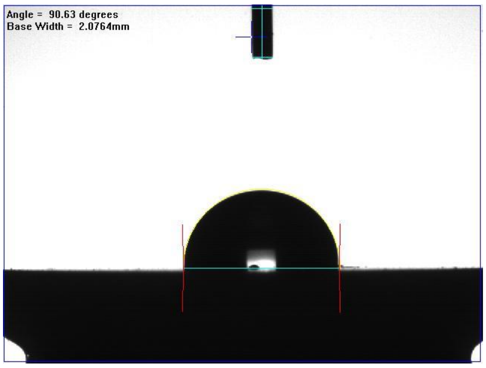

Figure 11b. An example Image showing the contact angle and base width of a sample polished CoCr disc after coating with a CrN-NbN superlattice as determined by sessile drop technique using deionised water, taken five seconds after impact with the sample on an FTA200. A higher than 90-degree contact angle can be seen here with a relatively low base width compared with previous results.

3.2.2.3 Scanning electron microscopy (SEM) Imaging

The SEM imaging of the coating shows the surface topography of the CrN-NbN superlattice coated CoCr disc, many pits can be seen in the coating of approximate surface density of 22 per 100 µm^3 or typical size range 3 µm to 20 µm along with droplets. The droplets, typically of size range 3 µm to 12 µm and of approximate surface density of 14.4 per 100 µm^3, were initially believed by the author to be chromium droplets on account of the lower melting point compared to niobium (2180 K and 2750 K respectively). The overall topography can be seen in Figure 12. Figure 13 shows an image of a pit in the surface. Figure 14 shows an image of a droplet that appears to be partially ejected from the surface. Figure 15 shows a general area of the surface, showing the presence of pits, droplets, and seams. Figure 16 shows a seam/valley in the material that appears to have been due to a surface scratch on the substrate that the coating has been deposited in.

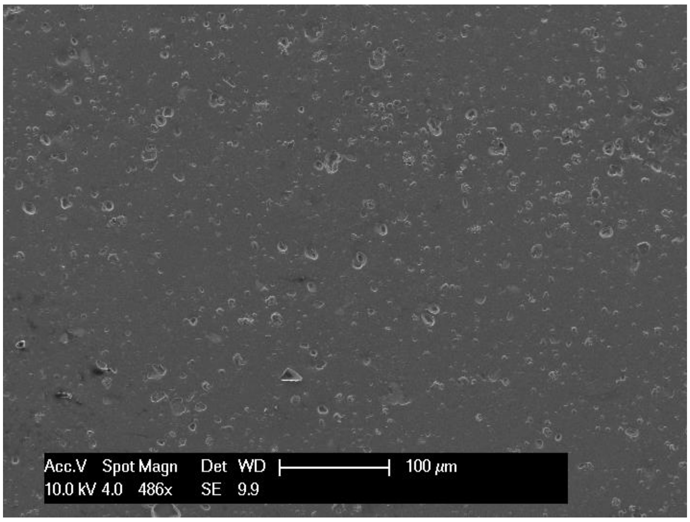

Figure 12. SEM secondary electron image of the surface of a CrN-NbN superlattice coated CoCr disc taken on a Philips XL30 SEM using secondary electron imaging. Small droplets and pits are seen to be regular features across the surface.

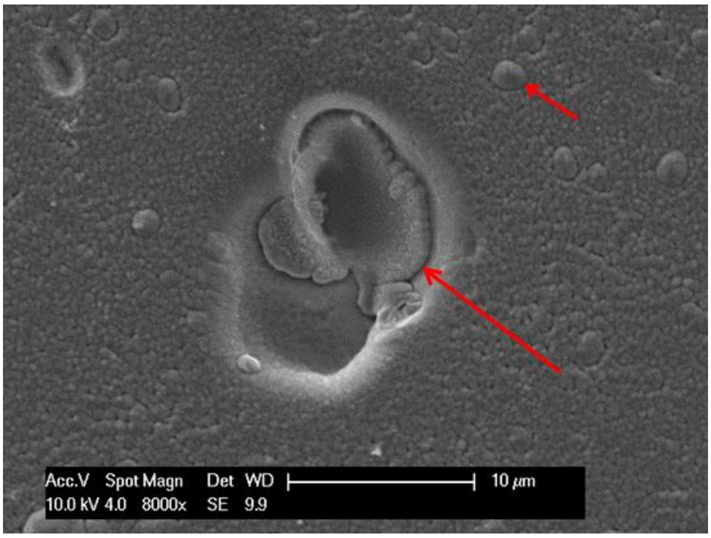

Figure 13. SEM secondary electron image of the CrN-NbN superlattice coated CoCr samples taken on a Philips XL30 SEM using secondary electron imaging showing a pit roughly 10 µm in diameter in the surface of the coating. The pit appears uneven and has a similar rounded structure as seen on the rest of the coating. Small droplets can also be seen on the coating.

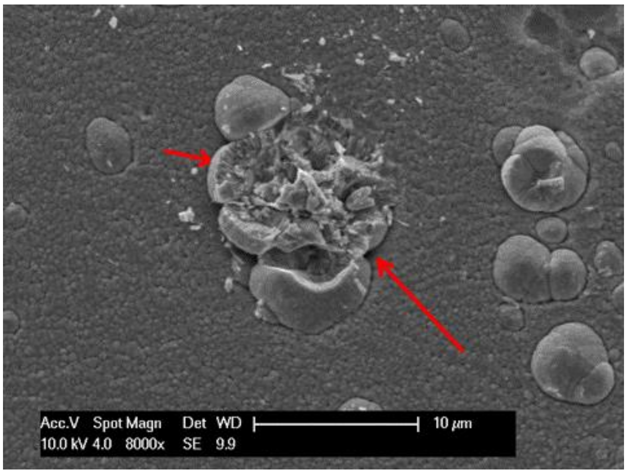

Figure 14. SEM secondary electron image of the CrN-NbN superlattice coated CoCr sample taken on a Philips XL30 SEM using secondary electron imaging showing a droplet on the surface of the superlattice coating. The large droplet is roughly 10 µm in diameter and a columnar structure can be seen to the left side of the droplet. There are many smaller droplets on the right of the image.

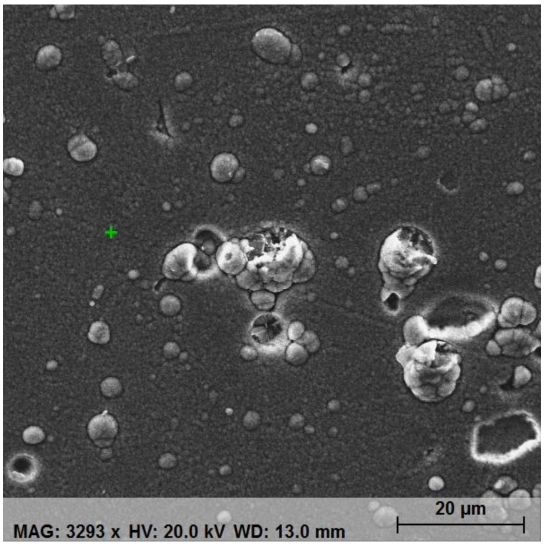

Figure 15. SEM secondary electron image of the CrN-NbN superlattice coated CoCr sample taken on a Philips XL30 SEM using secondary electron imaging showing the area that EDX was performed on in the following figures. Several droplets and pits are visible across the surface of the coating and is typical of the general surface morphology.

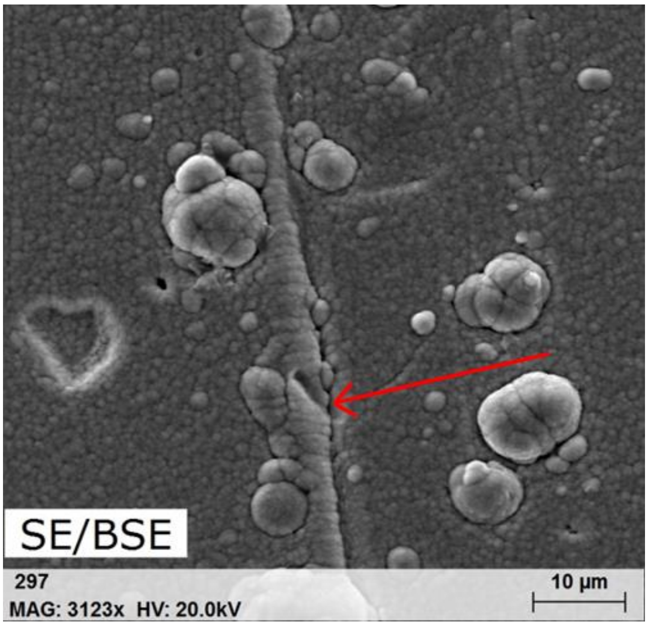

Figure 16. SEM secondary electron image of the CrN-NbN superlattice coated CoCr sample taken on a Philips XL30 SEM using secondary electron imaging. Here a seam like feature can be seen, likely to be caused by a surface scratch on the material before coating.

3.2.3 Surface Chemistry

The chemistry of the materials is presented here through EDX on the CrN-NbN coating and XPS of the substrate, coating, and coating after being stored in a biological environment.

3.2.3.1 EDX on CrN-NbN Coating

EDX analysis of the coating material's composition indicated the presence of Niobium, Chromium, Oxygen and Aluminium, as seen in figure 17. The surface EDX images for Cr, Nb and O are shown in figure 18. In other work on a similar coating Cr, Nb and N were found to be 39 %, 14 % and 47 % respectively in work performed by Biswas et al [134]. Though this was not a surface measurement and so will not have the oxygen expected from oxidation of the sample. This indicates a Cr:Nb ratio of 2.79:1, compared to our finding of a Cr:Nb ratio of 2.72:1.

Figure 18 shows the composition of Nb, Cr, and O on the surface of the CrN-NbN superlattice coating. It can be seen that oxygen is present throughout the sample. There is some shadowing from surface features though this is consistent through all images.

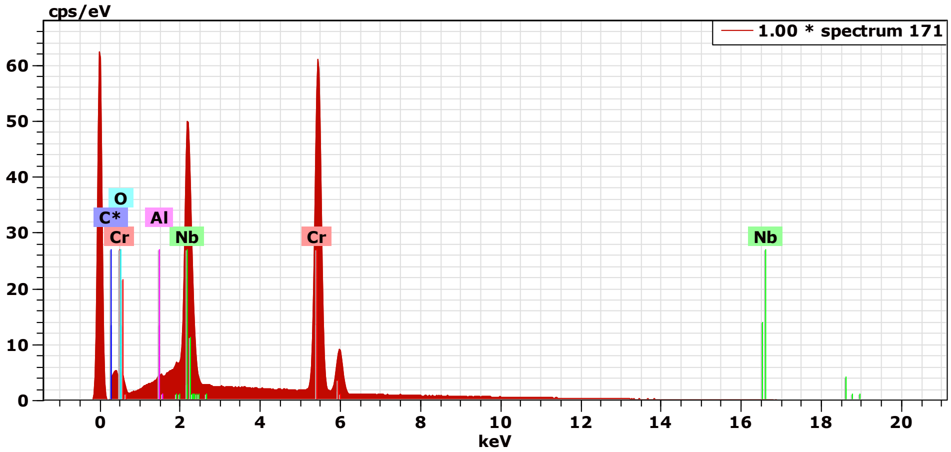

Figure 17. EDX spectrum of the CrN-NbN superlattice coating taken using a Philips XL30 SEM indicating the presence of Cr, Nb, O and Al.

Element	Normalised composition [wt.%]	Atom composition [at.%]	Atom composition % Error
Cr	58.95	67.18	±1.26
Nb	38.62	24.63	±1.13
O	1.89	7.01	±0.28
Al	0.53	1.17	±0.05

Table 6. Composition of the CrN-NbN superlattice coating. This shows trace amounts of aluminium, as well as the expected Cr, Nb, and oxygen. The oxygen is likely a result of surface oxidation or the CrN and NbN. The aluminium is believed to have originated from the wire frame that held the items for coating, like a small flake that became embedded in the coating.

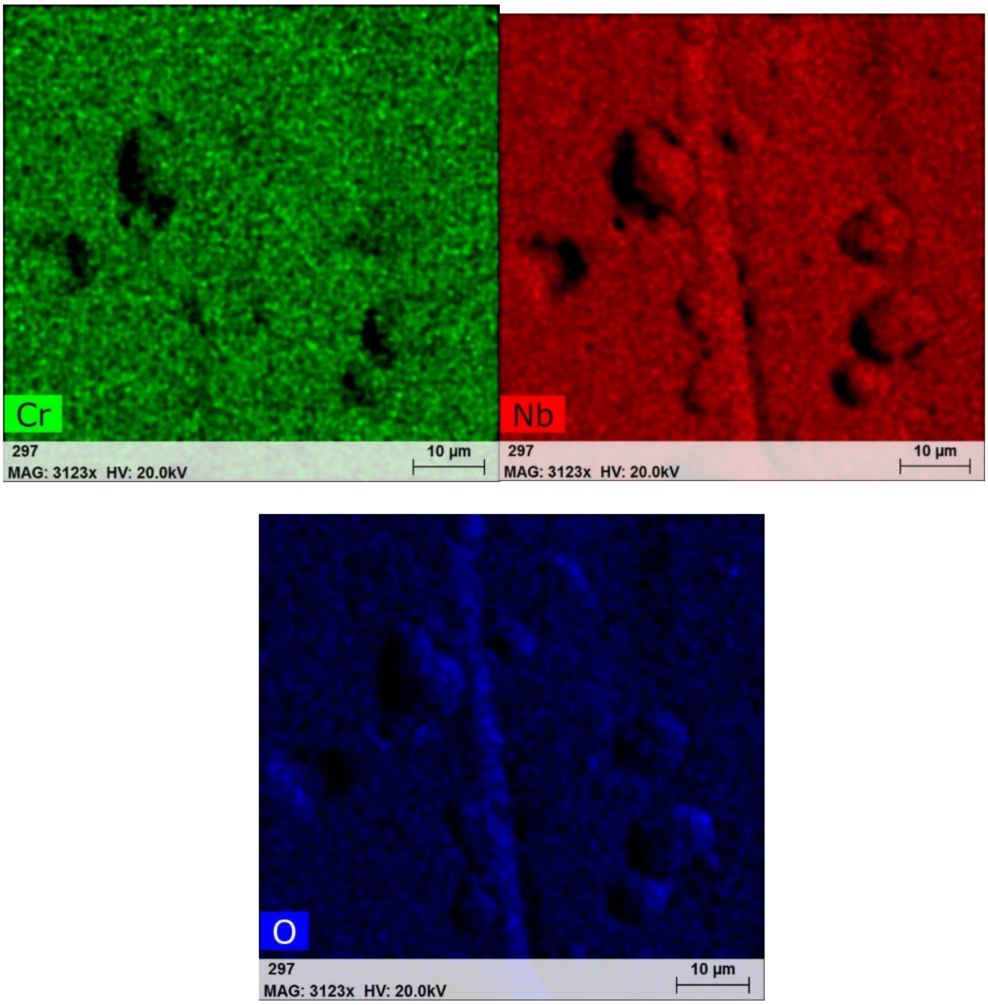

Figure 18. EDX image of the CrN-NbN superlattice coating taken using a Philips XL30 SEM showing visually the concentration of Cr, Nb, and O. The bright coloured areas indicate higher concentrations. These images are of the same area as seen in figure 16.

3.2.3.2 X-ray Photo-electron Spectroscopy (XPS)

XPS of the CoCr and CrN-NbN substrate and coatings are as follows.

3.2.3.2.1 CoCr disc substrates

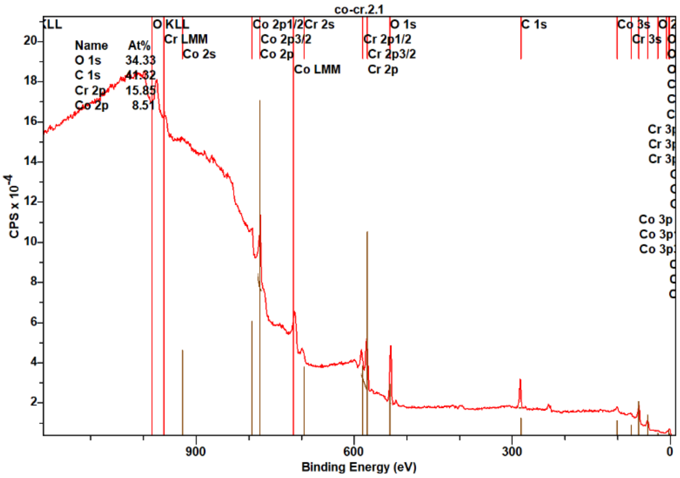

Figure 19. Survey XPS scan at 90° take-off angle of a CoCr disc taken on the VG ESCALab Mark II X-ray Photoelectron Spectrometer. Peaks can be seen for Cr, Co, C and O indicating their presence in the sample. The presence of oxygen and carbon is likely to indicate carbon contamination during handling and oxidation of the surface of the material.

A typical XPS survey scan of the CoCr discs is shown in figure 19 and the atomic percentage is tabulated in table 7. This shows Co:Cr ratio of 1.87:1 where the expected Co:Cr ratio is 2.04:1.

From the high-resolution scan of the C peak, it can be seen that the majority of C is adventitious, as is shown in figure 20. Three components of the peak can be seen when it is deconvoluted, although these are not labelled as any particular molecule as there are a large number of potential options for each peak.

Element	At% ± 0.5
O	34.3
C	41.3
Cr	15.9
Co	8.5

Table 7. Element percentages present in the CoCr disc using XPS using the VG ESCALab Mark II X-ray Photoelectron Spectrometer.

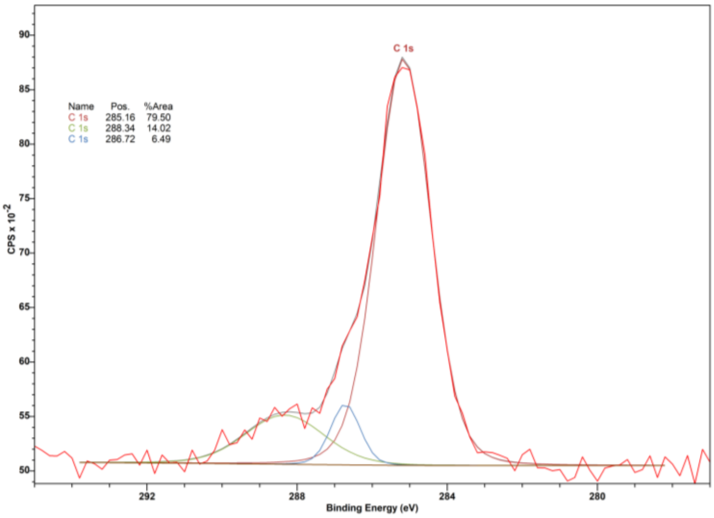

Figure 20. High resolution XPS scan of C 1s peak at 90° take-off angle of a CoCr disc taken on the VG ESCALab Mark II X-ray Photoelectron Spectrometer. Peaks fitting shows three elements to this Carbon 1s peak.

Compound	Position (eV)	% Area
C-C/C-H	285.16	79.50
C-O	286.72	14.02
C=O	288.34	6.49

Table 8. High resolution XPS scan of C 1s peak at 90° take-off angle of a CoCr disc taken on the VG ESCALab Mark II X-ray Photoelectron Spectrometer. Peaks fitting shows three elements to this Carbon 1s peak.

3.2.3.2.2 CrN-NbN coating

XPS of the CrN-NbN coating shows the presence of Chromium, Niobium, Oxygen, Carbon, and Nitrogen, which are the elements we would expect to see from minor contamination and surface oxidation can be seen in figure 21. The high-resolution scans of the C 1s peak and O 1s peak shown in figures 22 and 23 respectively show the presence of adventitious carbon on the sample, though these peaks are not identified as a single molecule due to the large number of potential carbon-containing molecules that could cause these peaks. Adventitious carbon is found on most air exposed samples although it’s possible that oils from the vacuum pump contribute to the presence of adventitious carbon here. The oxygen high-resolution scan also shows the presence of a niobium oxide peak at 530.3 eV.

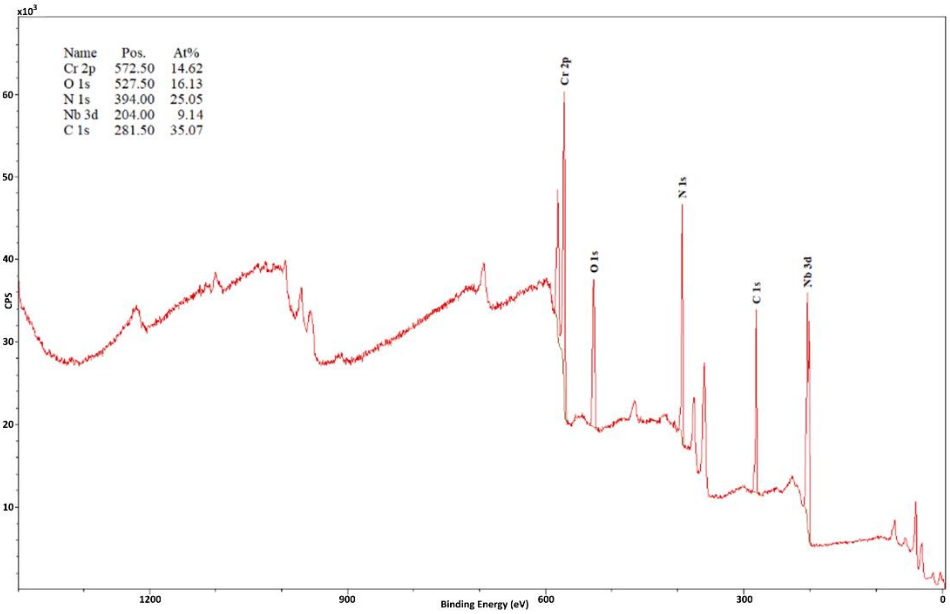

Figure 21. Survey XPS scan at 90° take-off angle of a CrN-NbN superlattice coated disc taken on the VG ESCALab Mark II X-ray Photoelectron Spectrometer. Peaks can be seen for Nb, C, N, O and Cr indicating their presence in the sample. The presence of oxygen and carbon is likely to indicate carbon contamination during handling and oxidation of the surface of the material.

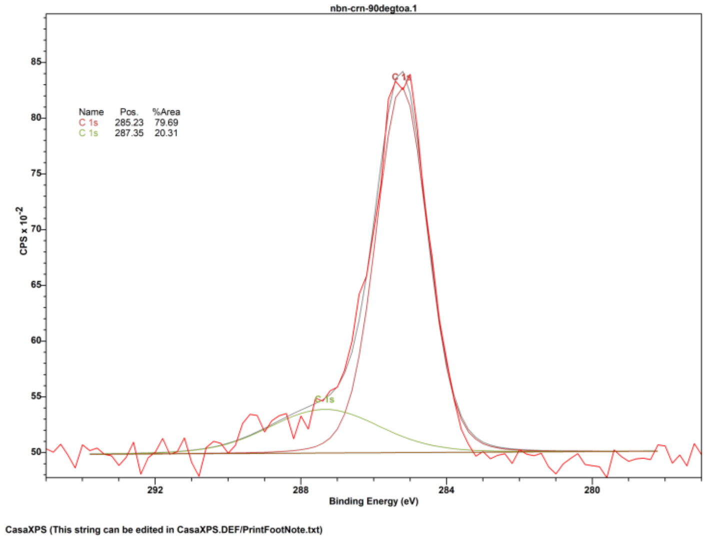

Figure 22. High resolution XPS scan of C 1s peak at 90° take-off angle of a CrN-NbN superlattice coated disc taken on the VG ESCALab Mark II X-ray Photoelectron Spectrometer. Two components can be seen to the peak when deconvoluted.

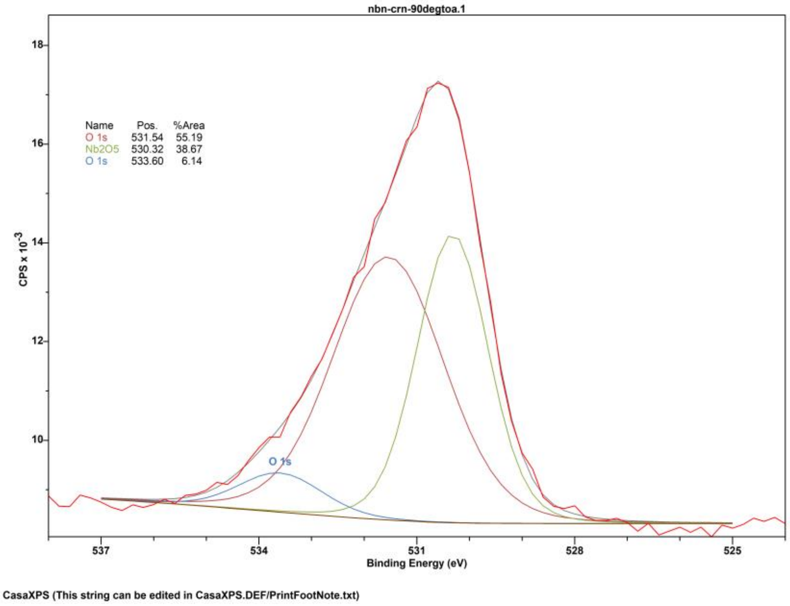

Figure 23. High resolution XPS scan of O 1s peak at 90° take-off angle of a CrN-NbN superlattice coated disc taken on the VG ESCALab Mark II X-ray Photoelectron Spectrometer. Three components of the peak can be seen when deconvoluted.

3.2.3.2.3 Changing take off angle

Survey scans of the superlattice sample using XPS at take-off angles of 90° and 20° can be seen in figure 24 and figure 25 respectively showing the elements present in the surface of the coating. As the angle is reduced only the top layer of the coating is analysed. A comparison of the element percentages between 3 samples at take-off angles of 90° and 20° can be seen in table 9. This shows agreement for the ratio of Cr:Nb between the EDX results in table 6 and the XPS results in table 9. With EDX showing a Cr:Nb ratio of 2.72:1 and XPS showing a Cr:Nb ratio of 2.38.

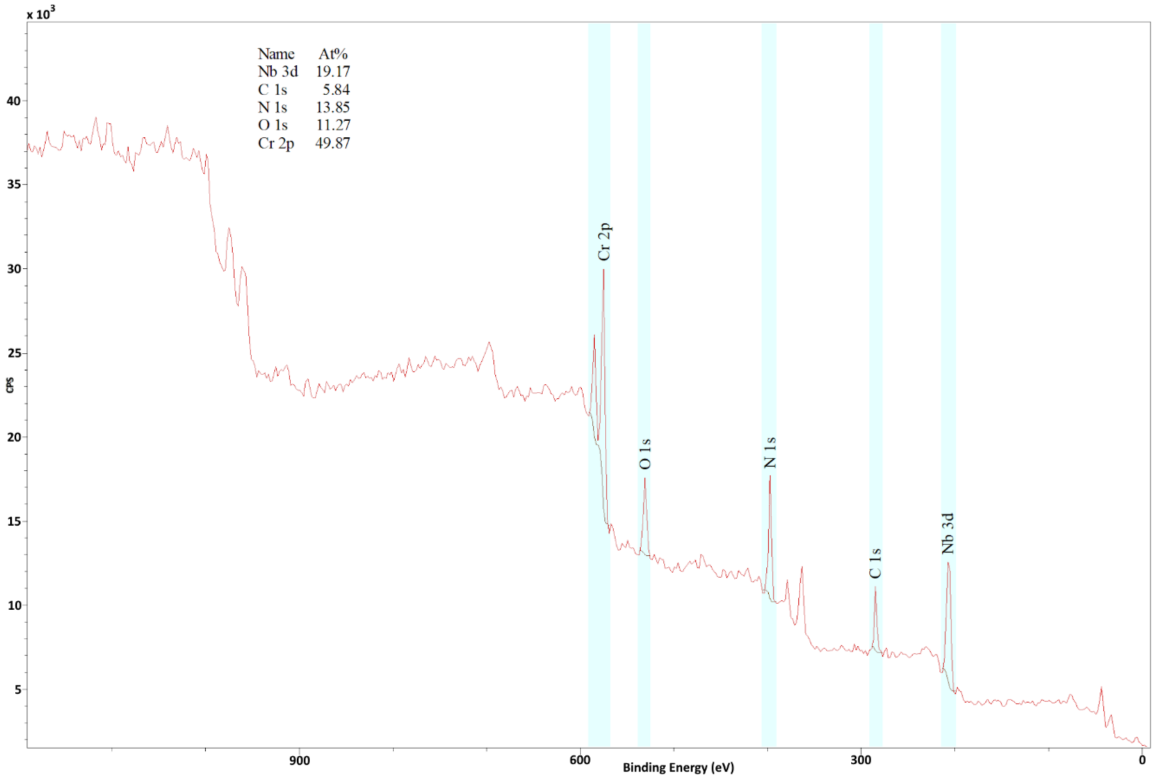

Figure 24. Survey XPS scan at 90° take-off angle of a CrN-NbN superlattice coated disc taken on the VG ESCALab Mark II X-ray Photoelectron Spectrometer. Peaks can be seen for Nb, C, N, O and Cr indicating their presence in the sample. This is a different sample to figure 21, indicating reproducibility of the results.

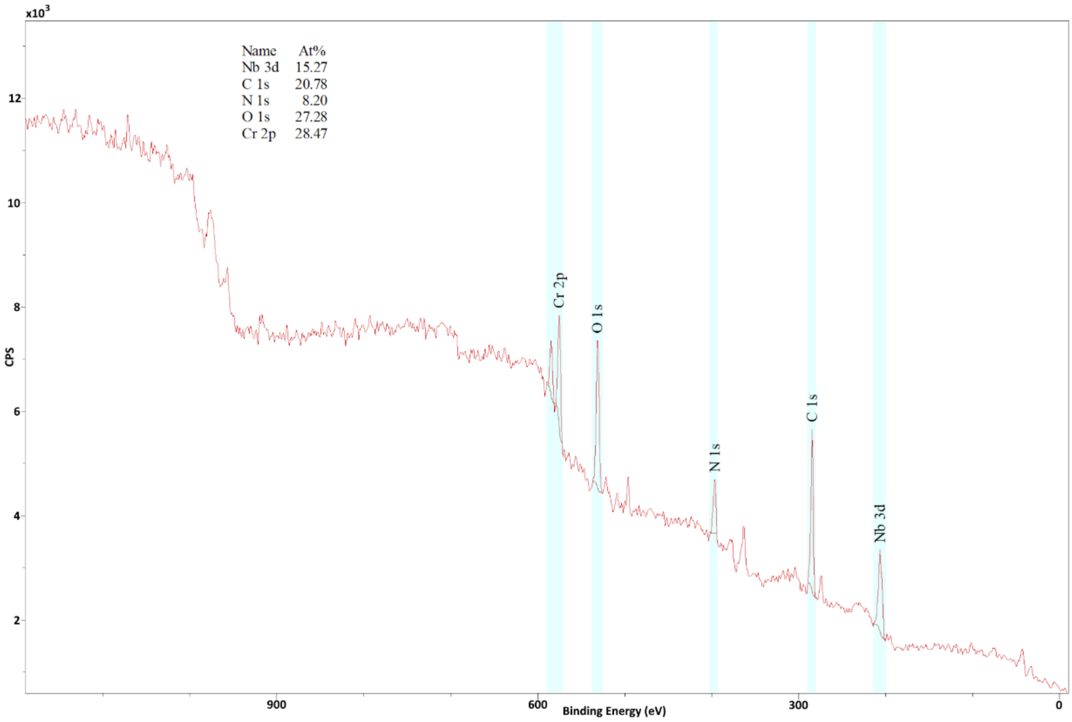

Figure 25. Survey XPS scan at 15° take-off angle of a superlattice coated disc taken on the VG ESCALab Mark II X-ray Photoelectron Spectrometer. Peaks can be seen for Nb, C, N, O and CR indicating their presence. A large carbon peak is seen which is likely to indicate surface carbon contamination. A large oxygen peak is also present indicating some oxidation of the CrN-NbN superlattice has occurred.

Sample	**TOA (°)**	**C 1s % ± 0.5**	**Cr 2p % ± 0.5**	**N 1s % ± 0.5**	**Nb 3d % ± 0.5**	**O 1s % ± 0.5**
1	90	5.6	46.6	5.6	19.6	22.6
2	90	7.0	45.1	5.6	18.9	23.3
3	90	7.5	44.4	6.0	18.7	23.5
1	20	12.9	31.5	5.6	23.1	26.9
2	20	7.9	39.2	6.2	21.6	25.0
3	20	8.6	39.2	6.8	18.9	26.5

Table 9. Element percentages present in the superlattice coated disc at 90° and 20° take-off angles for XPS for 3 CrN-NbN superlattice coated CoCr samples using the VG ESCALab Mark II X-ray Photoelectron Spectrometer.

Of interest is the surface that is presented in a biological environment. Therefore, the following section details the high-resolution scan before and after exposure to media.

3.2.3.2.4 Effect of a biological environment on surface chemistry

Here high-resolution scans of Cr, Nb, C, O, and N were performed and an example of the Cr and Nb high resolution scans are shown in figure 26, 27, 28, and 29 before and after exposure to biological media. Tabulated results before and after exposure to biological environment were analysed by CASA XPS the results for the superlattice coating can be seen in table 10. High resolution scans of the Cr and Nb peaks for both the samples left in media for 72 hours and the samples not left in media give insight into the potential environment of these elements.

Figure 26 shows a high-resolution scan of the Cr peak from the superlattice coated disc that was not in media, this shows the Cr doublet as expected from the Cr 2p doublet (2p 1/2 and 2p 3/2). Deconvolution of the peaks shows Cr_2N, CrN, Cr_2O_3, and CrO_3 and this is detailed in table 11. Figure 27 shows a high-resolution scan of the Cr peak from the superlattice coated disc that was in media.

Figure 28 shows a high resolution scan of the Nb doublet from the superlattice coated disc that was not in media, this shows a triplet appearance however this is due to a large energy shift in one of the doublet components [13]. Deconvolution of the peaks shows NbO_2, NbO, Nb_2O_5, and NbNO as shown in table 12. Figure 29 shows a high-resolution scan of the Nb peak from the superlattice coated disc that was left in media, the doublet to the right is a Cl peak.

Sample	C 1s % ± 0.5	Ca 2p % ± 0.5	Cr 2p % ± 0.5	N 1s % ± 0.5	Na KLL % ± 0.5	Nb 3d % ± 0.5	O 1s % ± 0.5	Media
1	49.2	-	11.6	18.6	-	5.3	15.3	No
2	35.7	-	16.8	24.5	-	8.8	14.2	No
3	38.0	-	16.7	23.9	-	7.3	14.0	No
13	58.4	0.9	7.4	13.7	1.2	4.8	13.7	Yes
14	47.4	2.0	7.2	14.4	3.4	4.3	21.4	Yes
15	41.2	0.2	8.5	15.3	9.5	3.0	22.3	Yes

Table 10. Element percentages present in the superlattice coated disc, samples 1-3 were not placed in media for 72 hours while samples 13-15 were. This data was produced using Kratos AXIS XPS Instrument operated by Dr. Emily Smith in the Nottingham Nanotechnology and Nanoscience Centre (NNNC). There is an increase in oxygen content of the samples that were placed in media as well as these samples showing sodium and calcium content.

While not a significant difference the Cr peak shows a decrease in oxidation following soaking of the samples in media. This can be seen as an increase in the proportion of CrN and Cr_2N compared to Cr_2O_3 and CrO_3, seen in tables 11 and 12 and figures 26 and 27. A similar effect is seen with the Nb peak, showing a non-significant decrease in oxidation state. This can be seen as an increase in the proportion of the lower oxidation states of NbNO and NbO when compared to NbO_2 and Nb_2O_5, as seen in tables 13 and 14 and figures 28 and 29. This indicates that there is no increase in oxidation as a result of soaking in media. Figures 30 and 31 show the high-resolution scans of the N 1s peak and along with tables 16 and 17 show a decrease in the CrN/NbN:Organic compound ratio.

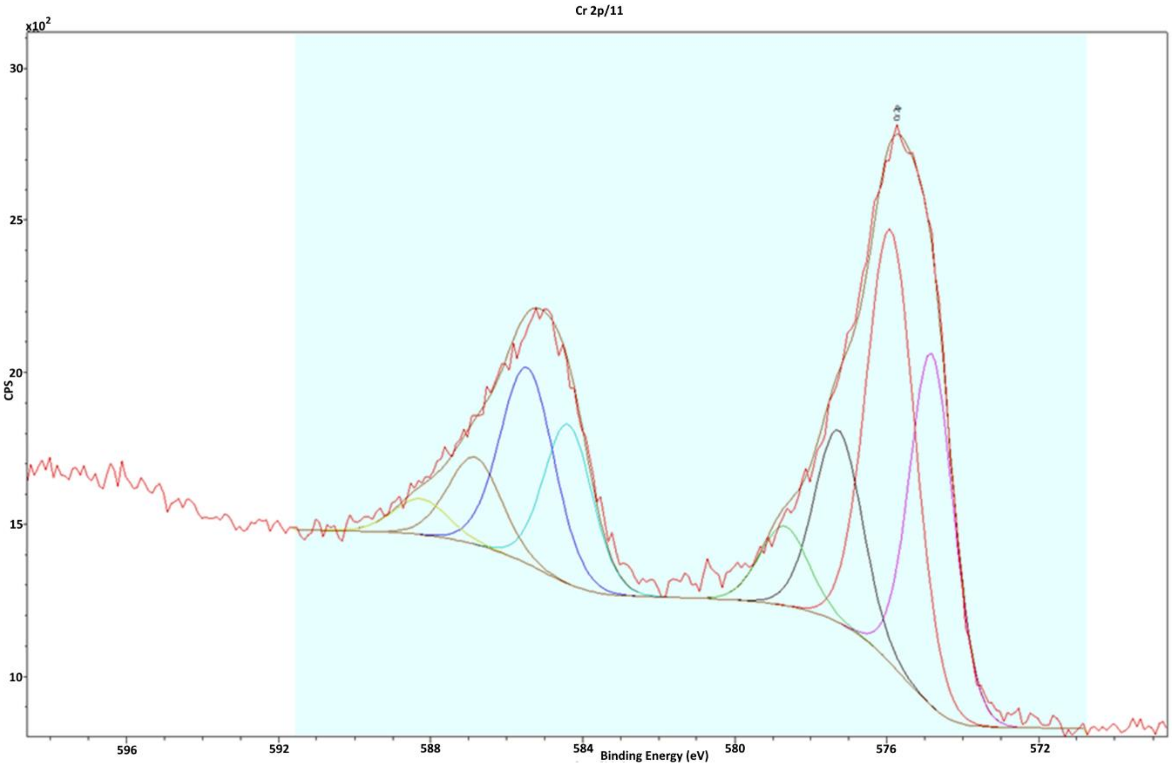

Figure 26. High resolution scan of the Cr 2p doublet produced using a Kratos AXIS XPS showing likely components of the doublet for the CrN-NbN superlattice sample not soaked in media.

Compound	Position (eV)	% Area
Cr_2N	574.82	20.8
Cr_2N	584.38	10.4
CrN	575.90	28.3
CrN	585.46	14.1
Cr_2O_3	577.27	12.5
Cr_2O_3	586.84	6.2
CrO_3	578.69	5.2
CrO_3	588.26	2.6

Table 11. Detailing the likely compounds found in the high-resolution scan of the Cr 2p doublet produced using a Kratos AXIS XPS for the CrN-NbN superlattice sample not soaked in media.

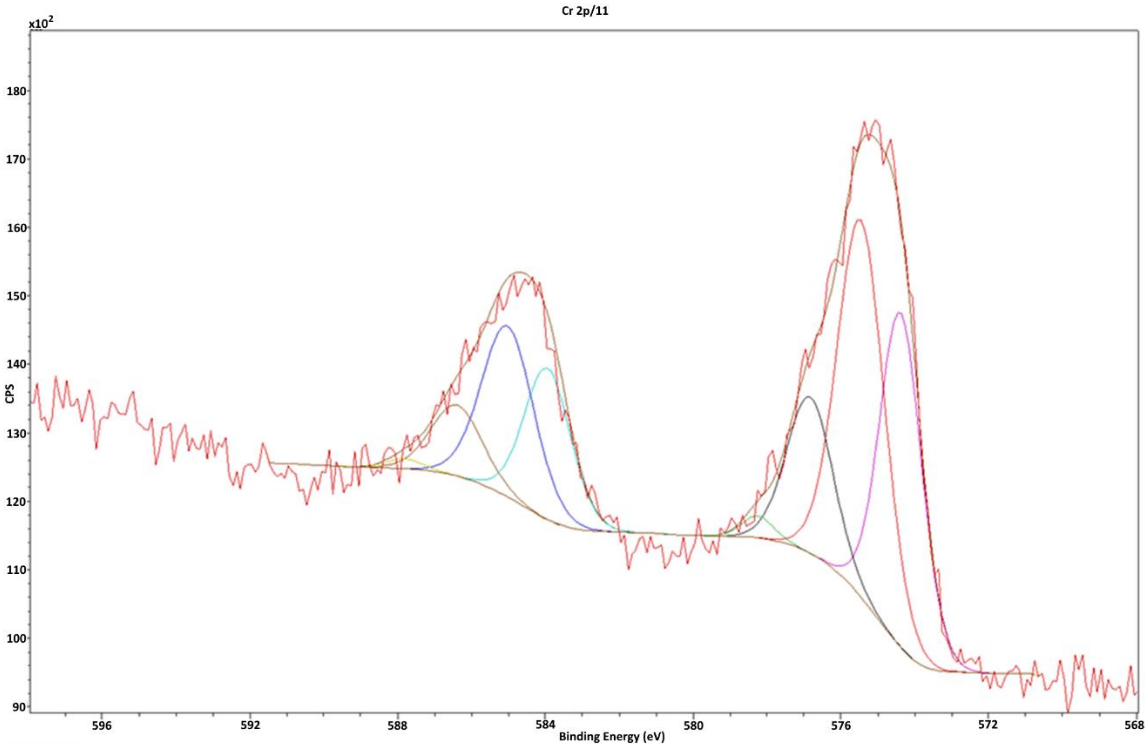

Figure 27. High resolution scan of the Cr 2p doublet produced using a Kratos AXIS XPS showing likely components of the doublet for the CrN-NbN superlattice sample soaked in media.

Compound	Position (eV)	% Area
Cr_2N	574.38	23.6
Cr_2N	583.95	11.8
CrN	575.46	29.8
CrN	585.02	14.9
Cr_2O_3	576.84	12.2
Cr_2O_3	586.40	6.1
CrO_3	578.25	1.2
CrO_3	587.82	0.6

Table 12. Detailing the likely compounds found in the high-resolution scan of the Cr 2p doublet produced using a Kratos AXIS XPS for the CrN-NbN superlattice sample soaked in media.

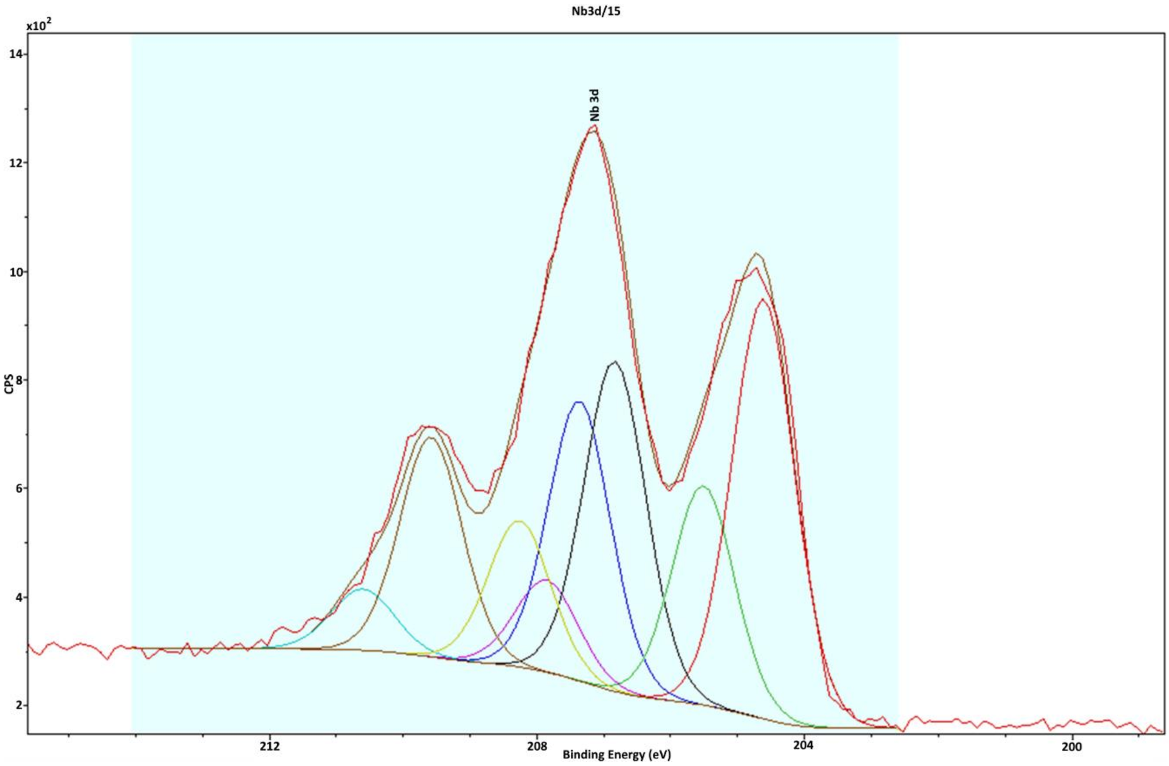

Figure 28. High resolution scan of the Nb 3d doublet produced using a Kratos AXIS XPS showing likely components of the doublet for the CrN-NbN superlattice sample not soaked in media. The triplet appearance comes from the large shift in one of the components.

Compound	Position (eV)	% Area
NbO_2	207.85	5.2
NbO_2	210.60	3.4
NbO	204.61	23.8
NbO	207.36	15.8
Nb_2O_5	206.83	18.7
Nb_2O_5	209.58	12.4
NbNO	205.51	12.5
NbNO	208.26	8.3

Table 13. Detailing the likely compounds found in the high-resolution scan of the Nb 3d doublet produced using a Kratos AXIS XPS for the CrN-NbN superlattice sample not soaked in media.

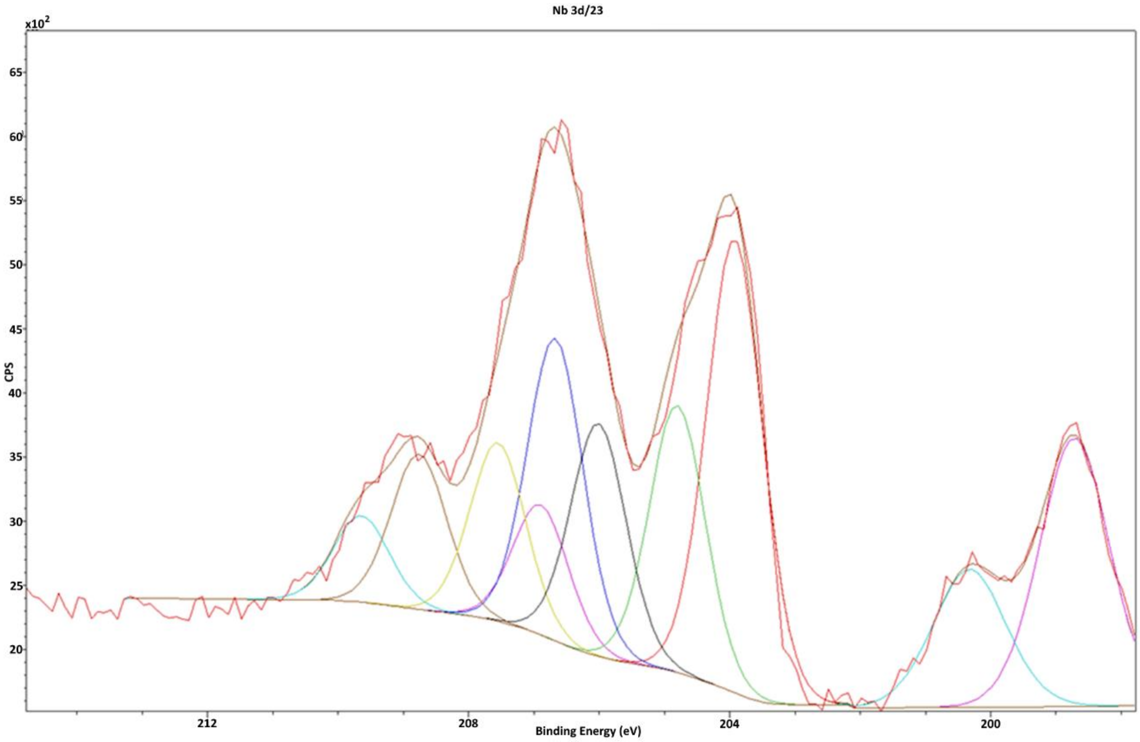

Figure 29. High resolution scan of the Nb 3d doublet produced using a Kratos AXIS XPS showing likely components of the doublet for the superlattice sample soaked in media. The triplet appearance comes from the large shift in one of the components. A Cl doublet is visible in the bottom right of the image indicating the presence of sodium chloride on the sample.

Compound	**Position (eV)**	**% Area**
NbO_2	206.90	7.2
NbO_2	209.65	4.8
NbO	203.92	25.2
NbO	206.67	16.7
Nb_2O_5	206.01	12.9
Nb_2O_5	208.76	8.6
NbNO	204.80	14.8
NbNO	207.55	9.8

Table 14. Detailing the likely compounds found in the high-resolution scan of the Nb 3d doublet produced using a Kratos AXIS XPS for the CrN-NbN superlattice sample soaked in media.

Sample	Media (Y/N)	Cr_2N	CrN	Cr_2O_3	CrO_3	NbO_2	NbO	Nb_2O_5	NbNO
1	N	26.5	46.8	20.2	6.5	8.8	43.3	26.5	21.4
2	N	28.3	44.4	18.7	8.6	9.3	38.5	31.4	20.9
3	N	29.8	42.8	19.4	8.1	9.3	42.2	27.9	20.6
Mean	**-**	**28.2**	**44.7**	**19.4**	**7.7**	**9.1**	**41.3**	**28.6**	**21.0**
Standard Deviation	**-**	**1.7**	**2.1**	**0.8**	**1.1**	**0.3**	**2.5**	**2.5**	**0.4**
4	Y	31.0	44.3	19.7	5.0	8.6	49.0	21.0	21.2
5	Y	30.1	45.0	18.7	6.2	7.5	39.8	30.6	22.1
6	Y	28.9	45.7	19.4	6.1	8.3	45.2	25.9	20.6
Mean	**-**	**30.0**	**45.0**	**19.3**	**5.8**	**8.1**	**44.7**	**25.8**	**21.3**
Standard Deviation	-	**1.1**	**0.7**	**0.5**	**0.7**	**0.6**	**4.6**	**4.8**	**0.7**

Table 15. Showing the percentage of the area of each compound in their respective peaks, either as part of the Cr 2p doublet in the case of Cr compounds or the Nb 3d doublet in the case of the Nb compounds before and after soaking in media.

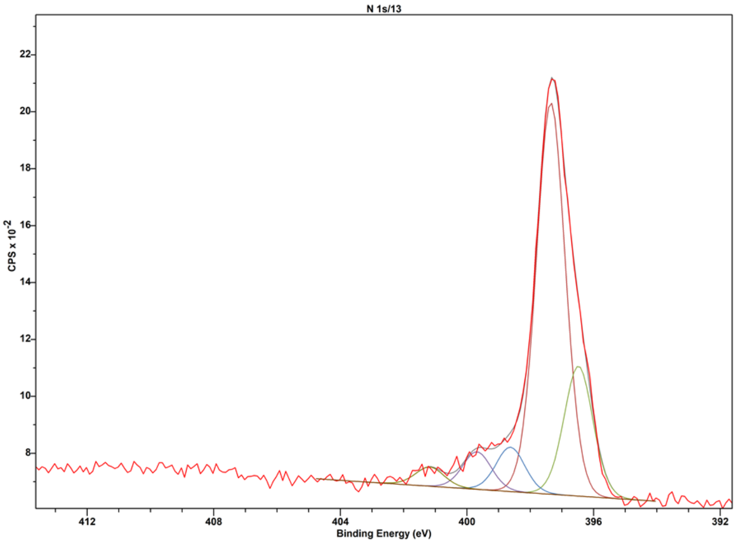

Figure 30. High resolution scan of the N 1s peak produced using a Kratos AXIS XPS showing likely components of the peak for the superlattice sample not soaked in media.

Compound	Position (eV)	% Area
NbN/Cr2N	397.35	62.9
CrN/NbN	396.48	20.9
Organic Compound	398.63	7.1
Organic Compound	399.68	6.0
Organic Compound	401.18	3.1

Table 16. Detailing the likely compounds found in the high-resolution scan of the N 1s peak produced using a Kratos AXIS XPS for the CrN-NbN superlattice sample not soaked in media.

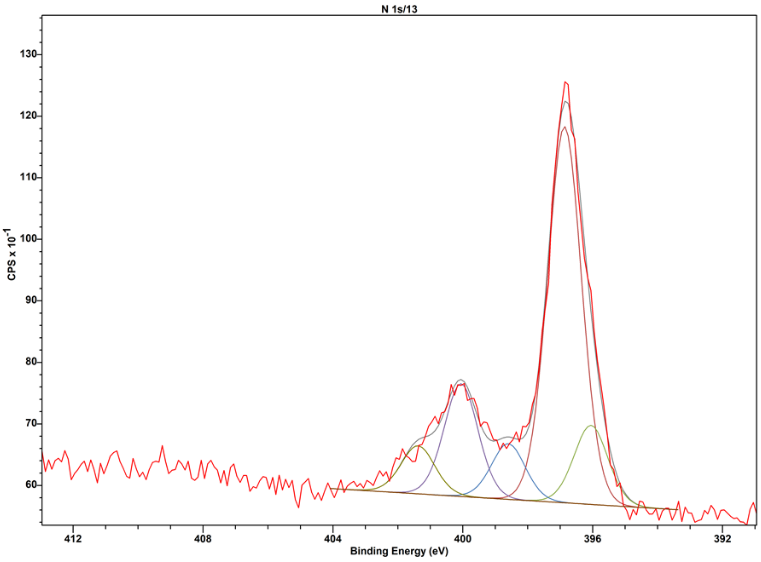

Figure 31. High resolution scan of the N 1s peak produced using a Kratos AXIS XPS showing likely components of the peak for the superlattice sample soaked in media.

Compound	Position (eV)	% Area
NbN/Cr2N	396.87	56.0
CrN/NbN	396.06	11.8
Organic Compound	398.60	8.3
Organic Compound	400.05	16.8
Organic Compound	401.38	7.1

Table 17. Detailing the likely compounds found in the high-resolution scan of the N 1s peak produced using a Kratos AXIS XPS for the CrN-NbN superlattice sample soaked in media.

3.2.4 Cross-Section Analysis

The cross section of the material is detailed below, showing the cross-section morphology through SEM and XRD along with the cross-section EDX analysis of the elements.

Cross section analysis shows an area below the surface droplet that is denser than the surrounding material as can be seen in figure 32a, this was present at the base of every surface droplet observed. The coating in figure 32a has failed during the polishing process and many fractures are present as dark lines visible in the image. In figure 32c this region is relatively chromium deficient when compared to the surrounding material while having a higher concentration of niobium as seen in figure 32d. Indicating that these surface features are caused by the formation of niobium particles in the coating process.

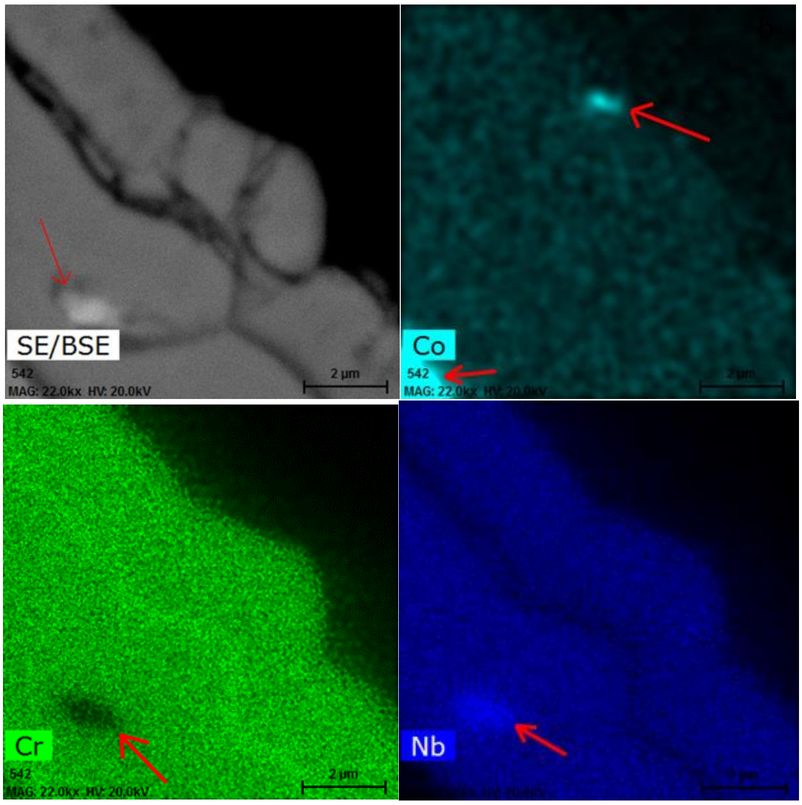

Figure 32. a) SEM image of a cross section of CrN-NbN superlattice coated CoCr disc embedded in resin taken through back scattered electron imaging using a Philips XL30. b,c,d) EDX images of the cross section of a CrN-NbN superlattice coated CoCr sample showing the presence of Co, Cr and Nb respectively.

3.2.5 Multi-layered Coating – layer thickness

Low 2θ XRD analysis of the superlattice coated sample to examine superlattice spacing revealed two peaks corresponding to a d spacing at 24.4Å, with a full width at half maximum (FWHM) of 7.6, and 59.3Å, with a FWHM of 10.7, as can be seen in figure 33. The peak at 24.4Å may be caused by either an incomplete surface layer or two layers of dissimilar thickness that result in a combined peak at 59.3Å. Two dissimilar thickness layers in the coating would produce a wider peak than a single incomplete layer that would deconvolute into two separate peaks. The peak at 24.4Å has been deconvoluted, using CASA XPS, in figures 34 and 35 to attempt to peak fit two peaks to determine if the peak at 24.4Å is caused by a combination of two smaller peaks. Deconvolution of the peak resulted in only a single peak fitting the data, rather than two peaks. This indicates that the CrN and NbN layers are consistently spaced at 59.3Å and the 24.4Å peak is likely a result of an incomplete surface layer.

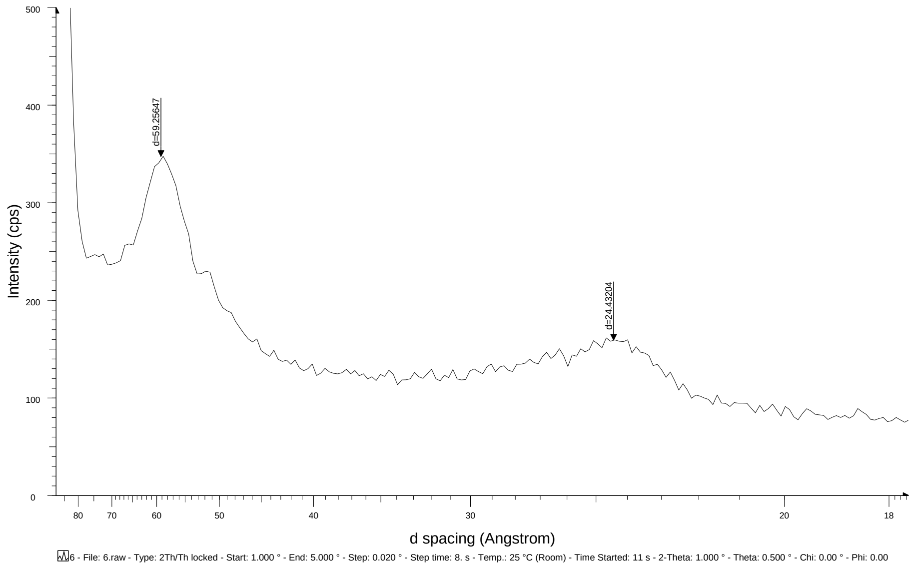

Figure 33. A graph of x-ray intensity against d spacing for the superlattice coated discs between 1° and 5° in 2θ determined using XRD with the Bruker D8 Advanced X-ray Diffractometer. A peak can be seen at 24.4Å and a peak can be seen at 59.3Å.

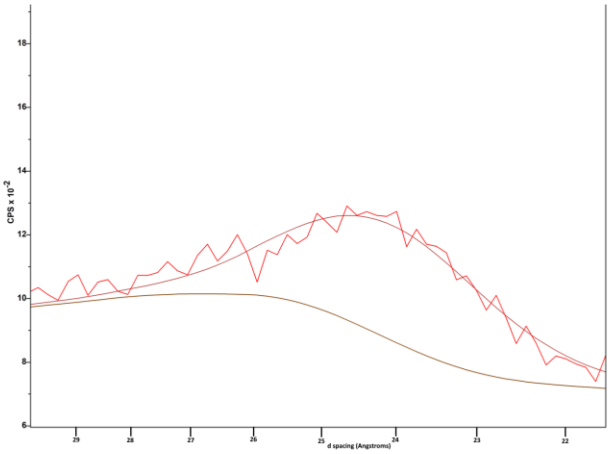

Figure 34. The peak at 24.4Å from the graph of x-ray intensity against d spacing, seen in figure 33, for the superlattice coated discs between 1° and 5° in 2θ determined using XRD with the Bruker D8 Advanced X-ray Diffractometer. This features a deconvolution of the peak produced in CASA XPS, indicating there is only a single component to this peak.

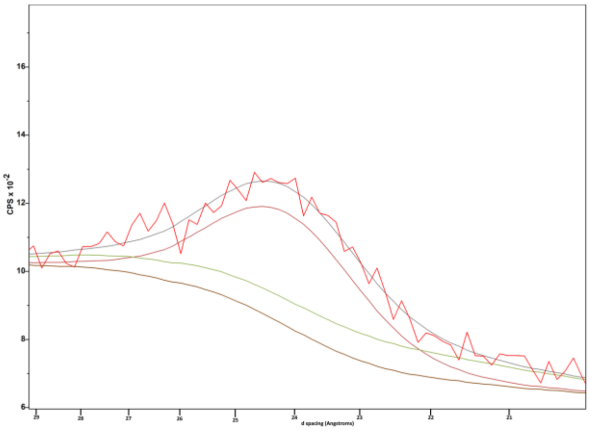

Figure 35. The peak at 24.4Å from the graph of x-ray intensity against d spacing, seen in figure 33, for the superlattice coated discs between 1° and 5° in 2θ determined using XRD with the Bruker D8 Advanced X-ray Diffractometer. This shows an attempt at fitting a second peak to the data.

3.3 DISCUSSION

The surface morphology and chemistry of the simulated CrN-NbN superlattice wear particles are important to characterise as both can influence the biological response to the material [24] [11] [27] [28]. Analysis of the surface chemistry also provides some insight into how it may change over time in a biological environment.

3.3.1 Surface properties of the material

The surface of the CrN-NbN superlattice coating, shown in figure 13, appears to show a very similar columnar ‘bubble-like’ surface texture to others produced through HIPIMS as found by Biswas et al [95] [134]. The surface appears to be free of deep voids although wider pits are present.

3.3.1.1 Surface Features

When investigating the surface properties of the material several features are widespread across the surface, droplets, pits, and seams as can be seen in figures 12, 13, 14, 15, and 16. Investigation into the origin and cause of these features may possibly provide the potential to reduce or eliminate these features which may prove beneficial as they significantly increase the surface roughness. Reducing this surface roughness may further reduce the wear produced by the material, as shown by Whittaker et al, and further decrease the potential for the material to cause osteolysis. [135] It has also been shown by Panjan et al that droplet formation in deposited coatings leads to increased coating degradation by providing nucleation sites for cracks and releasing abrasive particles between the bearing surfaces [136]. It may also improve the corrosion resistance of the material as similar defects in the literature were shown to provide a solution path for galvanic and crevice corrosion as found by Biswas et al [134].

It can be seen in figures 12 and 13 that both the pits and the droplets are around 10 µm, potentially meaning there is a similar process involved in the creation of both. It can also be seen in the cross-section analysis in figure 32 that there is an inclusion of niobium at the root of the droplet, this feature was seen across all 3 droplets observed. It can be inferred that this inclusion of niobium is the cause of the droplet like appearance above it, as the coating has been deposited on the uneven surface. The niobium inclusion in this case appears to act as a nucleation site for these droplets, with the coating being deposited on top of the niobium inclusion. A similar effect is shown by Biswas et al, where flakes from the vacuum chamber provided nucleation sites for nodule-like surface features that appear very similar to the droplets seen in figure 14 and figure 16 [134].

The niobium inclusions are a slight surprise as the melting point of niobium is 2,750K compared to 2,180K for chromium, it would be expected that the lower melting point material would produce larger and more frequent droplets [136]. It is seen however that the sputter yield of chromium is approximately double that of niobium, as shown by Wasa [137]. This means for that for a similar deposition rate, as would be needed for the HIPIMS set up shown in figure 7 to produce similar thickness layers, between the CrN and NbN layers the power density for the Nb target must be significantly higher than the power density for the Cr target. This would lead to higher surface temperatures for the niobium target and increase the formation of droplets from the niobium target. This does lead to a potential route to removing these surface features from the coating by reducing the power density for the niobium target. As this coating is produced through the HIPIMS method this could be done by decreasing the frequency or length of the pulses without needing to directly reduce the power applied to the target, although this is another method that could be employed to reduce the niobium target power density. This would however require a longer coating time for the niobium to produce the same layer thickness of NbN as decreasing the power density across the niobium target would result in a lowered rate of deposition. It would also be important if changing the coating deposition method in this manner that the composition of the plasma in the chamber is analysed as decreasing the power density across the niobium target may result in a shift from a Nb plasma to a Ar or other carrier gas plasma which may negatively affect the deposition rate and density of the NbN layer as found by Ehiasarian [138].

The droplets as a cause of the pits is also backed up by the appearance of cracks around some of the droplets in a similar shape to those found in the pits. This could occur during the coating process as a result of increasing compressive stress causing the droplet to be pulled out. As there is evidence of coating deposition within the pits, as seen in figure 13, it implies that these droplets were removed from the coating during the coating process.

The seams on the surface of the material, seen in figure 16, appear as perfectly straight lines across the material with no obvious directional preference and appear to overlap at many points. As this would follow the pattern of scratches left from polishing the material it is possible that these are a result of deep polishing marks on the substrate. Evidence in the literature, as shown by Lundin and Sarakinos, suggests that the HIPIMS coating method allows for coating of the surface with grain and coating growth perpendicular to the surface within indents [84]. This behaviour would explain how these features could be carried from the substrate to the surface of the material, although there is no direct evidence of such seams in the literature. There is also evidence of this effect seen in the coating surface, as seen in figure 13, showing a pit with grain growth of the coating perpendicular to the surface of the pit, this effect is particularly noticeable around the edges of the pit.

Overall reducing these features would provide a significant potential benefit to the coating. It could be seen in testing the endotoxin removal methods that these features were the sites of significantly more corrosion than the rest of the material, indicating that any potential corrosion is likely to occur through these areas. As these surface features lead to a rougher surface with many peaks and valleys the real area of contact in a bearing joint is reduced and this increases the forces on those areas of the coating. This concentration of the forces to the surface asperities can lead to crack initiation and propagation and the production of wear debris, reducing the performance of the coating, as found by Hosseinzadeh et al [139]. There is also evidence, shown by Constable et al, to suggest an increase in temperature relative to the surrounding material at the surface asperities during wearing [140]. This increase in temperature could affect the composition of the bearing surface, particularly in materials where the thermal conductivity is low [140].

3.3.1.2 Surface Roughness

It can be seen that the coating process significantly increases the roughness of the components (table 4). While a significant part of this may be due to the droplets, pits and seams, seen in figures 13, 14, 15, and 16, a ‘bubble-like’ texture can be seen between these features, as seen in figures 13, 14, 15, and 16. This bubble like texture is also seen in other investigations of HIPIMS coatings, shown by Biswas et al and Hovsepian et al [95] [134] [12]. This has been shown in these results to increase the surface roughness when compared to a highly polished substrate as seen in table 4. This measure of surface roughness is also of similar magnitude to that found in the literature for similar coatings, shown by Biswas et al, Lin et al, and Castilho et al, which show Ra values of 0.083µm, 0.021µm, and 0.014µm respectively [134] [141] [142]. Despite this increase in surface roughness as a result of the coating, improving the coating process to remove the droplets would still provide improved wear performance as these droplets are raised above this bubble-like texture.

The surface skewness of the coating, as shown in table 4, is negative indicating the presence of more valleys than mountains overall. This may indicate that there are more pits and seams present than droplets. A negative surface skewness usually implies improved performance as a bearing surface, with lower friction than surfaces of the same material with a positive surface skewness, as shown by Hashimoto et al, with a 50% decrease in Ra causing a 59% decrease in coefficient of friction [143]. Several HIPIMS deposited coatings with a similar bubble-like surface texture, but lacking the surface features of the pits, droplets, and seams, however, demonstrate a positive surface skewness as shown by Avila and by Krella and Marchewicz [144] [145]. We can then infer from this that the negative value of surface skewness for the CrN-NbN superlattice coating investigated here is as a result of the pits and seams in the surface. This is further supported by the approximate surface density of the pits being higher than the approximate surface density for the droplets, although this is not direct evidence as this does not provide an area for those features on the surface, although as they are of similar size it lends further weight to these features being the cause of the negative R_{sk} value.

3.3.2 Surface Chemistry

While the contact angle analysis, shown in table 5, would normally indicate a more hydrophobic surface for the coating, when compared to the substrate the change in surface morphology must be considered. Especially as the surface has many pit-like features, seen in figure 13, it is likely that these pits did not fully wet and contributed to an increase in the contact angle. As a result of this change in the surface morphology the decreased wettability of the coating when compared to the substrate cannot directly be attributed to the change in surface chemistry or morphology and will be produced through a combination of both. As increasing surface roughness will decrease the contact angle on a hydrophilic surface, as shown by Ryan and Poduska, typically defined as having a contact angle less than 90°, and increase the contact angle on a hydrophobic surface, typically defined as having a contact angle greater than 90°, and as we see an increase in surface roughness and the contact angle it may be inferred that this coating is more hydrophobic than the CoCr substrate [146] [147]. This decrease in wettability has been shown to increase the coefficient of friction, with a similar change of contact angle in the literature for a CrN-TiN superlattice from 84° to 93° resulted in a change of the coefficient of friction from 0.35 to 0.7, as shown by Paulitsch et al [148]. Thus, it is possible that additional modification to the surface chemistry of the CrN-NbN superlattice to increase the wettability of the coating may improve the wear performance of this coating.

The overall composition of the CrN-NbN found through EDX, as seen in table 6, shows the coating to made of approximately 52.8% more chromium than niobium by weight percentage or 143% by atomic percentage. These results are in alignment with the results from XPS, shown in figure 21, which show

137% more chromium than Nb by atomic percentage. The composition of this is driven by the deposition rate of each target, and as such is highly variable. This is also reflected in similar coatings in the literature, as indicated by Wang et al, where Cr-Nb-N coatings with between 925% and 59% more chromium than niobium were demonstrated depending upon the difference in target power [149].

There is also the presence of aluminium in the EDX results that was not seen in the XPS data. This is not however seen in the XPS results, likely as a result of EDX covering the through-thickness of the coating while XPS is a surface measurement. This would indicate that the aluminium is embedded in the coating below 10nm. It is thought that the origin of this aluminium is as a contaminant from the vacuum chamber during the HIPIMS coating process. This is supported by the literature that shows flakes of aluminium from the vacuum chamber as a contaminant during the HIPIMS method that acts as a nucleation site for the surface droplets, it is thought that these flakes originated from either the chamber wall, target shield or mechanism to hold the substrates, as shown by Biswas et al [134].

The EDX results also show the presence of carbon and oxygen in the CrN-NbN superlattice samples. This is thought to be from adventitious carbon as is a very common occurrence for all samples exposed to air, as shown by Greczynski and Hultman [150]. This is also confirmed when looking at the XPS results where the high-resolution C 1s peak shows evidence of adventitious carbon when deconvoluted into three separate peaks, most likely showing a C-C/C-H peak at 285.16, a C-O peak at 286.72 and a C=O peak at 288.34, as shown in table 8. The presence of oxygen is also likely to be attributed to the presence of Cr and Nb oxides which is once again also shown in the XPS results, showing many oxides and oxynitrides of those elements.

The low take-off angle XPS results, shown in table 9, provide significant data on the surface chemistry of the material. Most notably the increase in the ratio between Niobium and Chromium for the CrN-NbN superlattice samples as the take-off angle decreased indicates that the surface layer is Niobium, this was found to be the case in each measured sample. There is also an increase in the percentage of oxygen and carbon detected, this is likely to be as a result of adventitious carbon molecules as the literature, as shown by Piao and McIntyre, shows increase signal strength for thin films of adventitious carbon molecules as the take-off angle decreases [151].

Following exposure to a biological environment, specifically, cell culture medium, similar adventitious carbon can be observed on the CrN-NbN superlattice samples as seen in table 10. The cell culture medium used contained Dulbecco's Modified Eagle Medium, FBS, L-Glutamine, HEPES Buffer, NEAA and L-ascorbic acid. This provides a wide number of possible sources for the adventitious carbon, in particular FBS which contains proteins which will adsorb to the surface of the samples, as shown by Schmidt et al, including CrN-

NbN superlattice samples [152]. This is also seen in the results for the high-resolution scan of the nitrogen 1s peak, in figure 31, for the CrN-NbN superlattice samples exposed to cell culture medium, showing a significant increase in the fraction of nitrogen attributed to organic compounds, from 16.22% to 32.17%, as seen in tables 16 and 17. CrN-NbN superlattice samples not exposed to cell culture medium also show the presence of organic nitrogen-containing compounds, as can be seen in table 16, these are likely to be the same adventitious molecules seen in the carbon and oxygen peaks, in figures 22 and 23 respectively. There is evidence, as described by Vinnichenko et al, of exposure to cell culture medium producing significant contributions to the carbon 1s peak from a hydrocarbon layer on the surface [153]. There is also evidence, shown by Cimilla et al, of materials being exposed to cell culture media showing trace elements in their XPS spectra such as Zn, Ca, or K [154]. This is in line with the results found here indicating the presence of Na and Ca on the CrN-NbN superlattice coatings that were exposed to cell culture media.

The high resolution XPS scans, shown in figures 26, 27, 28, 29, 30, 31 and tables 10, 11, 12, 13, 14, 15, 16, and 17, provide a more detailed picture of the oxidation state of the material before and after exposure to cell culture media. It can also be noted from these scans that the niobium results show significantly more oxidation than the chromium results, as shown in tables 11, 12, 13, and 14, providing further evidence for NbN as the surface layer of the material alongside the increase in Nb:Cr ratio with decreasing take-off angle. The deconvolution of the high-resolution Nb 3d doublet scans, seen in figures

28 and 29, show various Nb oxides and oxynitride indicating that there is some oxidation of the surface of the coating. The peaks found correspond to oxides that would be expected from the oxidation of a niobium nitride as is seen in the literature, shown by Henry et al and Ermolieff et al, demonstrating the presence of Nb_2O_5, NbO_2, and NbO [155] [156]. The relatively high proportion of NbO compared to Nb_2O_5 and the presence of NbNO indicates that the surface NbN layers are not full oxidised as we would expect a significantly high proportion of Nb_2O_5, as demonstrated by Ermolieff et al [156]. These results largely agree with those found in the literature on the oxidation of NbN, showing NbON, Nb_2O_5, NbO and NbO_2, as shown by Darlinski and Halbritter [157].

The deconvolution of the high-resolution Cr 2p doublet scans, seen in figures 26 and 27, show Cr oxides and nitrides, indicating that some of the Cr layer has been oxidised but there is still clear evidence of surface nitrides. The oxides shown from the deconvolution of the high-resolution scan of the Cr 2p doublet fit with the oxides expected from the oxidation of CrN in the literature, shown by Milošev et al and Bardi et al, showing the presence of Cr_2O_3 and CrO_3 following the oxidation of CrN [158] [159].

As the maximum depth of measurement of XPS is roughly 10 nm, as described by Lefebvre et al, and the XRD results show a repeating layer thickness of approximately 6 nm, as shown in figure 33, it would be reasonable to assume that the XPS results are from the top two layers of the CrN-NbN superlattice

[160]. As the deconvolution of the high-resolution scan of the Cr 2p doublet, seen in figures 26 and 27, showed the presence of CrN and Cr_2N indicates that the CrN layer has been oxidised less than the NbN layer which showed no niobium nitrides, only oxynitrides. This would further support the findings from changing the take-off angle of the material that the surface layer of the material is NbN. The CrN layer contains Cr2O3 and CrO3 at an approximate ratio of 3:1 indicating CrN has produced a passivating layer of chromium oxides. This fits with similar behaviour of CrN found in the literature, shown by Lavigne et al [161]. This would indicate a resistance to oxidation in the CrN-NbN superlattice beyond the initial few layers of NbN and CrN.

This corrosion resistance is supported by comparing the oxidation states of samples exposed to cell culture media and those not exposed to cell culture media. Although not statistically significant, samples exposed to cell culture media showed generally lower percentages of oxides and a higher percentage of nitrides and oxynitrides when compared to samples not exposed to cell culture media. As the samples exposed to cell culture media did not exhibit higher oxidation than those not exposed to cell culture, it indicates that oxidation of the CrN-NbN superlattice coating did not progress beyond the top layers as a result of exposure to cell culture media, further supporting the idea that a passivating layer has formed.

3.3.3 Cross-Section Analysis

The cross section in figure 32 shows a coating thickness of approximately 6.5 µm although this is quite difficult to get an accurate reading of due to the fractured coating surface. This is comparable to other total joint replacement component coatings in the literature, with other coatings being shown at a thickness of 2-5 µm, as shown by Gallegos-Cantú et al, Hovsepian et al, and Ortega-Saenz et al [162] [163] [164]. This may present an issue if the coating wears quickly potentially exposing the substrate as the new bearing surface. This wear is not always uniform across the components and a wear stripe has been observed for metal-on-metal and ceramic-on-ceramic pairings, as demonstrated by Fisher and Ingham, Purdue et al, Esposito et al, and Clarke and Manley [11] [21] [165] [166]. In these instances, the wear rate at the wear stripe has been demonstrated to be up to 15.5 µm per year, as shown by Esposito et al [165]. As these wear stripes do not occur in all recovered implants it is important to understand the cause of them to prevent them occurring as they are associated with increased wear, demonstrating a median wear rate for anterosuperior wear stripes of 1.9 mm^3/year compared to 0.2 mm^3/year for the median for the total data set shown, as demonstrated by Esposito et al, and Fisher and Ingham [165] [11]. It is thought that the primary cause of these wear stripes is micro-separation of the joint and edge loading, as discussed by Esposito et al, and Clarke and Manley [165] [166]. It is therefore important when designing total joint replacements with this coating to avoid micro-separation and edge loading as the formation of a wear stripe when using this coating could result in the substrate becoming exposed. It is important to look at the size of components such as the femoral head for these designs as it has been shown that larger femoral heads (>36 mm) are at higher risk of micro separation and higher edge loads than smaller femoral heads, as discussed by Girard [167].

The cross section, shown in figure 32, shows a fractured surface, much of which can be attributed to the manner in which the sample was prepared. This pattern of cracking though is very similar around the surface droplets, as seen in figure 32, showing cracking in the same shape as the pits also seen in the surface, in figure 14. It is likely that the formation of these droplets also results in areas of poor coating cohesion surrounding the droplets, which would cause this pattern of consistent failure along these points. This is also seen in the literature, as shown by Biswas et al and Hovsepian, where cross sections of HIPIMS deposited coatings result in droplet formation around flakes from the vacuum chamber, the cross section of the resultant coating shows poor adhesion in a pit-like shape around the droplet [134] [95] [12]. This poor cohesion may lead to these droplets pulling out of the surface and may act as an origin of wear debris in the use of CrN-NbN superlattice coating as the bearing surface of total joint replacements.

The cross section, as seen in figure 32, shows the presence of droplets and pits although no evidence of the seams seen on the surface was found. No new features of the coating were discovered through the cross-section of the CrN-

NbN superlattice coating. All of the niobium droplets found, and the resulting defects, were found to be embedded rather than through thickness, indicating that the production of droplets is more likely after the first layers (roughly 1 µm of deposition). This is consistent with the above discussion that the surface of the HIPIMS target increasing with temperature with time with until it reaches steady state. Above a certain temperature, droplets of Nb have formed.

4 CELL CULTURE WORK WITH CRN-NBN COATING

4.1 MATERIALS AND METHODS

Here endotoxin removal methods are described. Removal of endotoxins is an important precursor for the cell work as endotoxins present on the samples would cause the release of inflammatory cytokines.

Then the methods used in the culture of cells are detailed, these include the methods for general cell culture as well as the assays carried out. The methods for alamarBlue® are detailed, this is a standard cell viability assay. Methodology for IL-6 and TNF-α sandwich ELISA assays are then detailed, these measure very small concentrations of the IL-6 and TNF-α cytokines present in the cell culture.

4.1.1 Endotoxin Removal

Two endotoxin removal methods were used in sample preparation, described by Brooks et al [168] and Gorbet et al [169].

4.1.1.1 Gorbet et al Method

Endotoxin removal method described by Gorbet et al was tested on one half of a CrN-NbN coated disc to examine the corrosive effect of the reagents on the samples [169]. This method involved sequential washes for 18-20 hours in alkali ethanol (0.1N NaOH in 95% ethanol) followed by 25% nitric acid. The CrN-NbN discs were then attached to stands using carbon tabs and carbon coated and examined through SEM for corrosion using backscattered electron imaging and secondary electron imaging using a Philips FEI XL30.

4.1.1.2 Brooks et al Method

The method described by Brooks et al was tested using CrN-NbN particles [170]. Particles were removed from suspension through centrifuging at 3150 x g for 5 minutes using a Jouan CR422 centrifuge and the supernatant removed. Fifty millilitres of pyrogen free water were added to the particles and the particles were sonicated for 10 minutes in an ultrasonic bath. The particle suspension was then incubated at 37°C for 6 hours before further sonication for 10 minutes. The particle suspension was then centrifuged at 4500 rpm, 3894 x g for 5 minutes using Jouan CR422 centrifuge and supernatant removed.

An extract was produced using the particles using the method recommended by the FDA [171]. Briefly, particles were rinsed with 40ml pyrogen free water, which was then centrifuged at 4500 rpm, 3894 x g for 5 minutes using a Jouan CR422 centrifuge, the supernatant was then removed and used for endotoxin analysis to ensure endotoxin removal.

Data produced from the endpoint chromogenic Limulus Amebocyte Lysate (LAL) assay was analysed by plotting each of the endotoxin standards against their absorbance. This was then used to plot a linear regression of best fit with an R-squared of 0.8730 as seen in figure 36. Interpolation was then used to calculate the endotoxin concentration of the extract from the sample and the spiked extract.

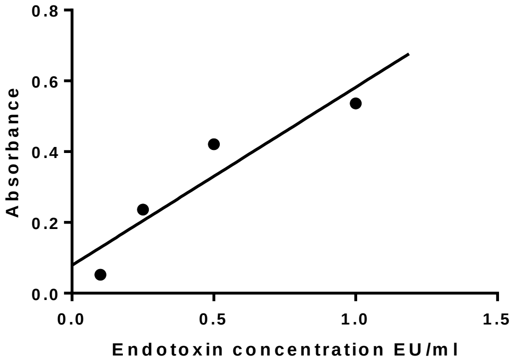

*Figure 36. A plot of the endotoxin standards made from the stock reconstituted endotoxin against their absorbance. A linear regression of best fit was calculated as Y=0.5031*X+0.07883 with an R-squared value of 0.8730.*

4.1.2 Endotoxin Analysis

Endotoxin testing using a Lonza endpoint chromogenic Limulus Amebocyte Lysate (LAL) assay was performed on the superlattice particles. The detection range for this assay was 0.1-1.0 EU/ml. A set of standard endotoxins concentrations (1.0, 0.5, 0.25, 0.1 EU/ml) were reconstituted from stock endotoxin supplied with the assay kit. The endotoxin standards, three samples of extract, one blank containing pyrogen free water and one sample spiked with 0.4 EU/ml were used. All the wells listed here were ran in triplicate. Samples were equilibrated on a Cole-Parmer StableTemp Dry Block heater at 37°C prior to beginning the assay. Fifty microlitres of reconstituted LAL were added to each well and then the well plate tapped on the side to facilitate mixing, the well plate was then placed back onto the dry block heater. After 10 minutes 100µl of pre-warmed chromogenic substrate was then added to each well plate, the well plate tapped and placed back onto the dry block heater. At 16 minutes 100µl of 25% acetic acid was added to each well plate to stop the reaction. The absorbance of the wells was then read at a wavelength of 405 nm using a Biotek Elx800 well plate reader with a reference wavelength of 630 nm.

4.1.3 Sterilisation of Materials

CrN-NbN and TiN coated ASTM F75 CoCr discs were sterilised by placing them into an autoclave bag and placing them in an autoclave at 127°C for 30 minutes.

CrN-NbN, TiN and Al_2O_3 were sterilised using an autoclave at 127°C for 30 minutes, this time and temperature were chosen to ensure the samples were sterile while reducing the risk of changing the particle morphology. The particles were kept in the glass bottles they were stored in for sterilisation, the tops were loosened slightly to ensure the integrity of the bottles remained intact.

4.1.4 Cell Culture

J774A.1 murine mouse macrophages and Primary Human Osteoblasts were chosen for cell culture. All cells were cultured in Corning 75cm^2 U-shaped canted neck with vented cap flasks. All cell cultures with materials used Corning Falcon 48 well clear flat bottom TC-treated Cell culture plates. Corning Falcon 96-well Polystyrene Microplates were used for the plate reading steps of the alamarBlue® assays. Cytokine assays used the well plates provided with their respective kits.

Measurements of the cytotoxicity and release of cytokines from both macrophages and osteoblast were also performed on other materials. This allows for a direct comparison between these materials using the same cell lines in the same conditions. Materials chosen as comparison materials were titanium nitride, alumina, and CoCr. All three materials chosen are common materials for the bearing surfaces of joint replacements, although only TiN is commonly seen a coating material.

4.1.4.1 Macrophage culture

Macrophage cell culture was performed using a J774A.1 murine macrophage cell line from Public Health England (ECACC 91051511). J774A.1 cells were cultured in a media consisting of 500ml Gibco Dulbecco's Modified Eagle Medium (DMEM) supplied by ThermoFisher, 50ml Gibco fetal bovine serum (FBS) supplier by ThermoFisher, 5ml L-Glutamine, 10ml of 4-(2-hydroxyethyl)-1-piperazineethanesulfonic acid (HEPES Buffer) (1M), supplied by ThermoFisher, 5ml of non-essential amino acids (NEAA) and 75mg of 99% L-ascorbic acid supplied by Sigma-Aldrich. Cell culture media did not contain antibiotics or antimycotics as per the instructions for feeding the cell line, as this could mask the presence of a low-level infection, no signs of infection were present throughout the cell culture. Cells were seeded into flasks at a cell density of $3x10^4$ cells/cm^2.

Cell culture media was changed every 2 days by removing the old media and washing with 5ml Phosphate Buffered Saline (PBS), the old media and PBS was then centrifuged at 4500 rpm, 3894 x g using a Jouan CR422 centrifuge. The supernatant was then removed through pipetting. The pellet was then resuspended in 15ml of fresh media and returned to the original flask. These steps were performed as the macrophages are semi-adherent and macrophages were present both attached to the flask and in the removed media.

Cells were passaged when the flask reached 90% confluence. Media was removed from the flask and stored in a 20ml universal tube. Cells were then detached from the flask using a cell scraper and checked using light microscopy for detachment. Five millilitres of media were then added to the flask, gently swirled, and then removed and added to the previously removed media, this was repeated with 3ml of media afterwards. The media was then centrifuged at 4500 rpm, 3894 x g for 5 minutes using a Jouan CR422 centrifuge. The resultant supernatant was then removed through pipetting and the pellet resuspended in 20ml of fresh media. This was then split into two and put into two new flasks and an additional 5ml of fresh media added to each flask.

Cryopreservation of macrophage cells was required between studies. This was done by removing the cell culture media and storing it in a 20ml universal tube. Cells were then detached from the flask using a cell scraper and checked using light microscopy for attachment. Five millilitres of media were then added to the flask, gentle swirled and then removed and stored in the same 20ml universal tube as the previously removed media. This was then repeated with 3ml of media. The removed media was then centrifuged at 4500 rpm, 3894 x g for 5 minutes using a Jouan CR422 centrifuge. The supernatant was then removed, and the pellet resuspended in 1ml of freezing mix. The freezing mix was 10% Dimethyl Sulphoxide (DMSO) in FBS. The suspension was then added to a cryovial and stored in a vapor phase box in the cell bank for 24 hours before being moved to the liquid phase box.

Seeding of cells on samples was done by removing media from the flask and storing in a 20ml universal tube. Cells were then detached from the flask using a cell scraper and checked using light microscopy for detachment. Five millilitres of media were then added to the flask, gently swirled, and then removed and added to the previously removed media, this was repeated with 3ml of media afterwards. The media was then centrifuged at 4500 rpm, 3894 x g for 5 minutes using a Jouan CR422 centrifuge. The resultant supernatant was then removed through pipetting and the pellet resuspended in 1ml of fresh media. Fifty microlitres of this media was then transferred to an Eppendorf and 50 µl of 0.008% Trypan Blue dye solution added to the Eppendorf, this was then thoroughly mixed using a pipette before being allowed to stand for 1 minute. This solution was then used to fill both sides of a Haemocytometer and used to count the cells, discounting those dyed with the Trypan Blue solution. The cell count was then used to calculate the concentration of cells in the suspension, and this was used to calculate the desired dilution. The macrophages were seeded at 40,000 cells/cm^2 at passage +8.

4.1.4.2 Osteoblast culture

Osteoblast cell culture was performed using Human Primary Osteoblasts from Sigma-Aldrich. Osteoblasts were cultured in Human Osteoblast Growth Media provided by Sigma-Aldrich. Cell culture media was changed every 2 days by removing the old media and washing with 5ml PBS and discarding both before replacing with 15ml of the human osteoblast growth media.

Cells were passaged when the flask reached 90% confluence. Media was removed and the flask washed with 5ml PBS. One and a half millilitres of 37°C 0.2% trypsin with HEPES buffer (1M), supplied by ThermoFisher, was then added to the flask, and gently swirled to ensure coverage of the entire flask. The flask was then incubated for 4 minutes. Cell detachment was checked visually using light microscopy. Six millilitres of media were then added to the flask, gently swirled, and then removed and added to a 20ml universal tube. Following this 4ml of media was added to the flask gently swirled and then removed and added to the same tube. This tube was then centrifuged at 4500 rpm, 3894 x g for 5 minutes using a Jouan CR422 centrifuge. The resultant supernatant was removed using a pipette and discarded, the pellet was resuspended in 10ml of media and 5ml of this was added to two new flasks. Ten millilitres of fresh media were then added to each flask.

Cryopreservation of osteoblast cells was required between studies at passage +6. This was done by washing the cells 3 times with 5ml of PBS. Then 1.5ml of 37°C 0.2% trypsin with HEPES buffer (1M), supplied by ThermoFisher, was added to the flask and gentle swirled before incubating for 4 minutes. Cell detachment from the flask was then checked using light microscopy and gentle tapping to ensure all cells were detached. Six millilitres of 37°C cell culture media was then added to the flask and gentle swirled before transfer to a 20ml universal tube. This was then repeated with 4ml of 37°C cell culture media. The media in the 20ml universal tube was then centrifuged at 4500 rpm, 3894 x g for 5 minutes using a Jouan CR422 centrifuge. The supernatant was then removed, and the pellet resuspended in 1ml of freezing mix. The freezing mix was 10% Dimethyl Sulphoxide (DMSO) in FBS. The suspension was then added to a cryovial and stored in a vapor phase box in the cell bank for 24 hours before being moved to the liquid phase box.

Cells were seeded on samples by removing the media and washing the flask with 5ml PBS. One and a half millilitres of 37°C 0.2% trypsin with HEPES buffer (1M), supplied by ThermoFisher, was then added to the flask, and gently swirled to ensure coverage of the entire flask. The flask was then incubated for 4 minutes. Cell detachment was checked visually using light microscopy. Six millilitres of media were then added to the flask, gently swirled, and then removed and added to a 20ml universal tube. Following this 4ml of media was added to the flask gently swirled and then removed and added to the same tube. This tube was then centrifuged at 4500 rpm, 3894 x g for 5 minutes using a Jouan CR422 centrifuge. The resultant supernatant was removed using a pipette and discarded, the pellet was resuspended in 1ml of media. Fifty microlitres of this media was then transferred to an Eppendorf and 50 µl of 0.008% Trypan Blue dye solution added to the Eppendorf, this was then thoroughly mixed using a pipette before being allowed to stand for 1 minute. This solution was then used to fill both sides of a Haemocytometer and used to count the cells, discounting those dyed with the Trypan Blue solution. The cell count was then used to calculate the concentration of cells in the suspension, and this was used to calculate the desired dilution. The osteoblasts were seeded at 30,000 cells/cm^2.

4.1.4.3 Cytotoxicity Assay

Cytotoxicity of coating was tested on both cell models using an alamarBlue® cell viability assay supplied by ThermoFisher. Cells were seeded on samples as described in the Macrophage and Osteoblast culture sections. At the time points used for the assays the media was removed from the samples.

In assays using Macrophages the media was then centrifuged at 4500 rpm, 3894 x g for 5 minutes using a Jouan CR422 centrifuge. The supernatant was then stored for use in cytokine assays. The wells were then washed with 1ml PBS and then this PBS was used to resuspend the pellet associated with each well. The suspended pellets were then centrifuged at 4500 rpm, 3894 x g for 5 minutes using a Jouan CR422 centrifuge and the PBS discarded. This cycle was repeated twice more before resuspending the pellets in 1ml alamarBlue®

solution (1:10 alamarBlue®: Hanks Balanced Salt Solution (HBSS)) and adding the suspended pellet and alamarBlue® mixture back into the appropriate wells. alamarBlue® solution was also added to three empty wells to use as a blank.

In the assays using Osteoblasts the supernatant was stored for use in the cytokine assays and the wells washed three times with 5ml PBS before adding 1ml alamarBlue® Solution (1:10 alamarBlue®:HBSS).

The wells were then incubated at 37°C for 80 minutes for both J774A.1 macrophages and primary human osteoblasts. Well plates were then removed, wrapped in aluminium foil, and placed on a well plate shaker at 150 rpm for 10 minutes. Three samples of 100 µl were then aliquoted into a 96 well plate. The Fluorescence of the samples was then read at 560 nm excitation and 590 nm emission using a Biotek FLx800 plate reader.

4.1.4.4 Cytokine Release

Cytokine Release was measured using ELISA assays provided by Sigma-Aldrich. The release of IL-6 and TNF-α was measured using both Osteoblasts and macrophages in response to the CrN-NbN coating and comparison materials. The time points used for each cytokine assay were 24 hours, 72 hours, and 168 hours.

The reagents of the ELISA assay were brought up to room temperature prior to use (25°C). All samples and standards were run in triplicate. Standards were prepared by diluting the provided cytokine with sterile distilled water as indicated on the kit, the volume of sterile distilled water varied per kit as per the instructions included with the kit. This solution was then used for a serial dilution with sterile distilled water to produce the standards for the standard curve, the volume of sterile distilled water varied between the kits.

One hundred microlitres of each standard and sample was then added to the appropriate wells and the plate incubated at 4°C overnight. This solution was then discarded, and the wells washed with 300 µl of a wash solution provided with the kit, this was then removed from each well and discarded. This washing procedure was repeated 4 times for each well and then the plate was inverted and blotted against a clean paper towel.

One hundred microlitres of the prepared biotinylated detection antibody (containing 0.1% sodiumazide) solution was then added to each well and incubated for 1 hour at room temperature with gentle shaking. After 1 hour this was then discarded, and the wells washed with the same washing procedure as in the above paragraph.

Following this washing procedure 100 µl of a prepared Streptavidin solution was added to each well and then the plate was incubated at room temperature for 45 minutes with gentle shaking. This was then discarded, and the plate washed with the same procedure as listed above.

One hundred microlitres of 3,3',5,5'-tetramethylbenzidine (TMB) One-Step Substrate Reagent was then added to the wells. The plate was then covered using aluminium foil and incubated at room temperature for 30 minutes. Fifty microlitres of stop solution was then added to the wells and the absorbance read at 450 nm immediately using an ELx800 well plate reader with a reference wavelength of 630 nm.

The data produced was then compared to the standard curve produced to calculate the concentration of each cytokine at each timepoint.

A calibration curve was used for each ELISA assay in order to calculate the concentration of the cytokines released. These calibration curves are show in figures 37, 38, 39, and 40.

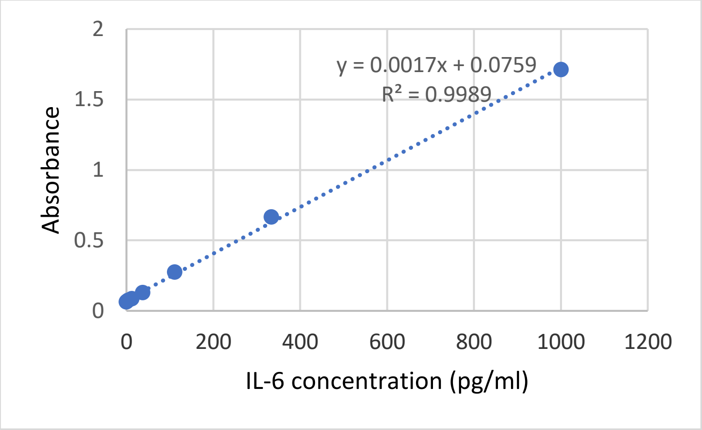

Figure 37. Calibration curve data for IL-6 release ELISA assay that was used with osteoblasts on the coating materials. For these results n=8.

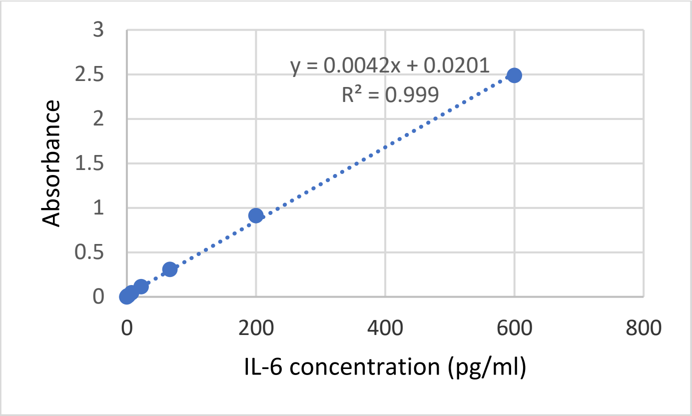

Figure 38. Calibration curve data for IL-6 release ELISA assay that was used with macrophages on the coating materials. For these results n=8.

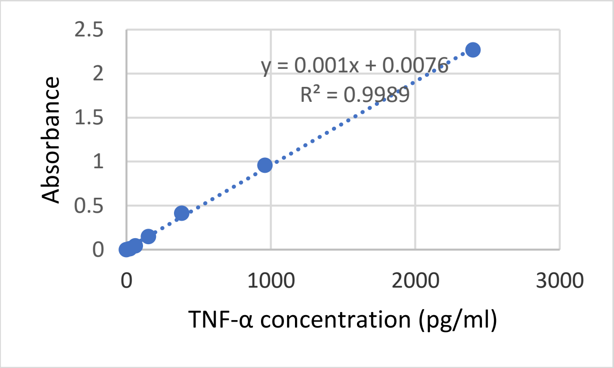

Figure 39. Calibration curve data for TNF-α release ELISA assay that was used with osteoblasts on the coating materials. For these results n=8.

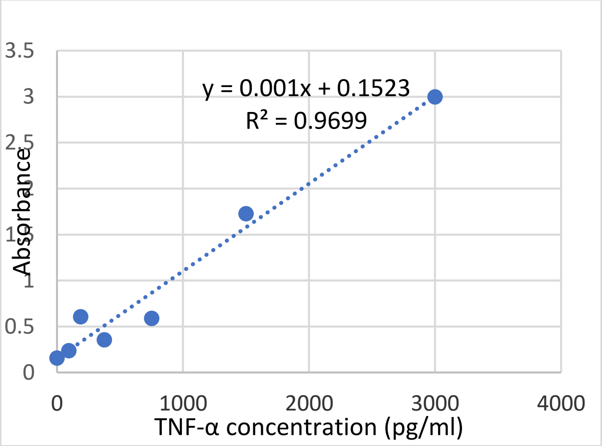

Figure 40. Calibration curve data for TNF-α release ELISA assay that was used with macrophages on the coating materials. For these results n=8.

4.2 RESULTS

The cellular response to the coating materials are detailed in this section through metabolic activity analysis and values for IL-6 and TNF-α release as these are significant markers of inflammation and the pathways that lead to late aseptic loosening. The results of the endotoxin removal methods are also shown below.

4.2.1 Endotoxin Removal

SEM secondary electron imaging of the superlattice coated disc that had undergone the endotoxin removal method described by Gorbet et al can be seen in figure 41 [169]. Here the right side of the sample was submerged in the nitric acid and alkali ethanol solutions while the left side was out of the solutions. The corrosion was most significant around the droplets as seen in figure 42. This is likely to be due to a mix of the changed morphology and dissimilar material accelerating the corrosion in these areas.

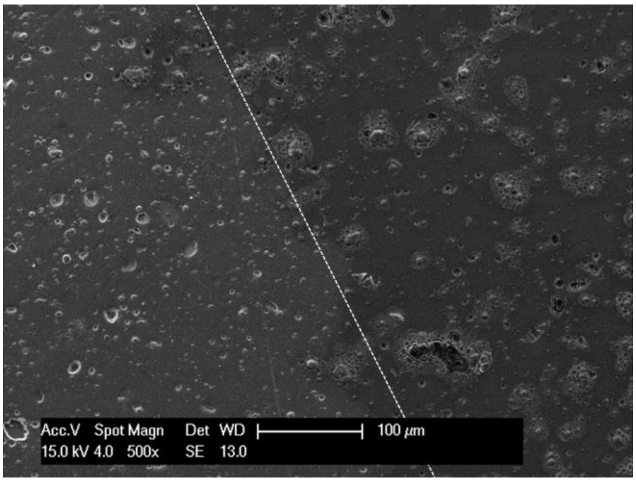

Figure 41. SEM image of a CrN-NbN coated CoCr disc, half of which was exposed to the endotoxin removal method described by Gorbet et al. The side on the left was not exposed to this method, right side shows corrosion of the coating caused by this method. This image was taken on a Philips XL30 SEM using secondary electron imaging.

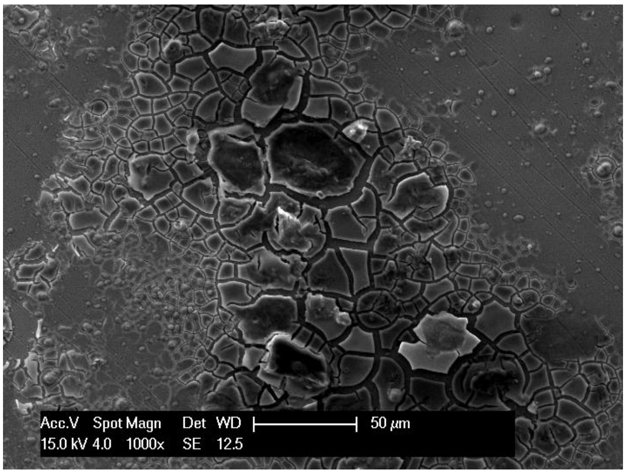

Figure 42. SEM image of a CrN-NbN coated CoCr disc, half of which was exposed to the endotoxin removal method described by Gorbet et al*. This image shows in higher magnification the detail of the corrosion surrounding the droplets in the surface. This image was taken on a Philips XL30 SEM using secondary electron imaging.*

No notable differences were seen through SEM with the Brooks method of endotoxin removal as can be seen in figure 43, it is important to note the dark patch in the upper left of the image was confirmed as debris in higher resolution imaging.

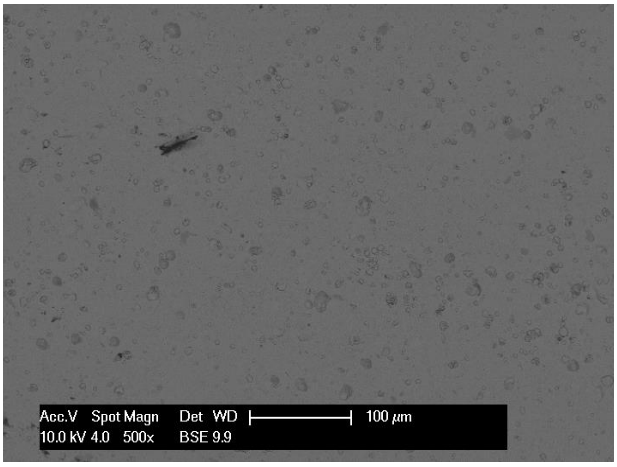

Figure 43. SEM image of a CrN-NbN coated CoCr disc, which was exposed to the endotoxin removal method by Brooks et al. This image was taken on a Philips XL30 SEM using backscatter electron imaging.

Endotoxin removal from all samples used in cell culture used the Brooks et al method [168], involving sonication in pyrogen free water. Following endotoxin removal from samples, the average endotoxin concentration for the sample extract was 0.212 EU/ml. The endotoxin concentration of the sample spiked with 0.4 EU/ml was calculated at 0.642 EU/ml.

4.2.2 Cytotoxicity Assays –Coatings

4.2.2.1 Macrophage

The macrophage metabolic activity in response to the CrN-NbN superlattice coating, TiN, CoCr, TCP, and TCP+LPS can be seen in figure 44. Generally, macrophage metabolic activity is higher on the first day for the CrN-NbN material and comparison materials than the TCP and TCP+LPS. Each sample type shows an increase in metabolic activity across the time points, as would be expected for a growing cell population.

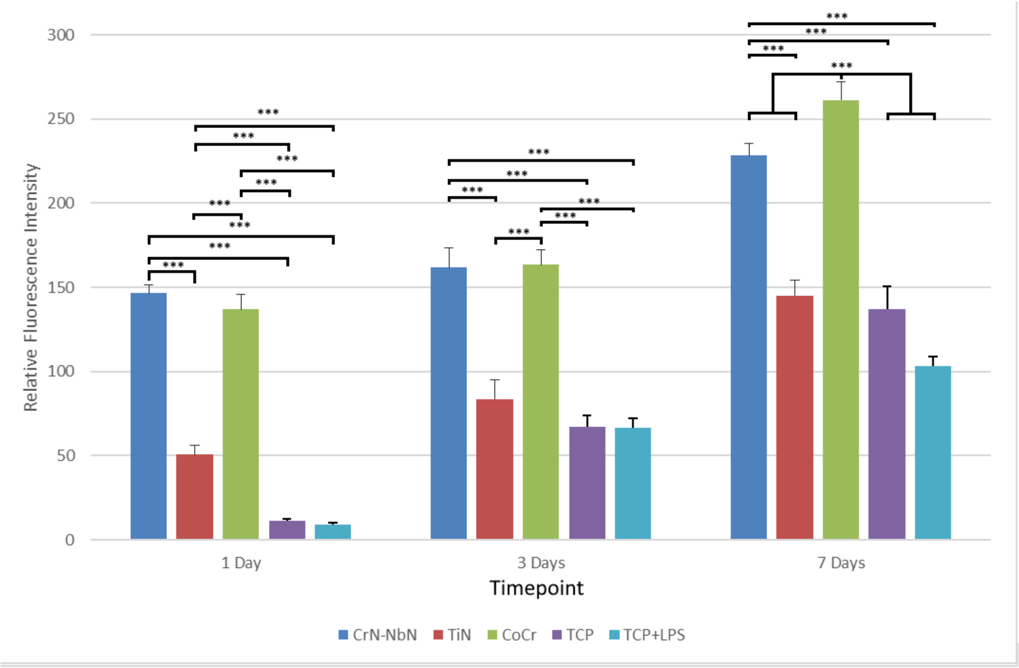

Figure 44. Average relative Fluorescence intensity for an alamarBlue® assay using J774A.1 macrophages on NbN-CrN superlattice coating, titanium nitride, cobalt chrome, and tissue culture plastic on day 1, 3 and 7. For these results n=6 and error bars are the standard error of the mean, results were repeated once, results shown here are the result of a combination of both results.

Significantly higher macrophage metabolic activity can be seen at day 1 in response to CrN-NbN coatings when compared to TCP, TCP+LPS, and TiN, it is also higher than CoCr, but this difference is not significant. The metabolic activity for CoCr is significantly higher than TiN, TCP, and TCP+LPS on day 1. The metabolic activity for TiN was significantly higher than TCP and TCP+LPS on day 1. There was no significant difference between TCP and TCP+LPS on day 1.

The metabolic activity for CrN-NbN on day 3 was significantly higher than TiN, TCP, and TCP+LPS but was slightly lower than the metabolic activity for CoCr though this difference was not significant. The metabolic activity for TiN was significantly lower when compared to CoCr, it was also slightly higher than TCP and TCP+LPS though this difference was not significant.

The metabolic activity for CoCr was significantly higher than all other samples and internal controls on day 7. The metabolic activity for CrN-NbN on day 7 was significantly higher than TiN, TCP, and TCP+LPS. The results for TiN on day 7 were slightly higher than TCP although this difference was not significant. There was no significant difference between the metabolic activity of TCP and TCP+LPS on day 7.

Overall, this shows a pattern of increased metabolic activity for the materials when compared to TCP, with the lowest increase being in TiN and with CrN-NbN and CoCr showing significantly higher metabolic activity.

4.2.2.2 Osteoblasts

The osteoblast metabolic activity in response to the CrN-NbN superlattice coating, TiN, CoCr, and TCP can be seen in figure 45. Generally, the metabolic activity increases across the timepoints for each type of sample. The samples generally appear to reach close to the maximum relative fluorescence after 7 days, with the exception of CoCr. All samples apart from CoCr show a slight decrease either at 7-14 or 14-21 days. This is likely to be as a result of the cell metabolic activity plateauing as the osteoblasts reach confluence.

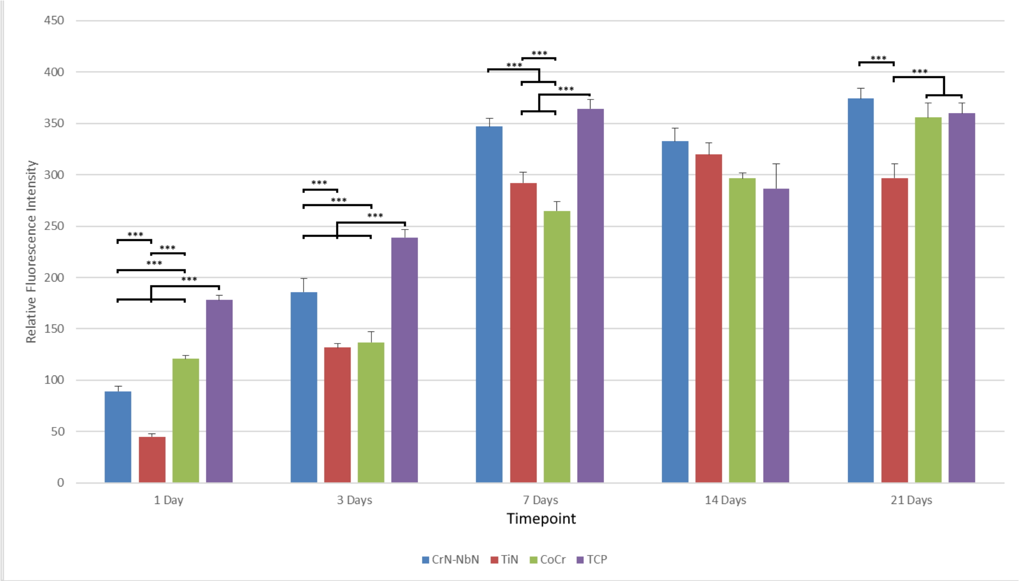

Figure 45. Relative Fluorescence intensity for an alamarBlue® assay using Primary human osteoblasts on NbN-CrN superlattice coating, titanium nitride, cobalt chrome, and tissue culture plastic on day 1, 3, 7, 14 and 21. For these results n=6 and error bars are the standard error of the mean, results were repeated once, data shown here is a combination of both results.

The metabolic activity for all samples was significantly lower on day 1 than the activity for TCP. The activity for CoCr is significantly higher than TiN or CrN-NbN with the activity for CrN-NbN being significantly higher than TiN for day 1.

The metabolic activity for TCP on day 3 is significantly higher than all other samples. CrN-NbN is significantly higher than TiN and CoCr on day 3, CoCr is also higher than TiN although this is not significant.

The activity for all samples is also lower at day 7 than TCP but this is only significantly lower for TiN and CoCr. CrN-NbN is significantly higher than TiN and CoCr on day 7 and TiN is significantly higher than CoCr.

At day 14 the activity is higher for all samples than for TCP though none of these are significant. For CrN-NbN metabolic activity is higher on day 14 than TiN and

CoCr though this is not significant. The activity for TiN is higher on day 14 than CoCr although this is not significant.

At day 21 TiN is significantly lower than all other materials. The activity for CrN-NbN on day 21 is higher than CoCr and TCP although this difference is not significant. TCP shows higher activity than CoCr though it is not significant.

Overall, this shows slightly reduced metabolic activity at early time points for all samples compared to TCP but by day 21 only TiN has significantly lower metabolic activity than TCP.

4.2.3 Cytokine Assays – Coatings

4.2.3.1 IL-6 Osteoblasts

The osteoblast IL-6 release in response to the CrN-NbN superlattice coating, TiN, CoCr, and TCP can be seen in figure 46. IL-6 release for osteoblasts on the materials overall showed a slight decrease over time in release although this was not significant for any of the materials it does appear consistent. Compared to the macrophages the osteoblasts show higher IL-6 release. There is evidence in the literature of osteoblasts releasing IL-6 in response to materials and stimuli and the concentration of IL-6 found is within the same order of magnitude as those shown and similar evidence for the range of IL-6 release found in macrophages [172] [173] [174] [175].

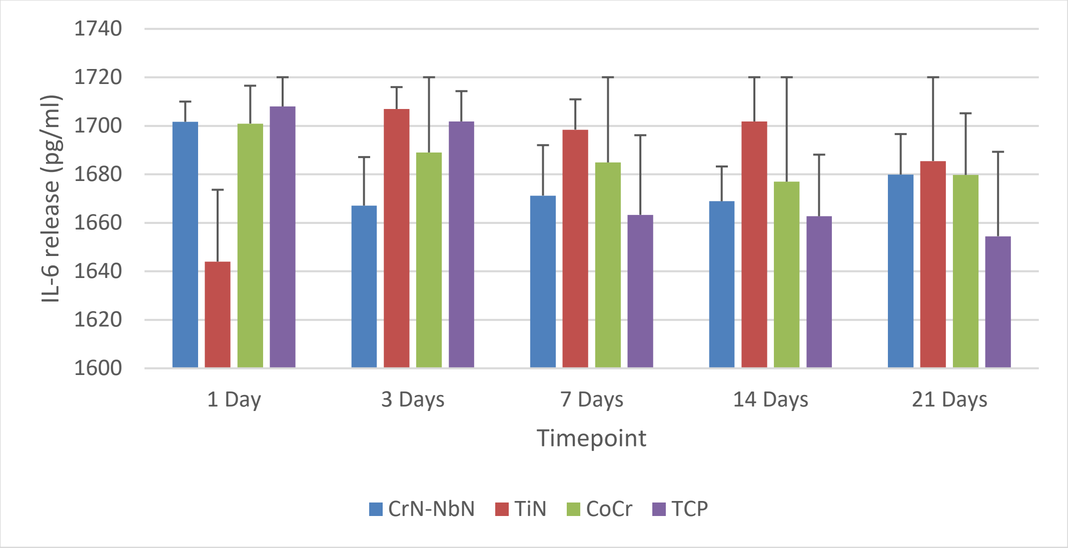

Figure 46. IL-6 release in pg/ml from primary human osteoblasts in response to bulk CrN-NbN, TiN, CoCr, and TCP. For these results n=4 and error bars are the standard error of the mean, results were repeated once.

On day 1 TCP showed higher IL-6 release when compared to all other materials though this was not a significant difference. CrN-NbN showed higher release than TiN and CoCr though this was also not significant. CoCr showed higher release than TiN, but this was not a significant difference.

On day 3 TiN had higher release of IL-6 than all samples although this was not significant for any comparison. TCP had higher IL-6 release on day 3 when compared to CrN-NbN and CoCr although this was not a significant increase. CoCr had higher IL-6 release on day 3 than CrN-NbN although this difference was not significant.

TiN had higher release of IL-6 on day 7 than all other samples though this was not significant for any of the samples. CoCr had higher release of IL-6 on day 7 than CrN-NbN and TCP although this was not a significant difference. CrN-NbN had higher release of IL-6 on day 7 than TCP although this difference was not significant.

On day 14 TiN had higher release of IL-6 than all other samples although this was not a significant difference for any samples measured. CoCr had higher IL-6 release on day 14 than CrN-NbN and TCP although this was not a significant difference. CrN-NbN had a higher release of IL-6 on day 14 than TCP although this difference was not significant.

TiN had higher IL-6 release on day 21 than all other samples though this was not significant for any comparison. CrN-NbN had higher IL-6 release on day 21 than CoCr and TCP though this was not significant in either case. CoCr had higher release on day 21 than TCP though this was not a significant difference.

The data is also shown as a % of the control for that day in figure 47. This more clearly illustrates the similar IL-6 release from osteoblasts in response to each material at each timepoint.

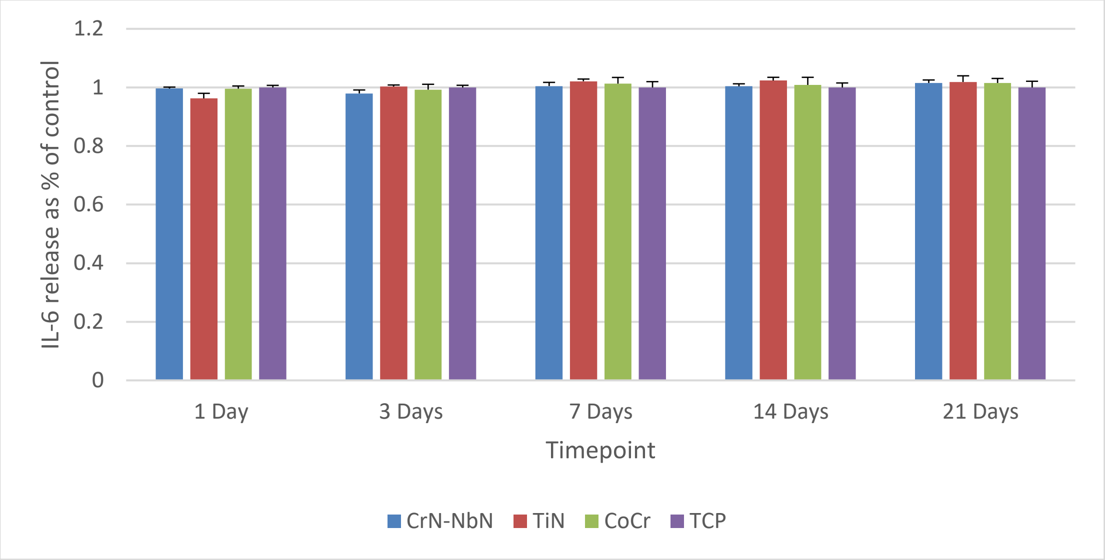

Figure 47. IL-6 release as % of control from primary human osteoblasts in response to bulk CrN-NbN, TiN, CoCr, and TCP. For these results n=4 and error bars are the standard error of the mean, results were repeated once.

4.2.3.2 IL-6 Macrophages

The macrophage IL-6 release in response to the CrN-NbN superlattice coating, TiN, CoCr, TCP, and TCP+LPS can be seen in figures 48a and b. The IL-6 release from macrophages shows the expected significantly higher increase from the samples with LPS. Many of the samples show a decrease in IL-6 over time with the exception of TiN which shows an increase at day 3 before decreasing. The CrN-NbN and comparison materials all show quite low IL-6 release, likely indicating that no macrophage activation is occurring.

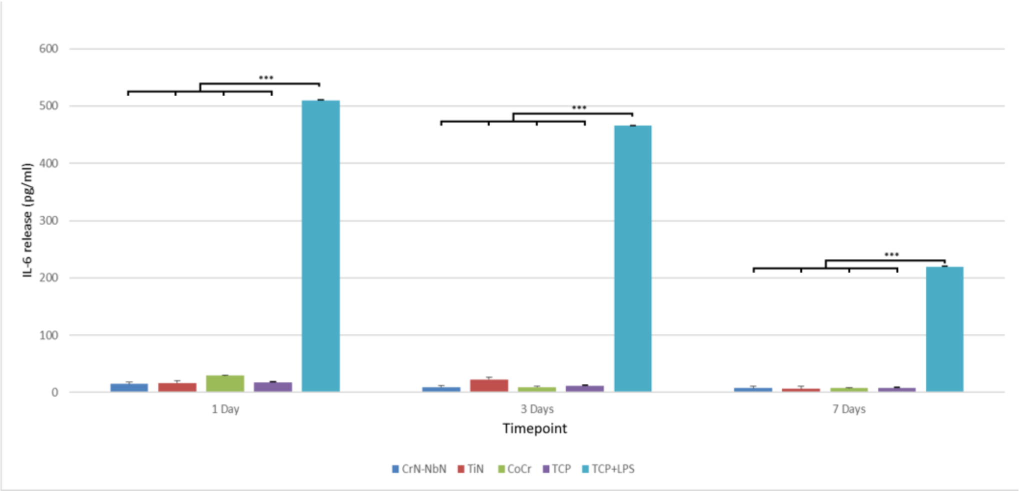

Figure 48a. IL-6 release in pg/ml from J774A.1 macrophages cultured with bulk CrN-NbN, TiN, CoCr, TCP, and TCP+LPS. For these results n=4 and error bars are the standard error of the mean, results were repeated once. Showing all results.

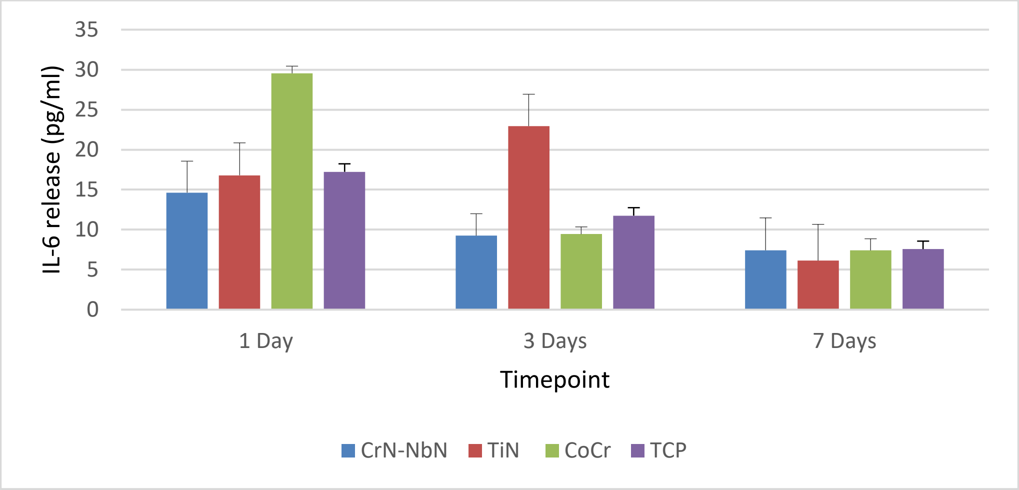

Figure 48b. IL-6 release in pg/ml from J774A.1 macrophages cultured with bulk CrN-NbN, TiN, CoCr, TCP, and TCP+LPS. For these results n=4 and error bars are the standard error of the mean, results were repeated once. Here the TCP+LPS results have been removed to improve clarity of other results.

IL-6 release from macrophages in response to TCP+LPS showed a significant increase across all time points when compared to all other samples as would be expected of the positive control. CoCr showed a higher release of IL-6 on day 1 when compared to TiN, CrN-NbN and TCP although this increase was not statistically significant. TCP showed an increased IL-6 release compared to TiN and CrN-NbN on day 1 although this was not a significant increase. TiN showed increased IL-6 release when compared to CrN-NbN although this was not a significant increase.

IL-6 release for TiN on day 3 showed higher release when compared to CrN-NbN, CoCr and TCP though this was not a significant difference. TCP showed increased IL-6 release on day 3 compared to CoCr and CrN-NbN although this difference was not significant. CoCr showed increased IL-6 release compared to CrN-NbN although this was not a significant difference.

The IL-6 release for TCP was higher than all other samples on day 7 although this was not a significant increase. The release of IL-6 on day 7 was higher for CrN-NbN than TiN and CoCr although this was not a significant increase. The release of IL-6 on day 7 for CoCr was higher than TiN although this was not a significant increase.

The data is also shown as a percentage of the control in figures 49a and b, with b showing the data with TCP+LPS excluded to allow for better visualisation of the data. This shows all the comparison materials cause a similar release of IL-6 to TCP, with exceptions for TiN on day 3 and CoCr on day 1. These however have large error bars, likely as a result of the low IL-6 release.

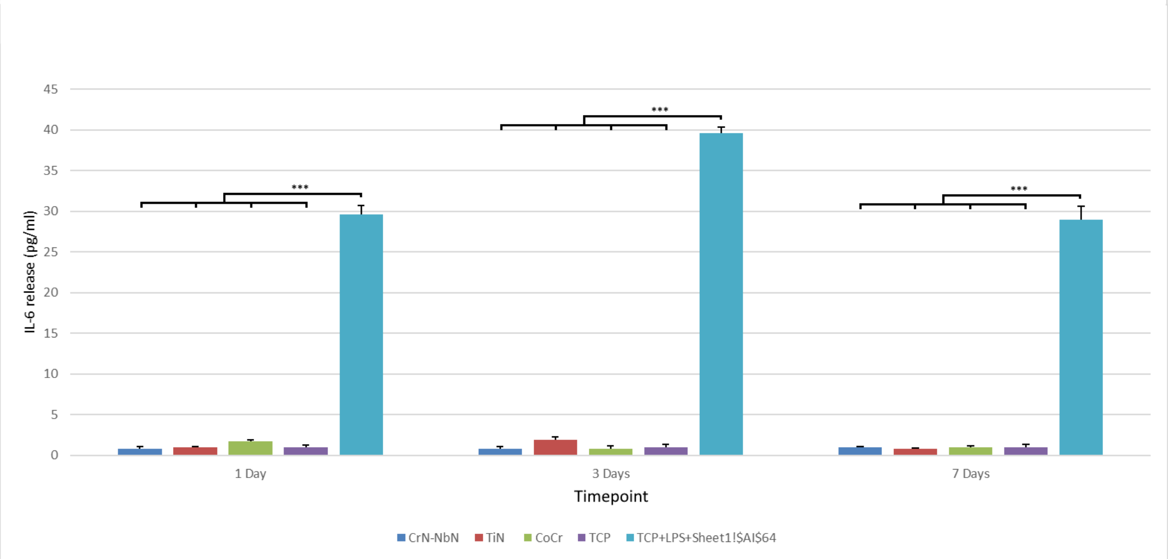

Figure 49a. IL-6 release as % of negative control from J774A.1 macrophages cultured with bulk CrN-NbN, TiN, CoCr, TCP, and TCP+LPS. For these results n=4 and error bars are the standard error of the mean, results were repeated once. Showing all results.

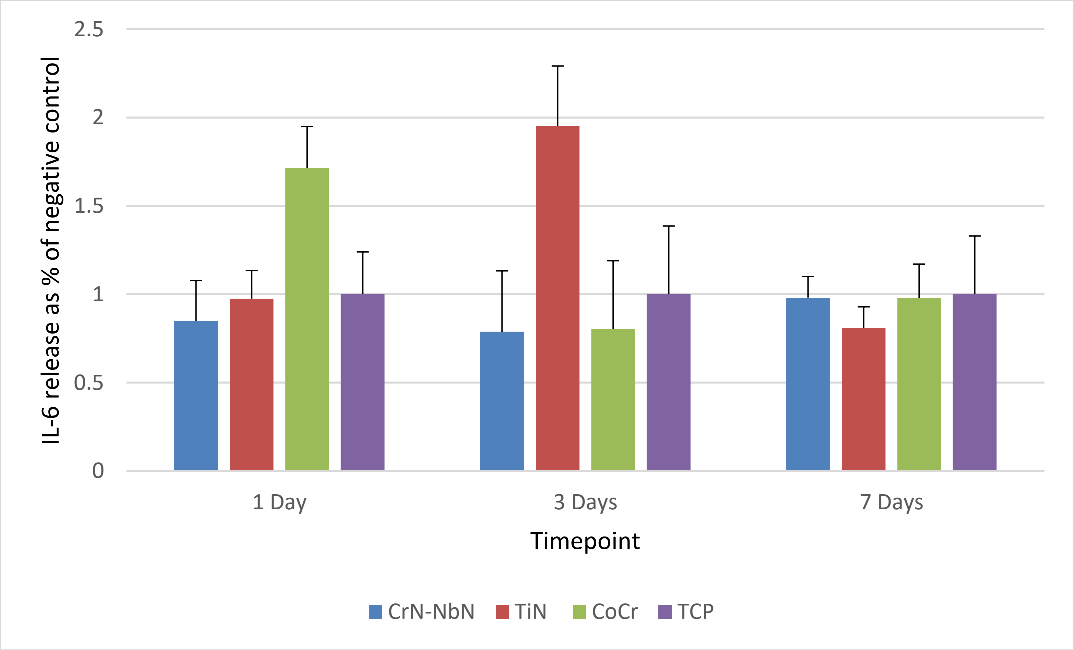

Figure 49b. IL-6 release as % of negative control from J774A.1 macrophages cultured with bulk CrN-NbN, TiN, CoCr, TCP, and TCP+LPS. For these results n=4 and error bars are the standard error of the mean, results were repeated once. TCP+LPS has been removed to improve clarity.

4.2.3.3 TNF-α Osteoblasts

The osteoblast TNF-α release in response to the CrN-NbN superlattice coating, TiN, CoCr, and TCP can be seen in figure 50. The TNF-α release from osteoblasts in response to the materials appears low in comparison to the release found in macrophages, although osteoblasts have been shown to release TNF-α [176] [177] [178]. The TNF-α release in response to CrN-NbN and TCP appear to follow quite similarly from day 1 to day 14 before CrN-NbN shows a higher decrease from day 14 to day 21 than TCP shows. These results, however, do not appear to show significant differences between the materials, and it is possible that this is a low level of background cytokine release.

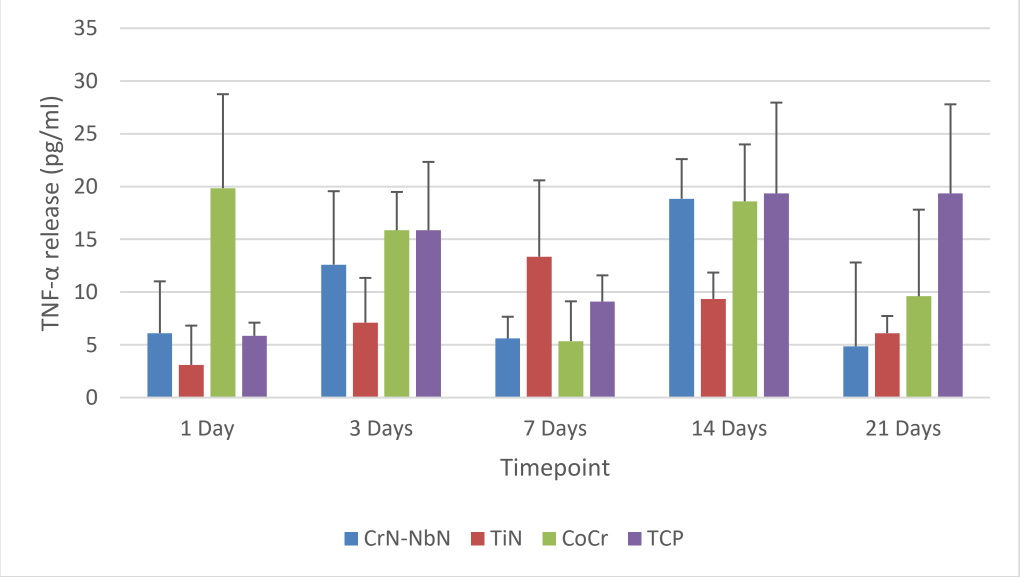

Figure 50. TNF-α release in pg/ml from primary human osteoblasts cultured with bulk CrN-NbN, TiN, CoCr, and TCP. For these results n=4 and error bars are the standard error of the mean, results were repeated once.

TNF-α release for osteoblasts on day 1 showed higher release for CoCr when compared to all other samples though this was not a significant difference.

TNF-α release on day 1 was higher for CrN-NbN than TCP and TiN although this was not a significant increase. The release of TNF-α in response to TCP was higher than the release of TNF-α in response to TiN although this was not a significant increase.

The release of TNF-α was equal for both CoCr and TCP on day 3 which was higher than CrN-NbN and TiN, this was not a significant difference. The release of TNF-α for CrN-NbN when compared to TiN was higher although this was not statistically significant.

The release of TNF-α in response to TiN was higher than all other samples on day 7 although this difference was not significant for any of the results. TNF-α release with TCP was higher than release in response to CrN-NbN and CoCr although this was not significant for either result. The release of TNF-α was higher for CrN-NbN when compared to CoCr although this was not significantly increased.

TNF-α release on day 14 was higher for TCP when compared to all other samples although this was not significant for any of the samples. The release of TNF-α on day 14 was slightly higher for CrN-NbN when compared to TiN and CoCr although this was not significant in either case. CoCr showed increased TNF-α release when compared to TiN on day 14 but this was not a significant increase.

TNF-α release on day 21 showed increased release for the TCP when compared to all other samples although this was not significant for any result. The release of TNF-α was higher for CoCr than TiN or CrN-NbN on day 21 although this wasn't a significant increase in either case. The release of TNF-α was higher on day 21 for TiN when compared to CrN-NbN although this was not a significant increase.

The data is also shown as a percentage of the control, as seen in figure 51. Similar to the data shown in figure 49b, the large error bars are a product of low TNF-α release. Likely indicating that TNF-α release by osteoblasts was not affected by the materials.

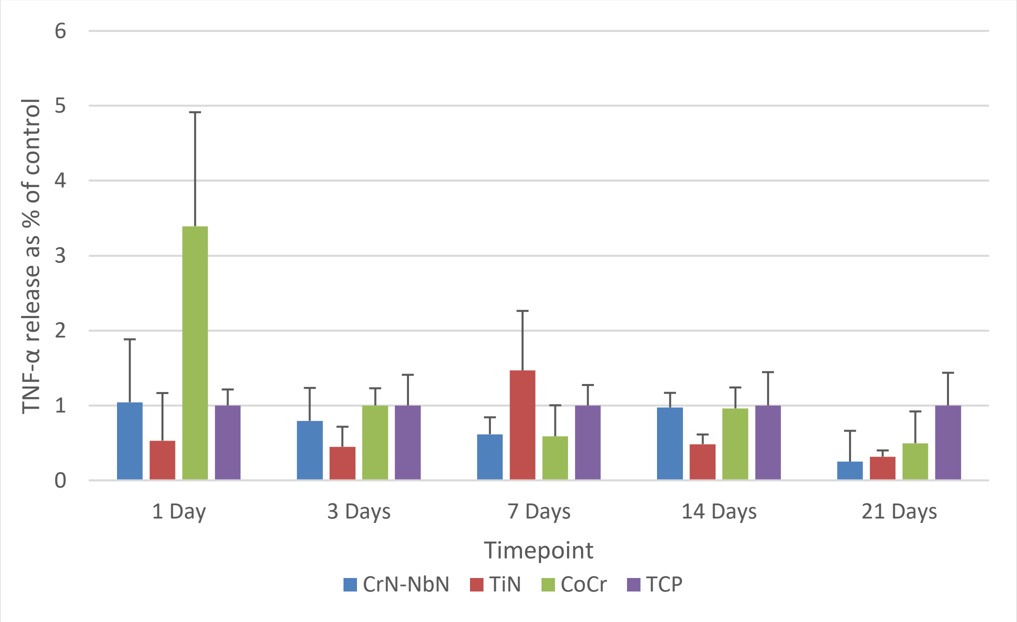

Figure 51. TNF-α release as a % of the control from primary human osteoblasts cultured with bulk CrN-NbN, TiN, CoCr, and TCP. For these results n=4 and error bars are the standard error of the mean, results were repeated once.

4.2.3.4 TNF-α Macrophages

The macrophage TNF-α release in response to the CrN-NbN superlattice coating, TiN, CoCr, TCP, and TCP+LPS can be seen in figure 52. The release of

TNF-α from macrophages shows increased release from the samples containing LPS, as would be expected. The materials show a lower release of TNF-α that increases across each timepoint, with the exception of TNF-α that decreases by day 3 before increasing by day 7. The samples with LPS show a peak of TNF-α release at day 3 which then decreases by day 7.

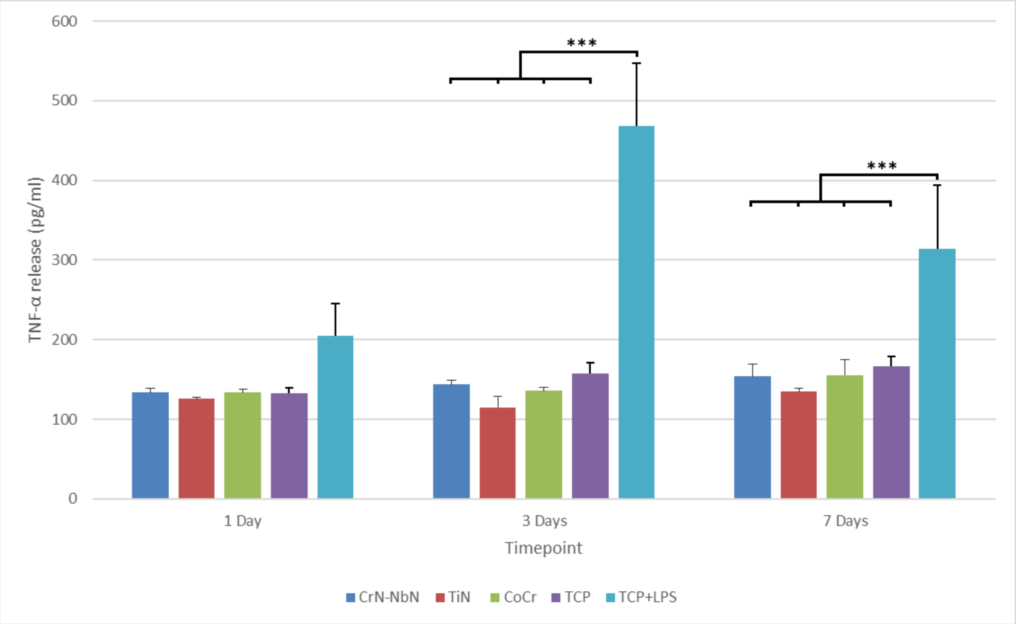

Figure 52. TNF-α release in pg/ml from J774A.1 macrophages cultured with bulk CrN-NbN, TiN, CoCr, TCP, and TCP+LPS. For these results n=4 and error bars are the standard error of the mean, results were repeated once.

TNF-α release on day 1 showed increased release for TCP+LPS when compared to all other samples though this was not significant. The release of TNF-α for CoCr was higher when compared to CrN-NbN, TiN and TCP on day 1 although this was not significant for any comparison. CrN-NbN showed increased release of TNF-α on day 1 when compared to TCP and TiN although this was not significant in either case. The result for TCP on day 1 shows an increase in TNF-α release when compared to TiN although this was not significant.

TNF-α release on day 3 shows a significant increase with TCP+LPS when compared to all other samples. TCP showed increased TNF-α release on day 3 when compared to CrN-NbN, TiN and CoCr although this increase was not significant. CrN-NbN showed increased TNF-α release on day 3 compared to TiN and CoCr although this not significant for either comparison. CoCr showed increased TNF-α release when compared to TiN on day 3 although this was not significant.

Day 7 showed significantly increased TNF-α release for TCP+LPS when compared to all other samples. TCP showed increased TNF-α release on day 7 when compared to CrN-NbN, TiN and CoCr although this was not significant for any comparison. CoCr showed increased TNF-α release when compared to CrN-NbN and TiN on day 7 although this difference was not significant in either case. CrN-NbN on day 7 showed increased TNF-α release when compared to TiN although this difference was not significant.

The data is also shown as a percentage of the control in figure 53. This more clearly illustrates the lower release of TNF-α from macrophages in response to CrN-NbN, TiN and CoCr when compared to TCP, while showing the higher release from TCP+LPS.

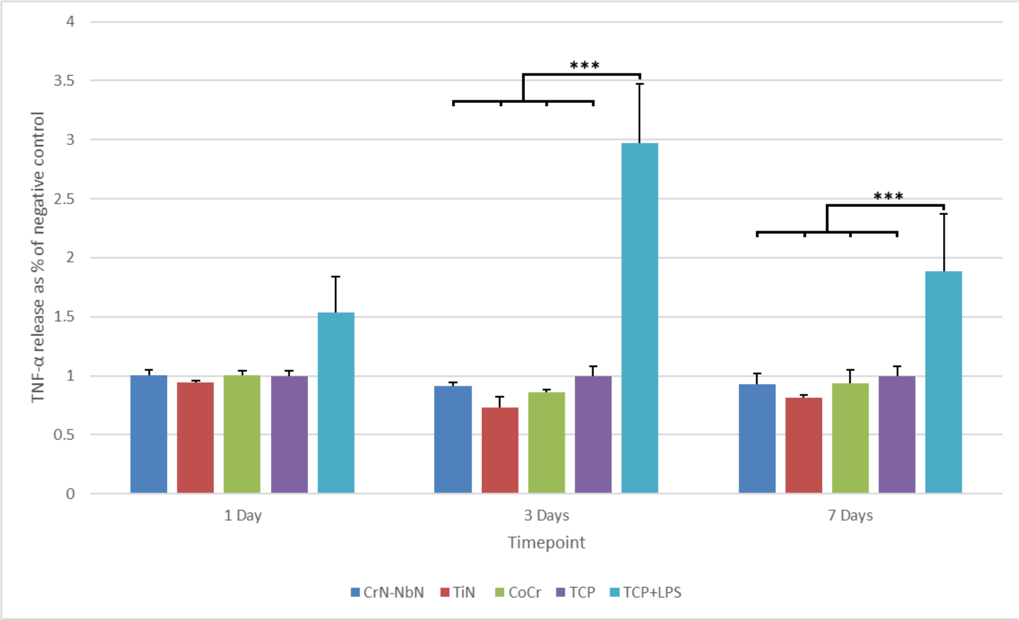

Figure 53. TNF-α release as % of negative control from J774A.1 macrophages cultured with bulk CrN-NbN, TiN, CoCr, TCP, and TCP+LPS. For these results n=4 and error bars are the standard error of the mean, results were repeated once.

4.3 DISCUSSION

Removing the endotoxins present on the samples used in cell culture down to the concentrations that are acceptable on an implanted medical device is a vital stage before using the samples in cell culture. While two methods were tested the results from the SEM on the samples treated with the Gorbet et al. method, sequential washes for 18-20 hours in alkali ethanol (0.1N NaOH in 95% ethanol) followed by 18-20 hours 25% nitric acid, indicated that it caused significant corrosion to the samples, see figures 41-42 [169]. This resulted in the use of the Brooks et al method which did not show any significant signs of corrosion or damage to the coating [168]. Thus, the Gorbet et al methodology is more suitable for polymer wear particles as shown in the literature [169].

The Brooks et al methodology did not entirely eliminate the presence of endotoxins from the materials, resulting in an endotoxin concentration of 0.212 EU/ml [170]. It did however bring the endotoxin concentration down to a concentration permitted for medical devices by the FDA (<0.5 EU/mL) [169]. While this does not limit the cell reaction to solely the CrN-NbN superlattice materials and comparison materials, it does produce more realistic results as there is evidence of adherent endotoxins on medical devices in vivo, for example circulating endotoxins being detectable following extracorporeal membrane oxygenation 0.07 U/mL, as shown by Knoch et al [179] [169]. While this could potentially be a more representative cell response to the materials as there is evidence of endotoxin adhering to particles enhancing the cell response that eventually leads to osteolysis, there is also no significant difference found between low concentrations of endotoxins (<1.0 EU/ml) [169] [180]. This means that while the Brooks methodology does not entirely eliminate the endotoxins present on the samples, this may have actually been beneficial in allowing for a cell response to the materials that is more representative of the cell response that would occur in vivo.

The corrosion that did occur in the Gorbet et al. method was most visible in the areas directly around droplets, see figure 41, this increase in corrosion was not seen in the pits [169]. There are a number of potential causes for this increase in corrosion, the droplets all showed small cracks surrounding them which is likely to have filled with both solutions during the endotoxin removal. This is likely to have led to crevice corrosion of the areas surrounding the droplets. The inclusions with significantly higher concentration of niobium and potentially being metallic niobium, compiled with the cracks surrounding the droplet, gives the solutions access to this area of high niobium concentration has the potential to form an electrochemical cell, as shown by Biswas [181]. If an electrochemical cell is formed in the areas of the niobium inclusions this would cause a significant acceleration in the corrosion of the material. If a Nb flake penetrates to the substrate there is the risk of an electrochemical cell forming between the Nb and Cr. An electrochemical cell formed between Nb and Cr in this instance will result in the oxidation of the niobium as Nb has higher reduction potential when compared to Cr, as shown by Lide and by Hwang [182] [183]. There is also evidence for galvanic corrosion to occur surrounding these droplets as shown by Wang et al [62]. While there was no evidence of galvanic corrosion found here for samples not exposed to the Gorbet et al methodology this is another avenue through which the niobium inclusions negatively impact the corrosion resistance of the CrN-NbN superlattice coating [169].

This potential for the niobium inclusions to corrode is also a potential method for the formation of the pits from the droplets. As the niobium oxidises it would expand as a result of the decrease in density from metallic niobium with a density of 8.57 g/cm^3 to niobium oxide with a density of 4.60 - 4.95 g/cm^3, as described by Harding, Yoo et al, and Berton et al [184] [185] [186]. This increased volume of the niobium inclusion as it oxidises may result in the ejection of the niobium inclusion from the NbN-CrN Superlattice coating. It is possible that this could occur as a build-up of stress eventually resulting in the ejection of the whole droplet, however, the partially ejected droplet, seen in figure 14, indicates this may occur in stages, resulting in disruption of the coating as the inclusion expands and partial ejection of the coating above the inclusion before the whole inclusion is ejected. It is important to note however that other studies, such as Biswas et al [134], have attributed similar surface features to the mechanical stresses resulting from coating deposition. Some of the pit formation occurs as a result of mechanical stress from the coating deposition, however the oxidation of the niobium inclusions may result in further pit formation, especially in environments that promote the oxidation of those inclusions.

The cell response to the CrN-NbN superlattice materials differs between the coating and the particles and is also dependent on the cell type interacting with those materials. There is however one notable point across all cell types for both the CrN-NbN superlattice coating and the CrN-NbN superlattice particles, there is no evidence for these being cytotoxic. ISO 10993-5 defines a cytotoxic effect as showing a 30% reduction in cell viability [187]. There is no evidence for a reduction in cell viability for osteoblasts or macrophages exposed to CrN-NbN superlattice coatings or particles when compared to TCP or samples with no particles respectively.

The macrophage response to the CrN-NbN superlattice coating, as seen in figure 44, shows an increase in macrophage metabolic activity when compared to macrophages exposed to TiN, TCP, and TCP+LPS across all timepoints, while showing comparable metabolic activity to macrophages exposed to CoCr, as seen in figure 44. This differs even at day 1 where cell numbers are likely to be very similar between materials, indicating that this difference in metabolic activity is likely as a result of increased macrophage activity. It is possible that this increase in macrophage metabolic activity in response to the CrN-NbN superlattice coating is as a result of increased cytokine release.

The observed IL-6 and TNF-α release from macrophages exposed to the CrN-NbN superlattice coating, shown in figures 50 and 52, however does not support the release of these as being the cause of the increased metabolic activity. The macrophages response to the CrN-NbN superlattice, in figure 48a, coating shows significantly increased IL-6 release across all timepoints in response to TCP+LPS when compared to all other samples, however the metabolic activity of macrophages exposed to TCP+LPS is significantly lower than the metabolic activity of macrophages exposed to the CrN-NbN superlattice coating, as shown in figure 44. The TNF-α release in response to the CrN-NbN superlattice coating from macrophages, shown in figure 52, is also significantly lower than in response to TCP+LPS. There is also evidence in the literature that LPS does not affect macrophage metabolic activity despite significant increases in TNF-α and IL-6 as found by Lankvelda et al [188]. This is also reflected in the results found here, showing similar metabolic activity from macrophages in response to TCP and TCP+LPS despite significantly increased IL-6 and TNF-α release in response to TCP+LPS, as seen in figures 44, 48a and 52. This further reinforces another effect resulting in increased macrophage metabolic activity in response to the CrN-NbN superlattice coating and CoCr when compared to TCP and TCP+LPS.

One potential reason for the higher cell metabolic activity for macrophages in response to the CrN-NbN superlattice coating, TiN and CoCr when compared to the TCP and TCP+LPS is the effects of macrophage attachment to the surface. It is reasoned in the literature, by Remes and Williams, that macrophage attachment may lead to the release of up to 50% of macrophage lysosomal enzymes [189]. While the macrophage attachment to the surface itself is not metabolically intensive it does lead to other cell responses, such as this release of macrophage lysosomal enzymes, that may be more metabolically intensive.

While two of these cell responses were measured, the release of IL-6 and TNF-α, not all of these could be. Therefore, this increased metabolic activity for macrophages exposed to the CrN-NbN superlattice coating is likely to be caused indirectly by macrophage attachment, leading to further responses which were not measured. Some possible examples of this include the release of other factors such as TGF-β1 and bone morphogenetic proteins (BMP), as shown by Takebe et al [190], or actin based cytoskeletal rearrangement allowing for cell adhesion, as shown by Godek et al [191]. While no measure of macrophage attachment was taken it should be noted that it was observed through light microscopy and estimated at 50% of cells not being adherent on TCP, this was not observed for the opaque CrN-NbN superlattice, CoCr, and TiN samples. The macrophages are a semi-adherent cell line so a significant proportion of the cells not adhering is to be expected. This is higher than the 20-30% non-adherent cells seen in rabbit macrophages by Hsueh et al [192], however this may be explained by the differing species the macrophages are derived from.

The IL-6 release in response to the coating materials in macrophages, shown in figure 48a, showed no significant differences or patterns between the sample materials although the release was significantly lower than the positive control for inflammation, this same effect is seen in literature by Kaufman et al demonstrating IL-6 release in response to LPS to be up to 30 times higher than comparison materials such as CoCr and UHMWPE [193]. This would indicate that the coating materials are not inducing the release of IL-6 in macrophages.

This is as would be expected as IL-6 release is usually induced by exposure to pro-inflammatory factors such as LPS and particles within the 0.1-10 μm range, as shown by Vermes et al [27]. Attachment to a surface does not usually alter or affect this release, as demonstrated by Tana et al [194].

The TNF-α release in macrophages in response to the coating materials, shown in figure 52, shows no significant pattern among the comparison materials but is lower than the positive control for inflammation, reinforcing the bulk materials not inducing the release of TNF-α in the macrophages. The release of TNF-α in these instances is very similar to those found in the literature, such as that shown by van Hove et al, being between 100-200 pg/ml with little change from days 1-7 [195]. Some studies, such as those performed by Li et al, and Luo et al, do show significantly lower TNF-α release, 2-4 pg/ml and 3-10 pg/ml respectively, in response to CoCrMo, TiCuN films and Ti-Mn-N films, however it should be noted that in these studies cells were seeded at a much lower seeding density, an order of magnitude lower, with no normalisation of this release [196] [197]. This lower cell seeding density is very likely to be the cause of the significantly lower TNF-α release seen in that study.

Overall, the IL-6 release and TNF-α release, shown in figure 48a and 52, from macrophages in response to the CrN-NbN superlattice coating material demonstrates very similar release compared to other common biomaterials and TCP. This shows the CrN-NbN superlattice coating is unlikely to result in an inflammatory reaction or pathways leading to osteolysis and late aseptic loosening. However, as inflammation, osteolysis, and late aseptic loosening are typically in response to the wear debris produced from the bearing surfaces, this result is to be expected [20]. The release of IL-6 and TNF-α from macrophages in response to the CrN-NbN superlattice coating in line with other biomaterials does however indicate that the CrN-NbN superlattice coating may be well tolerated in vivo.

The cytotoxicity results for the osteoblasts cultured with the coatings, shown in figure 45, shows the metabolic activity throughout the samples and timepoints was approximately equal. This indicates that the metabolic activity of the osteoblasts was not significantly affected by any of the samples used. This indicates that the CrN-NbN superlattice coating is not considered to be cytotoxic to osteoblasts by the definition shown in ISO 10993-5, where materials demonstrating 30% reduction in cell viability are defined to be cytotoxic [187].

The IL-6 release in response to the coating materials in osteoblasts, shown in figure 46, shows no significant patterns or differences in cytokine release across any of the materials, indicating that IL-6 release was not significantly affected by the coating materials in osteoblasts. The IL-6 release by osteoblasts in response to the coating materials was double that shown for macrophages, shown in figure 48a. While there is little direct comparison of IL-6 release between macrophages and osteoblasts there is individual evidence of similar IL-6 release in both cell types. Kramer et al [198] found murine osteoblasts to release approximately 1000ng/ml at 72 hours in response to TCP when seeded at a density of 1 x 10^5/ml. While not an ideal comparison this does show osteoblasts derived IL-6 in similar concentrations to those found, despite the differing species of origin and a seeding density a third of that used here (1 x 10^5/ml). While this comparison is not ideal, it does provide evidence of these concentrations of IL-6 to be released by macrophages.

The TNF-α release in response to the coating materials in osteoblasts, shown in figure 50, shows no significant patterns or differences in cytokine release across many of the materials, indicating that TNF-α release was not significantly affected by the coating materials in osteoblasts. It has been shown that while TNF-α gene expression may be increased in osteoblasts (in the case of this study through infection with Escherichia coli), there is little release of TNF-α and there is evidence, shown by Crémet et al, for cell surface TNF-α expression in osteoblasts [199]. However, as the measurement of TNF-α for osteoblasts in response to the CrN-NbN superlattice particles used an ELISA assay, any surface expression of TNF-α would not be measured. This is because the ELISA assays only measure the concentration of the cytokines in the cell supernatant and provide no measurement of cell surface cytokine expression. The low concentrations of TNF-α found in response to the coating materials may also indicate low TNF-α expression overall.

Overall, the TNF-α and IL-6 release from osteoblasts demonstrates similar results to other common biomaterials. This indicates that the CrN-NbN superlattice coating itself is well tolerated by osteoblasts and is unlikely to result in a response from osteoblasts that could lead to increased macrophage recruitment to the joint space or osteogenesis. It should however be noted that the wear particles produced by the coating is primarily responsible for this response in vivo so this result fits with expectations [20]. The release of IL-6 and TNF-α from osteoblasts exposed to the CrN-NbN superlattice coating is in line with the release of IL-6 and TNF-α from osteoblasts exposed to other common biomaterials, indicating it is likely to be well tolerated in vivo.

5 CHARACTERISATION OF CRN-NBN PARTICLES

5.1 MATERIALS AND METHODS

In order to properly characterise the effects of the CrN-NbN superlattice coating in an in-vivo environment it was also necessary to produce a suitable analogue to the wear debris that bearing surfaces produce in vivo. Several methods of particle production were tested, and the particles were compared to particles produced by wearing of bearing surfaces of total joint replacements in the literature, as seen in table 1, to ensure they were clinically relevant. It was decided to compare the particles produced to the particles produced by similar materials in the literature.

5.1.1 Production of Particles

5.1.1.1 Particle production methods

Particles of this coating were produced through ball milling of a steel housing and balls coated with the superlattice coating. The ball mill contained 10 CrN-NbN coated 10mm diameter steel balls and was run at 300 rpm for 2 hours on a Fritsch Pulverisette 5 Planetary ball mill. Particles were retrieved through three washes of the housing using deionised water and stored in suspension in order to improve ease of handling. A sample of the particles was then carbon coated for analysis using an Agar Turbo Carbon Coater, while the rest were stored for later analysis. Energy-dispersive X-ray spectroscopy (EDX) and SEM

Analysis as described later was performed on a Philips FEI XL30 SEM to ensure that the substrate of the ball mill did not contaminate the materials.

Reduction of steel contaminants in the ball milled CrN-NbN particles from the ball mill housing and balls was performed through repeated magnetic removal of the particles using a neodymium magnet until there was no further reaction with a magnet. The removal of this was then verified through XPS and EDX.

Further particle production used improperly cleaned knee implants, leaving surface grease on the part prior to coating, produced by Zimmer Biomet which resulted in a poorly adhering coating. This was removed using thermal shock by addition of liquid nitrogen to the knee implants in a clean plastic container. The particles were then removed through three washes of the container with deionised water and stored in suspension to ensure ease of handling.

The particles produced through thermal shock were then ground for 20 minutes manually using an agate pestle and mortar supplied by Agar scientific. The mortar was then rinsed with deionised water three times and the resulting suspension stored. A subset of these particles was then carbon coated using an Agar Turbo Carbon Coater. EDX and SEM Analysis as described later was performed on the Philips FEI XL30 SEM to ensure that neither the agate nor the knee implant substate contaminated the particles. Once characterised the remaining particles were used for cell culture work.

5.1.2 Storage of particles

CrN-NbN particles were stored in a glass bottle provided by ThermoFisher. Particles were stored in suspension with deionised water to ensure their ease of handling due to the small particle volume produced. TiN and Al_2O_3 particles were stored in the glass bottles they were provided in. All bulk, coating and powder materials were stored at room temperature.

5.1.3 Characterisation of Particles

5.1.3.1 LDPA

Particles produced through ball milling were then analysed through Laser Diffraction Particle Analysis (LDPA) using a Coulter LS23. LDPA works by passing particles in a solution past a laser and then capturing the light diffracted from particles passing through the laser beam. Utilising the diffraction pattern of the particles the approximate particle size is calculated. A suspension containing the particles produced through ball milling suspended in deionised water was used to measure the particle size distribution. The particles were stored in a glass bottle provided by ThermoFisher. The suspension was sonicated prior to use to try and prevent agglomeration of the particles during analysis. Particles were sonicated for 5 minutes in an ultrasonic bath by placing the bottle containing them into the bath.

5.1.3.2 Scanning electron microscopy (SEM)

SEM was performed on the CrN-NbN particles produced through ball milling. Two samples were prepared for use in SEM and Energy-Dispersive X-Ray Spectroscopy (EDX). One sample was prepared by air drying of the particle suspension directly onto a carbon tab and then carbon coated for use in EDX using an Agar Turbo Carbon Coater and Sputter Coater. One sample was produced through filtering the suspension through a Whatman® Nuclepore™ Polycarbonate Track Etched Membrane with a pore size of 15 nm. This was then air dried directly onto a carbon tab, this was then coated with platinum and used for SEM imaging. Images were taken using secondary electron imaging and back scattered electron imaging using a Philips FEI XL30 at 10.0 kV and a spot size of 4.0.

Further imaging of the particles produced through thermal shock took place using SEM with a platinum coated sample of the particles and EDX using a carbon coated sample of the particles. The carbon coating used an Agar Turbo Carbon Coater and Sputter Coater, and the platinum coating used a Q150V Quorum sputter coater. The CrN-NbN particles were dried onto a carbon tab prior to coating. Both samples were then mounted into a Philips FEI XL30 for imaging, at 20.0 kV and a spot size of 2.5, using back scattered electron imaging and secondary electron imaging and EDX for the carbon coated sample.

5.2 RESULTS

5.2.1 Particle Analysis

The morphology of the particles produced is presented here, which is vital as the size of the particles significantly affect the biological response. Here the results of both ball milling and thermal shock methods of particle production are presented, including SEM and EDX results.

5.2.2 Particle Morphology

Figure 54 shows the size distribution measured using LDPA for the ball milled particles of the CrN-NbN superlattice. Figure 54 shows a size distribution of 63.41-0.04µm with an average of 8.14µm, these sizes were calculated by the coulter software based on the particles being spherical. The particles within macrophage activation range (0.1-10 µm) make up 68.75% of the total volume of particles measured.

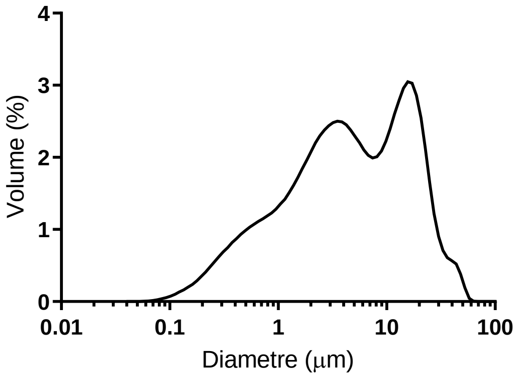

Figure 54. Particle size distribution of ball milled superlattice particles produced through LDPA using a Coulter LS230. The graph shows two peaks, one at 20 µm and another one at 3 µm. No particles below 0.05 µm or above 60 µm were found.

SEM imaging of the particles revealed two distinct morphologies of particles, plate like particles up to 10µm in size and smaller particles up to 1µm in size showing a granular morphology as can be seen in figure 55. No particles above 10µm in size were visible from the SEM imaging across the sample however agglomeration of the particles is clearly observed.

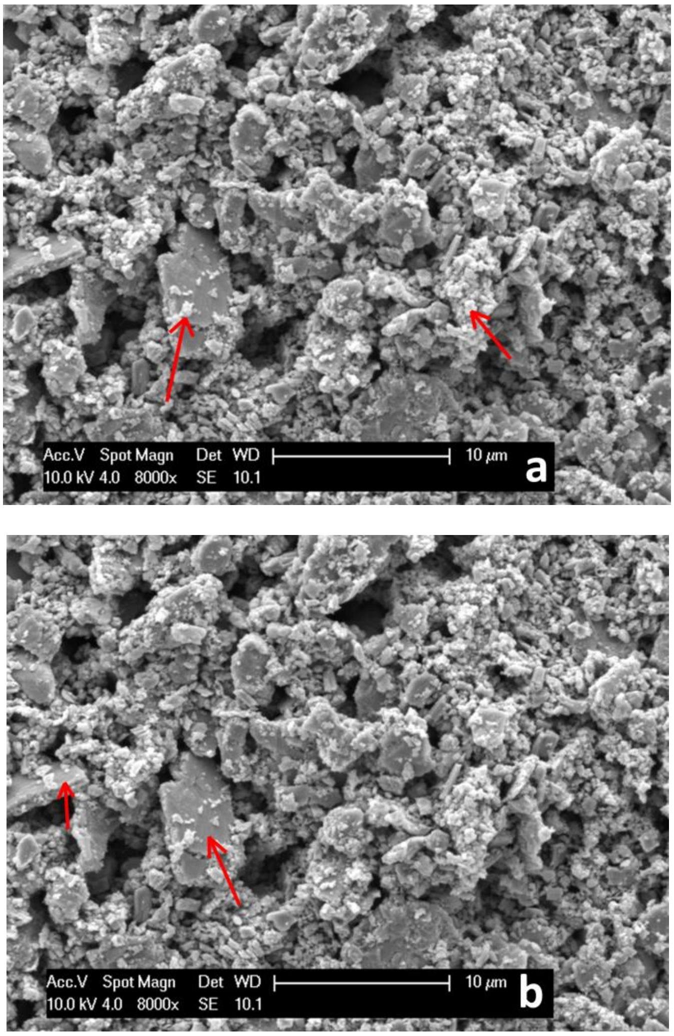

Figure 55. SEM image of platinum coated superlattice particles produced through ball milling at 8000x magnification taken using a Philips XL30 SEM using secondary electron imaging. Smaller granular particles can be seen agglomerating together, as highlighted in a or attached to larger plate like particles, highlighted in b.

Prior to further treatment the EDX analysis of the superlattice particles after ball milling revealed the presence of steel in the particles and can be seen in figure 56 from the presence of iron and nickel shown in the top right and bottom left respectively. The bottom right image shows the presence of niobium across the sample, likely indicating that the smaller particles are the superlattice ones.

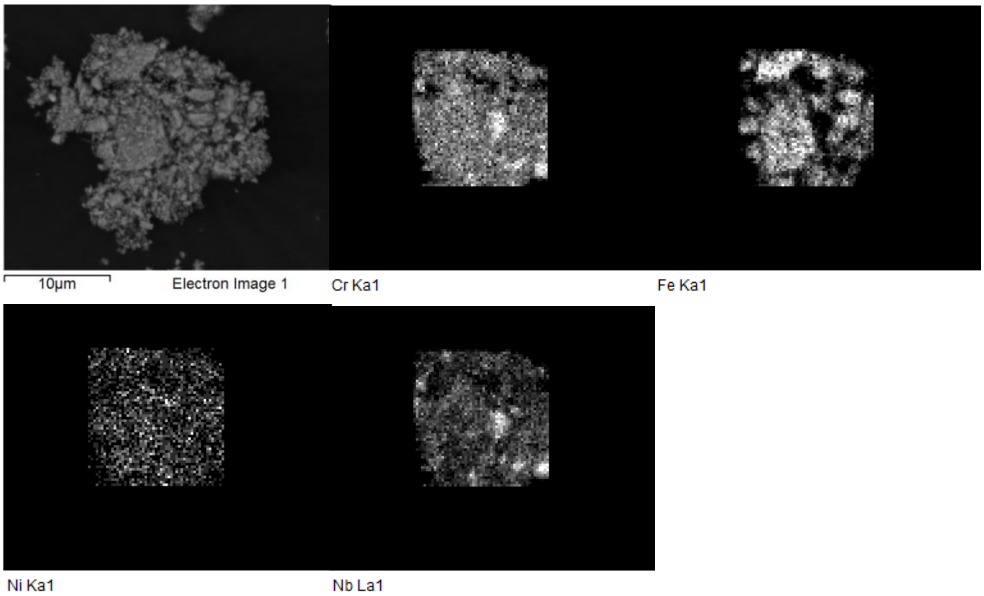

Figure 56. EDX images of the carbon coated particles showing the area analysed through backscatter electron emission (Top left), areas with Cr present (Top middle), areas containing Fe (Top right), areas with Ni present (Bottom left) and areas with Nb present (Bottom middle). These images were taken using a Philips XL30 SEM. The top right image shows high concentrations of iron that align with the larger particles in the top left image.

5.2.2.1 Post magnet removal of iron SEM EDX images

A post ball mill magnetic field method was used to remove the pickup of the ferritic steel components from the ball mill and balls. The EDX analysis of the particles following removal of the iron contaminant demonstrates the success of this removal, showing no evidence for the continued presence of iron. The area observed for EDX can be seen in figure 57. It does however indicate the presence of Chlorine and Calcium which was believed to be the result of salt contamination from contaminated glassware, and this was resolved through three washes with deionised water. The ratio of Cr:Nb for the particles is 2.39:1, indicating alignment with the results of the previous EDX and XPS on the coating material, found in tables 6 and 9.

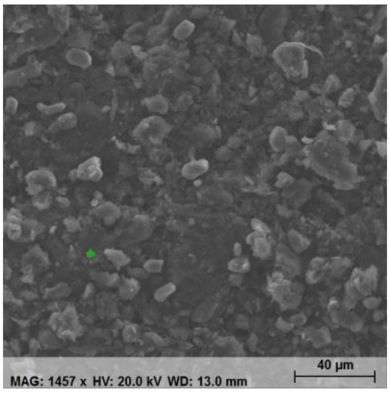

Figure 57. SEM image of CrN-NbN superlattice particles after magnetic removal of the iron contamination. This image was taken on a Philips XL30 SEM using secondary electron imagining. The particles are on a carbon foam tab here to ensure good adhesion.

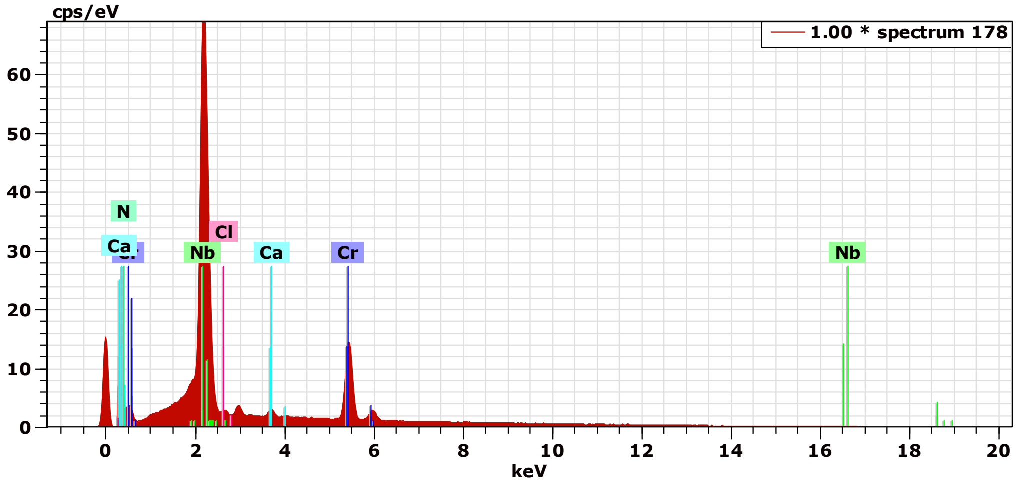

Figure 58. EDX spectrum results for the CrN-NbN superlattice following removal of the Fe contaminant. Peaks can be seen for Ca, Nb, Cl and Cr.

Element	Normalised composition [wt.%]	Atom composition [at.%]	Margin of Error
Nb	79.94	68.54	2.07
Cr	18.70	28.65	0.38
Ca	0.91	1.80	0.05
Cl	0.45	1.01	0.04
N	0.00	0.00	0.00

Table 18. Concentration calculations for the spectrum seen in figure 58. The composition of the particles is largely niobium and chromium with some calcium and chlorine contamination.

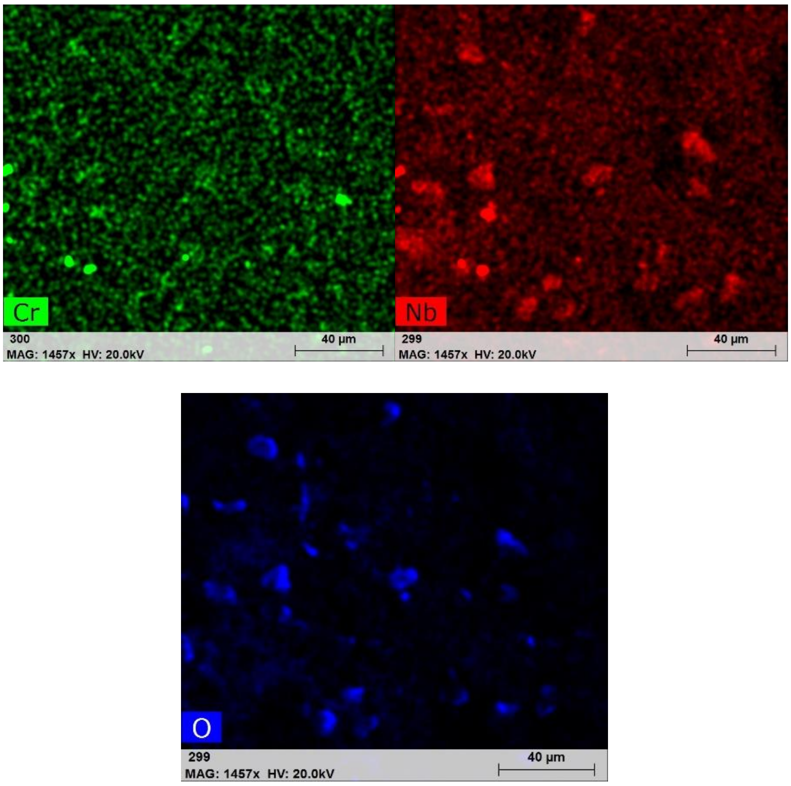

Figure 59. EDX image of the CrN-NbN superlattice particles taken using a Philips XL30 SEM showing the concentration of different elements. The bright coloured areas indicate concentrations of Cr, Nb and O as labelled.

5.2.2.2 Post agate pestle and mortar SEM EDX images

The particles produced through thermal shock and grinding with an agate pestle and mortar were investigated through SEM and EDX to measure the particle size and chemical composition. The particles were found to contain salt contaminants as chlorine, calcium and sodium were all detected, EDX showing calcium contamination can be seen in figure 62. This salt contamination was then corrected by washing the particles three times with 50ml deionised water and the materials checked for salt contamination using EDX. Prior to grinding the particles were significantly larger than 10 µm and outside the range for Macrophage activation (1-10 µm), as seen in figure 60. A columnar structure is visible along the side of the particle which may indicate the inner structure of the coating. The size of the CrN-NbN superlattice particles following grinding (seen in figure 61) was below 10 µm within the range for Macrophage activation (1-10 µm).

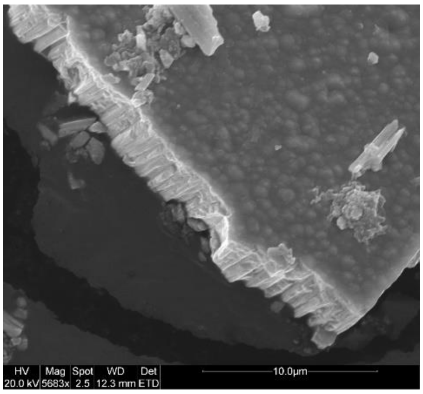

Figure 60. SEM image of the CrN-NbN superlattice particles taken using a Philips XL30 SEM using secondary electron imaging showing the particles before grinding with an agate pestle and mortar.

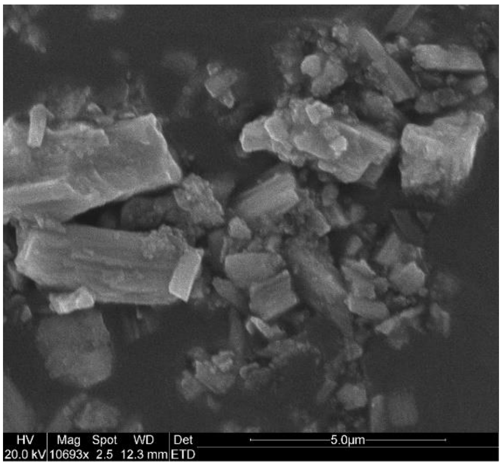

Figure 61. SEM image of the CrN-NbN superlattice particles taken using a Philips XL30 SEM using secondary electron imaging showing the particles after grinding with an agate pestle and mortar.

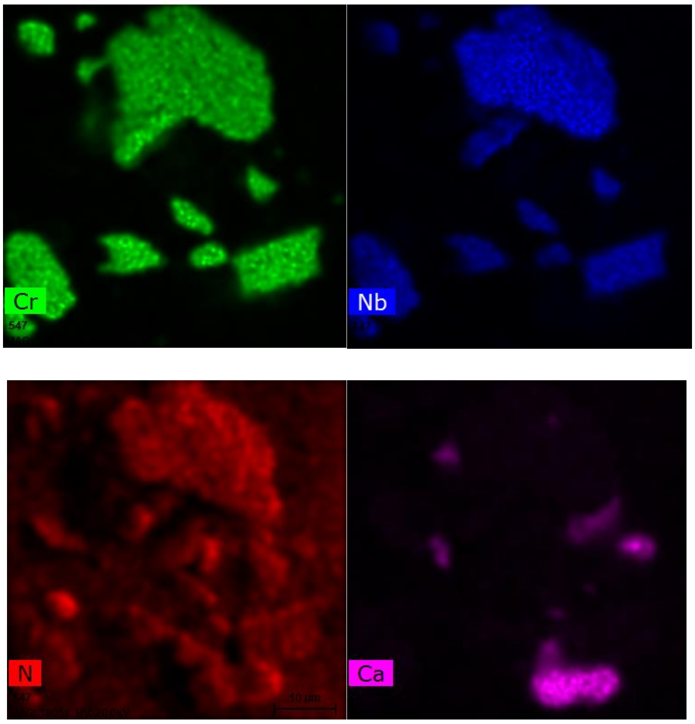

Figure 62. EDX image of the CrN-NbN superlattice particles taken using a Philips XL30 SEM showing the concentration of different elements following grinding with an agate mortar and pestle. The bright coloured areas indicate concentrations of Cr, Nb, N and Ca as labelled.

5.3 DISCUSSION

Production of CrN-NbN particles through ball milling posed significant problems with steel contamination of the particles produced from the ball mill, as shown in figure 56. The amount of steel contamination is likely to have occurred as a result of the significantly higher hardness of the CrN-NbN superlattice, 20-35 GPa, when compared to the steel of the ball mill housing, 3-3.5 GPa [95] [200]. While magnetic removal of the steel particles utilising a magnet appeared largely successful it could not be guaranteed that all steel particles had been removed and may have affected the cell response to the CrN-NbN superlattice particles. As a result of this it was decided to pursue another route to producing the particles through agate grinding of the CrN-NbN superlattice coating removed from the substrate through thermal shock with nitrogen. This provided a method of producing particles of the CrN-NbN superlattice without introducing significant contamination that would affect the cell response to the CrN-NbN superlattice particles. Some calcium contamination was found within the sample however no indication was found of agate contamination and the calcium is believed to have resulted from $CaCO_3$ contamination in the deionised water used to transport the particles.

The size range of CrN-NbN superlattice particles produced through thermal shock and grinding with an agate pestle and mortar was found to be below 10 µm as shown in figure 61. This is similar to the size range found for ceramic-on-ceramic pairings with alumina pairings producing a bi-modal distribution of particle sizes, with particles 5-20 nm and 0.2-10 µm in size, as demonstrated by Vinnichenko et al, Cimilla et al, and Henry et al [153] [154] [155]. While there is no clear bimodal distribution of the CrN-NbN superlattice particles produced through thermal shock there is evidence seen in the SEM of particles of approximately 50 nm in size although these do not make up the majority of the CrN-NbN superlattice particles observed. The majority of the CrN-NbN superlattice particles observed were approximately 3 µm polygonal particles showing evidence of the columnar structure of the CrN-NbN superlattice coating, as shown in figure 61. This columnar structure is also seen in other HIPIMS coatings, demonstrated by Price et al, Castilho et al, and Hashimoto et al [143] [122] [144].

These CrN-NbN particles produced are larger than particles usually found for other coatings such as TiN, CrN, and CrCN, which typically have a size range of up to 500 nm, demonstrated by Fisher et al [75]. The characterisation of wear particles produced from coatings, particularly superlattice coatings, is, however, not reported in the literature and so cannot be used to conclusively determine the size range of particles likely to be produced. It does however seem unlikely that particles of this size would be produced as this would represent almost half the thickness of the coating material. However, of the particles present some are less than 500nm so while all the particles may not be fully representative of those produced by other coating materials, there are approximately 1/5th that are.

The CrN-NbN superlattice particles produced through thermal shock and grinding with an agate pestle and mortar produced a morphology that largely comprised of flakes and angular or polygonal particles. Unfortunately, there is little characterisation of the morphology of wear debris produced from coatings in the literature and so it is currently impossible to compare the particles produced to typical particles produced from coated total joint replacements. It is reasonable but not ideal to compare the morphology of the CrN-NbN particles to particles produced by ceramic materials as the CrN and NbN are both ceramic materials. The CrN-NbN superlattice particle morphology of angular/polygonal particles fits with similar morphologies found in ceramic particles produced through ceramic-on-ceramic and ceramic-on-polymer pairings, as shown by Hatton et al, Tipper et al, and Stewart et al [72] [73] [74]. The flake-like morphology has also been found in patients with titanium components, as shown by Shanbhag, although the origin of these is believed to be from the non-bearing surfaces of the component [23].

Overall, the CrN-NbN superlattice particles produced through thermal shock and agate grinding are a mixed representation of the sizes and morphologies likely to occur from the wear of the CrN-NbN superlattice as a bearing surface. The CrN-NbN superlattice particles are larger than typical particles from coatings although they are still within the size range for other types of wear debris, such as UHMWPE and alumina, and within the range for macrophage activation (0.1-10 µm) as demonstrated by Fisher and Ingham, Shanbhag, and Elfick et al [24] [11] [23]. It is however possible that the CrN-NbN superlattice particles produced in vivo may not activate macrophages as similar coatings such as TiN, CrN, and CrCN produce wear particles below 0.5µm, as shown by Bloebaum et al, leaving only a small overlap between the particles and the particle sizes that result in macrophage activation [57]. The CrN-NbN superlattice coatings are however still suitable to measure the response of the cells as they are of similar size and morphology to other wear particles and may elicit a biological response similar to those found in vivo.

6 CELL CULTURE WORK WITH CRN-NBN PARTICLES

6.1 MATERIALS AND METHODS

6.1.1 Endotoxin Removal and Analysis

Endotoxin removal and analysis was performed on the CrN-NbN particles, the methodology for which is identical to that performed in sections 4.1.1 and 4.1.2.

Here endotoxin removal methods are described. Removal of endotoxins is an important precursor for the cell work as endotoxins present on the samples would cause the release of inflammatory cytokines.

Then the methods used in the culture of cells are detailed, these include the methods for general cell culture as well as the assays carried out. The methods for alamarBlue® are detailed, this is a standard cell viability assay. Methodology for IL-6 and TNF-α sandwich ELISA assays are then detailed, these measure very small concentrations of the IL-6 and TNF-α cytokines present in the cell culture.

6.1.2 Macrophage culture

The methodology for macrophage culture used with the CrN-NbN particles is identical to that described in section 4.1.4.1.

For the assays involving particles the cells were seeded onto tissue culture plastic (TCP) for 24 hours prior to changing the media to a particle laden media with a particle concentration of 4.81 mg/ml. This was calculated as a worst-case scenario based on the wear rate of 13mg over 10 million cycles within an average volume hip joint of 2.7ml with no removal of particles [95] [13] [201]. This offers a higher concentration of particles than many with those implants would experience but it provides a good worst case scenario in terms of inflammation produced, as could potentially be produced through third body wear occurring within the joint space. Other studies have shown wear particle concentrations of 0.0001-10 mg/ml for a wide variety of materials, including UHMWPE, CoCr and Alumina [202] [203] [204] [205] [206]. This puts the concentration of particles used in the cell culture within the range of those found within the literature.

6.1.3 Osteoblast culture

The methodology for osteoblast culture used with the CrN-NbN particles is identical to that described in section 4.1.4.2.

For the assays involving particles the cells were seeded onto TCP for 24 hours prior to changing the media to a particle laden media.

6.1.4 Cytotoxicity assay

Cytotoxicity of particles was tested on both cell models using an alamarBlue® cell viability assay supplied by ThermoFisher. The methodology for which is identical to that described in section 4.1.4.3.

6.1.5 Cytokine release

Cytokine Release was measured using ELISA assays provided by Sigma-Aldrich. The release of IL-6 and TNF-α was measured using both Osteoblasts and macrophages in response to pseudo wear particles.

The methods used here are identical to those described in section 4.1.4.4.

A calibration curve was used for each ELISA assay in order to calculate the concentration of the cytokines released. The calibration curves can be seen in figure 63, 64, 65, and 66.

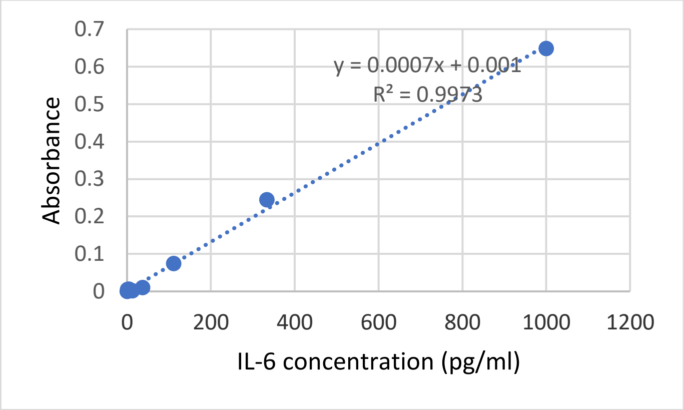

Figure 63. Calibration curve data for IL-6 release ELISA assay that was used with osteoblasts on the particles produced. For these results n=8.

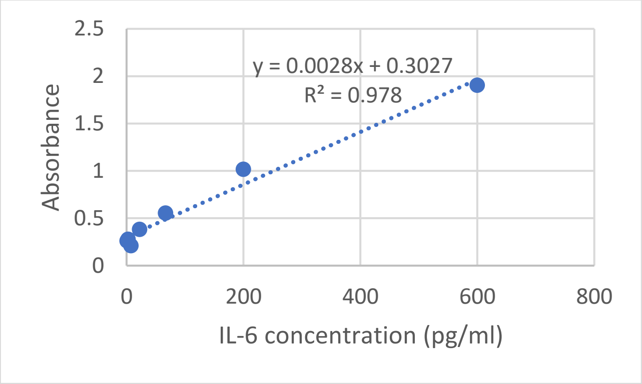

Figure 64. Calibration curve data for IL-6 release ELISA assay that was used with macrophages on the particles produced. For these results n=8.

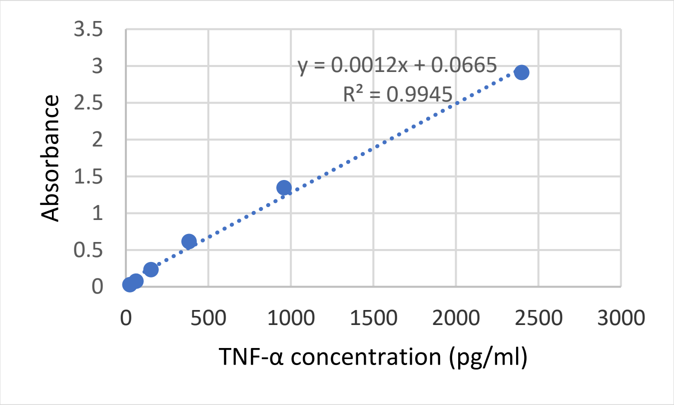

Figure 65. Calibration curve data for TNF-α release ELISA assay that was used with osteoblasts on the particles produced. For these results n=8.

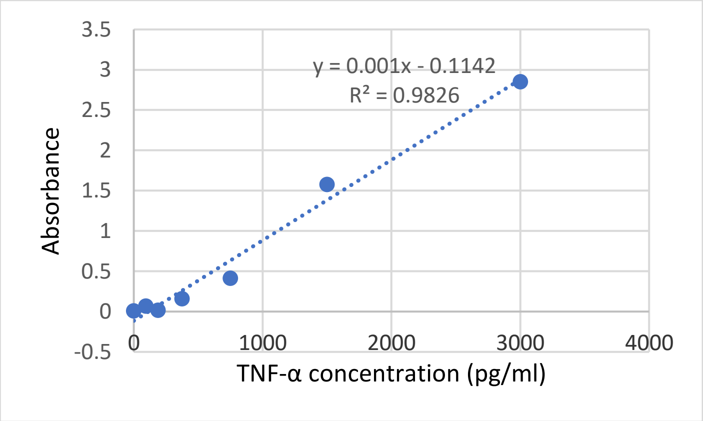

Figure 66. Calibration curve data for TNF-α release ELISA assay that was used with macrophages on the particles produced. For these results n=8.

6.2 RESULTS

The cellular response to the particulate materials are detailed in this section through metabolic activity analysis and values for IL-6 and TNF-α release as these are significant markers of inflammation and the pathways that lead to late aseptic loosening.

6.2.1 Cytotoxicity Assays – Particles

6.2.1.1 Macrophage

The macrophage metabolic activity in response to the CrN-NbN superlattice particles, TiN particles, alumina particles, no particles, and no particles + LPS can be seen in figure 67. The results for the alamarBlue® assay shows higher initial metabolic activity for CrN-NbN, Alumina and the samples with LPS, as at this point there is unlikely to be a difference in cell number this is likely to indicate macrophage activation which would lead to increased cell metabolic activity [207] [208]. This is followed by increased metabolic activity across each time point, as would be expected for a growing cell population, for all materials apart from CrN-NbN, which decreases across the timepoints.

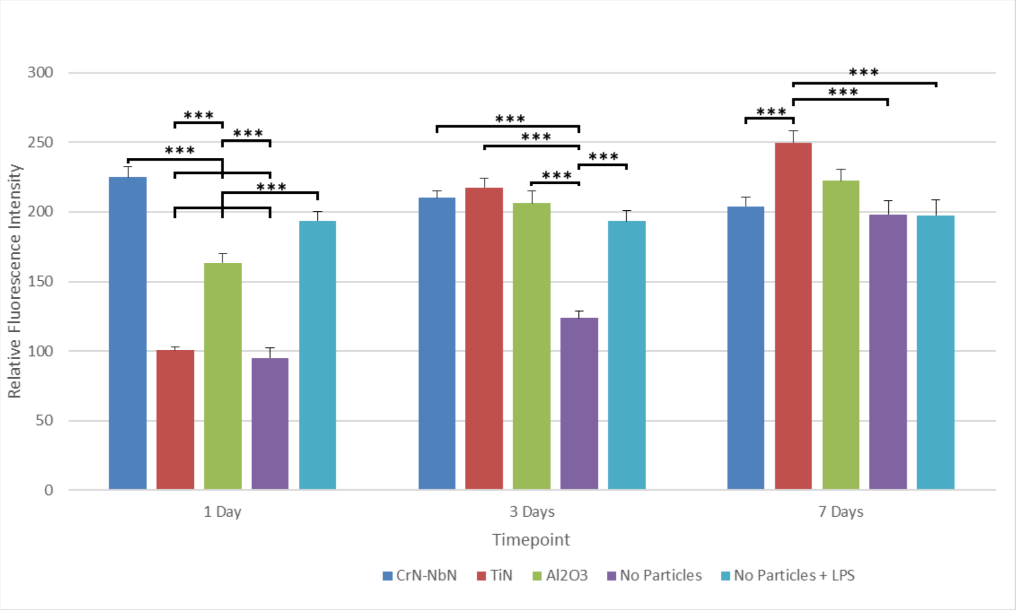

Figure 67. Relative Fluorescence intensity for an alamarBlue® assay using J774A.1 macrophages cultured with particles of CrN-NbN coating, TiN, Al_2O_3, no particles and no particles + LPS on day 1, 3 and 7. For these results n=6 and error bars are the standard error of the mean, results were repeated once.

The cell metabolic activity assay for macrophages cultured with particles showed significantly higher metabolic activity on day 1 for CrN-NbN when compared to all other materials apart from samples with no particles + LPS which showed a higher metabolic activity though the difference was not significant. TiN showed significantly lower metabolic activity on day 1 when compared to Alumina and no particles + LPS but higher metabolic activity when compared to no particles though this difference was not significant. Alumina showed significantly lower metabolic activity than no particles + LPS and significantly higher metabolic activity than no particles on day 1. Results for no particles showed significantly lower metabolic activity on day 1 than samples with no particles + LPS.

The metabolic activity on day 3 is significantly higher for CrN-NbN when compared to no particles, it is also higher than Alumina and no particles + LPS though this difference is not significant. The results for CrN-NbN on day 3 are lower than TiN though this difference is also not significant. The metabolic activity on day 3 is higher with TiN than all other samples though this is only significant when compared to no particles. Alumina shows higher metabolic activity on day 3 than no particles and no particles + LPS though this is only significant for no particles. Results for no particles showed significantly lower metabolic activity on day 3 than no particles + LPS.

On day 7 the metabolic activity for CrN-NbN is significantly lower than TiN, it is also lower than the metabolic activity for alumina though this is not a significant difference. The metabolic activity on day 7 for CrN-NbN is higher than no particles and no particles + LPS though this is not a significant difference. The metabolic activity for TiN on day 7 is higher than all samples though it is not significant when compared to alumina though it is significant for all other comparisons. Alumina shows higher metabolic activity on day 7 when compared to no particles and no particles + LPS though this is not significant in either case. Results for no particles showed higher metabolic activity when compared to no particles + LPS on day 7 though this is not a significant difference.

6.2.1.2 Osteoblasts

The osteoblast metabolic activity in response to the CrN-NbN superlattice particles, TiN particles, alumina particles, and no particles can be seen in figure 68. The metabolic activity shown for osteoblasts shows an immediate increase across timepoints for CrN-NbN and samples with no particles, as would be expected from growing cell populations. This increase does however appear delayed for TiN and Alumina, with cell viability remaining relatively stable to day 7 and day 3 respectively. The sample types with delayed increase in metabolic activity also reached lower metabolic activity by day 21.

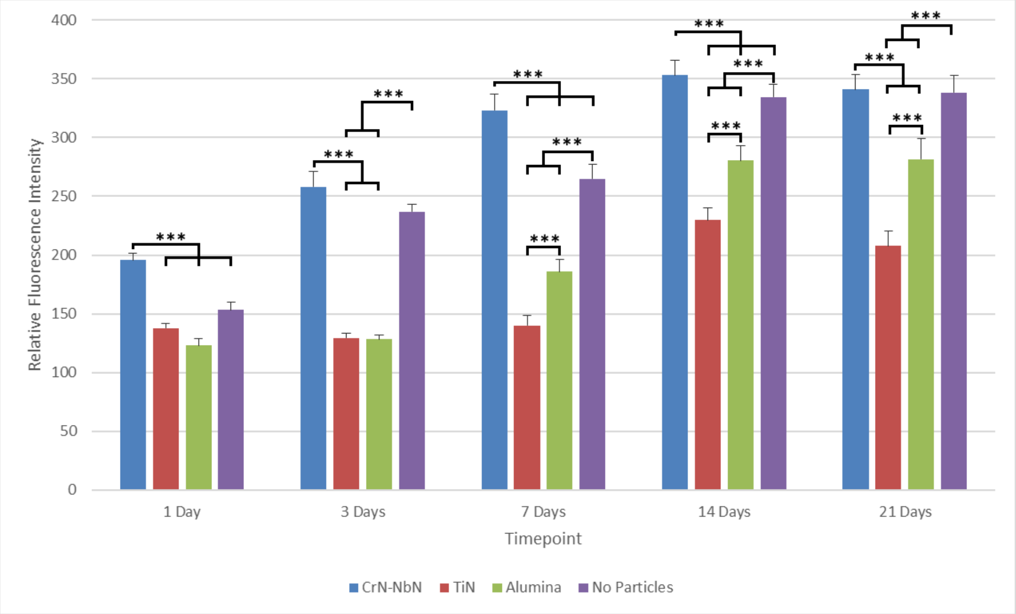

Figure 68. Relative Fluorescence intensity for an alamarBlue® assay using primary human osteoblasts cultured with particles of CrN-NbN coating, TiN, Al_2O_3 and no particles on day 1, 3, 7, 14 and 21. For these results n=6 and error bars are the standard error of the mean, results were repeated once.

Metabolic activity with the CrN-NbN particles was significantly higher than all samples and internal controls on day 1. The activity for Alumina and TiN were lower than no particles though this difference was not significant.

The metabolic activity for CrN-NbN was higher than all other samples on day 3 though this difference was only significant for TiN and Alumina and was not significant for no particles. The activity for no particles was significantly higher than that of TiN or Alumina on day 3. The activity for TiN was higher than alumina on day though this difference was not significant.

The result for CrN-NbN on day 7 is significantly higher than all other results. The activity for no particles is significantly higher than that of TiN or Alumina on day 7. Alumina also shows significantly higher metabolic activity on day 7 than TiN.

On day 14 CrN-NbN shows higher metabolic activity than all other samples though this was significant only for TiN and Alumina and was not significant for no particles. The result for no particles on day 14 was significantly higher than TiN and Alumina. The result for Alumina on day 14 showed significantly higher metabolic activity than TiN.

CrN-NbN showed higher metabolic activity on day 21 than all other samples though this was only significant for TiN and Alumina and was not significant when compared to no particles. For no particles the metabolic activity was significantly higher on day 21 than TiN and Alumina. Alumina also showed significantly higher metabolic activity on day 21 than TiN.

6.2.2 Cytokine Assays – Particles

6.2.2.1 *IL-6 Osteoblasts*

The osteoblast IL-6 release in response to the CrN-NbN superlattice particles, TiN particles, alumina particles, and no particles can be seen in figure 69. The osteoblasts show increased initial IL-6 release for TiN and Alumina when compared to CrN-NbN and no particles. There is a significant increase in IL-6 release for CrN-NbN and samples with no particles between day 3 and 7 for CrN-NbN, Alumina and samples without particles which is not seen in osteoblasts exposed to TiN particles. The IL-6 release seen in response to CrN-NbN particles follows a similar pattern to that seen with no particles, while TiN and Alumina show a different pattern of IL-6 release.

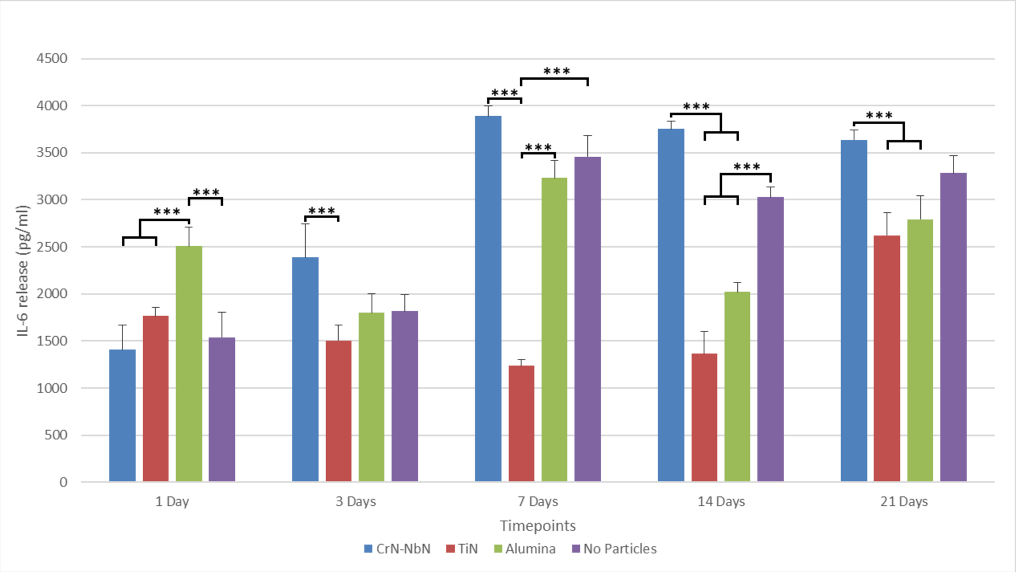

Figure 69. IL-6 release in pg/ml from Primary osteoblasts cultured with particles of CrN-NbN coating, TiN, Al_2O_3 and no particles on day 1, 3, 7, 14 and 21. For these results n=4 and error bars are the standard error of the mean, results were repeated once.

Release of IL-6 from osteoblasts showed significant increase with Alumina when compared to CrN-NbN, TiN and no particles on day 1. TiN showed increase IL-6 release on day 1 when compared to CrN-NbN and no particles though neither difference was significant. Results for no particles showed increased IL-6 release on day 1 when compared to CrN-NbN although this was not statistically significant.

The release of IL-6 with CrN-NbN was higher on day 3 than all other samples though this was only significant when compared to TiN. The release of IL-6 with no particles was higher than with Alumina and TiN on day 3 although this was not a significant increase in either case. Alumina showed increased IL-6 release when compared to TiN on day 3 although this was not a significant difference.

On day 7 the release of IL-6 with CrN-NbN was higher than that with TiN, Alumina, and no particles though this was only significant when compared to TiN. The release of IL-6 with no particles on day 7 was higher than Alumina and TiN although this was only statistically significant when compared to TiN. The release of IL-6 with Alumina is significantly higher than TiN on day 7.

On day 14 the release of IL-6 with CrN-NbN was higher when compared to all other samples though this was only significant when compared with TiN and Alumina and was not significant when compare with no particles. The release of IL-6 with no particles was significantly higher than the release with TiN and Alumina on day 14. The release of IL-6 with Alumina was higher than that released with TiN at day 14 though this difference was not statistically significant.

At day 21 the release of IL-6 was higher for CrN-NbN compared to all other samples, but this was only a significantly higher release for TiN and Alumina and was not significant when compared to no particles. IL-6 release was higher for no particles when compared to TiN and Alumina on day 21 though this difference was not significant in either case. The release of IL-6 was higher for Alumina on day 21 than TiN although this was not a statistically significant difference.

The data is also shown as a percentage of the control in figure 70. This more clearly illustrates the increased IL-6 release from osteoblasts exposed to CrN-NbN particles when compared to no particles across days 3-21. It also more clearly shows the decreased release when compared to no particles for TiN particles and alumina particles for days 7, 14, and 21.

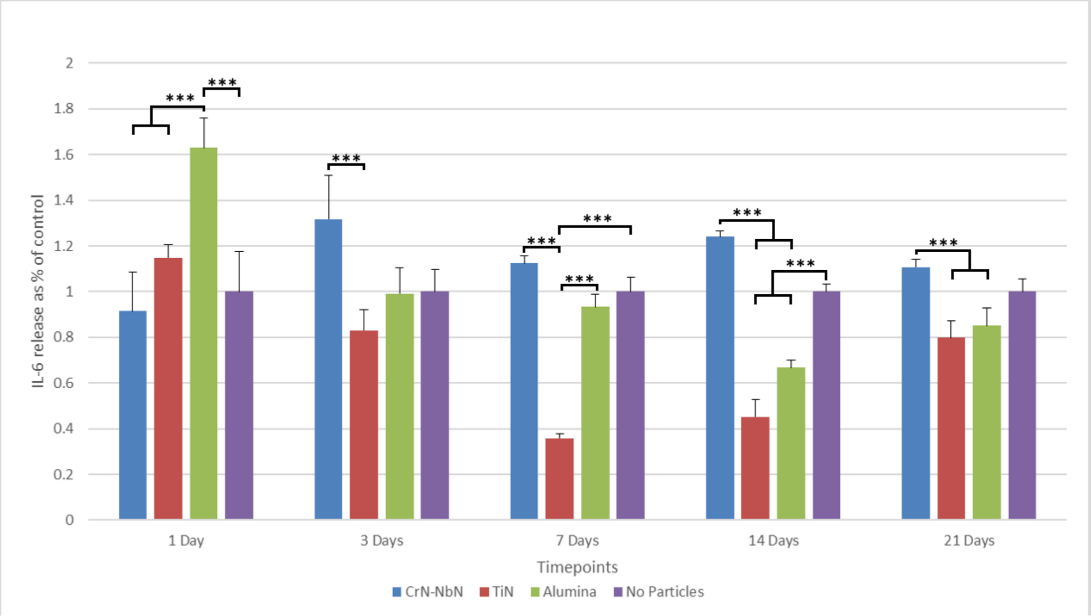

Figure 70. IL-6 release as % of control from Primary osteoblasts cultured with particles of CrN-NbN coating, TiN, Al_2O_3 and no particles on day 1, 3, 7, 14 and 21. For these results n=4 and error bars are the standard error of the mean, results were repeated once.

6.2.2.2 IL-6 Macrophages

The macrophage IL-6 release in response to the CrN-NbN superlattice particles, TiN particles, alumina particles, no particles, and no particles + LPS can be seen in figure 71. The IL-6 release from macrophages in response to particles shows high initial release for the CrN-NbN, TiN and Alumina that slowly decrease across the timepoints, this initial release for CrN-NbN and TiN was comparable to the release for samples with LPS. The sample containing LPS shows high initial release of IL-6 that is maintained across all timepoints. Samples with no particles or LPS showed very low initial release with a gradual increase across the timepoints.

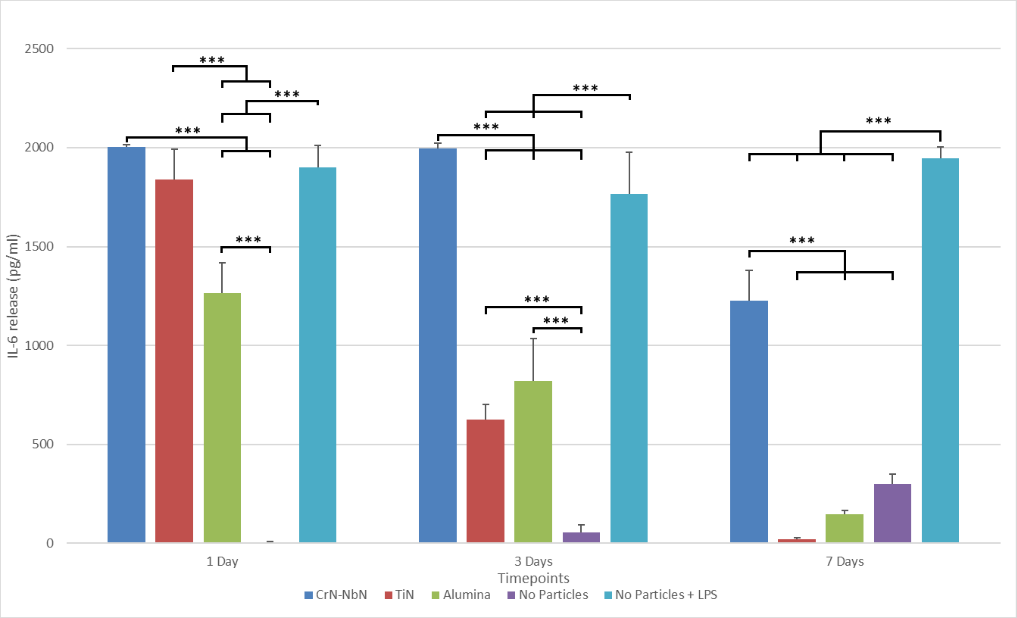

Figure 71. IL-6 release in pg/ml from J774A.1 macrophages cultured with particles of CrN-NbN coating, TiN, Al_2O_3, no particles and no particles + LPS on day 1, 3 and 7. For these results n=4 and error bars are the standard error of the mean, results were repeated once.

The release of IL-6 by macrophages on day 1 showed higher release with CrN-NbN particles when compared to all other samples including no particles + LPS, though this difference is only significant when compared to Alumina and no particles. IL-6 release was higher on day 1 for no particles + LPS when compared to TiN, Alumina, and no particles though this difference was only significant when compared to Alumina and no particles. TiN showed significantly higher IL-6 release on day 1 when compared to Alumina and no particles. Alumina showed significantly increased IL-6 release on day 1 when compared to no particles.

On day 3 the release of IL-6 with CrN-NbN was higher than all samples although this was only significant for TiN, Alumina, and no particles and was not significant when compared to no particles + LPS. The release of IL-6 with no particles + LPS was significantly higher than the release caused by TiN, Alumina, and no particles on day 3. The release of IL-6 caused by Alumina was higher than the release caused by TiN and no particles on day 3, although this was only significant when compared to no particles. The release of IL-6 with TiN was significantly higher than the release of IL-6 caused by no particles on day 3.

No particles + LPS caused significantly higher IL-6 release at day 7 when compared to all other samples. CrN-NbN caused significantly higher IL-6 release than TiN, Alumina, and no particles at day 7. IL-6 release with no particles at day 7 was higher than TiN and Alumina although this was not significant in either case. Alumina showed higher IL-6 release at day 7 than TiN although this was not a significant difference.

The data is also shown as a percentage of the control in figure 72. This illustrates the magnitude of initial release of IL-6 from macrophages in response to CrN-NbN particles, TiN particles, alumina particles, and LPS, although this is also affected by the increasing release between days 1, 3 and 7 when not exposed to particles.

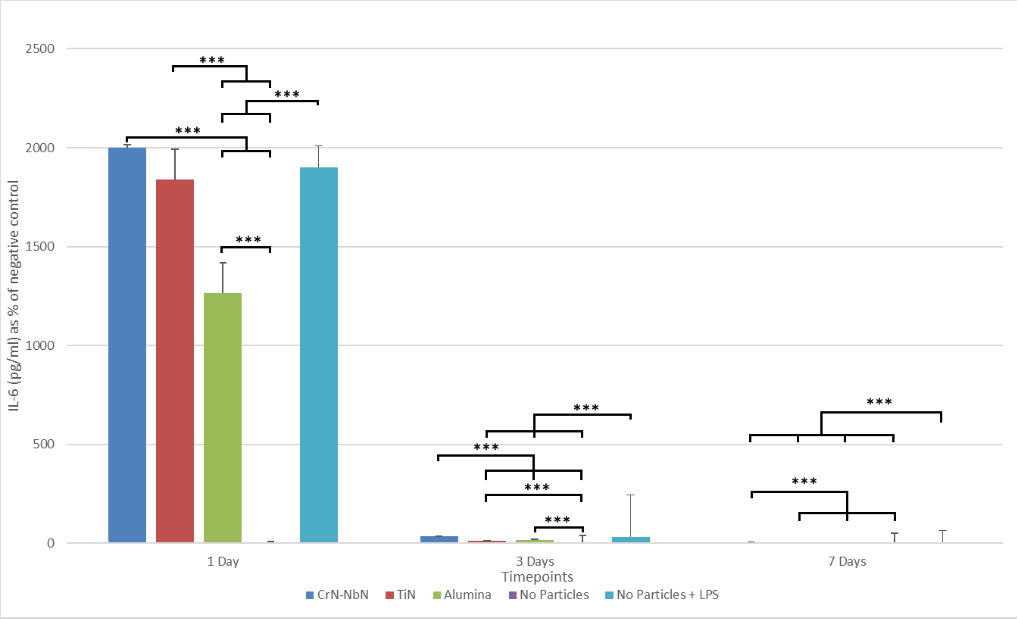

Figure 72. IL-6 release in pg/ml from J774A.1 macrophages cultured with particles of CrN-NbN coating, TiN, Al_2O_3, no particles and no particles + LPS on day 1, 3 and 7. For these results n=4 and error bars are the standard error of the mean, results were repeated once.

6.2.2.3 TNF-α Osteoblasts

The osteoblast TNF-α release in response to the CrN-NbN superlattice particles, TiN particles, alumina particles, and no particles can be seen in figure 73. The TNF-α release from osteoblasts in response to the materials shown here is similar to the TNF-α release in response to the coating materials seen in figure 50, with very little release of TNF-α and few significant differences in TNF-α release between materials. This likely indicates that, similarly to the previously mentioned results, the particles do not affect the release of TNF-α in osteoblasts.

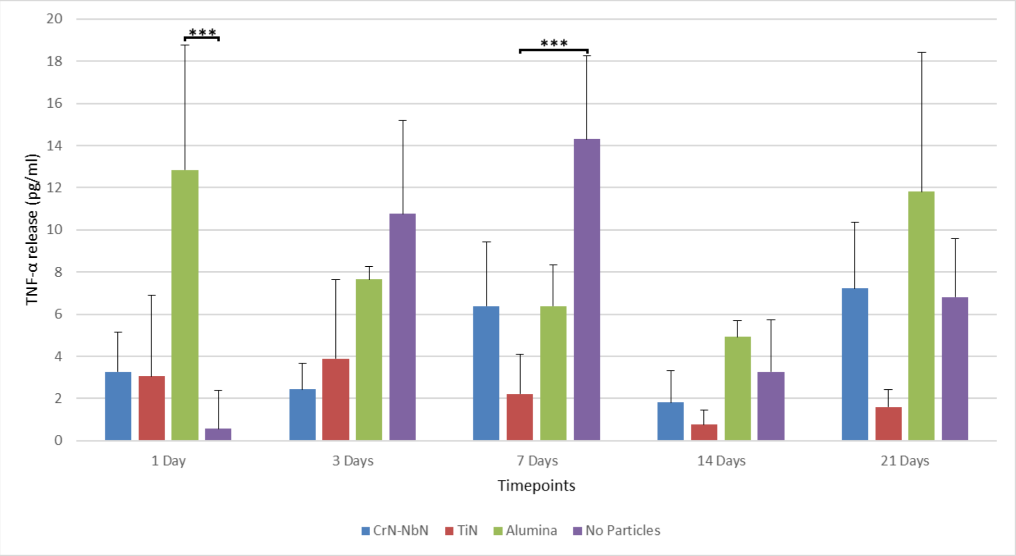

Figure 73. TNF-α release from osteoblasts in response to CrN-NbN, Alumina, TiN particles, and no particles at 1, 3, 7, 14, 21 days. For these results n=4 and error bars are the standard error of the mean, results were repeated once.

TNF-α release on day 1 shows higher release for Alumina when compared to all other materials although this is only significant when compared with no particles. CrN-NbN shows higher TNF-α release on day 1 when compared to TiN and no particles although neither of these are significant differences. TiN shows higher TNF-α release on day 1 compared to no particles however this is not significant.

Day 3 shows higher TNF-α release with no particles when compared to CrN-NbN, Alumina and TiN although this difference is not significant in any comparison. Release of TNF-α is higher on day 3 for Alumina when compared to TiN and CrN-NbN although this is not significant in either comparison. TiN shows higher TNF-α release when compared to CrN-NbN on day 3 although this difference is not significant.

TNF-α release on day 7 shows a greater release with no particles when compared to CrN-NbN, Alumina and TiN but this is only significant when compared to TiN. At day 7 TNF-α release by CrN-NbN was approximately equal to that of Alumina and both samples show higher release when compared to Al_2O_3, and TiN, although this not significant in either case.

Day 14 shows increased TNF-α release for Alumina when compared to all other samples although this was not significant for any comparison. Results for no particles showed higher TNF-α release at day 14 when compared to CrN-NbN and Al_2O_3 although this difference is not significant. CrN-NbN shows higher TNF-α release when compared to TiN on day 14 but this is not a significant difference.

TNF-α release at day 21 shows increased release for Alumina when compared to all other samples although this difference was not significant for any comparison. CrN-NbN shows higher TNF-α release at day 21 when compared to no particles and TiN although this was not a significant difference. Results for no particles showed an increase in TNF-α release on day 21 when compared to TiN although this is not significant.

The data is also shown as a percentage of the control in figure 74. While this follows the same pattern of few results being significantly different it does show a high initial release of TNF-α from osteoblasts in response to CrN-NbN particles, TiN particles, and alumina particles, when compared to the control.

This pattern is likely however a result of low overall release, resulting in a large margin of error.

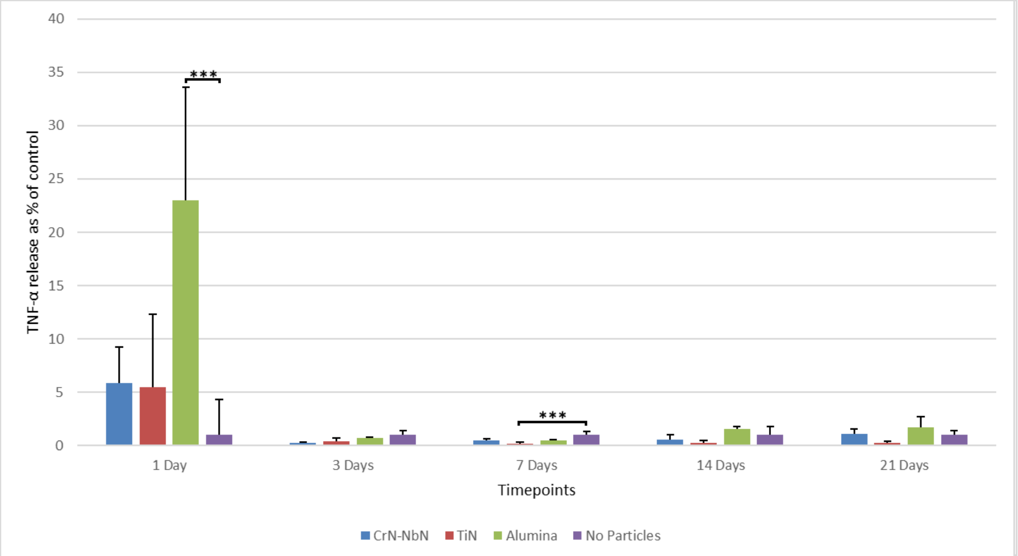

Figure 74. TNF-α release *as % of control from osteoblasts in response to CrN-NbN, Alumina, TiN particles, and no particles at 1, 3, 7, 14, 21 days. For these results n=4 and error bars are the standard error of the mean, results were repeated once.*

6.2.2.4 TNF-α Macrophages

The macrophage TNF-α release in response to the CrN-NbN superlattice particles, TiN particles, alumina particles, no particles, and no particles + LPS can be seen in figure 75. The TNF-α release from macrophages in response to these materials shows a high release from both CrN-NbN and samples with LPS at day 1. This is followed by a decrease to TNF-α release in line with the other materials which remains across day 3 and day 7, indicating that the TNF-α release in response to these materials is a short-lived response. TiN also shows an increased release at day 1 when compared to Alumina and samples without particles however this is not of the same magnitude as the release seen in response to CrN-NbN and LPS.

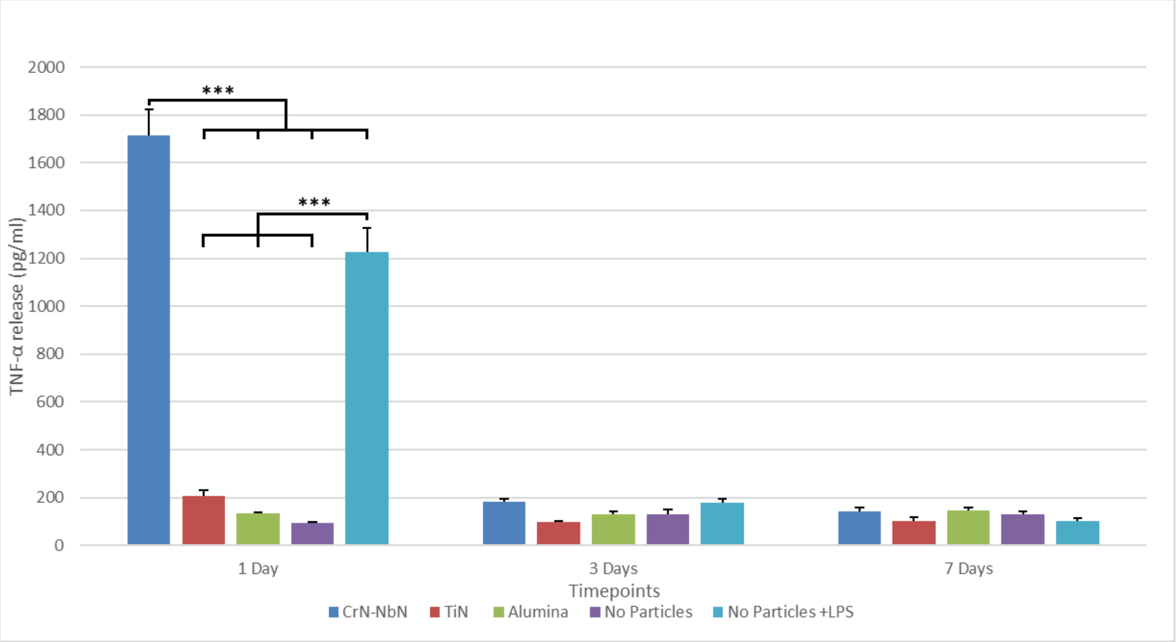

Figure 75. TNF-α release in pg/ml from J774A.1 macrophages cultured with particles of CrN-NbN coating, TiN, Al_2O_3, no particles and no particles + LPS on day 1, 3 and 7. For these results n=4 and error bars are the standard error of the mean, results were repeated once.

The TNF-α ELISA assay shows a large release of TNF-α at 1 day with both the CrN-NbN and no particles + LPS as can be seen in figure 75. The comparison materials and internal control, no particles, do not show this significant release of TNF-α within the first 24 hours. Following this first 24 hours period however the release of TNF-α is reduced and similar across all materials and controls.

TNF-α release at day 1 shows significantly increase release with CrN-NbN when compared to all other samples, including no particles + LPS which was used as a positive control. Results for no particles + LPS shows significantly increased TNF-α release at day 1 when compared to Alumina, TiN, and no particles. TiN shows higher TNF-α release at day 1 when compared to Alumina and no particles but this is not a significant difference. TiN shows increased TNF-α release at day 1 when compared to no particles but this is not a significant difference.

Day 3 shows higher TNF-α release for CrN-NbN when compared to all other samples although this is not significant for any comparison. Results for no particles + LPS shows a higher TNF-α release at day 3 when compared to Alumina, TiN, and no particles. Alumina shows higher TNF-α release at day 3 when compared to no particles and TiN although this was not significant in either case. Results for no particles showed increased TNF-α release at day 3 when compared to TiN although this is not a significant difference.

At day 7 higher TNF-α release is seen with Alumina when compared to all other samples, including no particles + LPS, this is however not significant for any comparison. CrN-NbN showed increased TNF-α release at day 7 compared to TiN, no particles, and no particles + LPS, this difference was not significant for any of the comparisons. TNF-α release at day 7 with no particles shows higher release than with TiN and no particles + LPS although this is not a significant difference. TiN shows increased TNF-α release at day 7 when compared to no particles + LPS though this difference is not significant.

The data is also shown as a percentage of the control in figure 76. This more clearly illustrates an increased TNF-α release from macrophages in response to TiN particles and alumina particles on day 1 when compared to no particles, though it is not to the same magnitude of increase as seen in response to CrN-NbN particles on day 1.

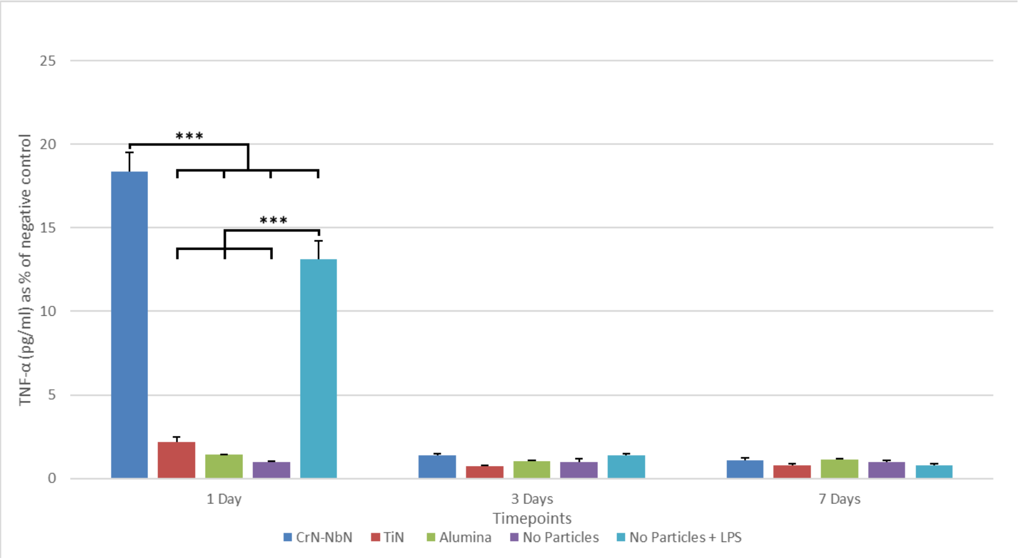

Figure 76. TNF-α **release** *as % of negative control from J774A.1 macrophages cultured with particles of CrN-NbN coating, TiN,* Al_2O_3*, no particles and no particles + LPS on day 1, 3 and 7. For these results n=4 and error bars are the standard error of the mean, results were repeated once.*

6.3 DISCUSSION

The metabolic activity results for the macrophages with particle laden media, shown in figure 67, show similar cell metabolic activity on day 1 between the CrN-NbN superlattice particles and the LPS, which could potentially be as a result of the release of TNF-α or IL-6 in response to the particles as the comparison and control materials have significantly lower metabolic activity at day 1 [209] [210]. At day 1 the CrN-NbN superlattice particles and LPS demonstrate significantly higher IL-6 release, as seen in figure 71, when compared to alumina particles and samples without particles, TiN particles however do show similarly high IL-6 release. The release of TNF-α for macrophages exposed to CrN-NbN superlattice particles or LPS however does show significant increase at day 1 when compared to the TiN and alumina particles and samples with no particles, as can be seen in figures 75 and 76. As high TNF-α release and high IL-6 release have been demonstrated at day 1 for both CrN-NbN superlattice particles and LPS, it is likely that this is the reason for the increased metabolic activity at day 1 for those samples, as seen in figure 67. The metabolic activity for both the CrN-NbN superlattice particles and the TCP + LPS remains steady across the time points while the others increase, the increase here is unlikely to be as a result of TNF-α and IL-6 causing proliferation as the same effect is seen in the sample with no particles and these samples do not show higher TNF-α or IL-6 release than the CrN-NbN superlattice particles or LPS which do not show these patterns.

The IL-6 release in response to particle laden media in macrophages, as shown in figure 71, shows significantly higher release for all materials when compared to samples with no particles, similar at day 1 to those of LPS. This is different when compared to findings in the literature, by Kaufman et al, which show significantly higher release (54.8-3000% increase depending on material) of IL-6 in response to LPS when compared to the response when exposed to particles. it is however important to note that particle sizes and concentrations differed between the work in the literature and the work presented here making a direct comparison difficult [193]. For all particles this decreases over the timepoints, from day 1 to day 7 there is a 38.7% decrease for CrN-NbN particles, a 98.9% decrease for TiN particles, and a 88.3% decrease for alumina particles, while the LPS remains relatively even by comparison, showing a 2.5% increase over the same time points. This consistent IL-6 release in response to LPS is supported by the literature, indicating a slowly building release over 48 hours, up to a concentration of 15,000 pg/ml, shown by Jakobsen et al and Naha et al, while a short-lived IL-6 release, reaching a maximum of 450 pg/ml at 24 hours, was seen in response to particles [211] [212]. Overall, the response for CrN-NbN particles appears to show a higher IL-6 release when compared to the other particles.

The TNF-α release in response to particle laden media in macrophages, as shown in figure 75, in response to CrN-NbN superlattice particles shows a significant release on day 1 before the TNF-α release falls to similar levels as the other materials. The release here is higher than the release for the positive control for inflammation indicating a significant cytokine release response and reinforcing the results from the IL-6 cytokine assay. This TNF-α release in response to particles aligns with the concentrations found in the literature (between 500-7500 pg/ml), demonstrated by Petit et al, Huk et al, and Catelas et al, although the exact concentration appears to vary based on concentration of particles and cells, this appears to be in a dose dependent manner with increasing TNF-α release in response to increasing particle concentration [213] [214] [215]. The immediate drop in release is also seen in the positive control for inflammation indicating that TNF-α release is a short-lived response to particles and LPS. This response was however not clear in all studies, with the release of TNF-α remaining steady or increasing between 24 hours and 48 hours in some studies, such as those of Wu et al and Liu et al, indicating decreases of approximately 4% or an increase of 21% respectively , with no 72 hour timepoint, while others showed a significant drop in TNF-α release between 24-48 hours, such as the work of Naha et al, showing an approximate decrease of 50%, while others showed a decrease between 48-72 hours, shown by Huk et al which shows a decrease of approximately 18% [216] [217] [212] [214]. The literature on the change of TNF-α release from macrophages in response to particles from 24-72 hours is sparse, with many studies being either a single timepoint or stopping at 48 hours. This unfortunately makes it impossible to draw a reasonable conclusion from the literature to compare this drop in TNF-α release between 24 and 72 hours to. This transient release of TNF-α however may be to prevent damage that could be caused by extended activation of the NF-κB pathway caused by prolonged TNF-α release. Extended release of TNF-α may result in significant osteolysis through osteoclastogenesis, regulated through increased RANKL expression.

The cytotoxicity results for the osteoblasts with particle laden media, as shown in figure 68, shows higher metabolic activity on day 1 for the CrN-NbN superlattice particles. It is possible that this is a result of decreased IL-6 release when compared to the other materials, as seen in figures 69 and 70, as it has been shown, by Li et al, that IL-6 reduces osteoblast proliferation, reducing cell number increase by approximately 15% over 3 days, at a concentration of 1ng/ml [218]. TNF-α at low doses, as seen in figures 73 and 74, has been shown to increase proliferation in osteoblasts, up to 25% at a concentration of 3pM, as demonstrated by Frost el al [219]. This is however unlikely to have had an overall effect on the proliferation or metabolic activity for the osteoblasts as no significant difference to the TNF-α release between materials was observed. Over many of the timepoints CrN-NbN particles show increased metabolic activity when compared to other test materials. At 14 days and 21 days the metabolic activity is similar to that of TCP but higher than that of the comparison materials.

The IL-6 release in response to particle laden media in osteoblasts, as shown in figure 69, shows higher release on later days for CrN-NbN particles when compared to the comparison materials apart from samples with no particles.

The TNF-α release in response to particle laden media in osteoblasts, as shown in figure 73, shows no significant pattern across the timepoints for many of the materials. The levels of release of TNF-α in response to particles from osteoblasts are very similar to the levels found in response to the coating materials. This would indicate that TNF-α release in osteoblasts is not significantly affected by the particles. This is in line with the above discussion point of TNF-α being expressed on the cell surface of osteoblasts as opposed to being released as seen in the literature, shown by Crémet et al [199].

Overall, this indicates that the CrN-NbN particles characterised are more likely to cause the release of inflammatory cytokines, IL-6 and TNF-α, than comparison particles when used in the same volume in vitro. As the CrN-NbN superlattice coating wears less than the comparison materials, with a wear rate of 1.3mg per 1 million cycles for the CrN-NbN when compared to 4.27mg per million cycles shown for titanium nitride pairings, demonstrated by Weisenburger et al, or 3.8-19mg per million cycles for alumina pairings, demonstrated by Nevelos, this may result in an overall lower inflammatory response in vivo [16] [93].

Using this as a guideline and we would expect approximately 3.25 times the weight of the CrN-NbN superlattice particles produced for TiN and 8.75 times the weight of the CrN-NbN superlattice particles produced for alumina. This results in an approximate IL-6 release from macrophages in response to the CrN-NbN superlattice particles to be 33% of that expected for TiN particles and 18% of that expected for alumina particles at day 1. This would indicate the potential for a significant reduction in IL-6 release compared to TiN and alumina. An approximation of TNF-α release from macrophages in response to the CrN-NbN superlattice particles would be 250% of that expected in response to TiN and 150% of that expected in response to alumina. This is still a significant increase in TNF-α release when compared to TiN and alumina.

Overall, this approximation would indicate that the potential for IL-6 release is likely lower when using the CrN-NbN superlattice coating as the bearing surface in vivo, while TNF-α release is likely to be higher. As IL-6 induces osteoclast differentiation and proliferation, through upregulation of RANKL leading to activation of NF-κB, it is reasonable to expect a reduction in osteoclast activity as a result, although IL-6 alone has been shown, by Fisher and Ingham, and Vermes, to not be responsible for late aseptic loosening [26] [11]. The increase in TNF-α release is likely to increase RANKL expression and through that increase osteoclast activity, by increased activation of NF-κB, and decrease osteoblast differentiation, through multiple factors such as inhibition of insulin-like growth factor (IGF-1) and inhibition of Runx2, as demonstrated by Purdue et al and Vermes et al [21] [27] [220]. As both IL-6 and TNF-α act to increase osteoclast activity, through RANKL upregulation, it is unclear on how decreasing IL-6 release while increasing TNF-α release would affect osteoclast activity in vivo. It is clear however that the increase in potential TNF-α release from macrophages in response to CrN-NbN superlattice particles would result in a decrease in osteoblast activity, as shown by Vermes et al [27].

Late aseptic loosening has been shown to be a serious issue in the efficacy and longevity of total join arthroplasties. There are several possible causes for this though wear debris as a root cause of late aseptic loosening has significant evidence in favour of it [18] [22] [21]. Therefore, wear resistant coatings such as the CrN-NbN superlattice coating are of significant interest in developing total joint replacements with an increased lifespan.

It has been shown that the rate of wear of a joint replacement has an effect on the lifespan of that joint replacement, with lower wear rates resulting in a lower failure rate through late aseptic loosening [21]. This has resulted in significant research into lower wearing materials and material pairings for total joint replacements [1] [3] [11]. One of the areas of research has involved metal-on-metal pairings and ceramic-on-ceramic pairings with these materials showing lower wear rates than the traditional metal-on-polymer or ceramic-on-polymer pairings [1] [3].

The metal-on-metal pairings show promising wear rates, 100 times lower than those of metal-on-UHMWPE [20]. Despite this promising wear rate, the metal-on-metal pairings suffer from several issues that has resulted in them falling out of favour with significantly fewer metal-on-metal pairings being used in the past few years when compared to the peak a decade ago [6].

The ceramic-on-ceramic pairings appear more promising than the metal-on-metal, having a wear rate approximately 50 times lower than that of metal-on-metal pairings [1]. They also are significantly less susceptible to ion leaching when compared to metal-on-metal pairings [221]. They are however not without issue, they are at risk of fast fracture, chipping and squeaking.

One method of improving on these two types of pairings is to produce coated metal-on-metal pairings. This results in a ceramic wearing surface without the risk of fast fracture as seen in ceramic-on-ceramic [21]. This also reduces the metal ion release from the material as the wear debris produced will be primarily the coating, though there is evidence of wear debris originating from other surfaces of the joint replacement [23]. Coating methods are however not without their own problems as they may fail due to delamination of the coating material from the substrate [92] [222]. This delamination can then lead to increased wear rates as a result of third body wear [19].

The CrN-NbN superlattice coating produced through the HIPIMS method offers a good solution to this issue of delamination through improved coating adhesion [223] [84]. This coating adhesion is improved by an intermediate layer between the substrate and the coating, formed through an etching step that results in the sub-plantation of metal ions into the substrate [87]. This improved coating adhesion and the improved wear rates of the CrN-NbN superlattice coating make it an excellent candidate for improving the longevity of total joint replacements.

There were other routes for investigation through both different cytokines to investigate and other cell lines or culture configurations. One cytokine that could have been investigated is IL-1β, which is released by monocytes in response to particles and has been demonstrated to be expressed at elevated concentrations surrounding failed prosthesis [118] [116].

Another possible cytokine for investigation is OPG which acts as a decoy to RANKL by binding to it, inhibiting RANKL function and regulating osteoclast maturation [21]. If OPG were to be investigated, then this would need to be coupled with investigation of RANKL release as the signalling of the two cytokines is linked. Investigating this would provide insight into the regulation of osteoclast maturation as a result of exposure to the particles of CrN-NbN.

PGE_2 was also an option for investigation, it has been found to be expressed by macrophages near the implant site and reduces the expression of procollagen α1 [11] [26]. Investigation of this cytokine would provide insight into regulation of osteoblast function and may be paired well with investigation of RANKL and OPG as part of an investigation of the effect of the particles on osteoblast and osteoclast function.

The investigation used osteoblasts and macrophages although there are other cell lines that play parts in late aseptic loosening and could provide alternate routes for investigation. Osteoclasts for instance play a large part in late aseptic loosening, as the primary cells involved in bone resorption. These however pose some complications in culturing when compared to other cells as they are multinucleated cells usually derived from osteoclast precursor cells. Culturing them requires the addition of RANKL and M-CSF to the media, which makes investigating the release of RANKL in response to particles from them more complicated.

Fibroblasts may also be a cell type worth investigation as they have been shown to produce inflammatory cytokines, such as TNF-α and IL-6, in response to wear debris [27]. They are also the cells that degrade the bone matrix, as such investigation into the activity of fibroblasts may be useful in observing the affect of particles on the potential degradation of the bone matrix.

Lymphocytes are also a cell type that may be involved in late aseptic loosening although this is disputed. Lymphocytes have been found to have infiltrated the periprosthetic space and are capable of releasing both RANKL and OPG, indicating some regulation of osteoclastogenesis, however, osteolysis in response to particles has still been observed in mice without lymphocytes, indicating that they do not play a major role in late aseptic loosening [21].

Co-cultures are also something to be considered as they allow for signalling between two different cell lines to affect each other. This would provide us with insight into the interaction between macrophages and osteoblasts or any of the cell types listed above. In the case of this work it may be necessary to use a different macrophage cell line to ensure that the difference in species does not result in interactions that otherwise wouldn't occur, one possible cell line would be monocytic cell line THP-1.

It is also possible to co-culture more than just two cell lines, which may be of benefit to observe the interaction between macrophages, osteoblasts, and osteoclasts, although this poses some problems surrounding ensuring osteoclast formation while maintaining a macrophage cell line as macrophages can act as osteoclast precursors. There is some added complication with culturing multiple cell lines, as they will have differing nutrient requirements and growth rates. Co-culturing would provide some significant benefits in allowing the cell types to affect each other; however, it is not without significant complication.

7 COMPARISON

The characterisation of the CrN-NbN superlattice material in both coating and particle form showed differing results, particularly in the cell response to the material.

There are few comparisons to be made between coating and particles for non-cell culture characterisation, however a comparison of the Nb-Cr ratio is possible. This shows good agreement between the two, with the coating demonstrating a Nb:Cr ratio of 1:2.72, as demonstrated in table 6, and the particles demonstrating a Nb:Cr ratio of 1: 2.39, as demonstrated in table 18. This indicates that the ratio of Nb:Cr is similar throughout the coating.

There are many comparisons to be made in the cytotoxicity and cytokine assays for CrN-NbN in both coating and particle form. The metabolic activity in macrophages in response to the CrN-NbN as a coating shows increasing metabolic activity and remains significantly higher than the negative control across all time points, as seen in figure 44. In comparison the metabolic activity in macrophages in response to CrN-NbN as particles shows decreasing metabolic activity across all time points and is not significantly different from the negative control at day 7, as can be seen in figure 67. This difference could potentially be due to increased initial metabolic activity in response to the CrN-NbN particles as a result of phagocytosis of the particles, this would slowly decrease as the particles are phagocytosed.

The metabolic activity in osteoblasts in response to the CrN-NbN coating and particles show some early differences but both plateau at day 7, as can be seen in figures 45 and 68. At day 1 and 3 however the metabolic activity is significantly lower in response to the CrN-NbN coating when compared to TCP, however it is the other way around in response to CrN-NbN particles, showing higher metabolic activity when compared to no particles. This is possibly due to phagocytosis of the cells, as osteoblasts have been shown to phagocytose wear particles [26] [25].

The cytokine release assays indicate a significant difference in the cell reaction to the CrN-NbN as a coating when compared to CrN-NbN as a particle. These differences are mostly as would be expected, with particles in the range 0.1-10 µm typically being in the size range for phagocytosis by macrophages and osteoblasts and causing macrophage activation and the release of inflammatory cytokines [22] [26] [27].

The release of IL-6 by osteoblasts is a clear example of the particle size affecting the release of cytokines. There is no significant difference between any samples for the release of IL-6 from osteoblasts in response to any of the coating materials, as can be seen in figure 46. It can however be seen in figure 69 that the presence of some particles affects the release of IL-6 from osteoblasts. While the comparison materials, TiN and alumina, demonstrated significant increases in IL-6 release when compared to CrN-NbN and no particles on day 1 and significant decreases for all other timepoints, CrN-NbN particles did not show a significant difference in IL-6 release from osteoblasts when compared to no particles.

This difference in cytokine release between coating and particles is seen again in the IL-6 release by macrophages in response to the CrN-NbN coating and particles. With the coatings showing no significant differences between any of the comparisons and negative control, as seen in figure 48b. This is in contrast to the significant increase in IL-6 release for all particles when compared to no particles on days 1 and 3, as seen in figure 71. This significant increase in IL-6 release also is seen on day 7 when comparing the CrN-NbN particles to no particles. This indicates that macrophages release IL-6 in response to these particles, with IL-6 release from the CrN-NbN particles being a longer lasting effect than that caused by TiN or alumina.

There is very little difference in the TNF-α release by osteoblasts in response to the CrN-NbN as either a coating or particles, as seen in figures 50 and 73. These results also show little significance in results which likely indicates that TNF-α is not released by osteoblasts in response to particles or the coating.

The TNF-α release from macrophages in response to CrN-NbN particles and coatings shows a significant difference on day 1, as can be seen in figures 52 and 75. This shows significantly higher TNF-α release from macrophages in response to CrN-NbN particles at day 1 when compared to the comparison materials, no particles, and the positive control for inflammation (LPS). This is in contrast to the response to the response to CrN-NbN coating which showed no significant difference in TNF-α release from macrophages.

These comparisons show a differing reaction to the CrN-NbN superlattice particles when compared to the CrN-NbN superlattice coating. The CrN-NbN particles result in increased release of cytokines from macrophages when compared to the coating, although the same is not observed in osteoblasts.

8 CONCLUSIONS

This thesis has shown characterisation of the CrN-NbN superlattice coating structure and chemistry. The CrN-NbN superlattice coating showed NbN was the surface layer on all coatings although it showed heavy oxidation, being comprised mostly of niobium oxides and oxynitrides. There is also evidence of the CrN layer below this being oxidised though not to the same extent. This oxidation was not increased as a result of exposure to cell culture medium, indicating that there is likely a passivating layer of a chromium oxide, likely Cr_2O_3. The CrN-NbN superlattice coating showed a layer size of 6nm for both CrN and NbN.

The production of CrN-NbN superlattice particles that while not identical to the wear that may be produced in vivo by coatings, were of a close size range to typical wear particles produced by ceramic materials and generally larger than those expected from coatings. The morphology of the CrN-NbN superlattice particles also followed closely with those seen in ceramic materials. It was not possible to compare the CrN-NbN superlattice particle morphology to that of wear particles produced from coatings as the literature on the morphology of wear particles produced from coatings is sparse. An ideal comparison would be to those produced through hip simulations.

The CrN-NbN superlattice coating demonstrated a bubble-like texture on the surface, very similar to other HIPIMS produced coatings. There several structures on the surface of the CrN-NbN superlattice coating were observed: pits, droplets, and seams. The origin of the droplets was seen to be niobium inclusions in the coating that nucleate a droplet as the coating is deposited on top. These droplets are then likely to produce the pits through pull-out of the droplet as a result of poor coating cohesion around the droplet and increasing compressive stress as the coating is deposited. The seams appear to occur as a result of scratches on the substrate as the coating is deposited perpendicular to the surface, maintaining, and exacerbating the appearance of the scratch.

The chosen method of thermal shock followed by agate grinding of the CrN-NbN superlattice coating was an adequate method to produce wear particles. This methodology did not suffer from the same steel contamination that ball-milling of a coated ball mill suffered from. This method also allowed for the production of the CrN-NbN superlattice particles in significant concentrations, allowing for sufficient cell culture analysis.

The CrN-NbN superlattice particles produced were observed to be under 10 µm and polygonal, with many showing the columnar structure of the coating. These particles were large enough that they comprised of both the CrN and NbN layers and both were found in the majority of particles.

A suitable concentration of particles for in vitro investigations was found at 4.81mg/ml. Inflammatory studies and analysis through the release of IL-6 and TNF-α showed no significant impact from the CrN-NbN superlattice coating on the release of these cytokines from macrophages or osteoblasts. These studies did, however, demonstrate a significantly increased release of TNF-α release from macrophages in response to the CrN-NbN superlattice particles when compared to particles of TiN or alumina. An increase in IL-6 release was also observed in macrophages in response to CrN-NbN superlattice particles in comparison to TiN and alumina, although the effect of this was not as pronounced as the increased release of TNF-α. This increase may be a result of the NF-κB signalling pathway being activated by the increased TNF-α release, although this would need to be investigated to confirm if this was an effect of the particles or the TNF-α. There was however no significant evidence of cytotoxicity found in either the CrN-NbN superlattice coating material or particles of that coating.

The potential for the CrN-NbN superlattice coating to cause late aseptic loosening appears similar to that of other coating materials if the lower wear rate is considered, although this is through increased TNF-α release and lower IL-6 release when compared to other materials. The potential for adverse soft tissue reactions appears limited as there is no evidence of cytotoxicity, however the significantly increased TNF-α release may indicate a potential inflammatory response to the material.

It has been observed that the CrN-NbN superlattice coatings have an upper surface consisting of NbN that has oxidised along with a partially oxidised CrN layer below it, indicating a passivating layer of Cr oxides forms, likely responsible for the corrosion resistance of the coating. The layers of the CrN-NbN superlattice have been observed to be approximately 6 nm and consistent for both the CrN and NbN layers. The surface of the CrN-NbN superlattice coating was shown to contain pits, droplets and seams as a result of the coating process, these features could be reduced through changing of the coating process parameters. The CrN-NbN superlattice coating was shown to not be considered to be cytotoxic and did not cause significantly higher release of IL-6 or TNF-α from macrophages or osteoblasts when compared to TiN or CoCr. Simulated wear particles of the CrN-NbN superlattice were generated through thermal shock and showed granular and columnar morphologies with sizes < 10 µm. The simulated wear particles of CrN-NbN were shown to not be considered cytotoxic, they did however result in higher release of IL-6 and TNF-α from macrophages when compared to TiN and alumina in the same particle concentration. The CrN-NbN superlattice coating has potential as a biomaterial for the bearing surface of total joint replacements. This is largely based on the low wear rate of the CrN-NbN superlattice coating at 1.3mg per million cycles in comparison to other bearing surface materials, such as TiN at 4.27mg per million or 3.8-19mg per million cycles for alumina pairings, and the corrosion resistance of the CrN-NbN superlattice coating.

9 FUTURE WORK

There is potential room for further cell culture work involving the wear particles produced through hip simulations as these wear particles would be more accurate to the wear debris that would be produced by the implants. This would give a more accurate measure of the cell response to the wear particles produced in vivo.

It would also be of interest to compare the wear volumes produced by the joint replacements with different coatings and materials in direct comparison to the CrN-NbN superlattice coating. This would allow for a comparison of the CrN-NbN superlattice coating and common bearing surface materials with differing volumes that would reflect the likely wear debris concentrations from the implants in vivo.

One area of further work that would be beneficial would be to measure the activation of NF-κB in response to the CrN-NbN superlattice coating and particles. NF-κB plays a role in several of the pathways discussed previously, playing a key role in osteoclast maturation and a role in the function of macrophages [21]. It has been shown that mice lacking NF-κB have defective macrophages and become osteopetrotic as they cannot produce functional osteoclasts [21]. It has also been shown that wear particles result in the activation of NF-κB in osteoclasts, osteoblasts, and macrophages [21] [26]. The mechanism for this NF-κB activation appears to be through activation of protein tyrosine kinases leading to translocation of NF-κB to the nucleus of the cells [27].

It can also be seen that many of the cytokines involved in late aseptic loosening affect the activation of NF-κB. RANKL acts directly on the receptor activation of NF-κB (RANK), leading to the activation of NF-κB [27]. IL-6 has been shown to lead to an upregulation of RANKL which means an increase in IL-6 will indirectly lead to increased NF-κB activation [27]. It has been shown that TNF-α produces the same NF-κB complex as titanium particles in osteoblasts [27]. This activation of NF-κB links together a significant proportion of the late aseptic loosening response and may provide a better way to measure this response in vitro.

The intracellular signalling in the NF-κB pathway may be a good way to measure this pathways activation through various routes. This could potentially be measured through the activity of IκB kinase (IKK), which activates NF-κB through phosphorylation of the IκBα protein on the NF-κB, causing it to dissociate from the NF-κB.

Other signalling pathways and intracellular signalling may be of benefit to investigate further to the NF-κB signalling pathway such as the MAPK pathway, which regulates cell differentiation, proliferation, and apoptosis and can be activated by wear debris.

Improving the manufacturing techniques for the CrN-NbN superlattice to remove the surface features would also be of potential benefit. These surface features represent a significant increase in the roughness of the surface, reducing the wear properties of the material. The droplets are also a potential source of wear debris and so wear rates may be further improved by reducing the incidence of droplets in the coating. Removal of these features would also improve the corrosion resistance of the coating.

References

[1] A. Essner, K. Sutton and A. Wang, “Hip simulator wear comparison of metal-on-metal, ceramic-on-ceramic and crosslinked UHMWPE bearings.,” *Wear,* vol. 259, no. 7-12, pp. 992-995, 2005.

[2] J.L.Tipper, “Characterisation of wear debris from UHMWPE on zirconia ceramic metal on metal and alumina ceramic on ceramic hip prostheses generated in a physiological anatomical hip joint simulator,” *Wear ,* vol. 250, no. 1-12, pp. 120-128, 2001.

[3] I. C. Clarke, V. Good, P. Williams, D. Schroeder, L. Anissian, A. Stark, H. Oonishi, J. Schuldies and G. Gustafson, “Ultra-low wear rates for rigid-on-rigid bearings in total hip replacements,” *Proceedings of the Institution of Mechanical Engineers, Part H: Journal of Engineering in Medicine,* vol. 214, no. 4, pp. 331-347, 2000.

[4] B. Arroll and F. Goodyear-Smith, “Corticosteroid injections for osteoarthritis of the knee: meta-analysis BMJ. 328 (7444): 869.,” *BMJ,* vol. 328, p. 869, 2004.

[5] K. S. Katti, “Biomaterials in total joint replacement,” *Colloids and Surfaces B,* vol. Biointerfaces, no. 39, pp. 133-142, 2004.

[6] Y. Ben-Shlomo, A. Blom, C. Boulton, R. Brittain, E. Clark, R. Craig, S. Dawson-Bowling, K. Deere, C. Esler, A. Goldberg, C. Gregson, P. Howard and L. Hunt, “The National Joint Registry 16th Annual Report 2019,” *National Joint Registry,* 2020.

[7] G. Tsikandylakis, M. Mohaddes, P. Cnudde, A. Eskelinen, J. Kärrholm and a. O. Rolfson, “Head size in primary total hip arthroplasty,” *EFORT Open Rev,* vol. 3, no. 5, pp. 225-231, 2018.

[8] J. R. H. Foran, “Total Hip Replacement - OrthoInfo - AAOS,” American Academy of Orthopaedic Surgeons, [Online]. Available:

https://orthoinfo.aaos.org/en/treatment/total-hip-replacement. [Accessed 8 2 2023].

[9] A. J. Smith, D. J. Wood and M.-G. Li, “Total knee replacement with and without patellar resurfacing,” *The Journal of Bone and Joint Surgery. British volume,* Vols. 90-B, no. 1, 2008.

[10] J. R. H. Foran, “Total Knee Replacement - OrthoInfo - AAOS,” American Academy of Orthopaedic Surgeons, [Online]. Available: https://orthoinfo.aaos.org/en/treatment/total-knee-replacement/. [Accessed 8 2 2023].

[11] J. Fisher and E. Ingham, “Biological reactions to wear debris in total joint replacement.,” *Proceedings of the Institution of Mechanical Engineers, Part H: Journal of Engineering in Medicine,* vol. 214, no. 1, pp. 21-37, 2000.

[12] P. E. Hovsepian, A. Ehiasarian, Y. Purandare, B. Biswas, F. Pérez, M. Lasanta, M. d. Miguel, A. Illana, M. Juez-Lorenzo, R. Muelas and A. Agüero, “Performance of HIPIMS deposited CrN/NbN nanostructured coatings exposed to 650 °C in pure steam environment,” *Material Chemistry and Physics,* vol. 179, pp. 110-119, 2016.

[13] Z. Biomet, *Personal Correspondence,* 2015.

[14] V. Saikko, T. Ahlroos, O. Calonius and J. Keränen, “Wear simulation of total hip prostheses with polyethylene against CoCr, alumina and diamond-like carbon,” *Biomaterials,* vol. 22, pp. 1507-1514, 2001.

[15] S. L. Smith, D. Dowson and A. A. J. Goldsmith, “The effect of femoral head diameter upon lubrication and wear of metal-on-metal total hip replacements,” *Proceedings of the Institution of Mechanical Engineers, Part H: Journal of Engineering in Medicine,* vol. 215, no. 2, 2001.

[16] J. Weisenburger, S. Hovendick, K. Garvin and H. Haider, “A883. HOW DURABLE ARE TITANIUM NITRIDE COATINGS ON TOTAL HIP REPLACEMENTS?,” *Orthopaedic Proceedings,* Vols. 93-B, 2018.

[17] N. Gougoulias, A. Khanna and N. Maffulli, “How Successful are Current Ankle Replacements?: A Systematic Review of the Literature,” *Clinical Orthopaedics and Related Research,* vol. 468, no. 1, pp. 199-208, 2010.

[18] T. Karachalios, G. Komnos and A. Koutalos, “Total hip arthroplasty: Survival and modes of failure,” *EFORT Open Reviews,* vol. 3, no. 5, p. 232–239, 2018.

[19] A. Unsworth and S. C. Scholes, “The tribology of metal-on-metal total hip replacements.,” *Proceedings of the Institution of Mechanical Engineers, Part H: Journal of Engineering in Medicine,* vol. 220, no. 2, pp. 183-194, 2006.

[20] S. C. Scholes, S. M. Green and A. Unsworth, “"The wear of metal-on-metal total hip prostheses measured in a hip simulator.",” *Proceedings of the Institution of Mechanical Engineers, Part H: Journal of Engineering in Medicine,* vol. 215, no. 6, pp. 523-530., 2001.

[21] P. E. Purdue, P. Koulouvaris, B. J. Nestor and T. P. Sculco, “The central role of wear debris in periprosthetic osteolysis.,” *HSS J,* vol. 2, no. 2, pp. 102-113, 2006.

[22] Y. Abu-Amer, I. Darwech and J. C. Clohisy, “Aseptic loosening of total joint replacements: mechanisms underlying osteolysis and potential therapies,” *Arthritis Research & Therapy,* vol. 9, no. S6, 2007.

[23] A. S. Shanbhag, “Composition and morphology of wear debris in failed uncemented total hip replacement.,” *Journal of Bone and Joint Surgery ,* vol. 76B, no. 1, pp. 60-67, 1994.

[24] A. P. Elfick, S. L. Smith, S. M. Green and A. Unsworth, “The quantitative assessment of UHMWPE wear debris produced in hip simulator testing: the influence of head material and roughness, motion and loading.,” *Wear,* vol. 249, no. 5-6, pp. 517-527, 2001.

[25] C. H. Lohmann, “Phagocytosis of wear debris by osteoblasts affects differentiation and local factor production in a manner dependent on particle composition.,” *Biomaterials ,* vol. 21, no. 6, pp. 551-561, 2000.

[26] C. Vermes, “The effects of particulate wear debris cytokines and growth factors on the functions of mg63 osteoblasts,” *The Journal of Bone and Joint Surgery ,* vol. 83A, no. 2, pp. 201-211, 2001.

[27] C. Vermes, T. T. Glant, N. J. Hallab, E. A. Fritz, K. A. Roebuck and J. J. Jacobs, “The potential role of the osteoblast in the development of periprosthetic osteolysis: Review of in vitro osteoblast responses to wear debris, corrosion products, and cytokines and growth factors,” *The Journal of Arthroplasty,* vol. 16, no. 8, pp. 95-100, 2001.

[28] A. L. Galvin, J. L. Tipper, E. Ingham and J. Fisher, “Nanometre size wear debris generated from crosslinked and non-crosslinked ultra high molecular weight polyethylene in artificial joints,” *Wear,* vol. 259, no. 7-12, pp. 977-983, 2005.

[29] A. Shanbhag, J. Jacobs, T. Glant, J. Gilbert, J. Black and J. Galante, “Composition and morphology of wear debris in failed uncemented total hip replacement,” *The Journal of Bone and Joint Surgery,* Vols. 76-B, no. 1, 1994.

[30] W. S, T. JL, I. E, S. MH and F. J, “In vitro analysis of the wear, wear debris and biological activity of surface-engineered coatings for use in metal-on-metal total hip replacements,” *Proceedings of the Institution of Mechanical Engineers, Part H: Journal of Engineering in Medicine,* vol. 217, no. 3, pp. 155-163, 2003.

[31] P. F. Doorn, P. A. Campbell, J. Worrall, P. D. Benya, H. A. McKellop and H. C. Amstutz, “Metal wear particle characterization from metal on metal total hip replacements: Transmission electron microscopy study of periprosthetic tissues and isolated particles,” *Journal of Biomedical Materials Research,* vol. 42, no. 1, pp. 103-111, 1998.

[32] A. Hatton, J. Nevelos, A. Nevelos, R. Banks, J. Fisher and E. Ingham, “Alumina–alumina artificial hip joints. Part I: a histological analysis and characterisation of wear debris by laser capture microdissection of

tissues retrieved at revision," *Biomaterials,* vol. 23, no. 16, pp. 3429-3440, 2002.

[33] E. Oral, A. S. Malhi, K. K. Wannomae and O. K. Muratoglu, "HIGHLY CROSSLINKED UHMWPE WITH IMPROVED FATIGUE RESISTANCE FOR TOTAL JOINT ARTHROPLASTY," *J Arthroplasty,* vol. 23, no. 7, pp. 1037-1044, 2008.

[34] J. Olofsson, T. M. Grehk, T. Berlind, C. Persson, S. Jacobson and H. Engqvist, "Evaluation of silicon nitride as a wear resistant and resorbable alternative for total hip joint replacement," *Biomatter,* vol. 2, pp. 94-102, 2012.

[35] M. Pettersson, S. Tkachenko, S. Schmidt, T. Berlind, S. Jacobson, L. Hultman, H. Engqvist and C. Persson, "Mechanical and tribological behavior of silicon nitride and silicon carbon nitride coatings for total joint replacements," *Journal of the Mechanical Behavior of Biomedical Materials,* vol. 25, pp. 41-47, 2013.

[36] A. Shenhar, I. Gotman, S. Radin, P. Ducheyne and E. Gutmanas, "Titanium nitride coatings on surgical titanium alloys produced by a powder immersion reaction assisted coating method: residual stresses and fretting behavior," *Surface and Coatings Technology,* vol. 126, no. 2-3, pp. 210-218, 2000.

[37] P. J. Firkins, "A novel low wearing differential hardness ceramic on metal hip joint prosthesis.," *Journal of Biomechanics ,* vol. 34, no. 10, pp. 1291-1298, 2001.

[38] L. A. Pruitt, F. Ansari, M. Kury, A. Mehdizah, E. W. Patten, J. Huddlestein, D. Mickelson, J. Chang, K. Hubert and M. D. Ries, "Clinical trade-offs in cross-linked ultrahigh-molecular-weight polyethylene used in total joint arthroplasty," *J Biomed Mater Res Part B,* vol. 101B, p. 476–484., 2013.

[39] J. Fu, Z.-M. Jin and J.-W. Wang, UHMWPE Biomaterials for Joint Implants: Structures, Properties and Clinical Performance, Springer, 2019.

[40] P. Prokopovich, “Interactions between mammalian cells and nano- or micro-sized wear particles: Physico-chemical views against biological approaches,” *Advances in Colloid and Interface Science,* vol. 213, pp. 36-47, 2014.

[41] S. M. Kurtz, The UHMWPE Handbook: Ultra-High Molecular Weight Polyethylene in Total Joint Replacement, Elsevier, 2004.

[42] A. A. Khalifa and H. M. Bakr, “Updates in biomaterials of bearing surfaces in total hip arthroplasty,” *Arthroplasty,* vol. 3, no. 32, 2021.

[43] S. Santavirta, Y. Konttinen, R. Lappalainen, A. Anttila, S. Goodman, M. Lind, L. Smith, M. Takagi, E. Gómez-Barrena, L. Nordsletten and J.-W. Xu, “Materials in total joint replacement,” *Biomechanics,* vol. 12, pp. 51-57, 1998.

[44] L. A. Pruitt, “Deformation, yielding, fracture and fatigue behavior of conventional and highly cross-linked ultra high molecular weight polyethylene,” *Biomaterials,* vol. 26, no. 8, pp. 905-915, 2005.

[45] W. H. Harris and O. K. Muratoglu, “A Review of Current Cross-linked Polyethylenes Used in Total Joint Arthroplasty,” *Clinical Orthopaedics and Related Research,* vol. 430, pp. 46-52, 2005.

[46] I. Pleşa, P. V. Noţingher, C. Stancu, F. Wiesbrock and S. Schlögl, “Polyethylene Nanocomposites for Power Cable Insulations,” *Polymers (Basel),* vol. 11, no. 1, 2018.

[47] M. G. Kenneth St. John, “Evaluation of the wear performance of a polycarbonate-urethane acetabular component in a hip joint simulator and comparison with UHMWPE and cross-linked UHMWPE,” *Journal of Biomaterial Applications,* vol. 27, no. 1, 2012.

[48] S. B. Kim, Y. J. Kim, T. L. Yoon, S. A. Park, I. H. Cho, E. J. Kim, I. A. Kim and J.-W. Shin, “The characteristics of a hydroxyapatite–chitosan–PMMA bone cement,” *Biomaterials,* vol. 25, no. 26, pp. 5715-5723, 2004.

[49] J. Y. Wong and J. D. Bronzino, Biomaterials, CRC Press, 2007.

[50] M. Mikulewicz and K. Chojnacka, “Cytocompatibility of Medical Biomaterials Containing Nickel by Osteoblasts: a Systematic Literature Review,” *Biological Trace Element Research,* vol. 142, p. 865–889, 2011.

[51] A. J. Mitchelson, C. J. Wilson, W. M. Mihalko, T. M. Grupp, B. T. Manning, D. A. Dennis, S. B. Goodman, T. H. Tzeng, S. Vasdev and a. K. J. Saleh, “Biomaterial Hypersensitivity: Is It Real? Supportive Evidence and Approach Considerations for Metal Allergic Patients following Total Knee Arthroplasty,” *Biomed Res Int,* 2015.

[52] H. R. Marc Long, “Titanium alloys in total joint replacement—a materials science perspective,” *Biomaterials,* vol. 19, no. 18, pp. 1621-1639, 1998.

[53] B. Bal, J. Garino, M. Ries and M. Rahaman, “A Review of Ceramic Bearing Materials in Total Joint Arthroplasty,” *HIP Int.,* vol. 17, no. 1, 2007.

[54] C. Piconi, G. Maccauro, F. Muratori and E. B. D. Prever, “Alumina and Zirconia Ceramics in Joint Replacements,” *Journal of Applied Biomaterials and Biomechanics,* vol. 1, no. 1, pp. 19-32, 2003.

[55] R. G. T. Geesink, “Osteoconductive Coatings for Total Joint Arthroplasty,” *Clinical Orthopaedics and Related Research,* vol. 395, pp. 53-65, 2002.

[56] R. D. Bloebaum, D. Beeks, L. D. Dorr, C. G. Savory, J. A. DuPont and A. A. Hofmann, “Complications with hydroxyapatite particulate separation in total hip arthroplasty,” *Clinical orthopaedics and related research,* vol. 298, pp. 19-26, 1994.

[57] M. K. Harman, S. A. Banks and W. Hodge, “Wear analysis of a retrieved hip implant with titanium nitride coating,” *The Journal of Arthroplasty,* vol. 12, no. 8, pp. 938-945, 1997.

[58] M. Pappas, G. Makris and F. Buechel, “Titanium nitride ceramic film against polyethylene. A 48 million cycle wear test.,” *Clinical Orthopaedics and Related Research,* vol. 317, pp. 64-70, 1995.

[59] R. R. P. Manuela Teresa, “The in-vivo wear performance of prosthetic femoral heads with titanium nitride coating,” *Biomaterials,* vol. 21, no. 9, pp. 907-913, 2000.

[60] R. P. v. Hove, I. N. Sierevelt, B. J. v. Royen and P. A. Nolte, “Titanium-Nitride Coating of Orthopaedic Implants: A Review of the Literature,” *BioMed Research International,* 2015.

[61] R. Ramadoss, N. Kumar, S. Dash, D. Arivuoli and A. Tyagi, “Wear mechanism of CrN/NbN superlattice coating sliding against various counterbodies,” *International Journal of Refractory Metals and Hard Materials,* vol. 41, pp. 547-552, 2013.

[62] H. Wang, M. Stack, S. Lyona, P. Hovsepian and W.-D. Münz, “The corrosion behaviour of macroparticle defects in arc bond-sputtered CrN/NbN superlattice coatings,” *Surface and Coatings Technology,* vol. 126, no. 2-3, pp. 279-287, 2000.

[63] J. Tipper, P. Firkins, A. Besong, P. Barbour, J. Nevelos, M. Stone, E. Ingham and J. Fisher, “Characterisation of wear debris from UHMWPE on zirconia ceramic, metal-on-metal and alumina ceramic-on-ceramic hip prostheses generated in a physiological anatomical hip joint simulator,” *Wear,* vol. 250, no. 1-12, pp. 120-128, 2001.

[64] J. Zeman, M. Ranuša, M. Vrbka, J. Gallo, I. Křupka and M. Hartl, “UHMWPE acetabular cup creep deformation during the run-in phase of THA's life cycle,” *Journal of the Mechanical Behavior of Biomedical Materials,* vol. 87, pp. 30-39, 2018.

[65] F. W. Chan, J. D. Bobyn, J. B. Medley, J. J. Krygier and M. Tanzer, “Wear and Lubrication of Metal-on-Metal Hip Implants,” *Clinical Orthopaedics and Related Research,* vol. 369, pp. 10-24, 1999.

[66] J. L. Tipper, P. J. Firkins, E. Ingham, J. Fisher, M. H. Stone and R. Farrar, "Quantitative analysis of the wear and wear debris from low and high carbon content cobalt chrome alloys used in metal on metal total hip replacements," *Journal of Materials Science: Materials in Medicine,* vol. 10, p. 353–362, 1999.

[67] R. M. Gul and F. J. McGarry, "Processing of ultra-high molecular weight polyethylene by hot isostatic pressing, and the effect of processing parameters on its microstructure.," *Polymer Engineering and Science,* vol. 44, no. 10, pp. 1848-1857, 2004.

[68] M. J. Nine, D. Choudhury, A. C. Hee, R. Mootanah and N. A. A. Osman, "Wear Debris Characterization and Corresponding Biological Response: Artificial Hip and Knee Joints," *Materials,* vol. 7, pp. 980-1016, 2014.

[69] C.-H. Huang, F.-Y. Ho, H.-M. Ma, C.-T. Yang, J.-J. Liau, H.-C. Kao, T.-H. Young and C.-K. Cheng, "Particle size and morphology of UHMWPE wear debris in failed total knee arthroplasties—a comparison between mobile bearing and fixed bearing knees," *Journal of Orthopaedic Research,* vol. 20, no. 5, pp. 1038-1041, 2006.

[70] A. K.Madl, M. Liong, M. Kovochich, B. L.Finley, D. J.Paustenbach and G. O. DVM, "Toxicology of wear particles of cobalt-chromium alloy metal-on-metal hip implants Part I: Physicochemical properties in patient and simulator studies," *Nanomedicine: Nanotechnology, Biology and Medicine,* vol. 11, no. 5, pp. 1201-1215, 2015.

[71] M. Kovochich, E. S. Fung, E. Donovan, K. M. Unice, D. J. Paustenbach and B. L. Finley, "Characterization of wear debris from metal-on-metal hip implants during normal wear versus edge-loading conditions," *Journal of Biomedical Research,* vol. 106, no. 3, pp. 986-996, 2017.

[72] A. Hatton, J. Nevelos, J. Matthews, J. Fisher and E. Ingham, "Effects of clinically relevant alumina ceramic wear particles on TNF-α production by human peripheral blood mononuclear phagocytes," *Biomaterials,* vol. 24, no. 7, pp. 1193-1204, 2003.

[73] J. Tipper, A. Hatton, J. Nevelos, E. Ingham, C. Doyle, R. Streicher, A. Nevelos and J. Fisher, "Alumina–alumina artificial hip joints. Part II:

Characterisation of the wear debris from in vitro hip joint simulations," *Biomaterials,* vol. 23, no. 16, pp. 3441-3448, 2002.

[74] T. Stewart, J. Tipper, R. Streicher, E. Ingham and J. Fisher, "Long-term wear of HIPed alumina on alumina bearings for THR under micro-separation conditions," *J Mater Sci Mater Med,* vol. 12, p. 1053, 2001.

[75] J. Fisher, X. Q. Hu, T. D. Stewart, S. Williams, J. L. Tipper, E. Ingham, M. H. Stone, C. Davies, P. Hatto, J. Bolton, M. Riley, C. Hardaker, G. H. Isaac and G. Berry, "Wear of surface engineered metal-on-metal hip prostheses," *Journal of Materials Science: Materials in Medicine,* vol. 15, p. 225–235, 2004.

[76] G. W. Blunn, "A novel ceramic coating for reduced metal ion release in metal-on-metal hip surgery," *Journal of Biomerdical Materials Research,* vol. 107, no. 6, pp. 1760-1771, 2018.

[77] J. D. Harris, "Autologous Chondrocyte Implantation: A Systematic Review," *The Journal of Bone and Joint Surgery: American Volume,* vol. 92, no. 12, p. 2220–2233, 2010.

[78] J. V. Wanschitz, O. Dubourg, E. Lacene, M. B. Fischer, R. Höftberger, H. Budka, N. B. Romero, B. Eymard, S. Herson, G. S. Butler-Browne, T. Voit and O. Benveniste, "Expression of myogenic regulatory factors and myo-endothelial remodeling in sporadic inclusion body myositis," *Neuromuscular Disorders,* vol. 23, no. 1, pp. 75-83, 2013.

[79] N. Heidari, T.-M. Borg, S. Olgiati, M. Slevin, A. Danovi, B. Fish, A. Wilson and a. A. Noorani1, "Microfragmented Adipose Tissue Injection (MFAT) May Be a Solution to the Rationing of Total Knee Replacement: A Prospective, Gender-Bias Mitigated, Reproducible Analysis at Two Years," *Stem Cells International,* 2021.

[80] A. Gobbi, I. Dallo, C. Rogers, R. D. Striano, K. Mautner, R. Bowers, M. Rozak and N. B. &. W. D. Murrell, "Two-year clinical outcomes of autologous microfragmented adipose tissue in elderly patients with knee osteoarthritis: a multi-centric, international study," *International Orthopaedics,* vol. 45, p. 1179–1188, 2021.

[81] T. E. Foster, “Platelet-Rich Plasma: From Basic Science to Clinical Applications,” *The American Journal of Sports Medicine,* vol. 37, no. 11, pp. 2259-2272, 2009.

[82] T. M. Southworth, N. B. Naveen, T. M. Tauro, N. L. Leong and B. J. Cole, “The Use of Platelet-Rich Plasma in Symptomatic Knee Osteoarthritis,” *The Journal of Knee Surgery,* vol. 32, no. 01, pp. 037-045, 2019.

[83] L. P. Peixoto, P. Goljan and M. J. Philippon, “Partial Joint Replacement,” *Hip Joint Restoration,* pp. 763-768, 2017.

[84] D. Lundin and K. Sarakinos, “An introduction to thin film processing using high-power impulse magnetron sputtering.,” *Journal of Materials Research,* vol. 27, no. 05, pp. 780-792, 2012.

[85] V. D. a. M. P. Suchea, Functional Nanostructured Interfaces for Environmental and Biomedical Applications: A volume in Micro and Nano Technologies, Elsevier, 2019.

[86] A. P. Ehiasarian, “High power pulsed magnetron sputtering CrN films,” *Surface and Coatings Technology ,* Vols. 163-164, pp. 267-272, 2003.

[87] K. Sarakinos, J. Alami and S. Konstantinidis, “High power pulsed magnetron sputtering: A review on scientific and engineering state of the art.,” *Surface and Coatings Technology,* vol. 204, no. 11, pp. 1661-1684, 2010.

[88] P. Hovsepian, D. Lewis, W. Münz, S. Lyon and M. Tomlinson, “Combined cathodic arc/unbalanced magnetron grown CrN/NbN superlattice coatings for corrosion resistant applications,” *Surface and Coatings Technology,* vol. 120–121, pp. 535-541, 1999.

[89] P. Hovsepian, D. Lewis and W.-D. Münz, “Recent progress in large scale manufacturing of multilayer/superlattice hard coatings,” *Surface and Coatings Technology,* vol. 133–134, pp. 166-175, 2000.

[90] Y. Ou, J.Lin, S.Tong, H.L.Che, W.D.Sproul and M.K.Leia, "Wear and corrosion resistance of CrN/TiN superlattice coatings deposited by a combined deep oscillation magnetron sputtering and pulsed dc magnetron sputtering," *Applied Surface Science,* vol. 351, pp. 332-343, 2015.

[91] W.-D. Münz, L. Donohue and P. Hovsepian, "Properties of various large-scale fabricated TiAlN- and CrN-based superlattice coatings grown by combined cathodic arc–unbalanced magnetron sputter deposition," *Surface and Coatings Technology,* vol. 125, no. 1-3, pp. 269-277, 2000.

[92] R. Lappalainen and S. S. Santavirta, "Potential of Coatings in Total Hip Replacement.," *Clinical Orthopaedics and Related Research,* vol. 430, pp. 72-79, 2005.

[93] J. Nevelos, "Microseparation of the centers of alumina-alumina artificial hip joints during simulator testing produces clinically relevant wear rates and patterns," *The Journal of Arthroplasty,* vol. 15, no. 6, pp. 793-795, 2000.

[94] D.B.Lewis, S.J.Creasey, C.Wüstefeld, A.P.Ehiasarian and P.Eh.Hovsepian, "The role of the growth defects on the corrosion resistance of CrN/NbN superlattice coatings deposited at low temperatures," *Thin Solid Films,* vol. 503, no. 1-2, pp. 143-148, 2006.

[95] B. Biswas, Y. Purandare, A. Sugumaran, I. Khan and P. Eh.Hovsepiana, "Effect of chamber pressure on defect generation and their influence on corrosion and tribological properties of HIPIMS deposited CrN/NbN coatings," *Surface and Coatings Technology,* vol. 336, pp. 84-91, 2018.

[96] L. C. Hernández, L. Ponce, A. Fundora, E. López and E. Pérez, "Nanohardness and Residual Stress in TiN Coatings," *Materials,* vol. Special Issue Hard Materials: Advances in Synthesis and Understanding, 2011.

[97] S. Datta, M. Das, V. K. Balla, S. Bodhak and V. K. Murugesanb, "Mechanical, wear, corrosion and biological properties of arc deposited

titanium nitride coatings," *Surface and Coatings Technology,* vol. 344, pp. 214-222, 2018.

[98] M. Alvarez-Vera, J.A.Ortega-Saenz and M.A.L.Hernandez-Rodríguez, "A study of the wear performance in a hip simulator of a metal–metal Co–Cr alloy with different boron additions," *Wear,* vol. 301, no. 1-2, pp. 175-181, 2013.

[99] P. Sahoo, S. K. Das and J. P. Davim, "Mechanical Behaviour of Biomaterials," in *1 - Tribology of materials for biomedical applications*, Woodhead Publishing Series in Biomaterials, 2019, pp. 1-45.

[100] C. Cuao-Moreu, M. Alvarez-Vera, E. García-Sánchez, D. Maldonado-Cortés, A. Juárez-Hernández and M. Hernandez-Rodriguez, "Characterization of a duplex coating (boriding + sputter-deposited AlCrON) synthesized on an ASTM F-75 cobalt alloy," *Thin Solid Films,* vol. 712, 2020.

[101] C. Nich, Y. Takakubo, J. Pajarinen, M. Ainola, A. Salem, T. Sillat, A. J. Rao, M. Raska, Y. Tamaki, M. Takagi, Y. T. Konttinen, S. B. Goodman and J. Gallo, "Macrophages – Key Cells in the Response to Wear Debris from Joint Replacements," *J Biomed Mater Res A,* vol. 101, no. 10, p. 3033–3045, 2013.

[102] M. Manlapaz, "In vitro activation of human fibroblasts by retrieved titanium allow wear debris," *Journal of Orthopaedic Research ,* vol. 14, no. 3, pp. 465-472, 2005.

[103] A. Harada, N. Sekido, T. Akahoshi, T. Wada, N. Mukaida and K. Matsushima, "Essential involvement of interleukin-8 (IL-8) in acute inflammation," *Journal of Leukocyte Biology,* vol. 56, no. 5, pp. 559-564, 1994.

[104] A. Yadav, V. Saini and S. Arora, "MCP-1: Chemoattractant with a role beyond immunity: A review," *Clinica Chimica Acta,* vol. 411, no. 21–22, pp. 1570-1579, 2010.

[105] K. K. Kim, D. Sheppard and H. A. Chapman, “TGF-β1 Signaling and Tissue Fibrosis,” *Cold Spring Harbor Perspectives in Biology,* vol. 10, no. 4, 2018.

[106] M. F. Young, “Bone matrix proteins: their function, regulation, and relationship to osteoporosis,” *Osteoporosis International,* vol. 14, pp. 35-42, 2003.

[107] X. Zhang, S. G. Morham, R. Langenbach, D. A. Young, L. Xing, B. F. Boyce, E. J. Puzas, R. N. Rosier, R. J. O'Keefe and E. M. Schwarz, “Evidence for a Direct Role of Cyclo-Oxygenase 2 in Implant Wear Debris-Induced Osteolysis,” *Journal of Bone and Mineral Research,* vol. 16, no. 4, pp. 660-670, 2001.

[108] H. Glantschnig, J. E. Fisher, G. Wesolowski, G. A. Rodan and A. A. Reszka, “M-CSF, TNFα and RANK ligand promote osteoclast survival by signaling through mTOR/S6 kinase,” *Cell Death & Differentiation,* vol. 10, p. 1165–1177, 2003.

[109] E. Luegmayr, H. Glantschnig, G. A. Wesolowski, M. A. Gentile, J. E. Fisher, G. A. Rodan and A. A. Reszka, “Osteoclast formation, survival and morphology are highly dependent on exogenous cholesterol/lipoproteins,” *Cell Death & Differentiation,* vol. 11, p. 108–S118, 2004.

[110] S. L. Teitelbaum, “Osteoclasts; culprits in inflammatory osteolysis,” *Arthritis Research & Therapy,* vol. 8, no. 201, 2005.

[111] T. Akisue, T. W. Bauer, C. F. Farver and Y. Mochida, “The effect of particle wear debris on NFκB activation and pro-inflammatory cytokine release in differentiated THP-1 cells.,” *Journal of Biomedical materials research,* vol. 59, no. 3, pp. 507-515, 2002.

[112] D. N. Cook, “The role of MIP-1α in Inflammation and hematopoiesis,” *Journal of Leukocyte Biology,* vol. 59, no. 1, pp. 61-66, 1996.

[113] S.-Y. Zhang, S. Boisson-Dupuis, A. Chapgier, K. Yang, J. Bustamante, A. Puel, C. Picard, L. Abel, E. Jouanguy and J.-L. Casanova, “Inborn errors of interferon (IFN)-mediated immunity in humans: insights into the

respective roles of IFN-α/β, IFN-γ, and IFN-λ in host defense," *Immunological Reviews,* vol. 226, no. 1, pp. 29-40, 2008.

[114] Z. Sheikh, P. J. Brooks, O. Barzilay, N. Fine and M. Glogauer, "Macrophages, Foreign Body Giant Cells and Their Response to Implantable Biomaterials," *Materials,* vol. 8, no. 9, pp. 5671-5701, 2015.

[115] J. M. Anderson, A. Rodriguez and D. T. Chang, "Foreign body reaction to biomaterials," *Seminars in Immunology,* vol. 20, no. 2, pp. 86-100, 2008.

[116] J. B. Matthews, "Evaluation of the Response of Primary Human Peripheral Blood Mononuclear Phagocytes to Challenge with In Vitro Generated Clinically Relevant UHMWPE Particles of Known Size and Dose," *Journal of Biomedical materials research,* vol. 52, no. 2, pp. 296-307, 2000.

[117] T. R. Green, "Effect of Size and Dose on Bone Resorption Activity of Macrophages by In vitro Clinically Relevant Ultra HighMolecular Weight Polyethylene Particles.," *Journal of Biomedical materials research ,* vol. 53, no. 5, pp. 490-497, 2000.

[118] K. Kohilas, M. Lyons, R. Lofthouse, C. G. Frondoza, R. Jinnah and D. S. Hungerford, "Effect of prosthetic titanium wear debris on mitogen-induced monocyte and lymphoid activation.," *Journal of Biomedical materials research,* vol. 47, no. 1, pp. 95-103, 1999.

[119] E. Kubota, H. Imamura, T. Kubota, T. Shibata and K.-I. Murakami, "Interleukin 1β and stromelysin (MMP3) activity of synovial fluid as possible markers of osteoarthritis in the temporomandibular joint.," *Journal of Oral and Maxillofacial Surgery,* vol. 55, no. 1, pp. 20-27, 1997.

[120] B. F. Boyce, "Functions of RANKL/RANK/OPG in bone modeling and remodeling," *Arch Biochem Biophys,* vol. 473, no. 2, p. 139–146, 2008.

[121] T. D. Price, M. J. Schoeninger and G. J. Armelagos, "Bone Chemistry and Past Behavior: an Overview," *Journal of Human Evolution,* vol. 14, pp. 419-447, 1985.

[122] M. D. Markel, “Bone Structure and the Response of Bone to Stress,” in *Equine Fracture Repair, Second Edition*, 2019.

[123] B. J. T. Jonathon DJ. Black, “Bone structure: from cortical to calcium,” *Orthopaedics and Trauma,* vol. 34, no. 4, pp. 113-119, 2020.

[124] P. Milovanovic, “Bone tissue aging affects mineralization of cement lines,” *Bone,* vol. 110, pp. 187-193, 2018.

[125] A. J. S. Fox, A. Bedi and S. A. Rodeo, “The Basic Science of Articular Cartilage: Structure, Composition, and Function,” *Sports Health,* vol. 1, no. 6, p. 461–468, 2009.

[126] A. M. Bhosale and J. B. Richardson, “Articular cartilage: structure, injuries and review of management,” *British Medical Bulletin,* vol. 87, no. 1, p. 77–95, 2008.

[127] B. Young, P. Woodford and G. O'Dowd, Wheater's Functional Histology: A Text and Colour Atlas, Churchill Livingstone, 2006.

[128] L. Morawietz, R.-A. Classen, J. H. Schröder, C. Dynybil, C. Perka, A. Skwara, J. Neidel, T. Gehrke, L. Frommelt, T. Hansen, M. Otto, B. Barden, T. Aigner, P. Stiehl, T. Schubert, C. Meyer-Scholten, A. König, P. Ströbel, C. P. Rader, S. Kirschner, F. Lintner, W. Rüther, I. Bos and C. H, “Proposal for a histopathological consensus classification of the periprosthetic interface membrane,” *Journal of Clinical Pathology,* vol. 59, no. 6, p. 591–597, 2006.

[129] S. W. Tohtz, M. Müller, L. Morawietz, T. Winkler and C. Perka, “Validity of Frozen Sections for Analysis of Periprosthetic Loosening Membranes,” *Clinical Orthopaedics and Related Research,* vol. 468, no. 3, p. 762–768, 2010.

[130] S. N. Rampersad, “Multiple Applications of Alamar Blue as an Indicator of Metabolic Function and Cellular Health in Cell Viability Bioassays,” *Sensors (Basel),* vol. 12, no. 9, pp. 12347-60, 2012.

[131] A. M and F. A, “Enzyme Linked Immunosorbent Assay,” *StatPearls [Internet],* 2022.

[132] Y. Purandare, A. Ehiasarian, M. Stack and P. Hovsepian, “CrN/NbN coatings deposited by HIPIMS: A preliminary study of erosion–corrosion performance.,” *Surface and Coatings Technology,* vol. 204, no. 8, pp. 1158-1162, 2010.

[133] “NIST X-ray Photoelectron Spectroscopy Database, Version 4.1,” National Institute of Standards and Technology, Gaithersburg, 2012.

[134] B. Biswas, Y. Purandare, I. Khan and P. Eh.Hovsepiana, “Effect of substrate bias voltage on defect generation and their influence on corrosion and tribological properties of HIPIMS deposited CrN/NbN coatings,” *Surface and Coatings Technology,* vol. 344, pp. 383-393, 2018.

[135] R. K. Whittaker, H. S. Hothi, A. Eskelinen, G. W. Blunn, J. A. Skinner and A. J. Hart, “Variation in taper surface roughness for a single design effects the wear rate in total hip arthroplasty,” *Journal of Orthopaedic Research,* vol. 35, no. 8, pp. 1784-1792, 2017.

[136] P. Panjan, A. Drnovšek, P. Gselman, M. Čekada and M. Panjan, “Review of Growth Defects in Thin Films Prepared by PVD Techniques,” MDPI, 2020.

[137] K. Wasa, Handbook of Sputter Deposition Technology, Elsevier, 2012.

[138] A. Ehiasarian, R. New, W.-D. Münz, L. Hultman, U. Helmersson and V. Kouznetsov, “Influence of high power densities on the composition of pulsed magnetron plasmas,” *Vacuum,* vol. 65, no. 2, pp. 147-154, 2002.

[139] H. R. S. Hosseinzadeh, A. Eajazi and A. S. Shahi., “The bearing surfaces in total hip arthroplasty–options, material characteristics and selection,” in *Recent Advances in Arthroplasty*, InTech, 2012, pp. 163-209.

[140] C. P. Constable, J. Yarwood, P. Hovsepian, L. A. Donohue, D. B. Lewis and W.-D. Münz, “Structural determination of wear debris generated from

sliding wear tests on ceramic coatings using Raman microscopy.," *Journal of Vacuum Science & Technology A: Vacuum, Surfaces, and Films,* vol. 18, no. 4, 2000.

[141] J. Lin, X. Zhang, F. Ge and F. Huang, "Thick CrN/AlN superlattice coatings deposited by hot filament assisted HiPIMS for solid particle erosion and high temperature wear resistance," *Surface and Coatings Technology,* vol. 377, 2019.

[142] B. C. N. M. d. Castilho, A. M. Rodrigues, P. R. T. Avila, R. C. Apolinario, T. d. S. Nossa, M. Walczak, J. V. Fernandes, R. R. Menezes, G. d. A. Neves and H. C. Pinto, "Hybrid magnetron sputtering of ceramic superlattices for application in a next generation of combustion engines," *Scientific Reports,* vol. 12, no. 2342, 2022.

[143] F. Hashimoto, R. G. Chaudhari and S. N. Melkote, "Characteristics and Performance of Surfaces Created by Various Finishing Methods," *Procedia CIRP,* vol. 45, pp. 1-6, 2016.

[144] P. R. T. Avila, "Manufacture and optimization of nanostructured Cr-Al-N coatings produced by reactive magnetron sputtering," *University of São Paulo,* 2021.

[145] A. Krella and A. Marchewicz, "Effect of the reversal of the layer thickness ratio in the CrN/CrCN multilayer coating on cavitation-induced degradation," *Tribology International,* vol. 168, 2022.

[146] B. J. Ryan and K. M. Poduska, "Roughness effects on contact angle measurements," *American Journal of Physics,* vol. 76, no. 1074, 2008.

[147] K.-Y. Law, "Definitions for Hydrophilicity, Hydrophobicity, and Superhydrophobicity: Getting the Basics Right," *J. Phys. Chem. Lett.,* vol. 5, no. 4, p. 686–688, 2014.

[148] J. Paulitsch, M. Schenkel, A. Schintlmeister, H. Hutter and P. Mayrhofer, "Low friction CrN/TiN multilayer coatings prepared by a hybrid high power impulse magnetron sputtering/DC magnetron sputtering

deposition technique," *Thin Solid Films,* vol. 518, no. 19, pp. 5553-5557, 2010.

[149] D. Wang, Y. Fu, M. Hu, D. Jiang, X. Gao, Q. Wang, J. Yang, J. Sun and L. Weng, "Effect of Nb content on the microstructure and corrosion resistance of the sputtered Cr-Nb-N coatings," *Journal of Alloys and Compounds,* vol. 740, no. 5, pp. 510-518, 2018.

[150] L. H. G. Greczynski, "Reliable determination of chemical state in x-ray photoelectron spectroscopy based on sample-work-function referencing to adventitious carbon: Resolving the myth of apparent constant binding energy of the C 1s peak," *Applied Surface Science,* vol. 451, pp. 99-103, 2018.

[151] H. Piao and N. S. McIntyre, "Adventitious carbon growth on aluminium and gold–aluminium alloy surfaces," *Surface and Interface Analysis,* vol. 33, no. 7, pp. 591-594, 2002.

[152] D. R. Schmidt, H. Waldeck and W. J. Kao, "Protein Adsorption to Biomaterials," in *Biological Interactions on Materials Surfaces*, 2009, pp. 1-18.

[153] M. Vinnichenko, T. Chevolleau, M. Pham, L. Poperenko and M. Maitz, "Spectroellipsometric, AFM and XPS probing of stainless steel surfaces subjected to biological influences," *Applied Surface Science,* vol. 201, no. 1-4, pp. 41-50, 2002.

[154] I. Cimalla, F. Will, K. Tonisch, M. Niebelschütz, V. Cimalla, V. Lebedev, G. Kittler, M. Himmerlich, S. Krischok, J. Schaefer, M. Gebinoga, A. Schober, T. Friedrich and O. Ambacher, "AlGaN/GaN biosensor—effect of device processing steps on the surface properties and biocompatibility," *Sensors and Actuators B: Chemical,* vol. 123, no. 2, pp. 740-748, 2007.

[155] M. D. Henry, S. Wolfley, T. Young, T. Monson, C. J. Pearce, R. Lewis, B. Clark, L. Brunke and N. Missert, "Degradation of Superconducting Nb/NbN Films by Atmospheric Oxidation," *IEEE Transactions on Applied Superconductivity,* vol. 27, no. 4, pp. 1-5, 2017.

[156] A. Ermolieff, M. Girard, C. Raoul, C. Bertrand and Tran Minh Duc, “An XPS comparative study on thermal oxide barrier formation on Nb and NbN thin films,” *Applications of Surface Science,* vol. 21, no. 1-4, pp. 65-79, 1985.

[157] A. Darlinski and J. Halbritter, “Angle-resolved XPS studies of oxides at NbN, NbC, and Nb surfaces,” *Surface and Interface Analysis,* vol. 10, no. 5, pp. 223-237, 1987.

[158] I. Milošev, H.-H. Strehblow and B. Navinšek, “XPS in the study of high-temperature oxidation of CrN and TiN hard coatings,” *Surface and Coatings Technology,* vol. 74–75, no. 2, pp. 897-902, 1995.

[159] U. Bardi, S. Chenakin, F. Ghezzi, C. Giolli, A. Goruppa, A. Lavacchi, E. Miorin, C. Pagura and A. Tolstogouzov, “High-temperature oxidation of CrN/AlN multilayer coatings,” *Applied Surface Science,* vol. 252, no. 5, pp. 1339-1349, 2005.

[160] J. Lefebvre, F. Galli, C. L. Bianchi, G. S. Patience and D. C. Boffito, “Experimental methods in chemical engineering: X-ray photoelectron spectroscopy-XPS,” *The Canadian Journal of Chemical Engineering,* vol. 97, no. 10, pp. 2588-2593, 2019.

[161] O. Lavigne, C. Alemany-Dumont, B. Normand, M. Berger, C. Duhamel and P. Delichére, “The effect of nitrogen on the passivation mechanisms and electronic properties of chromium oxide layers,” *Corrosion Science,* vol. 53, no. 6, pp. 2087-2096, 2011.

[162] S. Gallegos-Cantú, M. Hernandez-Rodriguez, E. Garcia-Sanchez, A. Juarez-Hernandez, J. Hernandez-Sandoval and R. Cue-Sampedro, “Tribological study of TiN monolayer and TiN/CrN (multilayer and superlattice) on Co–Cr alloy,” *Wear,* vol. 330–331, pp. 439-447, 2015.

[163] P. E. Hovsepian, A. P. Ehiasarian, Y. Purandare, A. A. Sugumaran, T. Marriott and I. Khan, “Development of superlattice CrN/NbN coatings for joint replacements deposited by high power impulse magnetron sputtering,” *Journal of Materials Science: Materials in Medicine,* vol. 27, no. 147, 2016.

[164] J. Ortega-Saenz, M. Alvarez-Vera and M. Hernandez-Rodriguez, “Biotribological study of multilayer coated metal-on-metal hip prostheses in a hip joint simulator,” *Wear,* vol. 301, no. 1-2, pp. 234-242, 2013.

[165] C. I. Esposito, W. L. Walter, A. Roques, M. A. Tuke, B. A. Zicat, W. R. Walsh and W. K. Walter, “Wear in alumina-on-alumina ceramic total hip replacements: A retrieval analysis of edge loading,” *The Journal of Bone and Joint Surgery. British volume,* Vols. 94-B, no. 7, 2012.

[166] I. C. P. Clarke and M. T. P. Manley, “How do alternative bearing surfaces influence wear behavior?,” *Journal of the American Academy of Orthopaedic Surgeons,* vol. 16 , pp. S86-S93, 2008.

[167] J. Girard, “Femoral head diameter considerations for primary total hip arthroplasty,” *Orthopaedics & Traumatology: Surgery & Research ,* vol. 101, no. 1, Supplement, pp. S25-S29, 2015.

[168] Brooks, R.A., J. Wimhurst and N. Rushton, “Endotoxin contamination of particles produces misleading inflammatory cytokine responses from macrophages in vitro.,” *Journal of Bone & Joint Surgery, British Volume,* Vols. 84-B, no. 2, pp. 295-299, 2002.

[169] M. B. Gorbet and M. V. Sefton, “Endotoxin: the uninvited guest,” *Biomaterials,* vol. 26, no. 34, pp. 6811-6817, 2005.

[170] R. A. Brooks, J. A. Wimhurst and N. Rushton, “Endotoxin contamination of particles produces misleading inflammatory cytokine responses from macrophages in vitro,” *Journal of Bone and Joint Surgery,* Vols. 84-B, no. 2, 2002.

[171] U.S. Department of Health and Human Services, “Guidance for Industry: Pyrogen and Endotoxins Testing: Questions and Answers,” 2012.

[172] G. Zambonin, S. Colucci, F. Cantatore and M. Grano, “Response of Human Osteoblasts to Polymethylmetacrylate In Vitro,” *Calcified Tissue International,* vol. 62, pp. 362-365, 1998.

[173] A. R. Kamer, N. El-Ghorab, N. Marzec, J. E. Margarone and R. Dziak, "Nicotine induced proliferation and cytokine release in osteoblastic cells," *International Journal of Molecular Medicine,* vol. 17, pp. 121-127, 2006.

[174] A. Rodrigo, G. Vallés, L. Saldaña, M. Rodríguez, M. E. Martínez, L. Munuera and N. Vilaboa, "Alumina Particles Influence the Interactions of Cocultured Osteoblasts and Macrophages," *Journal of Orthopaedic Research,* vol. 24, no. 1, pp. 46-54, 2005.

[175] F. Tessaro, T. Ayala, E. Nolasco, L. Bella and J. Martins, "Insulin Influences LPS-Induced TNF-α and IL-6 Release Through Distinct Pathways in Mouse Macrophages from Different Compartments," *Cellular Physiology and Biochemistry,* vol. 42, no. 5, 2017.

[176] Y. Zhou, H. Zhang, G. Zhang, Y. He, P. Zhang, Z. Sun, Y. Gao and Y. Tan, "Calcitonin gene-related peptide reduces Porphyromonas gingivalis LPS-induced TNF-α release and apoptosis in osteoblasts," *Molecular Medicine Reports,* vol. 17, no. 2, pp. 3246-3254, 2017.

[177] E. A. Moelants, A. Mortier, J. V. Damme and P. Proost, "Regulation of TNF-a with a focus on rheumatoid arthritis," *Immunology and Cell Biology,* vol. 91, pp. 393-401, 2013.

[178] A. Dalal, V. Pawar, K. McAllister, C. Weaver and N. J. Hallab, "Orthopedic implant cobalt-alloy particles produce greater toxicity and inflammatory cytokines than titanium alloy and zirconium alloy-based particles in vitro, in human osteoblasts, fibroblasts, and macrophages," *Society for Biomaterials,* vol. 100A, no. 8, pp. 2147-2158, 2012.

[179] F. v. Knoch, H. E. Rubash, A. Shanbhag, S. R. Goldring and D. R. Cho, "Role of Endotoxin in Implant Loosening," in *Joint Replacement and Bone Resorption*, 2006, p. 16.

[180] E. M. Greenfield, Y. Bi, A. A. Ragab, V. M. Goldberg, J. L. Nalepka and J. M. Seabold, "Does endotoxin contribute to aseptic loosening of orthopedic implants?," *J Biomed Mater Res B Appl Biomater,* vol. 72, no. 1, pp. 179-185, 2005.

[181] B. BISWAS, “Growth defects in CrN/NbN coatings deposited by HIPIMS/UBM techniques,” Sheffield Hallam University, 2017.

[182] D. R. Lide, CRC Handbook of Chemistry and Physics, CRC Press, 2006.

[183] H. Hwang, Electrochemical analysis, Seoul: Free Academy Press, 2007.

[184] J. T. Harding, “Density of Niobium,” *Journal of Applied Physics,* vol. 37, no. 928, 1966.

[185] J. E. Yoo, J. Park, G. Cha and J. Choi, “Micro-length anodic porous niobium oxide for lithium-ion thin film battery applications,” *Thin Solid Films,* vol. 531, pp. 583-587, 2013.

[186] M. Berton, J. Oliveira, O. Baron, E. Santiago and C. D'Alkaine, “Synthesis and Characterization of Nb2O5 Produced Electrochemically and by Combution Reaction,” *Metals Materials and Processes,* vol. 17, no. 3-4, pp. 381-388, 2005.

[187] I. O. f. Standardization, “Biological evaluation of medical devices — Part 5: Tests for in vitro cytotoxicity,” *10993-5,* 2009.

[188] D. P. Lankvelda, S. Bullb, P. V. Dijka, J. Fink-Gremmelsb and L. J. Hellebrekersa, “Ketamine inhibits LPS-induced tumour necrosis factor-alpha and interleukin-6 in an equine macrophage cell line,” *Veterinary Research,* vol. 36, no. 2, pp. 257-262, 2005.

[189] W. D. Remes A, “Review: Immune response in biocompatibility,” *Biomaterials,* vol. 13, p. 731–43, 1992.

[190] J. Takebe, C. M. Champagne, S. Offenbacher, K. Ishibashi and L. F. Cooper, “Titanium surface topography alters cell shape and modulates bone morphogenetic protein 2 expression in the J774A.1 macrophage cell line,” *Journal of Biomaterials Research,* vol. 64A, no. 2, pp. 207-216, 2003.

[191] M. L. GODEK, J. A. SAMPSON, N. L. DUCHSHERER, Q. McELWEE and a. D. W. GRAINGER, “Rho GTPase protein expression and activation in murine monocytes/macrophages is not modulated by model biomaterial surfaces in serum-containing in vitro cultures,” *J Biomater Sci Polym Ed.,* vol. 17, no. 10, pp. 1141-1158, 2006.

[192] W. Hsueh, I. Charles Kuhn and P. Needleman, “Relationship of prostaglandin secretion by rabbit alveolar macrophages to phagocytosis and lysosomal enzyme release,” *The Biochemical Journa,* vol. 184, no. 2, pp. 345-354, 1979.

[193] A. M. Kaufman, C. I. Alabre, H. E. Rubash and A. S. Shanbhag, “Human macrophage response to UHMWPE, TiAlV, CoCr, and alumina particles: Analysis of multiple cytokines using protein arrays,” *Journal of Biomedical Materials Research,* vol. 84A, no. 2, pp. 464-474, 2007.

[194] K. S. Tana, L. Qiana, R. Rosado, b. P. M. Flood and L. F. Cooper, “The role of titanium surface topography on J774A.1 macrophage inflammatory cytokines and nitric oxide production,” *Biomaterials,* vol. 27, no. 30, pp. 5170-5177, 2006.

[195] R. P. v. Hove, P. A. Nolte, C. M. Semeins and J. Klein-Nulend, “Differences in proliferation, differentiation, and cytokine production by bone cells seeded on titanium–nitride and cobalt–chromium–molybdenum surfaces,” *Journal of Biomaterials Applications,* vol. 28, no. 2, 2013.

[196] Y. Li, D. Ma, H. Liu, P. Jing, Y. Gong, Z. Ayaz, F. Jing, X. Jiang and Y. Leng, “Biocompatibility of Ti-Mn-N films with different manganese contents,” *Surface and Coatings Technology,* vol. 403, 2020.

[197] X. Luo, D. Ma, P. Jing, Y. Gong, Y. Zhang, F. Jing and Y. Leng, “In vitro analysis of cell compatibility of TiCuN films with different Cu contents,” *Surface and Coatings Technology,* vol. 408, 2021.

[198] A. R. Kamer, N. El-Ghorab, N. Marzec, J. E. Margarone and R. Dziak, “Nicotine induced proliferation and cytokine release in osteoblastic cells,” *International Journal of Molecular Medicine,* vol. 17, pp. 121-127, 2006.

[199] L. Crémet, A. Broquet, B. Brulin, C. Jacqueline, S. Dauvergne, R. Brion, K. Asehnoune, S. Corvec, D. Heymann and N. Caroff, “Pathogenic potential of Escherichia coli clinical strains from orthopedic implant infections towards human osteoblastic cells,” *Pathogens and Disease,* vol. 73, no. 8, 2015.

[200] J. Roaa, G. Fargasa, A. Mateo and E. Jiménez-Piqué, “Dependence of nanoindentation hardness with crystallographic orientation of austenite grains in metastable stainless steels,” *Materials Science and Engineering: A,* vol. 645, pp. 188-195, 2015.

[201] S. G. Moss, M. E. Schweitzer, J. A. Jacobson, J. Brossmann, J. V. Lombardi, S. M. Dellose, J. R. Coralnick, K. N. Standiford and D. Resnick, “Hip joint fluid: detection and distribution at MR imaging and US with cadaveric correlation.,” *Radiology,* vol. 208, no. 1, 1998.

[202] K. Lochner, A. Fritsche, A. Jonitz, D. Hansmann, P. Mueller, B. Mueller-Hilke and R. Bader, “The potential role of human osteoblasts for periprosthetic osteolysis following exposure to wear particles,” *International Journal of Molecular Medicine,* vol. 28, no. 6, pp. 1055-1063, 2011.

[203] A. K. Dominique P.Pioletti, “The influence of wear particles in the expression of osteoclastogenesis factors by osteoblasts,” *Biomaterials,* vol. 25, no. 27, pp. 5803-5808, 2004.

[204] D. Granchi, I. Amato, L. Battistelli, G. Ciapetti, S. Pagani, S. Avnet, N. Baldini and A. Giunti, “Molecular basis of osteoclastogenesis induced by osteoblasts exposed to wear particles,” *Biomaterials,* vol. 26, no. 15, pp. 2371-2379, 2005.

[205] P. Lei, Z. Dai, Y. S. Zhang, H. Liu, W. Niu, K. Li, L. Wang, Y. Hu and J. Xie, “Macrophage inhibits the osteogenesis of fibroblasts in ultrahigh molecular weight polyethylene (UHMWPE) wear particle-induced osteolysis,” *Journal of Orthopaedic Surgery and Research,* vol. 14, no. 80, 2019.

[206] A. Jonitz-Heincke, K. Lochner, C. Schulze, D. Pohle, W. Pustlauk, D. Hansmann and R. Bader, “Contribution of human osteoblasts and

macrophages to bone matrix degradation and proinflammatory cytokine release after exposure to abrasive endoprosthetic wear particles," *2016,* vol. 14, no. 2, 2016.

[207] A. Viola, F. Munari, R. Sánchez-Rodríguez, T. Scolaro and A. Castegna, "The Metabolic Signature of Macrophage Responses," *Frontiers in Immunology,* vol. 10, no. 1462, 2019.

[208] M. I. Stunault, G. Bories, R. R. Guinamard and S. Ivanov, "Metabolism Plays a Key Role during Macrophage Activation," *Mediators of Inflammation,* 2018.

[209] L. J. Guilbert, B. Winkler-Lowen, A. Smith, D. R. Branch and M. Garcia-Lloret, "Analysis of the synergistic stimulation of mouse macrophage proliferation by macrophage colony-stimulating factor (CSF-1) and tumor necrosis factor a (TNF-α)," *Journal of Leukocyte Biology,* vol. 54, no. 1, pp. 65-72, 1993.

[210] J. Braune, U. Weyer, C. Hobusch, J. Mauer, J. C. Brüning, I. Bechmann and M. Gericke, "IL-6 Regulates M2 Polarization and Local Proliferation of Adipose Tissue Macrophages in Obesity," *Journal of Immunology,* vol. 198, no. 7, pp. 2927-2934, 2017.

[211] S. S. Jakobsen, A. Larsen, M. Stoltenberg, J. Bruun and K. Soballe, "EFFECTS OF AS-CAST AND WROUGHT COBALT-CHROME-MOLYBDENUM AND TITANIUM-ALUMINIUM-VANADIUM ALLOYS ON CYTOKINE GENE EXPRESSION AND PROTEIN SECRETION IN J774A.1 MACROPHAGES," *European Cells and Materials,* vol. 14, pp. 45-55, 2007.

[212] P. C. Naha, M. Davoren, F. M. Lyng and H. J. Byrne, "Reactive oxygen species (ROS) induced cytokine production and cytotoxicity of PAMAM dendrimers in J774A.1 cells," *Toxicology and Applied Pharmacology,* vol. 246, no. 1-2, pp. 91-99, 2010.

[213] A. Petit, I. Catelas, J. Antoniou, D. J. Zukor and O. L. Huk, "Differential apoptotic response of J774 macrophages to alumina and ultra-high-molecular-weight polyethylene particles," *Journal of Orthopaedic Research,* vol. 20, no. 1, pp. 9-15, 2002.

[214] O. L. Huk, D. J. Zukor, J. Antoniou and A. Petit, "Effect of pamidronate on the stimulation of macrophage TNF-α release by ultra-high-molecular-weight polyethylene particles: a role for apoptosis," *Journal of Orthopaedic Research,* vol. 21, no. 1, pp. 81-87, 2003.

[215] I. Catelas, A. Petit, R. Marchand, D. J. Zukor, L. Yahia and O. L. Huk, "Cytotoxicity and macrophage cytokine release induced by ceramic and polyethylene particles in vitro," *The Journal of Bone and Joint Surgery: British Volume,* Vols. 81-B, no. 3, 1999.

[216] M.-H. Wu, T.-M. Pan, Y.-J. Wu, S.-J. Chang, M.-S. Chang and C.-Y. Hu, "Exopolysaccharide activities from probiotic bifidobacterium: Immunomodulatory effects (on J774A.1 macrophages) and antimicrobial properties," *International Journal of Food Microbiology,* vol. 144, no. 1, pp. 104-110, 2010.

[217] F.-x. Liu, C.-l. Wu, Z.-a. Zhu, M.-q. Li, Y.-q. Mao, M. Liu, X.-q. Wang and D.-g. Y. &. T.-t. Tang, "Calcineurin/NFAT pathway mediates wear particle-induced TNF-α release and osteoclastogenesis from mice bone marrow macrophages in vitro," *Acta Pharmacologica Sinica,* vol. 34, p. 1457–1466, 2013.

[218] Y. Li, C.-M. Bäckesjö, L.-A. Haldosén and U. Lindgren, "IL-6 receptor expression and IL-6 effects change during osteoblast differentiation," *Cytokine,* vol. 43, no. 2, pp. 165-173, 2008.

[219] A. Frost, K. B. Jonsson, O. Nilsson and Ö. Ljunggren, "Inflammatory cytokines regulate proliferation of cultured human osteoblasts," *Acta Orthopaedica Scandinavica,* vol. 68, no. 2, pp. 91-96, 1997.

[220] B. Osta, G. Benedetti and a. P. Miossec, "Classical and Paradoxical Effects of TNF-α on Bone Homeostasis," *Front Immunol.,* vol. 5, no. 48, 2014.

[221] L. Savarino, M. Greco, E. Cenni, L. Cavasinni, R. Rotini, N. Baldini and A. Giunti, "Differences in ion release after ceramic-on-ceramic and metal-on-metal total hip replacement," *The Journal of Bone and Joint Surgery. British volume,* Vols. 88-B, no. 4, 2006.

[222] P. W. Grieco, S. Pascal, J. M. Newman, N. V. Shah, S. G. Stroud, N. P. Sheth and A. V. Maheshwari, “New alternate bearing surfaces in total hip arthroplasty: A review of the current literature,” *J Clin Orthop Trauma,* vol. 9, no. 1, pp. 7-16, 2018.

[223] W.-D. Münz, M. Schenkel1, S. Kunkel1, J. Paulitsch and K. Bewilogua, “Industrial applications of HIPIMS,” *Journal of Physics: Conference Series,* vol. 100, no. 8, 2008.